Icing Impacts on Wind Energy Production

Davis, Neil

Publication date:
2014

Document Version
Publisher's PDF, also known as Version of record

Icing Impacts on Wind Energy Production

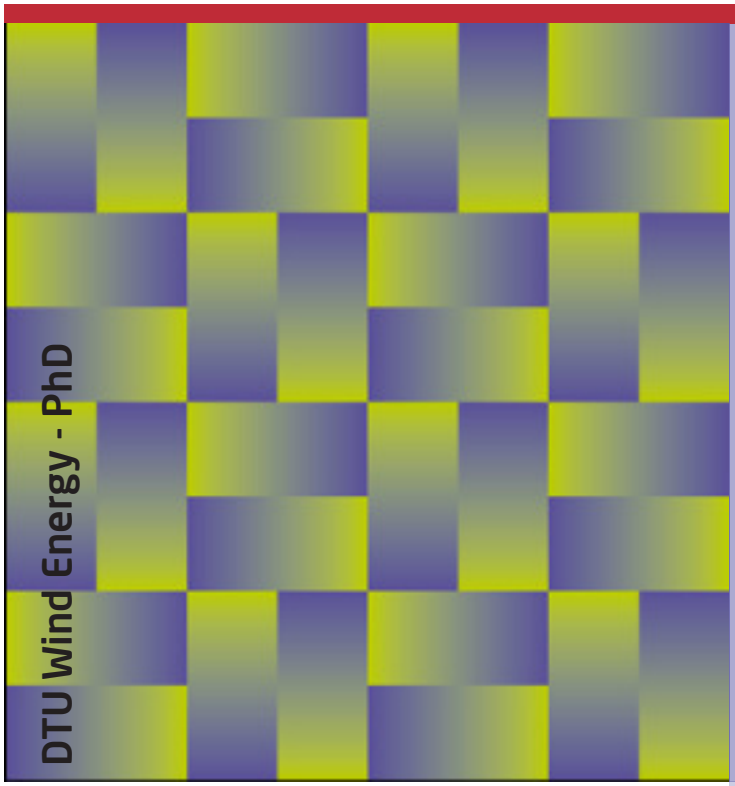

Neil N. Davis
DTU Wind Energy PhD-0025 (EN)
October 2014

DTU Wind Energy
Department of Wind Energy

Icing Impacts on Wind Energy Production

by

Neil N. Davis

B.Sc., Valparaiso University, 2003
M.Sc., North Carolina State University, 2007

A THESIS SUBMITTED IN PARTIAL FULFILLMENT OF
THE REQUIREMENTS FOR THE DEGREE OF

DOCTOR OF PHILOSOPHY

in

The Department of Wind Energy

(Meteorology Section)

TECHNICAL UNIVERSITY OF DENMARK

(Risø Campus)

January 6, 2015

Abstract

Icing on wind turbine blades has a significant impact on the operation of wind parks in cold climate regions. One of the largest impacts is to the power produced when ice is present on the turbine blades. This has a large effect on the annual energy production and the accuracy of short-term power forecasts. This thesis explores the impact of icing on produced power through observational analysis and numerical modeling.

I begin by investigating the impact of icing on power production through observations. Since there are no direct observations of ice growth on the turbine blades, a methodology was developed for the identification of icing periods from the turbine power data and the nacelle wind speeds. This method was based on the spread of power production observations at cold temperatures that was not seen during warmer periods.

Using the insights gained through the observational analysis, a modeling system was designed using a combination of physical and statistical models.

The first model in the system was the Weather Research and Forecasting (WRF) numerical weather prediction (NWP) model. The NWP model's estimation of cloud parameters (hydrometeors) was investigated, and it was found that their estimates varied greatly depending on the selection of microphysical parameterization. The results of the icing model, ice mass and duration, were similar when using the WSM5 parameterization of WRF or the more advanced Thompson parameterization.

The second model, iceBlade was a physical icing model developed to estimate ice mass on wind turbines. It was based on the Makkonen model for ice growth on a rotating cylinder to which several ice removal algorithms were added. The main difference from the Makkonen model was an increase in the incoming wind speed to account for the rotational speed of the turbine blade. The ice ablation algorithms also had a large impact on the duration of the icing events. The iceBlade model was found to better capture periods of turbine icing than the unadjusted model.

Finally, a statistical model was developed to simulate the relationship between the ice model results and the turbine power loss. The model took the shape of a hierarchal model that combined a decision tree model, based on the existence of ice on the turbine blade, and two Generalized Additive Models (GAM). The GAM for periods where icing was forecast included the parameters wind speed, total ice mass, and accumulated ice mass for the current period. This model was evaluated at six wind farms and found to improve the RMSE and mean bias at all wind farms except one. The model result was also compared with results from three other power production models that included icing impacts, and was found to have a similar range of performance.

The final conclusion was that the statistical model approach was not as important for correcting the power forecast for icing impacts as the quality of the physical model results. This was seen through the similar performance of the different power models in the intercomparison. Therefore, future research into the impact of turbine blade icing on power performance should focus on improvements to the physical icing model and NWP model estimation of hydrometeors.

Dansk Resumé

Dannelse af is på vingerne af vindmøller kan have stor indflydelse på driften af vindmølleparker i egne med koldt klima. Et af de største problemer er tab af produktion af elektricitet som følge af isdannelse på rotoren, hvilket påvirker såvel den årlige produktion såvel som prognoserne for el-produktion på kort sigt d.v.s. 1-2 dage frem til brug for elmarkedet. Denne afhandling beskriver hvorledes dannelse af is påvirker produktionen ved hjælp af computermodeller såvel som ved en analyse af relevante observationer.

Første del af arbejdet omhandler en analyse af hvordan isdannelse påvirker produktionen baseret på observationer. Idet direkte målinger af isdannelsen på en vindmølles blade ikke var tilgængelige blev der udviklet en metode til at identificere perioder med aktiv isdannelse baseret på sammenhørende observationer af elproduktion og målinger af vindhastighed fra nacellen. Metoden baserer sig på en analyse af mønstre i spredningen af samtidige observationer af vindhastighed og produktion ved henholdsvis lave temperaturer og ved temperaturer væsentligt over 0°C.

Baseret på disse indledende studier af isdannelse er der udviklet et modelkompleks bestående af en fysisk del og en statistisk del.

Den første model i systemet er baseret på Weather Research and Forecasting (WRF) numerical weather prediction (NWP) modellen. Denne NWP model benyttes til estimering af skyparametre (hydrometeorer) og resultaterne viser at disse parametre er meget følsomme over for valget af mikro-fysik parameteriseringen i WRF simuleringerne. Derimod er modellens estimater af ismasse og varighed af isdækket mindre følsomhed over for hvorvidt WSM5 parameteriseringen eller den mere avancerede Thompson parameterisering anvendes.

Den anden model, udviklet i dette arbejde (IceBlade) er en isdannelsesmodel som er baseret på fysiske principper. Formålet med denne model er at estimere ismassen på vindmøllevinger og modellen er baseret på Makkonen's model for isdannelse på en roterende cylinder tilføjet en række algoritmer til modellering af fjernelse af isen. Hovedforskellen mellem Makkonen modellen og den her udviklede model er højere lokale hastigheder gennem hensyntagen til rotorens rotationshastighed. Det demonstreres at iceBlade modellen bedre repræsenterer observeret isdannelse end Makkonen modellen. På rund af algoritmerne til modellering af isfjernelse er det muligt at modellere varigheden af perioder med is.

Endelig udvikledes en statistisk model til simulering af forholdet mellem isdannelse og tab af elproduktion. Denne model er opbygget hierarkisk og består af et beslutningstræ, baseret på hvorvidt isdannelse forekommer på vindmøllevingen, samt to generaliserede additive modeller (GAM). For perioder med aktiv dannelse af is er de vigtigste variable vindhastighed, samlet ismasse, og akkumuleret ismasse for en forudsigelse af tab. Modellen blev sammenlignet med observationer for 6 vindmølleparker og forbedrede RMSE samt den gennemsnitlige afvigelse for de 5 af vindmølleparker. Resultaterne blev derudover sammenlignet med tilsvarende resultater fra tre andre modeller for vindkraft produktion der indkluderede påvirkning fra isdannelse og udviste sammenlignelig nøjagtighed.

Sammenligningen af de forskellige modeller peger i retning af at den statistiske model ikke er lige så vigtig for modellering af tabet af elproduktion som den fysiske model. Det anbefales derfor at fremtidigt arbejde med modeller for tab af produktion som følge af isdannelse på vindmøllers vinger fokuserer på bedre fysiske modeller for isdannelsen og bedre NWP modellering af hydrometeorer (skydække).

Contents

Appendices

Preface

This thesis was prepared at the Department of Wind Energy at the Technical University of Denmark (DTUWind Energy) from June 2011 to July 2014 as partial fulfillment of the requirements for a PhD degree. The work was carried out at the Risø Campus except for two (one-month) research stays at Vestas Wind Systems A/S in Aarhus, Denmark. It was completed, under the supervision of Dr. Andrea N. Hahmann at DTU Wind Energy and co-supervision of Dr. Niels-Erik Clausen at DTU Wind Energy and Dr. Mark Žagar at Vestas Wind Systems A/S. Financial support was provided by the Top-Level Research Initiative (TFI) project, *Improved Forecast of Wind, Waves and Icing (Icewind)*, Vestas Wind Systems A/S, and the Nordic Energy Industry. The thesis consists of a summary report that includes some additional investigation into the the areas of study, with the main body of work contained in a collection of four appendices (1 published journal article, 2 submitted journal papers, and a chapter from the Icewind project report).

Acknowledgements

I would like to thank my advisors, Andrea Hahmann, Niels-Erik Clausen and Mark Žagar for their help, encouragement and advice throughout this project. I am also extremely grateful to Pierre Pinson who explained the statistical modeling approaches available in a way that was very understandable to a non-statistician. I would additionally like to thank DTU Wind Energy for providing me with this opportunity. Special thanks to everyone at the MET group, for the pleasant and engaging working environment.

Thanks to all of my office mates and fellow PhD students. Special thanks to Joakim and Patrick for being sounding boards when digging into the complexities of WRF modeling. I would like to thank Martin Haubjerg Rosgaard for the discussions about statistical modeling and data analysis, and for translating the abstract to Danish. I would also like to thank Claire Vincent for all the help she has provided in getting set up on the DTU computer systems and providing interesting ideas throughout my project.

I am very grateful for the support of my family especially since I am the first to move away from the U.S. I am particularly thankful to my wife, Amanda, who has been willing to put her career on hold and enthusiastically take on the adventure of moving to a new country, as well as proving to be a sounding board for countless presentations and reviewing the thesis many times over.

Finally, I would like to thank Vestas Wind Systems for supporting my PhD through the Icewind project and for hosting me on two research stays where I could discuss the project directly with industry partners.

Chapter 1

Introduction

Atmospheric icing affects many industries including: power transmission network operation (Farzaneh, 2008), aviation (Gent et al., 2000), and wind energy (Ilinca, 2011; Ronsten et al., 2012). Icing impacts all phases of a wind energy project, from the initial site assessment, through the installation, and during operation.

During the assessment phase, meteorological sensors measuring wind speed and wind direction can become iced, leading to faulty measurements (Tammelin, 1994). Also, the impact of icing on the expected power production needs to be quantified. Icing sensors have been developed to detect the icing potential at a site, however, these sensors have been shown to be unreliable (Homola et al., 2006) and do not correlate well with periods of production loss (Wickman, 2014). The combination of these factors increases the uncertainty of the production assessment for sites located in regions with a risk of icing.

The installation of wind turbines in cold climate regions requires special attention. Installations should be made during warm weather, for ease of access and safety. Additionally, consideration must be given to the ground conditions, particularly the existence of permafrost, when installing roads and other structures (Baring-Gould et al., 2012).

During the operation of a wind park, icing generates additional risks. Ice leads to a shortening of component lifespans, increased safety risks, and decreased annual energy production (AEP). When ice builds up on the turbine blades, it dramatically changes the aerodynamic forces (Jasinski et al., 1998). These changes combined with the increased mass on the blades can lead to increased loads on the turbine (Ronsten et al., 2012) increasing maintenance costs and potentially shortening turbine lifespans. Uneven shedding of the ice can result in a structural imbalance, further increasing loads (Frohboese and Anders, 2007). Ice shedding can also lead to increased safety risks due to ice throw, where ice is "thrown" from the turbine during the shedding process. Jowitt (2013) showed that for a modern turbine, Vestas V90, a 1-kg piece of ice could be thrown up to 200-m from the turbine. This falling ice can injure people or wildlife in the area and damage nearby structures (Morgan and Bossanyi, 1996). The safety risk is especially high for service personnel who have to attend to issues on site. Finally, there are economic risks associated with turbine icing. Commonly, the growth of ice on the blade leads to decreased performance. This is largely the result of an increase in aerodynamic drag (Virk et al., 2010). The decreased performance can have a large impact on the energy production of the turbine. Depending on the site, power losses may be up to 20% to 50% of AEP (Tammelin et al., 1998; Seifert and Richert, 1998; Barber et al., 2011). Additionally, for electricity markets in many European countries, where energy is priced on a day ahead market, icing can lead to penalties for underproduction from forecast values that do not include an adjustment for icing impacts.

Despite all of these challenges, a substantial number of wind energy parks are installed in cold climate regions. This is due to both the proximity of these regions to population centers, and the additional energy in the wind at colder temperatures due to the increased air density. Cold climate turbines refer to turbines that are installed both in regions where it is common for temperatures to fall below the normal operating limits of a wind turbine and in regions that have favorable conditions for ice growth on the wind turbine blades. These regions are found throughout the world, but are most commonly found in the northern parts of North America and Europe and in mountainous regions (Fig. 1.1).

The BTM World Market Update 2012 included a chapter on cold climate turbines (Wallenius et al., 2013). They estimated that 24% (69 GW) of global installed turbine capacity was located in cold climate regions at the

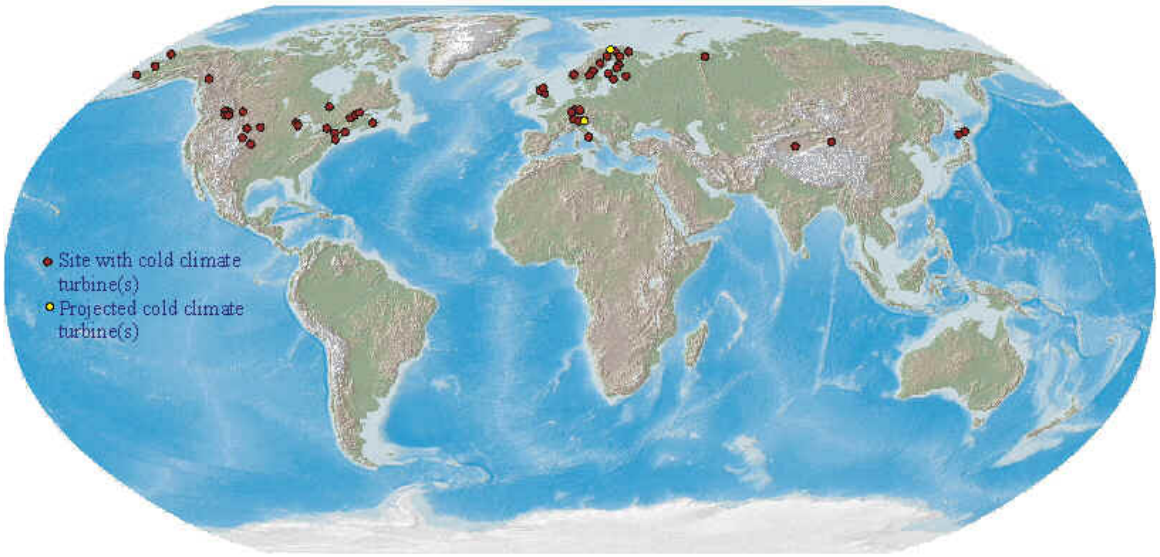

Figure 1.1: Locations of cold climate wind park installations. From http://arcticwind.vtt.fi/.

Table 1.1: IEA ice classification from Ronsten et al. (2012).

IEA Ice Class	Duration of meteorological icing [% of year]	Duration of Instrumental icing [% of year]	Production loss [% of AEP]
5	> 10	>20	>20
4	5-10	10-30	10-25
3	3-5	5-15	3-12
2	0.5-3	1-9	0.5-5
1	0-0.5	<1.5	0-0.5

end of 2012. For comparison, the installed capacity of offshore wind energy was only 5 GW at the end of 2012. Of the 69 GW of cold climate capacity, 72.5% had risk of icing. Wallenius et al. (2013) also included a forecast for installed capacity through 2017. They estimated that 20% of the planned 243 GW would be located in cold climate regions. Because of the wide geographic spread of cold climate regions, and the significant portion of installed wind energy capacity located in these regions, icing related research for wind energy has seen substantial growth in recent years.

Research into wind energy installations in cold climates has been on-going for many years. The BOREAS conferences were held approximately every two years from 1992 to 2005 in Finland. These conferences focused on the challenges of developing wind energy in cold climate regions, introduced new methods for analyzing wind park performance, and studied the fundamentals of the impact of ice growth on airfoil performance. Following the BOREAS conferences, the first Winterwind conference took place in 2008 in Sweden. Since 2010, this conference has been held annually and brings together researchers and industry experts to discuss recent advances in cold climate wind energy. In 2001, an international energy agency task (IEA Task 19) was created to focus on supplying industry with information about the operation of wind turbines in cold climates. Throughout this time, many advancements have been made into the improvement of the observational methods and modeling of icing on wind turbines.

IEA Task 19 has developed a five tier classification for icing (Ronsten et al., 2012), in an attempt to help developers identify the magnitude of icing related risks before developing a wind park. The classification has 3 independent criteria for identifying the severity of icing at a given location (Table 1.1). Meteorological icing is defined as periods when the meteorological conditions are right for the growth of ice to occur (Cattin et al., 2008). This is also known as active icing, since it corresponds to the time when ice is actively growing on a structure.

Instrumental icing refers to the time that ice remains on the structure. The instrumental icing period usually begins shortly after meteorological icing, but can last much longer, particularly when there are very cold temperatures reducing the ablation of the ice from the structure. Finally, the production loss corresponds to the percentage of annual energy production (AEP) that is lost due to icing. These three criteria may vary from site to site, for example a site may have an IEA Ice Class of 1 for meteorological icing, but of 4 for instrumental and production loss. Estimates of these three criteria can be created through numerical modeling studies.

Meteorological icing atlases have been created using ice accretion models to provide a measure of the number of hours of icing above a given threshold value (e.g., Byrkjedal, 2012a). These atlases typically use the ISO standard methodology of modeling ice growth on a freely rotating cylinder that is 1-m long and has a 0.03 m diameter (ISO standard 12494) to capture the number of icing hours expected for a given location. The ISO standard uses the Makkonen model (Makkonen, 2000, which will be discussed in detail in Chapter 6). The Makkonen model has been extensively used by the power network community (Farzaneh, 2008; Kringlebotn Nygaard et al., 2013) to model ice loads on power lines that can lead to tower collapse. It has also been used for the evaluation of cloud prediction in numerical weather prediction (NWP) models. In these studies, ice growth is observed on rotating cylinders and the estimated cloud parameters from an NWP model are used as inputs to the Makkonen model for comparison with the observed ice growth (Drage and Hauge, 2008; Fikke et al., 2008; Kringlebotn Nygaard et al., 2011; Yang et al., 2012). The aircraft industry also focuses largely on meteorological icing. The aviation community has developed advanced statistical models to identify regions with high probability of ice accumulation on aircraft (Bernstein et al., 2005; Ellrod and Bailey, 2007). By identifying these regions, pilots can hopefully avoid regions where the largest ice accumulation would occur reducing the risk to aircraft. The use of meteorological icing in wind energy research can be helpful for safety risk analysis, but is less important for icing impact studies. Although Bernstein et al. (2012) described active icing as the most important factor for ice growth, studies by Oechslin (2011) and Byrkjedal (2012b) show the importance of instrumental ice growth on the turbine production.

Instrumental icing has not been a large focus in either power network or aircraft icing, as the length of time the ice remains on the structure is not as important as it is to the wind industry. To model instrumental icing, ice removal (ablation) algorithms are used. These algorithms allow for ice models that can simulate the duration of the ice accumulation. The Finnish Icing Atlas (See http://www.tuuliatlas.fi/icingatlas/index.html; Ljungberg and Niemelä, 2011) has been developed for instrumental icing on a wind turbine by retaining ice on the blade until the temperature has exceeded 0.5°C for 6 hours. Other instrumental icing models (as described in detail in Chapter 6) include physical ice ablation algorithms for sublimation and melting. Ice shedding is also recognized as an important term in the ablation process, but is challenging to simulate.

Finally, the impact of icing on AEP has been studied largely through the use of computational fluid dynamics (CFD) models, such as TURBICE (Makkonen et al., 2001), LEWICE (Wright, 2002), and FENSAP-ICE (Habashi et al., 2004). CFD simulations have been common in aviation icing research to analyze the impact of ice growth on airfoil performance. This approach has also been used in the wind industry. In these studies, ice growth is simulated on an airfoil and the change in lift and drag are calculated (Barber et al., 2011; Homola et al., 2012; Turkia et al., 2013). These studies follow on experimental work by Seifert and Richert (1997) who created iced profiles for use in wind tunnels to estimate the change in lift and drag. Other studies used results from instrumental icing models coupled to NWP models to estimate the impact of icing on AEP (Oechslin, 2011; Byrkjedal, 2012b; Söderberg et al., 2013). These studies rely on statistical methods to relate the estimated ice mass to the loss in power production.

The goal of this Ph.D. project, part of the Icewind Nordic energy project and funded by the Top-Level Research Initiative (TFI), Vestas Wind Systems A/S, and the Nordic Energy Industry, was to advance the understanding of icing on wind turbines to improve the estimation of icing induced power losses through observational analysis and numerical modeling. By better understanding the icing process and its impact on turbine production, the risks of installing wind parks in cold climate regions can be better communicated with wind park developers. Additionally,

by running the NWP models in a forecast mode, a better estimate of the day-to-day production from turbines in cold climate regions can be made, through the inclusion of icing impacts on power production.

There were four goals in this project that relate to the four main areas of investigation.

1. *Observations:* Develop a robust consistent method for identifying icing from a turbines power curve using SCADA data.

2. *NWP model sensitivity:* Explore the sensitivity of ice model's results to different NWP parameterizations.

3. *Ice Models:* Investigate alternatives to the current state-of-the-art icing models through a more realistic representation of the turbine blade conditions, alternative accretion algorithms, and improved ablation algorithms.

4. *Power Loss Models:* Study the statistical relationship between modeled icing and production loss.

This thesis consists of this report, three journal papers and a chapter from the Icewind project report. The bulk of the research is contained in the three papers and project report chapter that are included in the Appendices. Each of these papers will be introduced in the thesis, summarizing the key results and conclusions. Additional research, not included in the papers, is presented throughout the rest of the thesis. The thesis is divided into chapters based on the four areas of investigation described above, after a brief chapter providing a background on atmospheric icing (Chap. 2).

Chapter 3 describes the use of wind park SCADA data for icing studies. Section 3.2 lays out the quality assurance method developed for this project, and examines its potential impact on ice detection. A paper defining three methods of creating ice threshold curves for identifying icing from the observed power curve is introduced in Section 3.3. In Section 3.4, an evaluation of nacelle temperatures, which are relied upon for identifying icing related power loss in de-icing systems and when using indirect approaches, was carried out at the DTU wind energy test site in Høvsøre to examine the reliability of such measurements. Temperature measurements have not been investigated throughout the icing literature, but was shown to be an important factor for identifying icing from observations, thereby also impacting the icing model evaluations.

Chapter 4 presents the framework designed for investigating wind turbine power loss. This chapter highlights the key components of the system and describes how it can interface with existing power production systems.

Chapter 5 contains the research into NWP model sensitivity. A background of the use of NWP models in icing studies is provided in Section 5.1. Section 5.2 introduces a journal article that describes the iceBlade ice model, developed during this thesis (see Section 6.2) and uses the iceBlade model to study the impact of NWP physics parameterizations on the estimation of icing periods for a one month period at a wind park in Sweden. Section 5.3 presents an in-depth investigation of the cloud parameters (hydrometeors) produced by the nine different NWP sensitivity experiments to better understand the impact of the physics parameterizations.

Chapter 6 focuses on the physical ice models. Section 6.1 provides a background on icing models used in wind turbine icing studies. The iceBlade model is introduced in Section 6.2. An investigation of the ice shape grown on a cylinder is explored in Section 6.3, through the use of the OMNICYL ice accretion model (Finstad, 1986).

Chapter 7 describes the icing power loss model. First an overview of previous models that include the impact of icing on wind turbine power production is provided in Section 7.1. The power loss model is introduced in Section 7.2. Section 7.3 introduces the paper that covers the development of the power loss model and its initial evaluation. Finally, Section 7.4 introduces a chapter of the Icewind project report that compares the DTU icing power loss model to three other power models with icing impacts.

The main conclusions of the thesis are summarized in Chapter 8, and Chapter 9 lays out the future research needs based on the findings of this thesis. As described above, the appendices include copies of the three papers and the chapter of the project report.

Chapter 2

Atmospheric icing on structures

This chapter contains definitions of important icing phenomena and provides a brief overview of research into the physical phenomena of atmospheric icing. Atmospheric icing can be defined as all processes where any phase of water in the atmosphere freezes or sticks to an exposed object (ISO standard 12494). The ice that accumulates on a structure can take different forms depending on the method of ice formation and the thermal characteristics at the ice formation interface. As part of the COST 727 project (Fikke et al., 2006), four types of ice were defined based on their physical characteristics: glaze, wet-snow, hard rime and soft rime. However, these groups are often generalized into two categories: glaze ice (wet-growth icing) and rime ice (dry-growth icing; of which wet-snow, hard rime, and soft rime are subtypes). The different types of ice are formed under different atmospheric conditions, and are most closely related to the speed at which the incoming water freezes.

Table 2.1 shows the physical properties of the different atmospheric ice types, and Figure 2.1 shows examples of three of the types of ice. *Glaze ice* has a similar appearance to ice cubes or icicles and it is the result of a slow freezing process. It is mostly smooth and very clear with few air bubbles due to the abundance of liquid water at the freezing surface during its growth. The slow freezing time allows for trapped air to escape the ice before it fully freezes leading to a high ice density. Glaze ice has strong adhesion to the structure, because the slow freezing process allows the water to fill any rough surfaces leading to a large contact area. *Wet-snow ice* is a type of rime ice that grows under specific meteorological conditions. Wet-snow ice is formed when falling snow melts or becomes covered with liquid water allowing the snow to stick to a surface. Since this process occurs with minimal liquid water, the ice is often only weakly connected to the structure during formation. However, when there are high winds and cold temperatures shortly after it forms, wet snow ice compresses while continuing to freeze leading to strong ice adhesion. It retains the opaque, white color that the snow flakes had originally. *Soft rime icing* forms when incoming water droplets freeze immediately on contact with the structure. This allows for a large amount of air to be trapped during the freezing process, leading to a white color. *Hard rime* occurs when the liquid water takes a little longer to freeze than under soft rime ice growth allowing for stronger adhesion, higher ice density, and less white appearance.

As discussed above, the key factor for which type of ice is formed, or whether ice will be formed at all, is the heat balance at the surface of the ice during accretion. This is mainly a function of the temperature, liquid water content, and wind speed (Fig. 2.2). The liquid water content and wind speed define the amount of incoming water that reaches the surface (mass flux). When water freezes, there is a large release of latent heat that warms the surface of the ice and will prevent further ice growth, unless the heat is transfered to the atmosphere. As discussed above, the rate at which the ice can freeze controls the type of ice which is formed. Therefore, at colder temperatures or with a smaller mass flux, rime ice is formed. If the temperature or amount of incoming water increases, the ice transitions to glaze, and eventually the conditions are such that ice will not form at all.

Table 2.1: Typical properties of accretion atmospheric ice, reproduced from (Fikke et al., 2006).

Type of ice	Density (kg m^{-3})	Adhesion & Cohesion	Color	Shape
Glaze	900	strong	transparent	evenly distributed / icicles
Wet snow	300-600	weak (forming) strong (frozen)	white	evenly distributed / eccentric
Hard rime	600-900	strong	opaque	eccentric, pointing windward
Soft rime	200-600	low to medium	white	eccentric, pointing windward

(a) Glaze Ice, from http://www.stormchaser.ca

(b) Soft Rime Ice. "Fleurgivre-1" by softrime2006 - Own work. Licensed under Creative Commons Attribution 2.5 via Wikimedia Commons - http://commons.wikimedia.org/wiki/File:Fleurgivre-1.jpg#mediaviewer/File:Fleurgivre-1.jpg

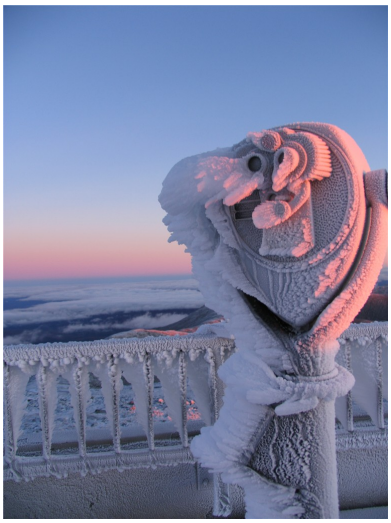

(c) Hard Rime Ice from http://photo.accuweather.com/photogallery/size/44959/Deck+Viewer+with+Rime

Figure 2.1: Photographs of different types of ice.

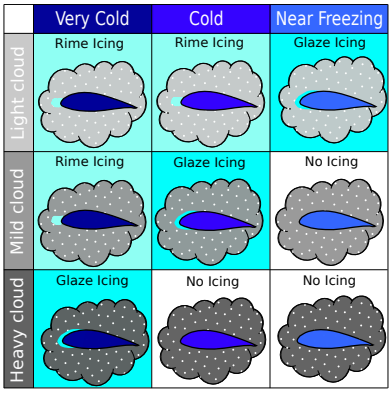

Figure 2.2: Relationship between amount of cloud (mass flux), temperature, and ice type / existence.

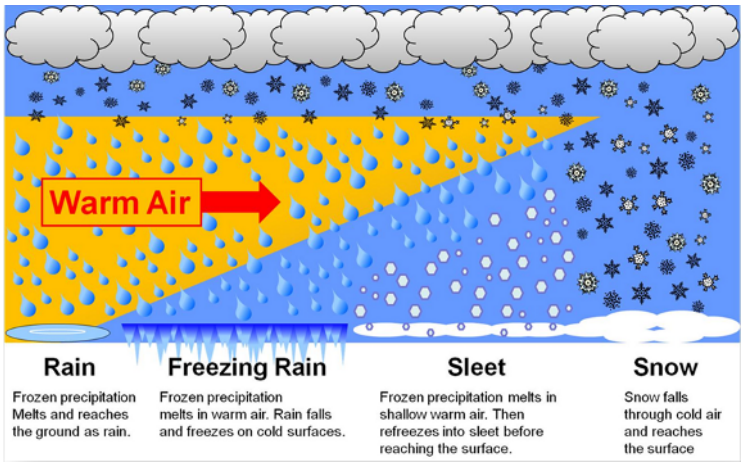

Figure 2.3: Meteorological conditions which lead to different forms of winter precipitation. Rain and snow do not lead to ice formation. Image from NOAA, USA (*http://www.srh.noaa.gov/hun/?n=winterwx_awarenessweek_2013)*

Atmospheric ice can form under four different meteorological conditions: two types of precipitation icing (wet-snow and freezing rain), in-cloud icing, and hoar frost. The ISO standard includes descriptions of the processes for precipitation icing and in-cloud icing, but does not discuss hoar frost.

Precipitation icing can take the form of freezing rain or wet-snow icing. Under freezing rain conditions (Fig. 2.3), there is a large temperature inversion aloft with temperatures above 0°C. This causes frozen precipitation falling through that region to melt. When the liquid water droplets impact surfaces with temperatures below 0°C they freeze, however, because there is typically a large amount of incoming water it generally freezes slowly allowing some of the water to drip forming icicles. Ice that forms under these conditions is generally glaze ice. Although, if the temperature at the surface is cold enough, hard rime ice will also form. Models have been designed specifically for freezing rain icing using the precipitation rate (Jones, 1998). Wet snow icing occurs when there is a very high water vapor content, and the temperature at the surface is slightly above 0°C. Under these conditions a layer of liquid water forms on the outside of the snow flakes. This is similar to the conditions that lead to sleet (Fig. 2.3), except the structure is located in or near the warm layer preventing the snow from refreezing. When the partially melted snow particle impacts the surface it sticks because of the liquid water. The snow then freezes due to the exchange of heat with the surface. Wet snow icing can lead to very high accumulations of ice over a rather short period of time (Kringlebotn Nygaard et al., 2013).

Hoar frost is generated when water vapor deposits on a structure. This tends to result in a very small accretion on the surface with a short duration. Therefore, hoar frost is not typically of concern for masts or towers, however, Turkia et al. (2013) found that even very small amounts of ice accretion could have a large impact on the lift

and drag coefficients of a wind turbine blade. Therefore, hoar frost may be of significance for power production estimates, but not for safety concerns.

In-cloud icing occurs when a structure is located inside of a cloud allowing the super-cooled liquid water droplets to come into contact with a structure at temperatures below 0°C. At the Earth's surface, this occurs during freezing fog events and typically results in soft rime ice due to the low wind speed during these events. At elevation or on tall structures, it is fairly common to have large ice growth from in-cloud icing when there is a low cloud-base. During these events hard rime or even glaze ice can occur depending on the amount of liquid water in the cloud. Due to their height, up to 200 m above the surface, and placement on hills to take advantage of the increased wind speed, turbine blades commonly rotate inside of clouds and therefore are at significant exposure to icing during cold conditions.

For wind energy power production, in-cloud rime icing has been identified as the key type of ice. Glaze ice has been identified as a concern for loadings of turbines as it can occasionally lead to over-production (Ilinca, 2011) and since it is higher density adds more mass to the turbine blades. Throughout the research presented in this report, only in-cloud icing is studied, however, it will be shown in Chapter 5 that freezing rain events are also included, due to the way the cloud rain hydrometeors are handled in the microphysical schemes.

Chapter 3

Ice detection on wind turbines

Direct observations of icing at wind parks are uncommon, and direct observation of ice on the turbine blades is not currently possible. Homola et al. (2006) provided an in-depth review of icing sensors. Their study identified three broad methods for the detection of icing relevant to wind energy: 1) direct measurements; 2) indirect measurements from field sensors; and 3) indirect measurements from the turbine. All current direct measurement systems are installed on either a nearby meteorological mast or a turbine's nacelle. These sensors measure changes in mass or signal properties. The signal properties include the change in resonant frequency of a proper or the damping of ultrasonic waves. Tammelin et al. (2005) provides a comprehensive list of sensors with photos and descriptions of their detection methods. One of the problems with these sensors is that they have a different shape, size, and incoming velocity than the turbine blades. The incoming particle velocity differs due to the rotational speed of the turbine blades. As described in Chapter 2, the incoming velocity has a large impact on the incoming mass flux (how many particles collide with the object), which in turn impacts the rate and type of ice growth that occurs. The direct measurement sensors also only sample one layer of the atmosphere, while modern turbine blades rotate through approximately 100-m of the atmosphere. Finally, the direct measurement devices have been shown to be unreliable (Fikke et al., 2006; Homola et al., 2006; Wickman, 2014) particularly in the heaviest icing regions. Therefore, indirect measurements are often used for identifying icing events at wind parks. Ice can be indirectly detected at a meterorological mast by comparing observations from heated and unheated meteorological sensors. After determining the relationship between the sensors, ice can be identified by the periods where the sensors deviate from thier normal relationship. Cup anemometers and wind vanes are often used for these measurements since they are already installed at wind parks. The final type of ice detection is the indirect measurement of ice on the turbine blades using either vibration or power data from the turbines SCADA system. For vibration data, a reference vibration is identified and the data is monitored to identify deviations from the reference value (Skrimpas et al., 2014). These periods are then studied and likely causes are examined. One of the possible causes is the accumulation of ice on the turbine blades. When using power data, the deviation of the observed power from an expected value based on the ambient wind speed is used.

The power deviation approach has been used throughout the research presented in this study, as it is the most directly applicable approach for studying icing related power production losses. The use of the power deviation has been discussed at several conferences, however a thorough review of the process has not been identified. In this chapter, three methods of developing threshold curves for ice detection will be examined (Section 3.3). Before the threshold curves could be determined, a method of identifying points where the turbine was in non-standard operation for reasons other than icing was created (Section 3.2). Additionally, it was found while cleaning the dataset that a using threshold nacelle temperature value of 0°C for data impacted by icing did not capture all of the iced data points. Through the use of data from the Høvsøre test site an examination into the performance of the nacelle temperature measurements was made (Section 3.4).

3.1 Datasets

Four different wind park datasets were used in this study. Three of the datasets are specific to their studies, and will be described within the sections relating to those studies. These include: data from four wind parks used for the analysis of ice detection methods and described in Section 2 of appendix A, data from the Høvsøre test

Figure 3.1: Map of Wind Parks used in the study.

site used for the temperature analysis in Section 3.4, and a single month of data from all turbines in a Swedish wind park described in Section 2 of appendix B. The fourth dataset, used throughout the rest of the report, will be described here in more detail.

Two years of wind park data from 15 sites across the Northern Hemisphere was obtained. Seven of the sites were located in Scandinavia and the remaining eight sites were from North America (Fig. 3.1). To prevent identification of the wind parks, a random subset of the wind turbines in each park were selected for inclusion in the dataset. The data included 10-minute measurements of the turbine power output, the temperature and wind speed measured on the nacelle of each turbine, and several quality assurance (QA) variables. The QA variables included measures such as: a counter for the amount of time the measured wind speed was below cut-in, the standard deviation of the blade pitching during the 10-minute period, and the maximum power the turbine could produce. Section 3.2 will describe the process of identifying periods of non-standard performance using these QA variables.

3.2 Quality Assurance of SCADA Data

The first step in processing any data is performing quality assurance. In this process, outliers and other points not matching the desired test conditions are flagged for removal during the data-analysis phase. For ice identification using the power curve method, the test conditions require the removal of points where the turbine was not in normal operation. This prevents non-iced points from being identified as icing and provides a clean dataset to fit threshold curves. In this section, the method used for flagging non-optimal turbine operation will be described, and subsets of the data will show how much data was typically removed.

For the empirical approaches to identifying icing, described in Section 3.3, the input data needs to be as clean as possible. Because of this, the QA thresholds were tuned to prevent the inclusion of outliers that would skew the fitting of the empirical power curves. This resulted in a large number of good data points, points that fall along the manufacturer's power curve, to also be removed (Fig. 3.2). The removal of these points from the evaluation of the icing models may have an impact on their evaluation.

The data used in this section is the dataset described in Section 3.1. When wind speed is used in this section it refers to the nacelle wind speed from the SCADA dataset, which has already been corrected for the impact of the turbine. Power refers to the output power from the SCADA dataset, which has been normalized by dividing by the turbine's rated power, and power curve refers to the manufacturer's power curve.

From the SCADA data, seven different fields were used to determine if the turbine was in normal operation or if a fault had occurred during the 10-minute period (Table 3.1). All potential QA fields were initially examined, but many were discarded because they were redundant. The threshold values shown in Table 3.1 were refined using both years of data from the 15 wind parks. A consistent set of threshold values was applied to all wind

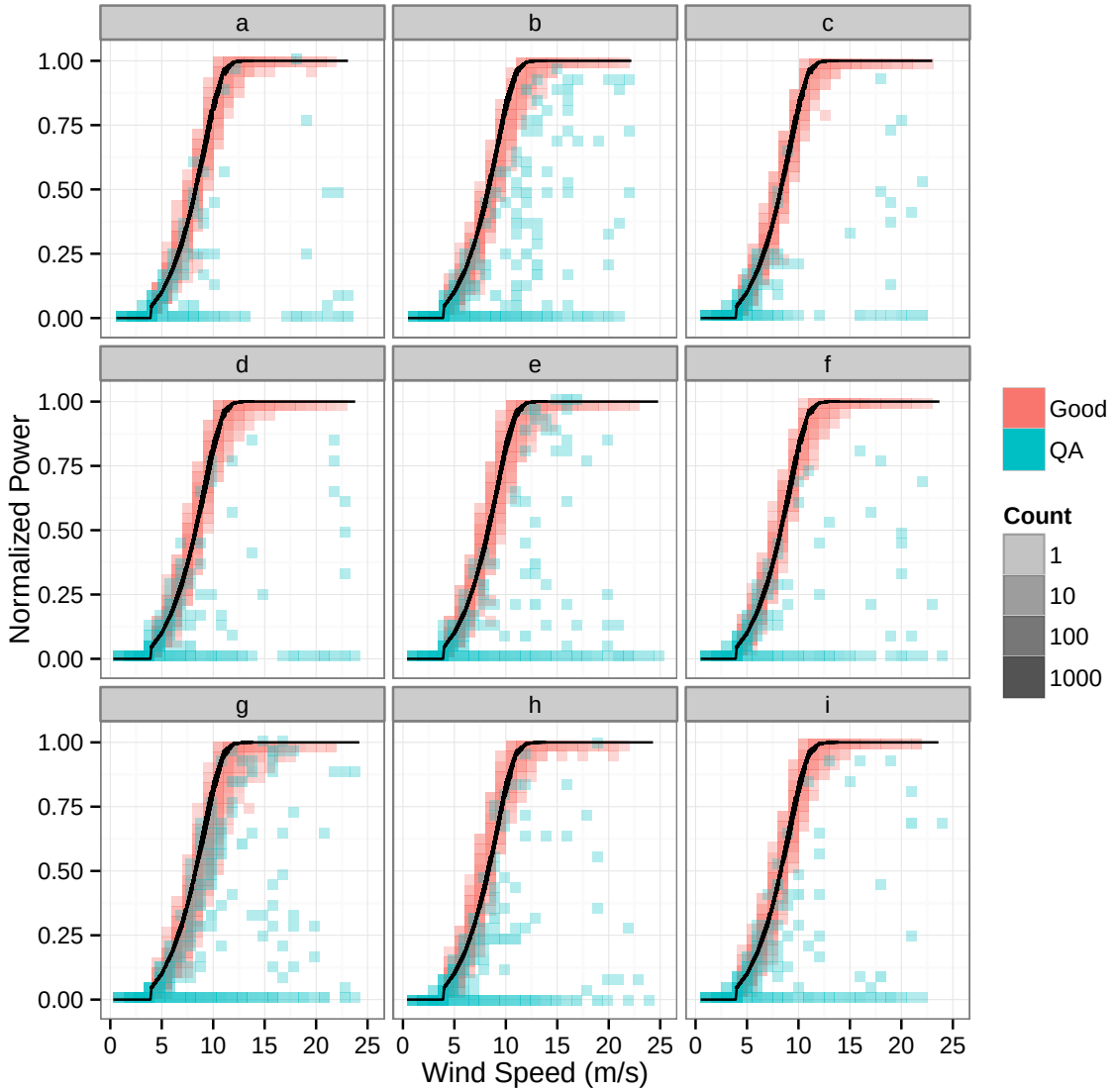

Figure 3.2: Wind Speed vs normalized power for each turbine in wind park A for temperatures at or above 5°C. The different subplots show the different turbines labeled (a-i). Each box on the plot represents a 1 $\mathrm{m\,s^{-1}}$ by 0.04 area with the transparency is based on the number of points in that area. More transparent boxes have fewer points as signified in the count legend. The different colors signify points which were marked as QA (blue), and those that were marked as good (Pink). The black line is the manufacturer's power curve.

Table 3.1: Name and description of each quality flag used to identify points when the turbine was not in normal operation. The flags were identified for each 10-minute averaging period using a 1 second sampling rate.

QA Field	Description
Bad Wind	Less than 590 of the 600 seconds of wind speeds are above cut-in or below cut-out
Wind Error	Standard deviation of the wind speed is equal to 0.0 $\mathrm{m\,s^{-1}}$
Yaw	The relative wind direction is more than 10 degrees, signifies a yaw error.
Pitch	Standard deviation of the pitch is more than 8.0 degrees.
Generator	The generator is not operating for 10 for the 600 second period
Remote Derate	Derated power limit and observed power is more than 2% below the manufacturer's estimated power curve.
Internal Derate	Possible power, from nacelle measurement, more than 100 W above observed power

parks, however, some fields impacted some of the turbines more than others. This was particularly true of the derating flags, because derating was applied frequently at some sites and less frequently at others. The desire for a consistent approach across the different sites furthered the conservative nature of the thresholds, since a stricter criteria would be applied to all turbines if any site required it. This decision was made to allow for the automated processing of new sites and to remove site specific adjustments. If any of the QA fields were violated, the point was marked as QA and removed from the rest of the analysis.

The thresholds for *Bad Wind* and *Generator* were quite strict as the 10s limit would allow for a maximum power deviation of 1.6%. This value was selected due to the small deviation (approximately 2%) in power above rated wind speed. The *Wind Error* criteria was only met when the wind speed was identical for the entire 600 seconds of the period. Other periods could also have bad wind speed measurements, but these could not be identified using the available data. This was because just a few good wind measurements would cause the standard deviation to be non-zero. A rather large 10-degree *Yaw* error was used because power output was not very sensitive to smaller differences in the relative wind direction. The *Pitch* criteria identified points where the controller could not identify a fixed pitch angle given the power output and nacelle wind speed, thereby causing the turbine blades to rapidly change pitch. This had a large impact on the power generation. The two *derating* criteria were found based on the deviation from the power curve. When a turbine is derated, the controller has limited the maximum power to a value below its nameplate rating. For example, when a 1 MW turbine is set to a maximum power output of 500 kW it is derated. This can occur when the grid has too much power at a given time *(Remote derate*), or when conditions require the turbine produce less power to protect its components from overheating (*Internal derate*). When a turbine is remotely derated a derated power limit value is set in the SCADA data. However, the existence of the derated power limit does not ensure that the turbine was not producing the normal amount of power. For example, if the produced power was below the derated power limit, the turbine would likely still produce the estimated power even when derated. Therefore, a secondary criteria was added to ensure that the observed power deviated from the power curve by more than 2%. The *Internal derate* state was harder to identify, as there was not a derated power value set in the SCADA data. So this state was identified by comparing the possible power value with the observed power. The possible power is the amount of power that the turbine would be expected to produce if it was not derated. When the turbine is not derated, the possible power and observed power should be identical, although this was not always the case. Therefore, 100W threshold was used when comparing the two values for turbines in the 2 to 3 MW range.

Figure 3.2 shows a summary of the observed power curve for each of the 9 turbines at wind park A grouped by their QA classification. Rather than plotting each point, the data were binned into rectangles of 1 $\mathrm{m\,s^{-1}}$ of wind speed and 25 power bins equally spaced between zero and full production, which were shaded based on the number of points in each bin. This allows the identification of the locations on the power curve where most of the points were clustered. For most turbines, the bulk of the points removed via the QA process had wind speeds less

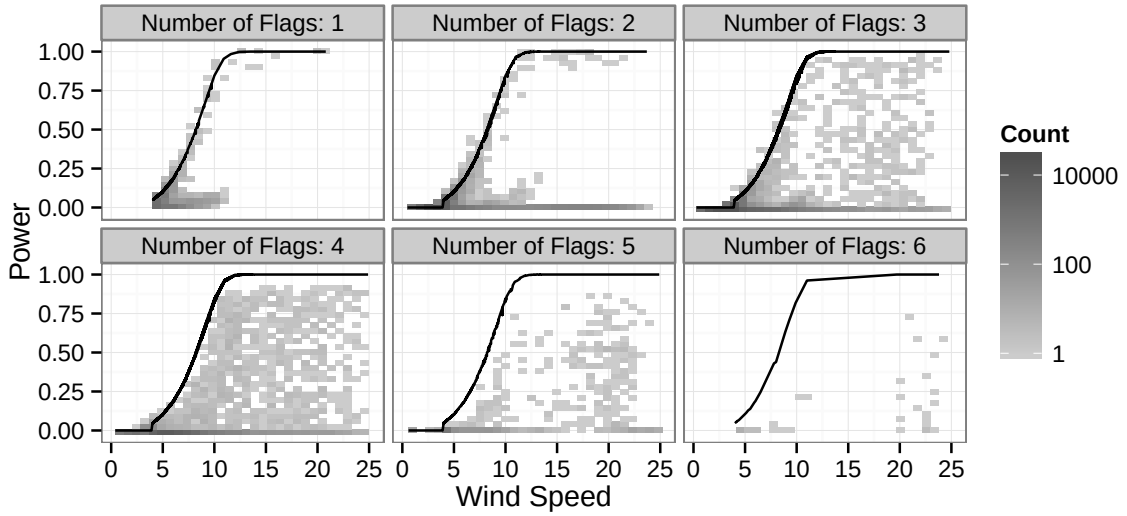

Figure 3.3: Wind speed vs power for points identified as QA by the *Generator* flag at wind park A. The shaded regions on the plot show the number of points in each area that were marked as QA. Darker colors signify more points in that area. The different subplots show the number of QA flags from Table 3.1, so the top-left plot identifies points that were removed only by the *Generator* flag, while bottom right plot shows points that were identified as failing all size of the criteria. The black line is the manufacturer's power curve.

than 10 $\mathrm{m\,s^{-1}}$, and a corresponding low normalized power output, less than 0.25. For turbine g, many of the QA points overlapped the non-QA points. This suggests that the criteria may have been too strict for this turbine.

Figure 3.3 shows a summary of the points that were flagged by the *Generator* criteria. This was the most common flag at most sites and had a lot of overlap with the *Bad Wind* flag. For the points which were uniquely identified by this threshold, the top left plot, many fall close to the power curve. However, there were also a large number of points with zero power identified by this flag as well. As more flags were added, the number of zero value points continued to increase. It is very important to remove the points with zero power output, as clearly the turbine was not in normal operation at those times. It is also clear that as more criteria were violated, the QA points were further from the power curve. This suggests that the combined criteria were doing a good job of identifying points where the turbine was not in normal operation.

Figure 3.4 is the same as Figure 3.3, but for the *Remote Derate* criteria. At this site very few points were removed only by this criteria (top left plot). This was common at most sites as the two derate criteria had significant overlap. The points which were identified by two or three flags stand out. For both plots, a horizontal line at 0.25 power extends across a range of wind speeds. These points were clearly derated signifying that the algorithm was working as intended. A similar straight line was present around 0.8 power, but is harder to make out here. While derated points at higher wind speeds are fairly easy to identify visually, points where the derated value was closer to the expected power were harder to identify. Therefore, the derate criteria has the most uncertainty attached to it. It is likely that during the winter season, the two *Derate* criteria removed some points which were actually icing induced power loss.

After setting the various thresholds, statistics were run to determine how many points were removed by each threshold and the total number of points removed. This value is not a downtime or any other metric for the wind park, and is only significant in terms of the amount of data being retained for the icing analysis. Table 3.2 lists the number of points removed by each QA metric for wind park A, which is representative of all 14 wind parks. For wind park A, the total percentage of points removed was 31.08% of the available data. This falls toward the middle of the range for the other parks (22.3% to 58.2%). It should be noted again that for many of the QA points the turbine produced power, simply the power was not as much as would be expected based on the nacelle wind

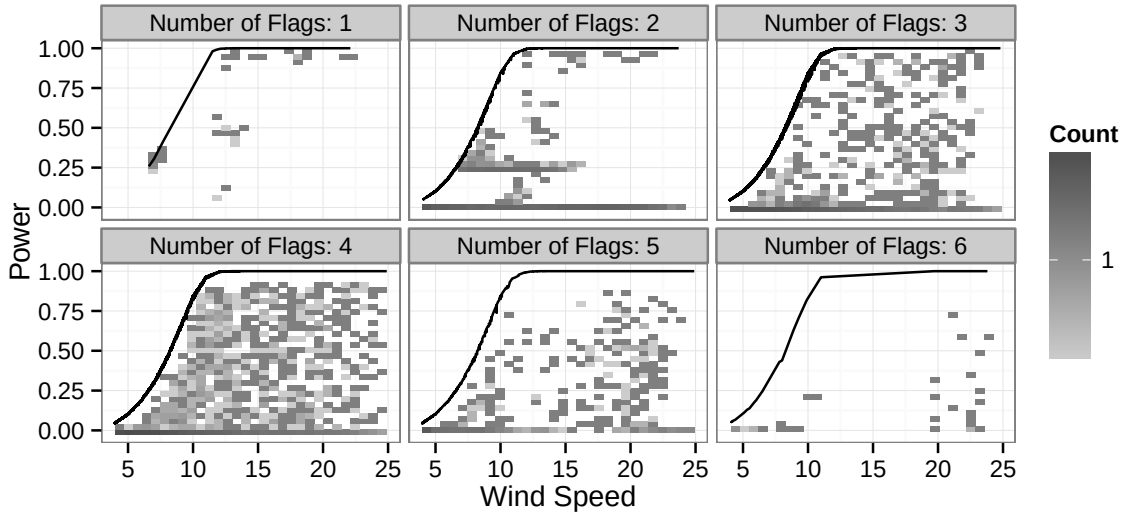

Figure 3.4: Same as Figure 3.3 but for the *remote derate* criteria. The power curve is only drawn for wind speeds that had missing values.

speed.

Most of the QA data was flagged by either the *Bad Wind* or the *Generator* criteria. These criteria relate to whether there is enough wind to power the turbine, and whether or not the turbine generator was engaged. Just over two-thirds of the QA data fell into the *Bad Wind* category. That was also consistent across the different parks, with a range of 50% to 85% of the QA points coming from the *Bad Wind* category for 13 of the 14 parks. At the last park the *Bad Wind* flag only identified 34.8% of the QA points. The *Generator* flag accounted for more than 65% of all QA points at all of the parks, and 8 of the 14 parks had *Generator* based QA data account for more than 80% of the missing values. The *Derating* flags had the most variation across the parks which is to be expected given that this is largely an external factor.

Table 3.2: The number of points removed from each QA metric at wind park A. **All Count** is the number of QA points which were identified by that category. **Unique Count** is the number of points that were only identified by that category. **All Percent** was the percentage of the total data identified as QA by that category, and **Unique Percent** is the same for points only identified as QA by that category. The **Total QA** field is the total number of points identified as QA at the site, and **Missing** is the number of points which were not included at all in the dataset.

QA Field	All Count	Unique Count	All Percent	Unique Percent
Bad Wind	208014	24915	22.30	2.67
Wind Error	576	0	0.06	0.00
Yaw	65748	517	7.05	0.06
Pitch	86658	7	9.29	0.00
Generator	263219	8351	28.22	0.90
Remote Derate	71448	49	7.66	0.01
Internal Derate	69884	29	7.49	0.00
Total QA		289864		31.08
Missing		0		0.00

It was also useful to investigate the months during which each of the QA flags occurred. Figure 3.5 uses a wind rose style plot to show the percentage of flags that occur during a given month. The months give the radial direction of the plot, with winter on the top and summer on the bottom. The magnitude is given by the percentage of points that were removed for a given month. The *Bad Wind* and *Yaw* criteria tend to remove points during the

summer (May to September). This was expected because this wind park is known for having weaker winds during the summer months. The *Generator* errors are fairly consistent throughout the year, with minimums in March and October. The *Pitch* field shows a definite peak of occurrence in January and February, with a fair number of points throughout the rest of the year as well. This could suggest that the *pitch* threshold is capturing points that are actually the result of icing during January and February and not only removing QA points. In fact, Lindahl (2014) presented an ice detection method that relied on the pitch angle and generator torque. Finally, the two *Derate* thresholds have the majority of their points during the winter (November to February). This suggests that the *Derate* thresholds were set such that they identified a large number of iced points as QA, causing them to be removed from the analysis. Based on these results and the fact that they are at least in part based on power deviation from the expected value, the identification of derated turbines is the main challenge to the cleaning of SCADA data for icing analysis. Therefore, it would be helpful if additional information could be included in the SCADA system, so that these points could be appropriately filtered for power curve studies.

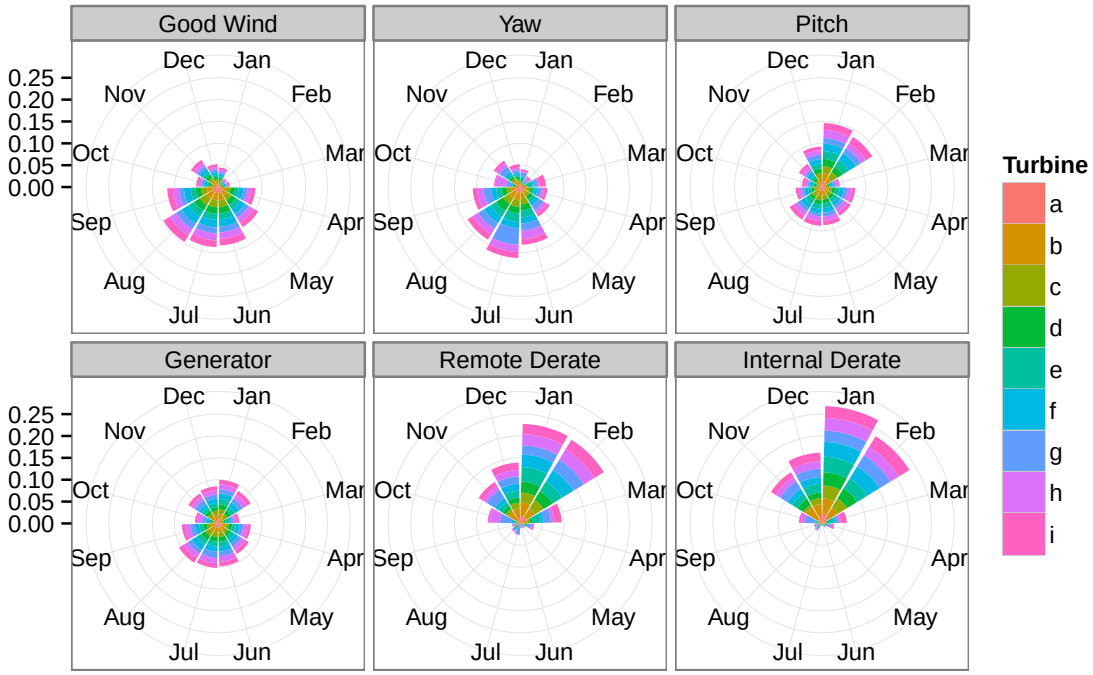

Figure 3.5: Rose plot showing the percentage of QA flags by month and turbine at park A. The QA flags are described in Table 3.1. The different colors denote the different turbines, while the different directions correspond to the months which are marked with abbreviations.

In this Section, several QA criteria were described and their impact on the data was examined. The *Bad Wind* and *Generator* criteria were the most common cause of turbine anomalies. The *Derating* criteria also had a significant impact at certain sites, however the approach used in this report likely mis-categorized icing related power losses as *Derated* periods due to the lack of a strong identifier. Additional information from turbine manufacturers and wind park developers would be helpful for the data cleaning processes. The approach used in this thesis was very hands-on, and therefore required tuning of the different metrics by hand. Now that this has been completed, statistical classification approaches could be used to fine tune the criteria in the future.

3.3 Introduction to Appendix A - Paper I

Paper I "Ice Detection Using the Observed Power Curve" (appendix A) presents different approaches for creating threshold power curves to identify icing on wind turbines. All three approaches calculated threshold curves relating the nacelle wind speed to the power output of the turbine. The standard approach has been to use a flat percentage deviation from the manufacturer's power curve (Wadham-Gagnon et al., 2013). However, it has been suggested that this curve does not accurately represent the inherent variability of power at higher wind speeds, potentially underestimating the impact of icing. Two approaches have been developed to address this limitation. Karlsson et al. (2014) described a quantile based approach, which used the quantiles of a cleaned power curve to approximate icing. Davis et al. (2014b) described an alternative approach using the standard deviation of the power curve and subtracting it from the empirical power curve, this approach was used in the papers included in Appendices C and D. The three methods were tested at four different wind parks and compared with web-cam observations of ice from the nacelle of one of the turbines. It was found that the quantile approach works best when a historical dataset of turbine performance is available. However, the percentage based approach was still useful, when there is not a long enough record for determining the quantiles for each wind speed. The standard deviation approach was limited in this study as it is not a robust method. Therefore, it required a dataset with fewer outliers than was available in the test dataset for fitting both the empirical power curve and the standard deviation. This led to large challenges in fitting the standard deviation and fairly large differences between it and the other two approaches.

3.4 Nacelle Temperature Evaluation

3.4.1 Introduction

Temperature measurements are not usually of primary concern for wind park measurements. They have been included as a standard measurement on the nacelle of each turbine for calculating the air density, which is then used to adjust the power curve of the turbine. However, the air density is not sensitive to temperature errors of a few degrees Celsius. For icing studies, temperature is a key parameter because the detection of icing is often restricted to temperatures below 0°C (Wadham-Gagnon et al., 2013). However, when examining turbine power curves, the strict 0°C threshold was often not applicable. In all of the provided datasets, it was found that the SCADA system only recorded rounded integer values of the temperature; therefore, a 0°C threshold would exclude data between 0°C and -0.5°C. Also, at many sites the visual icing signal, determined by deviation from the power curve, could be found at temperatures up to 3°C (Fig 2. Appendix A). In addition to the visual icing identification, Vestas found, in an internal study, that results from the Weather Research and Forecasting (WRF) NWP model significantly underestimated nacelle temperatures during the spring. At several sites throughout Sweden, they found 4°C to 5°C biases during the spring, while only a 1.5°C to 2 °C bias in the summer. The summer bias is fairly consistent with other studies that have found biases in WRF to be around 1°C to 1.5°C (Cheng and Steenburgh, 2005; Heikkilä et al., 2010). The large cold bias in the WRF model results led to a large icing loss estimate in spring that was not found in the observational record.

These findings motivated a deeper investigation into the accuracy of the nacelle based temperature measurements. The question was asked: is the model error found by Vestas solely the result of model errors or could nacelle observations also include systematic biases? To explore this question further, temperature measurements from the Høvsøre test site from June of 2011 to November of 2013 will be examined in this study.

3.4.2 Datasets

Vestas provided two datasets for this study. The first included nacelle temperature observations, and the second was a corresponding dataset containing results from a simulation using the WRF model. In addition to

these datasets, a mast based dataset was provided by the Department of Wind Energy at the Technical University of Denmark (DTU Wind Energy). This dataset included temperature measurements at several heights and was considered to measure the true ambient temperature.

Nacelle Temperatures

The nacelle data included 10-minute averages of wind speed, wind direction, and temperature measurements for two turbines that were sited at Høvsøre between 2010 and 2012 and will be identified by their approximate hub height. The first turbine was a Vestas V100 turbine (80m) with a hub height of 80-m. Data was provided for approximately 6 months, from 2010 December 31 23:00:00 UTC until 2011 May 26 10:40:00 UTC. The second turbine was a Vestas V90 turbine (100m) with a hub height of 106-m. Data for this turbine was provided for more than 17 months, from 2011 June 10 11:30:00 UTC until 2012 November 20 12:30:00 UTC. The 17 month period of the V90 turbine allowed for seasonal differences to be examined, which can then be compared against the more limited time-period in the V100 dataset. Since there were no quality assurance flags included in the dataset, unphysical temperatures were removed from the data manually. This process will be described in Section 3.4.3.

Meteorological Model Data

The meteorological model results came from a global modeling study at Vestas Wind Energy Systems, and are from the same internal study that motivated this research. For the modeling study, the WRF model (Skamarock et al., 2008) was run at a 3 km grid spacing with 62 vertical levels, 17 of which were located within the lowest 1 km of the surface. The input and boundary conditions were provided using the Global Forecast System (GFS) analysis (documented and available online at http://rda.ucar.edu/datasets/ds083.2/)), with the boundary conditions updated every 6 hours. The simulation used the WRF single moment 5-class microphysics scheme (Hong et al., 2004), rapid radiative transfer model for longwave radiation (Mlawer et al., 1997), the Dudhia shortwave radiation scheme (Dudhia, 1989), Eta Similarity surface layer physics, the Noah Land Surface Model (Chen and Dudhia, 2001), the MYJ PBL scheme (Janjić, 1994), and the Kain-Fritsch cumulus scheme (Kain, 2004).

For this study, wind speed, wind direction, turbulent kinetic energy, air density, relative humidity and temperature were provided at heights interpolated to 80-m and 106-m above ground level. The data was provided from 2000-01-01 07:00:00 UTC until 2012-09-30 06:00:00 UTC, but only the periods overlapping the observational data were used.

Mast Temperature Measurements

The mast measurements were provided by DTU Wind Energy, which operates two meteorological masts at the site at the Høvsøre test site. The data in this study comes from the 114-m mast, which includes temperature measurements at several heights. Only the 80-m and 100-m heights are used as they are closest to the hub heights of the turbines. Table 3.3 provides a brief description of each observation, and the abbreviations that will be used in the graphics.

There were four different temperature measurements at 100-m in the dataset. The sensors are: an absolute temperature measurement using a thermistor developed at DTU Wind Energy (abs_100), a temperature difference from the temperature measured at 2-m (diff_100), an absolute temperature measurement from a combination Vaisala relative humidity and temperature sensor sensor (vais_100), and a temperature derived from a sonic anemometer (son_100) (Schotanus et al., 1983).

At 80-m, only the temperature difference between 2-m and 80-m (diff_80) and the sonic anemometer derived temperature (son_80) were available. The temperature difference is measured rather than the absolute temperature to provide a more accurate temperature profile on the mast. Section 3.4.4 will show a comparison of the various

Table 3.3: Measurements used in the temperature evaluation. Abbreviation of each instrument, a longer description of the instrument and its availability dates.

Abbreviation	Description	Period (UTC)
turb_106	Vestas V90 with hub height of 106 m	2011-06-10 11:30:00 2012-11-20 12:30:00
turb_80	Vestas V100 with hub height of 80 m	2010-12-31 23:00:00 2011-05-26 10:40:00
abs_100	DTU thermistor at 100 m	2010-12-31 21:00:00 2012-11-19 23:00:00
diff_100	Reconstructed temperature at 100 m using difference between DTU thermistors at 100 m and 2 m.	2010-12-31 21:00:00 2012-11-19 23:00:00
diff_80	Reconstructed temperature at 80 m using difference between DTU thermistors at 80 m and 2 m.	2010-12-31 21:00:00 2012-11-19 23:00:00
vais_100	Vaisala temperature and humidity sensor at 100 m	2010-12-31 21:00:00 2012-11-19 23:00:00
son_100	Temperature derived from sonic anemometer at 100 m	2010-12-31 21:00:00 2012-11-19 23:00:00
son_80	Temperature derived from sonic anemometer at 80 m	2010-12-31 21:00:00 2012-11-19 23:00:00
wrf_80	WRF temperature interpolated to 106 m	2000-01-01 07:00:00 2012-09-30 06:00:00
wrf_106	WRF temperature interpolated to 80 m	2000-01-01 07:00:00 2012-09-30 06:00:00

sensors at 100-m to determine if the difference or sonic sensor should be used for the baseline temperature at both 80-m and 100-m.

3.4.3 Methods

The methods used in this study were mostly standard statistical measures of comparisons between two time-series, including root mean squared error (RMSE), mean bias (MB), regression lines, arithmetic mean, and standard deviations. The bias adjusted RMSE (RMSE_adj) is calculated by first removing MB from all points in the comparison data set and then calculating the RMSE

$$RMSE\_adj = \sqrt{\overline{((M - \overline{(M-O)} - O)^2}}, \tag{3.1}$$

where M is the comparison value and O is the trusted value. The bar over the fields denotes the mean. This provides a measure of the spread of the errors assuming an unbiased input.

Data Quality Assurance

Erroneous data-points were removed from all observational data by identifying points where the temperature changed by more than 2°C from a neighboring time interval. Points identified through this method were plotted for 20 consecutive time periods. If the point was determined visually to be an outlier, it was removed from the dataset. Outliers typically had the form of a dramatic drop in temperature followed by a dramatic increase back to the previous value. This removed 20 points from the nacelle temperature measurements, and 2 points from the Vaisala 100m dataset. Large deviations in the temperature measurement from the nacelle corresponded to times when the turbine was not in normal operation, for the one month dataset used in Davis et al. (2014a).

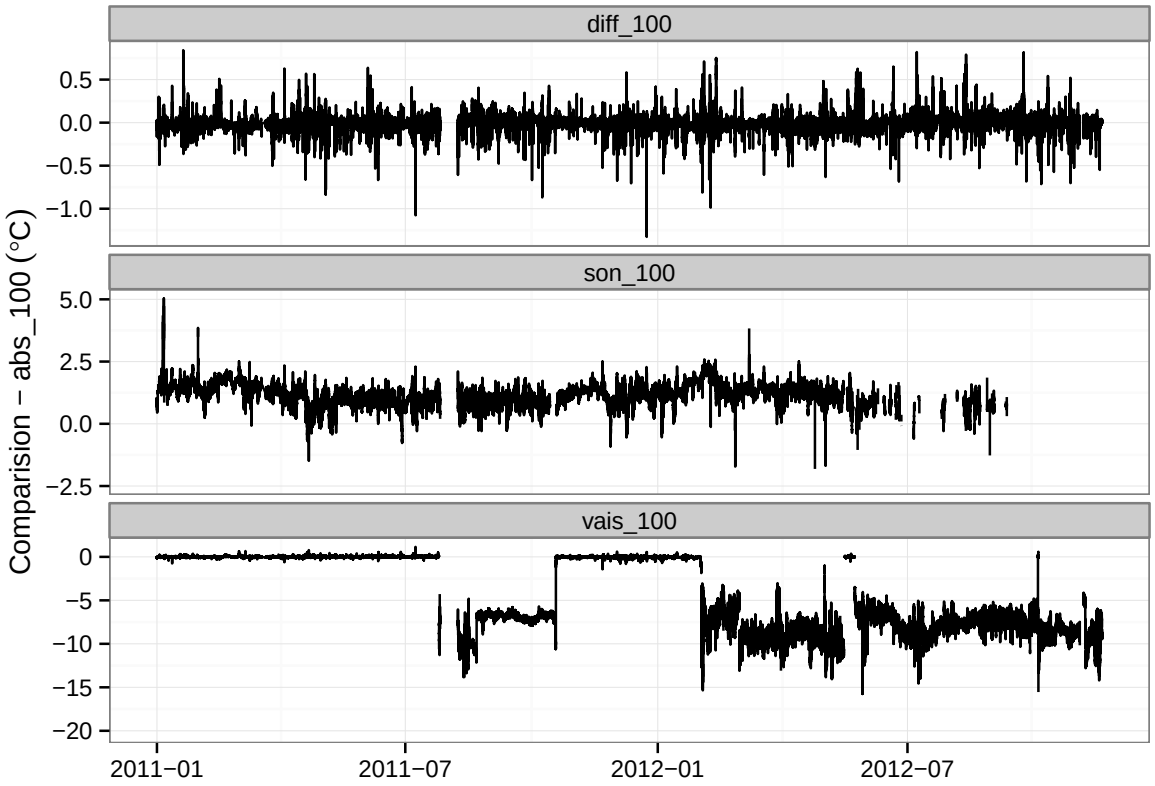

Figure 3.6: Temperature difference as a function of time (UTC 10-minutes) from abs_100 for each of the other sensors at 100-m (rows). Note the different y-axis scales for each panel.

3.4.4 Results

This section provides a comparison of the various temperature measurements at Høvsøre. The mast measurements were first evaluated to determine which of the measurement methods were the most trustworthy. The trusted measurements were then compared with the turbine nacelle data. Finally, both the mast and nacelle measurements were compared with the WRF modeled temperatures.

Mast Measurements

The first step in evaluating this dataset was comparing the various mast measurements at 100-m. From discussions with the data provider, abs_100 was identified as the most trusted measurement. Therefore, it will be used as the reference value. Figure 3.6 shows the temperature difference between each of the sensors at 100-m and the abs_100 sensor as a function of time. The vais_100 measurement fell out of alignment with the abs_100 sensor during two different periods. This suggests either a calibration error or a data recording problem. Both periods had missing values in the time-series around the time of the wrong temperatures as well. The scale of the different sensors was quite different, since the diff_100 sensor only varies from the abs_100 by a maximum of 1.5°C, while the other sensors have much larger differences. The noise in both the diff_100 and son_100 sensor was spread evenly from the positive to the negative. In addition to the better agreement with abs_100, the diff_100 dataset was more complete than the other two sensors.

Figure 3.7 is a binned scatter plot comparing abs_100 with the three other temperature measurements at 100-m. The diff_100 measurement had very good agreement with abs_100, while the other two measurements had significant differences. The measurement from the sonic anemometer had good agreement at warmer temperatures, but at colder temperatures son_100 had a warm bias. The comparison between abs_100 and son_100 had

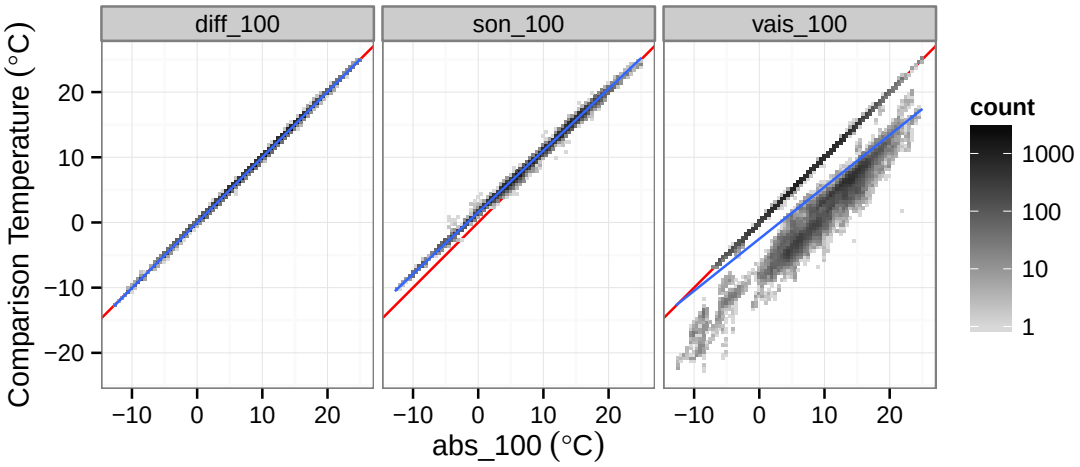

Figure 3.7: Comparison of the various mast measurements at 100-m (diff_100, son_100, vais_100 in Table 3.3; columns) to the abs_100 measurement. The red line is the identity line and the blue line is the linear regression line. The points have been binned into 1°C by 1°C squares, with the number of points in each square identified by the shading.

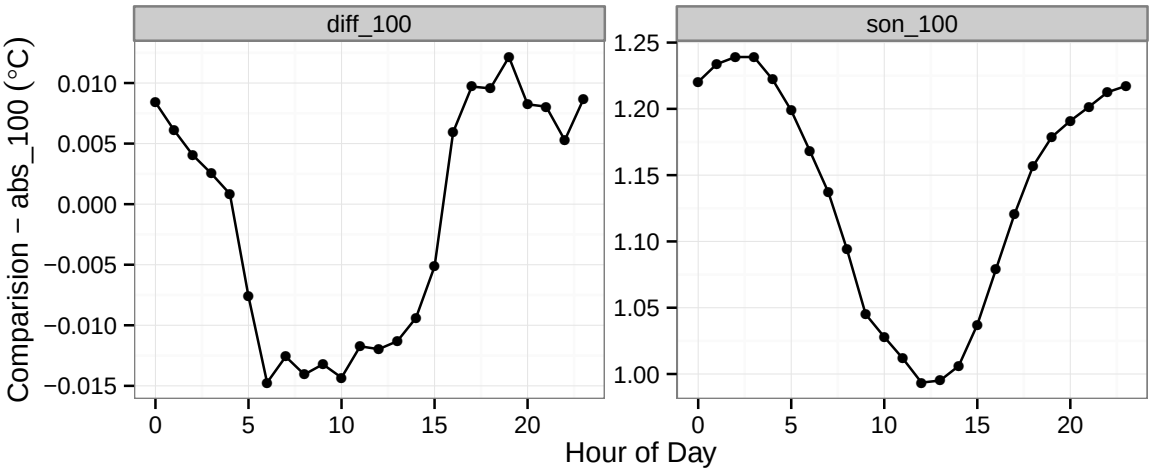

Figure 3.8: Mean temperature bias bias of diff_100 and son_100 (columns) compared with abs_100 as a function of time of the day (UTC hours) . Note the different y-axis scales for each panel.

very little spread as the values were tightly concentrated around the regression line. The vais_100 measurement had a large cloud of points that did not agree with the abs_100 sensor. The cloud represents a significant amount of data with very different values than the other three sensors. Some of the data agreed very well with the abs_100 sensor, located under the red identity line, but the large cloud of points was enough to influence the correlation.

Another interesting feature in the diff_100 and son_100 datasets was the identification of distinct seasonal and diurnal patterns in the mean bias with the abs_100 sensor. The seasonal pattern in the son_100 data was large enough that it can be identified in the time-series (Fig. 3.6). During the summer months, when there was more light and warmer temperatures, the bias was lower than during the winter months. The same signal was found in the diurnal results with a smaller bias during the day than at night (Fig. 3.8). The seasonal and diurnal signals were smaller for the diff_100 sensor, but still evident.

The diff_100 sensor most closely matched the values from the abs_100 sensor in all of the comparisons. Therefore, the diff measurement was chosen to represent that mast value throughout the rest of the analysis, so that the same type of measurement could be used at both 80-m and 100-m. The differences were small between

diff_100 and diff_80 with a MB of only 0.04 and RMSE of 0.29 for the period with the 80m turbine data. These measurements will be labeled as MAST throughout the rest of the analysis.

Turbine comparison

Figure 3.9 compares the nacelle temperature measurements with the MAST values. The two turbines were identified by their approximate hub height, with 80m signifying the V100 turbine, and 100m signifying the V90 turbine. It is clear that the bias in the nacelle temperature for 80m was much larger than the bias for 100m. Another key feature was the impact of the rounding of the nacelle temperature values. For both turbines, there were a range of MAST temperatures that correspond to the rounded nacelle temperature. The rounding led to an error in the nacelle temperature values even with perfectly matched instruments. Interestingly, in the 100m data there was a larger spread in the MAST temperature to the left of the identity line, but the regression line fell along the identity line. This means that there were more points to the right of the identity line, but those points had smaller deviations from the MAST temperature. The 80m data had a more equal distribution around the regression line, but the spread on both sides of the regression lines was substantially larger.

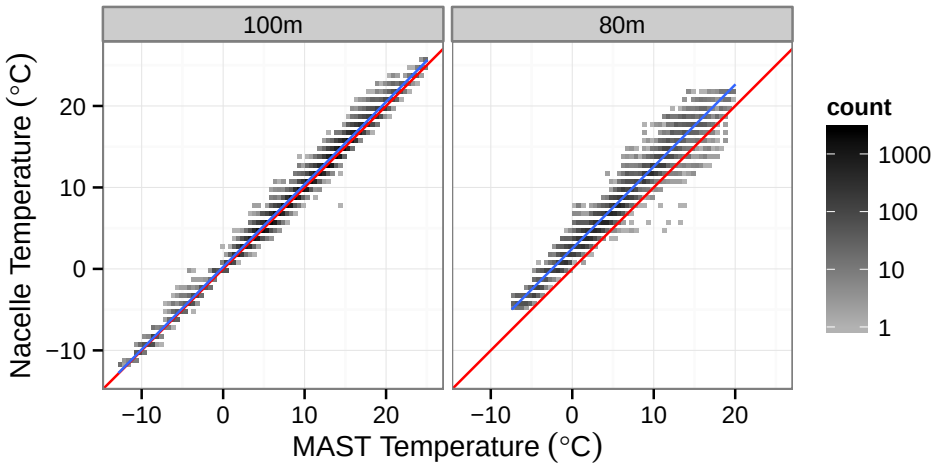

Figure 3.9: Same as Figure 3.7, but comparing the nacelle temperature values with the MAST temperature values for the different turbines (columns).

Comparison statistics are shown in Table 3.4. The 100m turbine had relatively good agreement, with a bias of only 0.37°C and a bias adjusted RMSE of 0.56°C. The differences were much larger at the 80m turbine, where the mean bias was 2.52°C and the bias adjusted error was almost double that of the 100m case. However, both turbines had high correlation with the MAST observations and have a slope close to 1. This suggests that the bias was fairly consistent across the entire temperature range (Fig. 3.9).

Table 3.4: Statistics comparing turbine and MAST measured temperature values for the different turbines (type). Mean bias (MB; °C), Root mean squared error (RMSE; °C), Pearson's R (Cor_R), Slope of regression line (slope), and bias adjusted RMSE (RMSE_adj; °C; Eq. 3.1).

type	MB	RMSE	Cor_R	slope	RMSE_adj
80m	2.52	2.75	0.98	1.01	1.09
100m	0.37	0.67	0.99	1.01	0.56

The outliers seen in Figure 3.9 are easy to identify in the time-series plot (Fig. 3.10). The temperature difference for 100m had more extreme warm biases than cold biases, in terms of both frequency and peak value. This was particularly evident during the spring and early summer (January 2012 to July 2012) where several peaks occur that are larger than the normal noise in the data. These peaks are also consistent with the slightly positive

mean bias for the 100m turbine. The comparison for 80m also shows large deviations from the normal bias during the period from April until mid-May. Additionally, there are potentially erroneous results in the data gap between March and April. The difference in the 80m turbine measured temperatures is centered around a value near 2°C for the entire period, with only the largest negative peaks showing a cold bias.

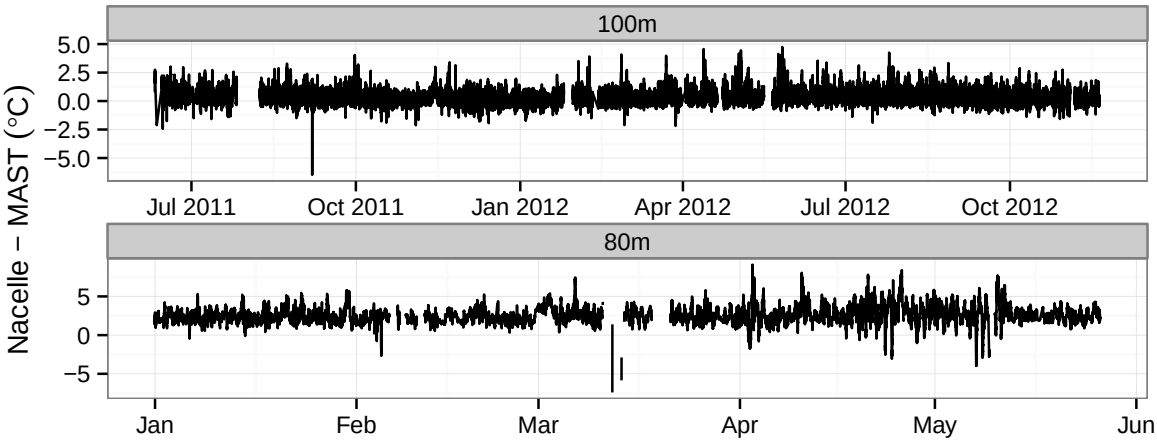

Figure 3.10: Same as Figure 3.6, but for the nacelle and MAST temperature difference for each turbine (rows). Note the different scales on the x and y axes.

The diurnal plot (Fig. 3.11) shows a large fluctuation in the bias for both turbines, with the mid-day bias being significantly larger than the night-time bias. This was particularly evident for the 100m turbine measurements, where the peak bias occured near local noon (13 UTC) and the overnight hours (20 to 04 UTC) had the lowest values. The magnitude of the diurnal change in bias was approximately 0.6°C for the 100m comparison, which was very large compared to the overall bias of 0.37°C. Comparing the 0.6°C diurnal difference in bias to the diurnal change in the MAST plots (Fig. 3.8), highlights the significance of the diurnal change, as the largest diurnal fluctuation for the MAST measurements was only 0.25°C. The fluctuation for the 80m turbine measurements was even larger, with a diurnal change of almost 0.8°C, however the shape of the bias curve was not as symmetric. The peak value occured in the late afternoon (15 UTC), and the minimum value occured in the morning (8 UTC), for 80m.

WRF comparison

There was a larger spread in the scatter plot comparing the WRF derived temperatures (WRFT) to the observational temperatures than was found in the previous comparisons between the various observed temperatures (Fig. 3.12). This was also found in the error statistics, where the RMSE_adj values were all over 1°C (Table 3.5). Additionally, all of the regression lines had a slope less than 1. This highlights that the bias in WRFT changed depending on the observed temperature value. At colder observed temperatures WRFT compared better with the observations, but there was a cold bias in all of the comparisons at observed temperatures above 10°C. The mean bias of WRFT was found to be significantly smaller for the MAST temperatures than the nacelle temperatures. This was the result of WRFT being cold biased compared to the MAST temperature, while the nacelle temperature values are shown to have a warm bias when compared with the MAST temperature. WRFT had a much better agreement with the MAST temperature values than the measured temperature from either turbine. The WRF results were reasonable, for all observations, except the 80m turbine.

Figure 3.13 shows the monthly mean bias between WRFT, and the four observed temperatures. In all four of the comparisons, there was a trend for smaller biases in the winter and larger biases in the summer. There did not seem to be a significant deviation in the bias in the summer or fall seasons.

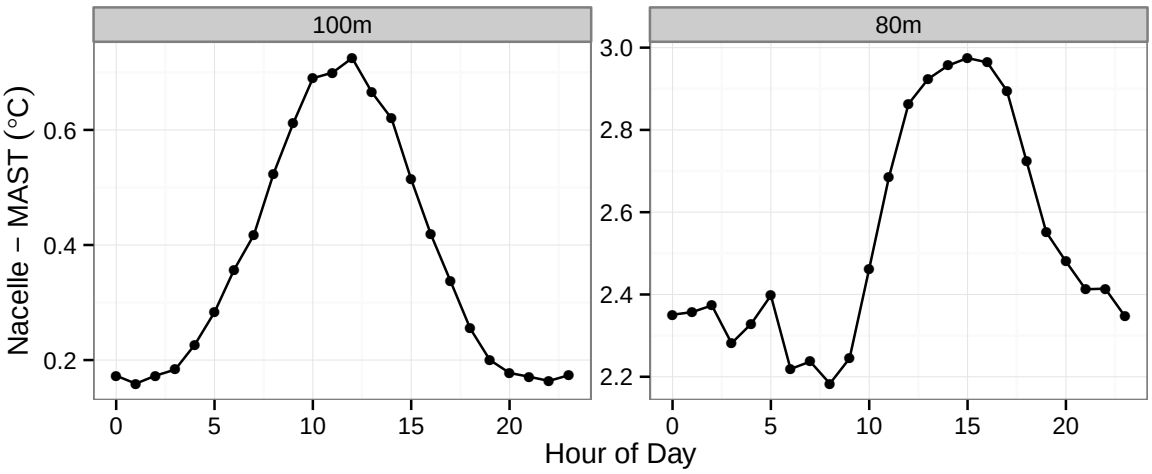

Figure 3.11: Same as Figure 3.8, but for the nacelle and the MAST temperature bias for the different turbines. Note the different scales on the y-axis.

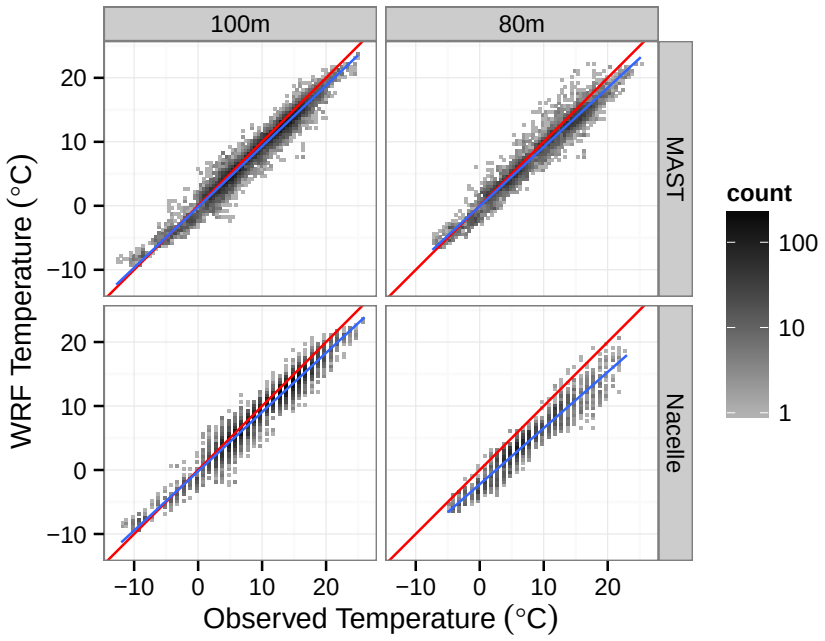

Figure 3.12: Same as Figure 3.7, but comparing WRFT to the two observational temperature values. MAST temperature values are on the top row and nacelle temperature measurements are on the bottom row, the columns compare the two heights.

Table 3.5: Statistics comparing WRFT to the nacelle and MAST temperatures for both turbines. Metrics are the same as in Table 3.4.

lbl	MB	RMSE	Cor_R	slope	RMSE_adj
MAST 80m	-0.71	1.55	0.98	0.92	1.37
Nacelle 80m	-3.12	3.44	0.96	0.88	1.46
MAST 100m	-0.64	1.27	0.98	0.95	1.10
Nacelle 100m	-0.99	1.55	0.98	0.93	1.20

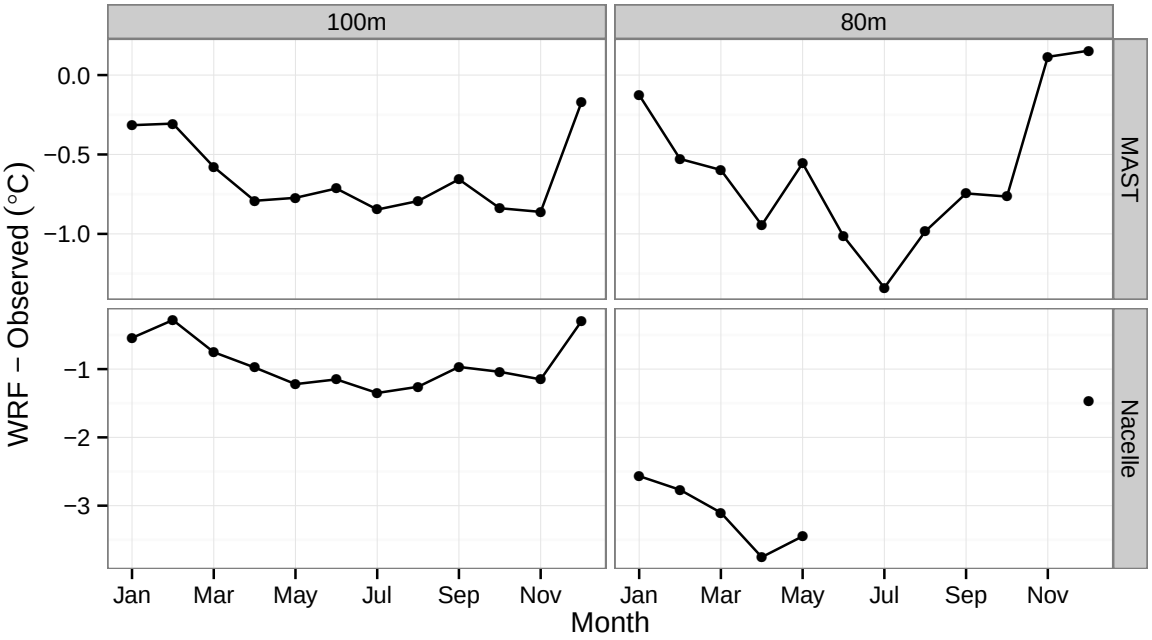

Figure 3.13: Monthly mean bias comparing the WRF derived temperature with of MAST observed temperature and nacelle temperature measurements (rows) for both turbines (columns). Note the different scales on the y-axis.

3.4.5 Discussion and conclusions

The results of this study highlight some of the challenges in measuring temperature. Even the mast measurements, which are exposed to almost identical conditions showed large differences depending on the measurement device (Fig. 3.7). While the son_100 temperature had a good agreement with the abs_100 temperature measurement there was still a significant slope to the regression line. The offset of the temperature was largest at temperatures below 0°C, where the son_100 temperature was too warm compared to the abs_100 temperature. This suggests an additional correction term for the sonic derived temperatures may be needed for temperatures in this range.

The diurnal signal in the nacelle observed temperatures compared to the MAST measured temperatures (Fig. 3.11) suggests that the thermometer was not properly shielded. The strong agreement between the 100m signal and expected solar radiation suggest that the incoming solar radiation was causing the thermometer to heat up unrealistically for that turbine. For the 80m turbine, the offset in the peak temperature from solar noon suggested that the thermometer may not be properly shielded from the warming of the nacelle around the thermometer. Another potential source of the nacelle temperature error is the exhaust heat from the turbine. This seems unlikely, however, given the pattern of the diurnal temperature bias. If there was a constant exhaust temperature, it would be expected that the exhaust heat would lead to warmer temperatures when the ambient temperature is lower. But, we did not have information about the exhaust heat of the turbine, so it was not possible to make a definitive statement about this possibility.

In addition to the diurnal influence on the nacelle temperature, it appeared that the calibration of the nacelle temperature was also not consistent between the two turbines. The mean bias for the 100m turbine was only 0.37°C, while for the 80m turbine it was 2.52°C, nearly a factor of 7 difference. Considering the larger bias at warmer temperatures shown in the diurnal plot, it could be expected that the bias of the 80m turbine temperature measurements would have been even larger if it was calculated over a full year. These results confirm that sticking to a strict 0°C threshold for icing identification may be missing key icing events. While the rounding of the temperatures reduces their accuracy for ice identification, it does not appear to influence the overall temperature

bias. It should be noted that if a 0°C temperature threshold is used, it will include some data points either above or below the threshold, depending on if 0°C is included or excluded.

The derived temperatures from the WRF model, as configured for this study, had a cold bias compared with all observations (Table 3.5). The bias was much smaller for the MAST temperatures. For the 80m turbine, the bias was more than 3°C. Davis et al. (2014a) found that out of nine WRF setups, the WSM5 and MYJ combination used in this study had derived temperatures with the largest cold bias, when compared with WMO 2-m temperature measurements. This suggests that the cold bias could be reduced by switching to the YSU PBL scheme (Hong et al., 2006), which was the warmest of the PBL schemes tested.

The temperature bias in WRFT was found to vary with both temperature and time of the year, as suggested by Vestas (Fig. 3.13). The largest bias occurred during the summer months, when the temperature was warmer. The slope of the regression line also showed the change in model bias with temperature; therefore, to properly adjust WRFT a conditional bias correction would need to be applied. Interestingly, when compared with the 80m MAST measured temperatures WRFT has a local minimum bias in April, which was the month Vestas identified as problematic in their ice modeling. However, as discussed above, the lack of icing in the April observations may also be due to errors in the nacelle temperature measurement leading to cases of observed icing that are missed.

This study has confirmed that there can be large biases in the measurement of temperature on the nacelle of a wind turbine. Additionally it found that these errors tend to result in a warm bias, which amplifies the cold bias found in the WRF derived temperatures. This has large implications for the identification of turbine icing from both the nacelle data and in the model development process.

Chapter 4

Icing forecast system

The main goal of this Ph.D. project was to develop a system for modeling icing on wind turbine blades with a focus on estimating the impact of ice accumulation on production losses. The model was designed to be used both for production forecasts in the 24 – 48 hour window and for retrospective studies that could be used for wind park siting. So far, only tests of the system using historical observational data and hindcast NWP results have been carried out. Figure 4.1 shows a schematic of the forecast system. It was designed with the assumption that a reasonable production estimate without icing could be made using existing tools. Based on this assumption, the icing system could be developed independently, without the need for a detailed understanding of the non-iced power prediction method. There is an added benefit to this approach; when new approaches to non-iced power prediction are made, the improvements can be added to the forecast system with relatively small modifications to the icing portion.

The green boxes show a common approach for forecasting power production using the output from an NWP model. NWP models are used for weather forecasts in a wide range of fields and can also be run using historical data to produce hindcasts. The NWP wind estimate is passed to a microscale model, which uses either statistical or meteorological downscaling and interpolation techniques to adjust the NWP wind estimate for the local effects at the wind park location. These models are designed to take into account the surface roughness and topographic changes near the individual wind turbines. The downscaled wind is then passed to a power prediction model (PPM) that uses statistical methods to estimate the power production. Foley et al. (2010) provides a summary of modern techniques for wind power forecasting. Courtney et al. (2013) described a power prediction system using the method described with an ensemble of NWP predictions. In that study, they used the NWP winds directly in the PPM, allowing the statistical model to handle both the downscaling and power prediction in one step, which is

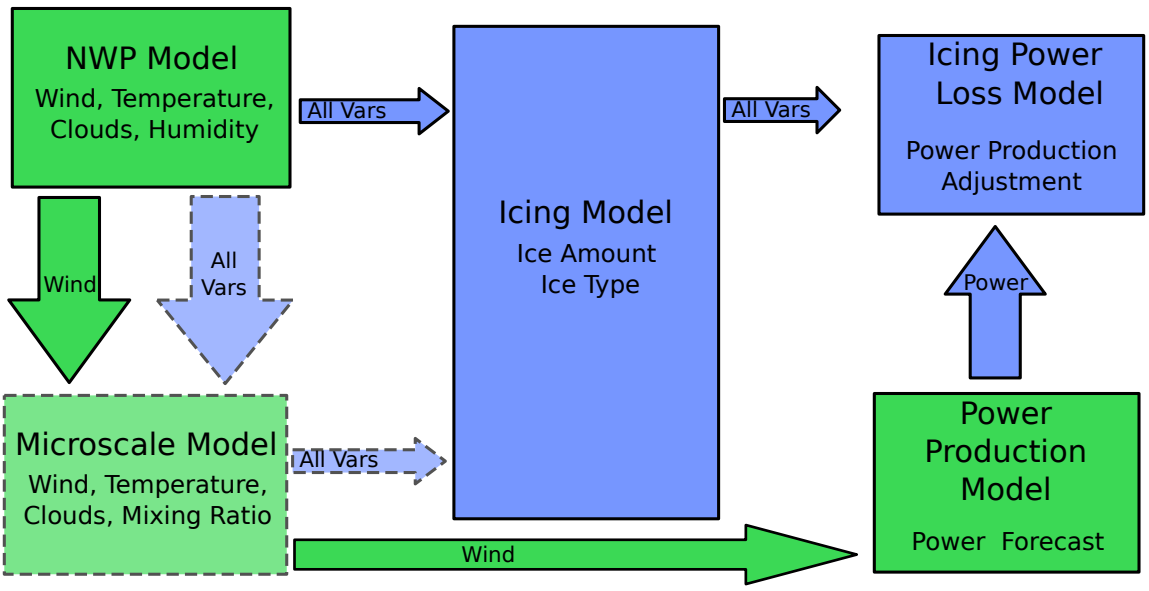

Figure 4.1: Flow chart of the production forecast system with icing impacts. Green boxes are existing models, blue boxes are the pieces developed during this PhD. Areas which are faded and include dashed outlines are areas in need of future development for advancing the icing prediction.

possible when the long term observed power is available. Since the focus of the thesis was on icing, time was not spent investigating different PPMs. Instead, the non-iced power was estimated using an empirical power curve fit to the specific wind farm using the nacelle wind speed. Therefore, the non-iced power predictions will be more reliable than if a power production model using NWP output was used, since there is limited error in the observed wind speed compared with a model estimated wind speed.

Just as the NWP model provides the wind speed estimates that are used in the PPM, it also generates the necessary meteorological parameters for estimating the impact of icing on the power production. These parameters include standard meteorological fields such as wind speed, pressure, and temperature, but also include detailed estimates of the cloud particles (hydrometeors). Many studies (Drage and Hauge, 2008; Fikke et al., 2008; Kringlebotn Nygaard et al., 2011; Oechslin, 2011; Yang et al., 2012) have investigated the ability of NWP models to estimate the supercooled liquid clouds that are important for icing studies, and these will be described in Chapter 5. These studies provide confidence that the NWP model could capture the necessary inputs for a physical icing model to be used in this study. However, most of these studies used complex microphysical schemes that added significant computational time to the NWP forecast. The wind power production systems have often opted for simpler microphysical schemes, as clouds were not a priority. Therefore, in Chapter 5, a set of model sensitivity experiments will be described that evaluated the impact of the microphysical scheme on the cloud parameters and thereby the icing model result.

In the current power production system with icing (PPM_i), the results from the NWP model are passed directly to the icing model. In Figure 4.1, an alternative path of passing the relevant NWP results to a microscale model is shown. The microscale model approach was briefly investigated, but was dismissed due to a lack of verification data. There are also large uncertainties surrounding the downscaling of clouds due to their thermodynamic feedbacks on the atmosphere, so the downscaling was expected to be too computationally expensive to be carried out in this thesis. Finally, estimating the impact of icing on wind park performance was more difficult and uncertain than originally thought, complicating the investigation of the microscale factors that could lead to differences in icing on the different turbines.

The icing model used in the PPM_i system is the iceBlade model, which has been developed as part of this Ph.D. thesis and will be described in detail in Chapter 6. The iceBlade model takes input variables from the NWP model results and produces a forecast for ice mass, ice density, and ice type. The iceBlade model was developed specifically for modeling ice on wind turbine blades under changing meteorological conditions. This required algorithms for both ice accretion and ice ablation. Ice accretion was modeled using the Makkonen model (Makkonen, 2000). The Makkonen model is developed to model ice growth on a rotating cylinder, but in iceBlade, modifications are made to better represent a rotating turbine blade. These include updates to the wind speed due to the blade rotation, and the removal of the cylinder rotation requirement since the blade does not rotate like a cylinder (Fig. 4.2). Algorithms for ice ablation due to sublimation, shedding, and wind erosion in the iceBlade model allowed the model to be run for the entire winter.

The final part of the PPM_i system was the icing power loss model (IPLM). An IPLM was designed to update the non-iced power forecast from the PPM using the results from both the NWP and iceBlade models. Because iceBlade did not have a high enough resolution to capture the icing induced changes to lift and drag, a statistical model was used for IPLM. The statistical model was initially fit using all relevant parameters, but only the ice mass and wind speed were found to be significant, using a cross-validation approach. The development of the power loss model will be described in Chapter 7. PPM_i models have been developed for other studies. The first attempts used the Makkonen model estimated ice mass to fit a three-dimensional power curve (power, wind speed, and an icing term) that would estimate the turbine power production with icing impact (Byrkjedal, 2012b; Söderberg et al., 2013). During this project, other approaches have also been developed. One approach used the three-dimensional power curve, but rather than using ice mass used the duration of the icing period to fit the power curve (Karlsson et al., 2014). Two other approaches made use of ice models similar to iceBlade, with the enhanced wind speed due to blade rotation before coupling the ice model results to advanced statistical techniques

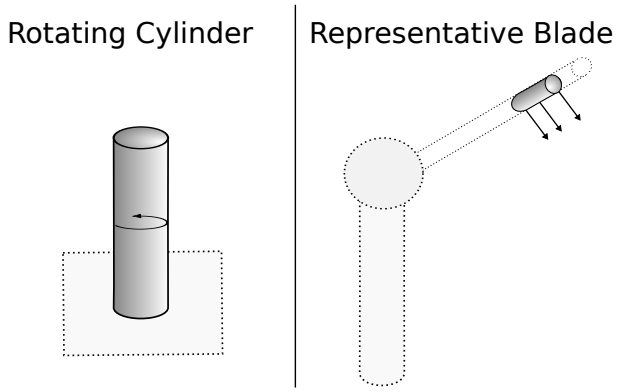

Figure 4.2: Representative shapes of the ice models. For both images the wind can be assumed to be going into the paper. The rotating cylinder is the standard way of modeling ice using the Makkonen model, while the representative blade is how the collecting structure is represented in iceBlade.

to provide power production estimates (Baltscheffsky, 2013; Haupt, 2014).

Chapter 5

Numerical weather prediction model

5.1 Background

An NWP model estimates meteorological parameters through the discretization of physical and mathematical equations that describe the atmosphere. An NWP model requires starting (initial) conditions that describe the state of the atmosphere at the beginning of the integration. A limited area NWP model, such as the WRF model used in this study, also requires the input of values at the boundaries of the domain to update the model state as it moves forward in time. The NWP model provides a four-dimensional representation of the atmosphere, filling the gaps in the observational network. Also, NWP models output many parameters that are not commonly measured. One such parameter that is important for icing studies is the liquid water content (LWC) of clouds.

Clouds are one of the more challenging parameters to accurately represent in an NWP model. This is due, in large part, to the number of parameters that control cloud formation, all of which need to be simulated accurately for clouds to form in the correct place and at the correct time. Clouds are typically simulated using two different parameterizations at mesoscale resolutions. Subgrid scale clouds are parameterized in convective parameterization schemes that create updrafts and downdrafts at scales smaller than a grid cell, removing atmospheric instability. Since convective clouds often have cloud bases above the turbine blade tips they do not typically result in turbine icing. Therefore, the convective parameterization was not a focus for this thesis. The second type of cloud parameterization in NWP models is the microphysics scheme. These schemes attempt to simulate clouds at the grid scale and include algorithms for the various processes that occur during the cloud's lifecycle. This includes the initial formation of the hydrometeors, when the air becomes saturated, the interaction between the different hydrometeors (collision, freezing, melting, etc.), and the eventual dissipation of the cloud due to either evaporation or precipitation. The microphysical schemes were the focus of the sensitivity studies presented later in this chapter.

As mentioned in the introduction, NWP models, and specifically the WRF model used in this study, have been used in several studies to investigate icing for different applications. The modeled hydrometeors have been of particular focus in these studies, as they will be in this chapter. Yang et al. (2012) provides a good overview of past studies that have used NWP models to simulate cloud parameters and icing near the surface at locations around the globe. Drage and Hauge (2008) used the MM5 model, a predecessor to the WRF model, to model icing on a mountain on the coast of Norway using a non-rotating steel rod. During the period of study there was one large observed icing event. The ice model they used was similar to the Makkonen model, which will be described in Section 6.2. Drage and Hauge (2008) found that even when using a 1-km by 1-km model grid spacing, the height of the mountain was smoothed significantly from 723 m above sea level (a.s.l) to 554 m a.s.l.. This was likely due to the MM5 input data. They found that MM5 slightly underestimated the LWC, and therefore underestimated the ice amount, which they attributed to the smoothing of the topography. However, they also found that the start and end times of the icing event were "captured to a high degree of accuracy". These results agree with the majority of studies into icing on cylinders near ground level using NWP models (Fikke et al., 2008; Kringlebotn Nygaard et al., 2011; Yang et al., 2012). The consistent theme across these studies was that higher resolutions were required to capture the magnitude of the icing in mountainous regions, and that the icing model was highly sensitive to the median volumetric diameter (MVD) of the water droplets. The MVD is used to represent the size of the droplets in the icing model, and is determined in part based on the number of condensation nuclei in the atmosphere. A resolution dependent simulation was not done for this thesis as it was decided that

a focus on the model parameterizations would be more useful since there were previous studies investigating the impact of model resolution.

In addition to the studies comparing icing models driven by NWP models on cylinders, a few studies have looked at the ability to represent production loss periods of wind turbines with icing periods from NWP models. For example, Oechslin (2011) used the WRF model to simulate icing during periods of production loss for a wind park in the Swiss Jura. In this study, the Makkonen model was used and, as in Drage and Hauge (2008), the periods of icing were found to match well with periods of production loss, and therefore assumed observed icing. These results have been replicated in several other studies of turbine production loss in cold climates as well (Byrkjedal, 2012b; Yang, 2012; Söderberg et al., 2013). One limitation of these studies was that they all used advanced microphysics schemes, and did not explore the sensitivity of the icing forecasts to different physics parameterizations.

The WRF model is a community NWP model developed for both research and operational forecasting uses. As a community model, the WRF model contains many different physics packages to parameterize the various processes in the atmosphere. The microphysical scheme and planetary boundary layer (PBL) schemes are the most important for icing studies, assuming that the dynamic aspects of the evolution of the atmosphere are carried out accurately by the model. The microphysical parameterizations as described above represent the various processes relating to grid scale clouds in an NWP model. The PBL schemes attempt to represent the vertical transport of meteorological fields through the lower atmosphere. They control much of the mixing in the atmosphere, including the mixing of hydrometeors located in the PBL. Hydrometeors provide the estimation of the cloud mass at each level in the atmosphere, and an estimation of the distribution of the various water particles, both liquid and frozen, that make up the cloud.

To examine the influence of these physics schemes on icing model results, nine sensitivity experiments were designed using version 3.3 of the WRF model. Section 5.2 introduces a paper that studied the results from the nine sensitivities and their impact on the iceBlade model. Section 5.3 examines the different structures of boundary layer clouds with the different microphysics schemes at nine different locations in Scandinavia, and addresses several of the questions raised in the paper.

5.2 Introduction to Appendix B - Paper II

Paper II “Forecast of Icing Events at a Wind Farm in Sweden” introduces the iceBlade model for modeling ice growth on wind turbines, which will be described in Chapter 6. The iceBlade model was provided inputs from the results of nine WRF simulations using different combinations of microphysical and PBL parameterizations. The iceBlade results were compared against periods of decreased power production from a wind farm in Sweden during January 2011. The aims of the study were to investigate the impact of the changes made in iceBlade compared to the standard cylinder model approach of ice growth, and to study the impact of different PBL and microphysical schemes on the icing results. It was found that the iceBlade model outperformed a 1-day persistence model and standard cylinder model for capturing icing periods. There was a significant difference between iceBlade and the standard cylinder model in terms of both the periods of icing predicted and the accumulated ice mass. The different microphysical schemes had a larger impact on the ice forecast than the different PBL schemes, but the PBL schemes still showed significant differences in the amount of accumulated ice mass.

The paper also highlighted differences in the makeup of the clouds in the model. The SBU-YLin microphysics scheme (Lin and Colle, 2011) was found to have much smaller total hydrometeor amounts than either the WSM5 (Hong et al., 2004) or Thompson (Thompson et al., 2008) schemes. It was found that the number concentration of cloud droplets (N_c) parameter in the SBU-YLin scheme was set to 10 cm^{-3}. This value was an order of magnitude smaller than the value provided Lin and Colle (2011). It was hypothesized that the low N_c value may be the cause of the low cloud amounts in the SBU-YLIN scheme. Additionally, it was noted that the WSM5 model was the only

microphysics scheme which created large amount of cloud ice, both other schemes retained more cloud water.

5.3 Parameterization of cloud properties in NWP models

As described in Section 5.2, Davis et al. (2014a) used nine sensitivity studies to examine the impact of the NWP model physics on the icing model. In this section, these simulations are examined in more detail. The nine sensitivities were a combination of three different microphysical schemes and three different PBL schemes. The three microphysical schemes were the Stony Brook University–Y. Lin (SBU-YLin; Lin and Colle, 2011), Thompson (Thompson et al., 2008), and WRF single-moment five-class cloud microphysics (WSM5; Hong et al., 2004). They provide a reasonable range of complexity with the Thompson scheme containing the most predicted cloud parameters (mixing ratios of cloud liquid water (q_c), cloud rain (q_r), cloud ice (q_i), cloud snow (q_s) and cloud graupel (q_g), as well as number values for the rain and ice hydrometeor types). WSM5 and the SBU-YLin scheme only contain estimates for q_c, q_r, q_i, and q_s, allowing for shorter run times. The three PBL schemes were the Mellor–Yamada–Janjić (MYJ; Janjić, 1994), version 2 of the Mellor–Yamada–Nakanishi–Niino (MYNN2; Nakanishi and Niino, 2006), and the Yonsei University (YSU; Hong et al., 2006) schemes. MYJ and MYNN2 are 1.5-order turbulent kinetic energy local closure schemes. The MYNN2 scheme only has equations for the mixing of q_c, but MYJ has equations for mixing both q_c and q_i. The YSU scheme also has equations for the mixing of both q_c and q_i, but is a nonlocal k-mixing scheme. While version 3.3 of WRF was used for these simulations the YSU scheme was modified to correct an error found in WRF 3.4.1, relating to turbulence values in stable conditions.

5.3.1 Model Setup

The simulations in this study were the same as those used in Davis et al. (2014a). WRF Version 3.3 was run in limited area mode, for two domains with grid spacing of 30 km and 10 km. The extent of the 10 km domain can be seen in Figure 5.1. The input and boundary conditions were from the Global Forecast System's Final Analysis Product (FNL; documented and available online at http://rda.ucar.edu/datasets/ds083.2/). Sea surface temperatures were updated daily using the NOAA Optimum Interpolation Sea Surface Temperature (OISST) version 2 (Reynolds et al., 2007). Grid based four dimensional data assimilation (FDDA) nudging was applied on the outer domain using the FNL data, for all levels above model level 15 (approximately 200m above ground level), with all nudging coefficients set to 7.5×10^{-5}. The simulation was run from January 1 to January 30, in three 10-day periods, with 24 hours of spin-up for each period. There were a total of 63 vertical levels, 26 of which were in the lowest 1000 m above ground level. In addition to the physics options used in the sensitivity studies mentioned above, the default physics parameterizations of the RRTM longwave radiation scheme (Mlawer et al., 1997), Dudhia shortwave radiation scheme (Dudhia, 1989), the Noah Land Surface Model (Chen and Dudhia, 2001), and the Kain-Fritsch cumulus parameterization scheme (Kain, 2004) were used.

In Davis et al. (2014a), the sensitivity of the iceBlade model to the number concentration of cloud droplets N_c for the Thompson and SBU-YLin schemes was examined, but the N_c sensitivities were only applied in the estimation of the MVD from the model results as in Kringlebotn Nygaard et al. (2011), but not in the WRF simulations themselves. Instead, all simulations used the default values for N_c. It was noted that the default value for N_c was an order of magnitude different between the Thompson (100 cm^{-3}) and SBU-YLin (10 cm^{-3}) schemes, and that this difference could potentially explain the small q_c values in the SBU-YLin results. To test the sensitivity of the cloud results to the N_c parameter, two additional simulations were run using the MYNN2 PBL scheme. The Thompson sensitivity was run with N_c = 250 cm^{-3} and the SBU-YLin sensitivity used an N_c = 100 cm^{-3}.

The results from Davis et al. (2014a), focused only on the grid cell which contained the wind farm. However to understand the sensitivity of the cloud prediction to different climate regions, nine locations were selected for this analysis (Fig. 5.1). Site 4 is located in a similar region to the wind farm, and is the point that corresponds

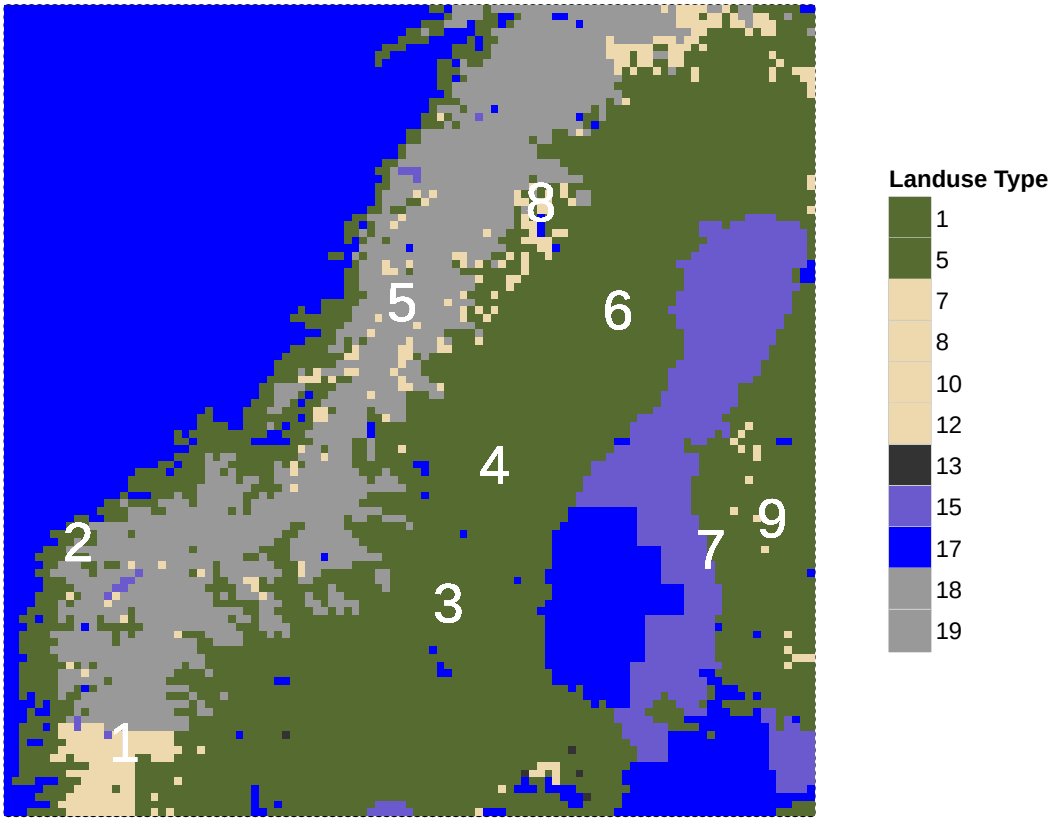

Figure 5.1: Map of the locations used for the cloud study. The white numbers indicate the locations where the data was extracted. Colors denote the different land use types, **1–5** is forest, **7–12** is grassland, shrub land, or cropland, **13** is urban, **15** is snow or ice, **17** is water, and **18–19** is tundra.

most closely to the results found in the previous study. Additionally, rather than only using the level closest to 80m above ground level, data was extracted from all vertical levels, to gain an understanding of the vertical structure of the hydrometeors in the various schemes.

5.3.2 Results

As described in Davis et al. (2014a), the WSM5 parameterization was the only scheme that produced a significant amount of q_i. It was hypothesized that the q_i came largely at the expense of q_c at temperatures below 0°C. Figure 5.2 shows the amount of hydrometeor by temperature bin, for all levels below level 15. Comparing the WSM5 and Thompson schemes, the amount of q_c in the Thompson scheme between -5°C and -10°C is approximately equal to the amount of q_c and q_i in the WSM5 scheme. This agrees with the theory that the WSM5 scheme is converting hydrometeors, particularly q_c, to q_i too quickly and thereby reducing the amount of liquid water available for icing.

The total hydrometeor mixing ratio is fairly consistent across the different schemes, with the exception of the large increase in q_c in the Thompson scheme at temperatures below -10°C. The SBU-YLin and WSM5 schemes perform as would be expected with their clouds consisting of mostly liquid hydrometeors at warmer temperatures, and increasing fractions of frozen hydrometeors as the temperature decreases. All three schemes show peaks in

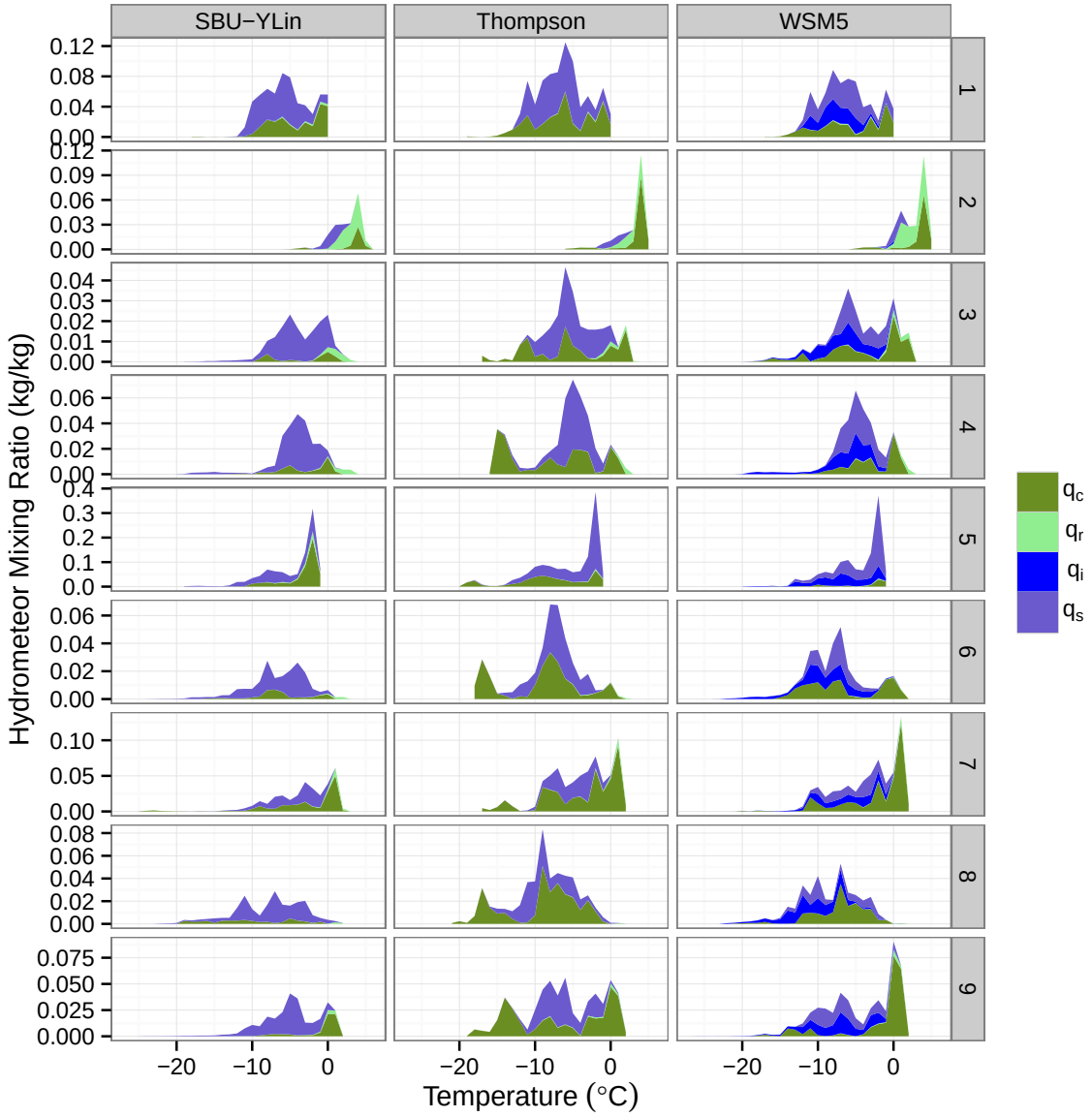

Figure 5.2: Vertically integrated water content (levels 1–15) for all 30 days of simulation by 1°C bins of temperature for model levels below 15 from simulations using the MYNN2 PBL scheme. The hydrometeor values are stacked so that total height is the sum of the total cloud mixing ratio for that temperature. Columns represent the different microphysical parameterizations, and the rows are the different locations shown on the map (Fig. 5.1). The hydrometeor types are represented with different colors.

the total hydrometeor mixing ratio between 0°C and −10°C. However, the large increase in q_c in the Thompson scheme at temperatures below −10°C approaches the value at 0°C for several sites. The Thompson scheme has a peak of q_s between −5 and −10 °C, but after approximately −10°C q_s decreases while q_c increases with decreasing temperature. This behavior needs to be investigated further and compared with observations. The Thompson scheme has been identified repeatedly as the best scheme for ice studies, but those studies typically did not have temperatures below −10°C. For long term studies the increased q_c needs to be understood as this would likely lead to an overestimation of ice mass. Site 2, which is located on the western coast of Norway, was warmer than the other sites, and was the only site with significant q_r.

The other outstanding question from Davis et al. (2014a), was the impact of the value of the N_c parameter on the cloud mixing ratio. Figure 5.3 shows the absolute difference in cloud mixing ratio from changing the value of N_c for the SBU-YLin and Thompson microphysics schemes. The N_c parameter adjusts the initial gamma

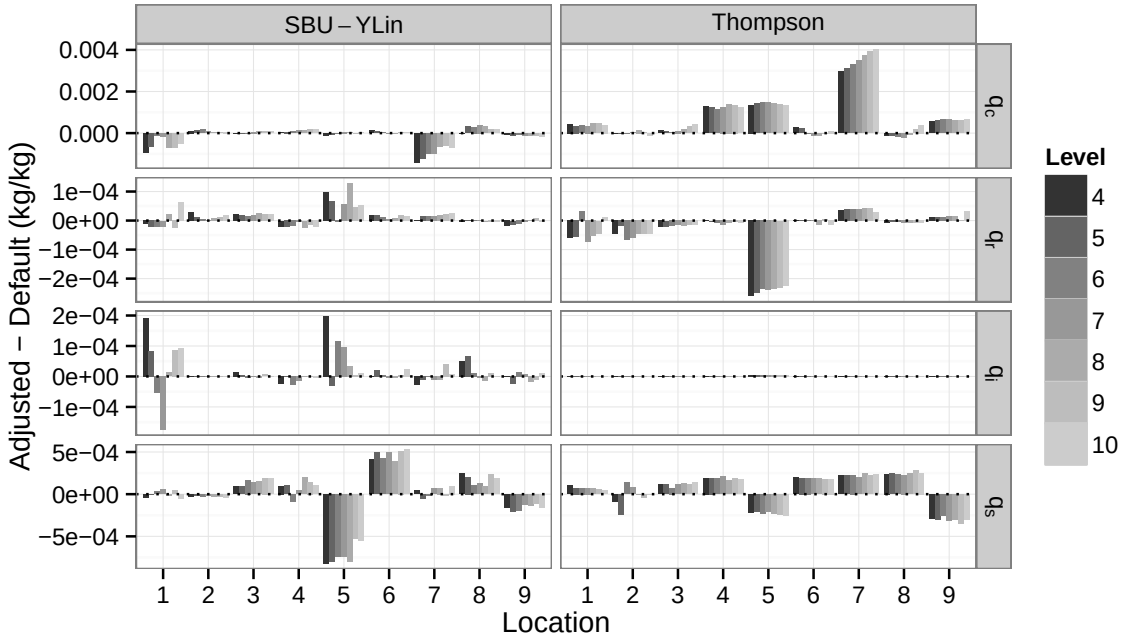

Figure 5.3: Difference in mixing ratio (kg/kg) for the WRF simulation using the adjusted N_c (SBU-YLin 100 cm^{-3}; Thompson 250 cm^{-3}) and the default N_c (10 cm^{-3}; 100 cm^{-3}) at each location (1–9) shown in the map (Fig. 5.1). The rows signify the different hydrometeor types, and the columns signify the microphysical parameterization. The colors identify different levels of the NWP model. The levels selected correspond to the levels that are in the rotor plane of a modern wind turbine.

distribution of the cloud droplet size in these schemes. This should impact the auto-conversion of q_c to q_r and the freezing rate of q_c to q_i and q_s. Therefore, the largest impact is expected to occur in q_c and q_r. For the SBU-YLin scheme, the largest changes were in q_c, but the next highest were in q_i. Increasing N_c should make the initial cloud droplets smaller. Therefore, it is expected that there would be more total cloud mass (q_t) in the SBU-YLin scheme, since the cloud mass would remain in the atmosphere longer before falling as precipitation. At most sites, q_t decreased with the N_c adjustment, because of the large decreases in q_c and q_s. The relative changes were much larger at some of the sites (not shown), notably sites 4 and 8, due to the already small mixing ratios in the SBU-YLin simulations. For example at site 8, the percentage change in q_c was more than 40%.

The Thompson scheme showed changes that better fit the initial assumptions. The q_c term in the adjusted simulation increased compared to the default simulation at almost all sites and levels, while the q_r term decreased by a lesser amount. This would suggest that the clouds were made up of smaller and lighter droplets that converted more slowly from q_c to q_r, remaining in the atmosphere for a longer time. There was almost no change in q_i for the simulations with the Thompson scheme, but q_s did have rather large absolute differences. However, the relative change of q_s was typically less than 2%. For the liquid hydrometeors (q_c and q_r), both the absolute and relative changes were large. For example, the large decrease in q_r at Site 5 was a difference of more than 20%, while the large increase in q_c at Site 7 was an increase of more than 10%. Neither model showed a significant trend in the difference across the vertical levels. The changes in q_t were highly site specific, as seen in the comparison of Sites 2 and 7 in the Thompson scheme. At site 7, q_t increased significantly, while at site 2 there was only a small increase in q_t due to the increase in q_s. Given the large differences seen in the Thompson scheme at some locations, it is clear that for certain locations the icing model results would change significantly with different values of N_c.

Figure 5.4 examines q_t for all model levels below level 50 at all nine locations. The shape of the cloud mass with height depends more on the site than the microphysical parameterization used. For example, Site 5 has most

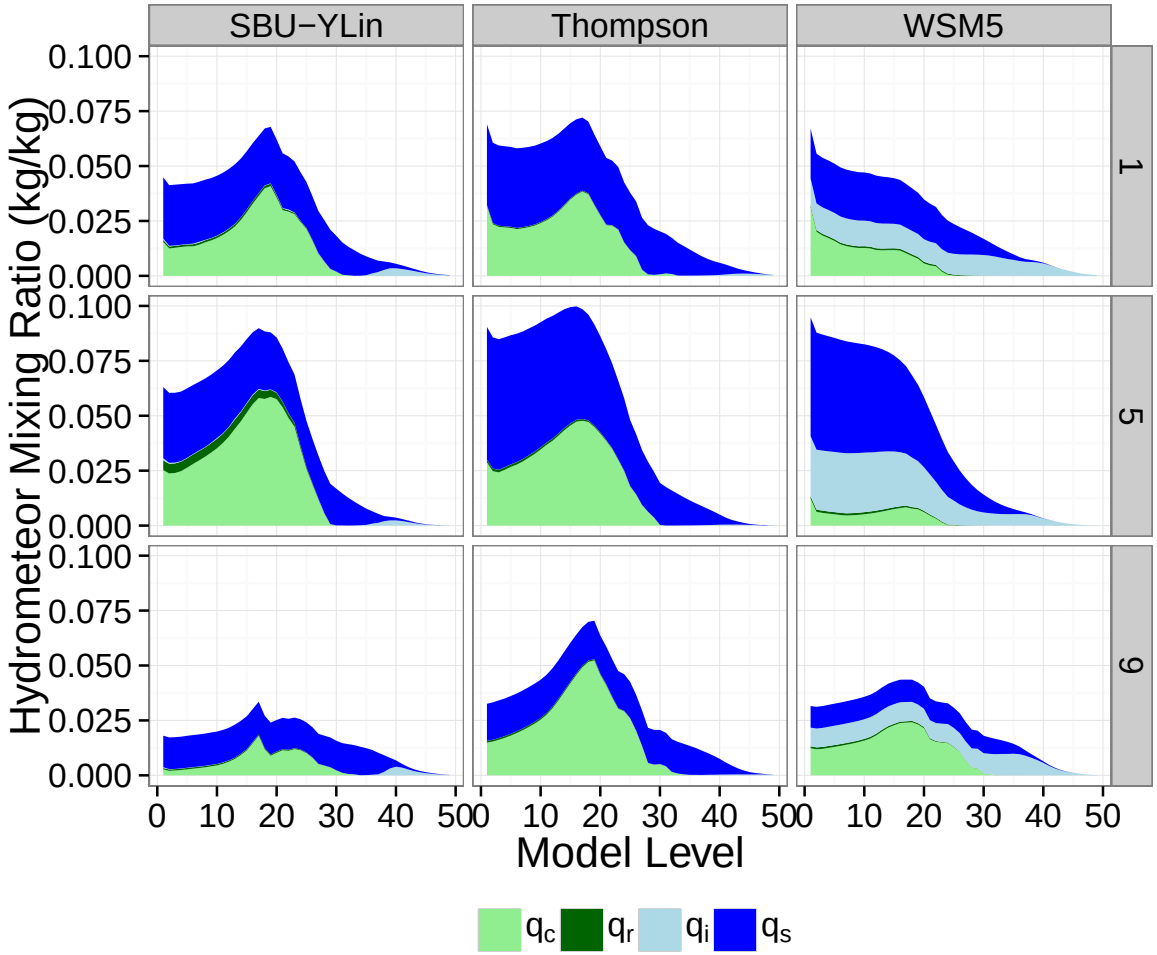

Figure 5.4: Same as Figure 5.2, but dependent on level instead of temperature.

of the cloud mass in the lowest model levels, while Site 9 has more cloud mass between levels 10 and 20. As shown in Davis et al. (2014a), only the WSM5 scheme has significant q_i. Adding the q_i and q_c fields from the WSM5 simulation produces a value which is comparable to the q_c from the Thompson simulation. For all results, except Site 2 and the lower levels of Site 5 in the SBU-YLin based results, q_r is very small. While the SBU-YLin scheme generally has less q_c than the other schemes, at Sites 1 and 5 the q_c values are close to or even larger than those of the Thompson scheme depending on the model level. These sites are at higher elevation than the rest of the sites, suggesting there may be some correlation between the SBU-YLin scheme and elevation.

The treatment of freezing rain for wind turbines has been debated. Some have suggested that the same models used for cloud icing can be used for freezing rain, while others have suggested using dedicated models. Jones (1998) developed a model for freezing rain ice accretion that relied on common meteorological parameters such as the precipitation rate. Alternatively, in the study by Davis et al. (2014a), the q_r field from the NWP model was included directly into the iceBlade model and used to simulate a combination of in-cloud and freezing rain icing, depending on the cloud conditions at turbine hub height. To compare these two approaches the relationship between cloud mass at the hub height of the turbine, and the precipitation rate have been studied (Fig. 5.5). In Figure 5.5, the points are grouped by the dominant type of hydrometeor (Rows). The shading represents the ratio of the dominant type to the total cloud mass. For the large hydrometeors (q_r and q_s), a clear linear relationship can be seen between the amount of cloud mass at model level 7 and the precipitation rate at the surface. This relationship is seen for all three of the microphysics models, and suggests that when using mesoscale model

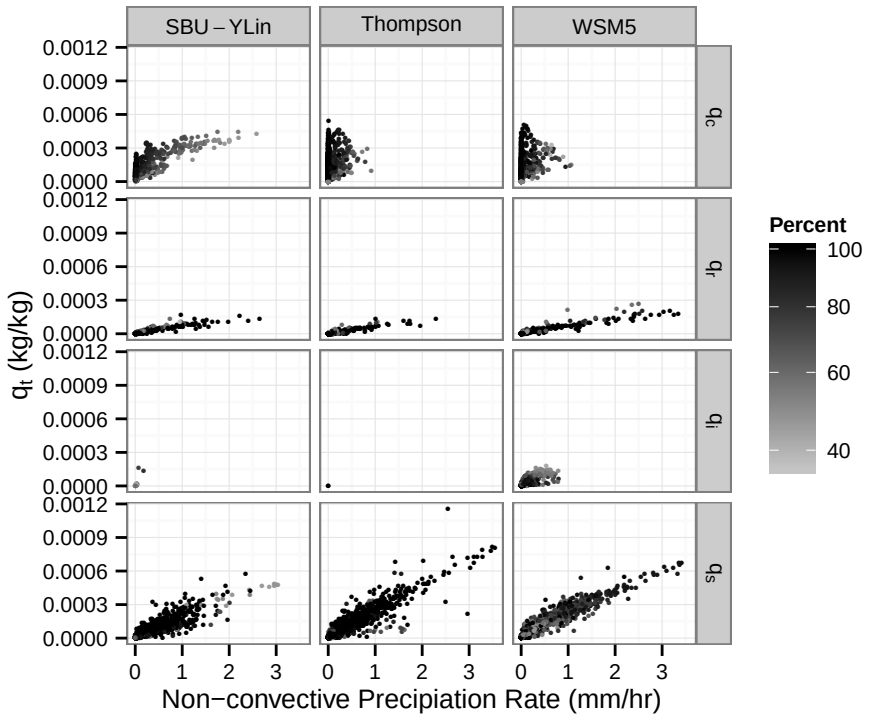

Figure 5.5: Total cloud mixing ratio (q_t; kg/kg) versus non-convective precipitation rate for model level 7 at all 9 locations and for all 30 days. The columns represent the different microphysical schemes, all with the MYNN2 PBL scheme. The rows show the dominant hydrometeor type, and the scale shows the percentage of that type which makes up r_t.

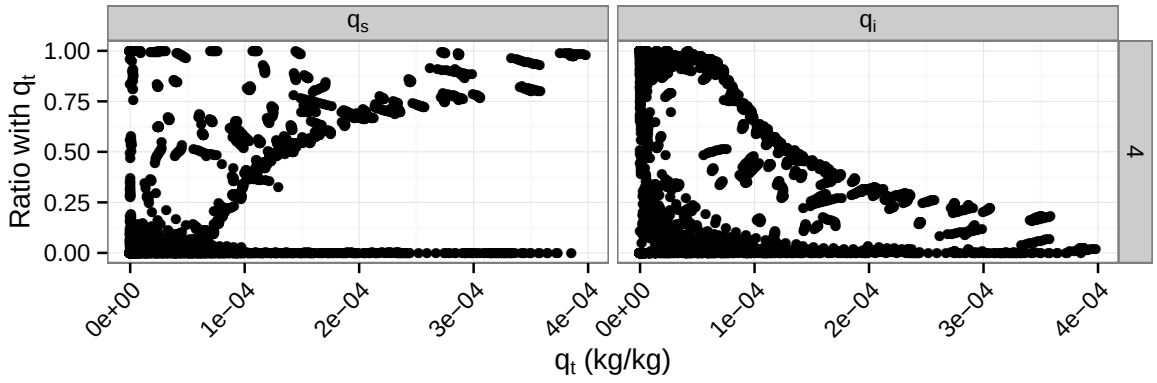

Figure 5.6: Ratio of hydrometeor mixing ratio and q_t versus q_t for WRF simulation using WSM5 microphysics and MYNN2 PBL at Site 4. The columns separate the two frozen hydrometeors that are used in the ratio.

input for ice modeling only one of these parameters should be used. For q_c, the relationship between the total hydrometeor and precipitation is weak. When there is a larger precipitation rate and q_c is the dominant type, it makes up a smaller percentage of q_t. This is particularly evident in the SBU-YLin scheme, which is the only scheme that has precipitation rates above 1 m s^{-1} for the q_c hydrometeor. For q_i in the WSM5 scheme there is less of a relationship than with q_s, but there is still a relationship between q_i and the rate of precipitation. This is due to the relationship between q_i and q_s in the WSM5 scheme. In that scheme, when there are frozen hydrometeors, q_i dominates for low total cloud mass, but as the q_t increases, q_i decreases and q_s increases. An example of this can be seen in Figure 5.6. This holds throughout most of the temperature range, but at higher temperatures (above 5°C), the result is not as clear as there is a larger percentage of non-frozen particles. At colder temperatures it

appears that the WSM5 scheme treats almost all of the cloud as frozen, which is important to know when using this scheme for simulations that will be used in icing studies.

5.3.3 Conclusions

As shown in Davis et al. (2014a), the choice of microphysical scheme can have a large impact on the cloud parameters simulated by the WRF model and therefore a large impact on the ice model results. In this chapter, the differences between the different microphysics models were examined more deeply, and several additional questions about the use of NWP models for ice modeling were studied.

It was shown that the WSM5 scheme converted more cloud mass to frozen hydrometeors at temperatures close to 0°C than either the Thompson or SBU-YLin schemes. Also, it was shown that at temperatures close to −15°C, the Thompson scheme contained very few frozen hydrometeors, with the bulk of the cloud being made of q_c. This was in contrast to the ratio of hydrometeors at −7.5°C, where q_s was the dominant hydrometeor type. This relationship between temperature and hydrometeor type was unexpected and is something that should be verified in newer versions of the Thompson microphysics scheme.

The setting of N_c was shown to be significant for the amount of clouds generated in the Thompson and SBU-YLin schemes, this is a user controlled variable and should be adjusted for each location when the WRF results will be used for icing studies. In the latest release of WRF (Version 3.6), an aerosol-aware version of the Thompson scheme (Thompson and Eidhammer, 2014) was added that includes profiles of cloud condensation nuclei and ice nucleating aerosols instead of using the N_c parameter. This update may be useful for icing studies due to the sensitivities shown in this study. Finally, the question about whether including both q_r and the precipitation rate in an icing model would lead to a double counting was investigated. It was shown that there was a strong relationship between the amount of cloud mass and the precipitation for the precipitating species q_r and q_s, but not for q_c. For the WSM5 scheme, which was the only scheme with significant q_i events, q_i was shown to act more like a precipitating species. This was likely due to the relationship between q_i, q_s and q_t in the WSM5 scheme.

It was shown throughout this chapter that the choice of microphysical scheme can have a large impact on the cloud mixing ratios predicted by the WRF model. Given the known impact between the cloud forecast and the icing model results, it is important to understand the microphysical scheme being used when setting up an icing model. One example of this will be discussed in chapter 7, where the WSM5 was again used as input to an icing model for the power loss studies.

Chapter 6

Ice Model

This chapter focuses on the ice model developed as part of this thesis for use in calculating the amount of ice mass accumulated on a turbine blade. The first section will provide a background of ice-model development. The second section will describe the iceBlade model, and the third section compares the results from two ice accretion models to observations of ice growth on rotating cylinders in a climatic wind tunnel.

6.1 Background

Atmospheric icing has been studied for a long time because it is important for many industries. An ISO standard (12494:2001, E) has been developed for measuring and modeling atmospheric icing on a 1 meter long freely rotating cylinder (Fig. 4.2; left). The standard is useful for small structures such as towers, power lines, and bridge cables. By using the ISO standard for modeling icing, maps of icing have been created for many parts of the world allowing for comparisons between different locations, e.g., Byrkjedal (2012a). The aviation industry has also long studied icing, as it is recognized as a problem for the safety and reliability of air travel. Gent et al. (2000) provides a detailed background on aircraft icing. The focus has largely been on the wings of airplanes, but ice accretion on helicopter blades has also seen significant research.

The majority of models for atmospheric icing have focused solely on ice growth, known as ice accretion. For aircraft icing, ice removal mechanisms are installed on airplane wings due to safety concerns. Therefore, ice does not remain on the wing for long enough for atmospheric ice removal to be of concern. For structures such as tubular masts, bridge cables, and power lines, the main problem caused by ice growth is the static load on the structure, which can lead to a collapse. Since extreme icing events, those large enough to cause a collapse, are rare, only individual icing events are modeled. This is because it can be assumed that the events will be spaced far enough apart in time that each event would largely start from an ice-bare surface. For wind energy studies, ice ablation processes are as important for ice modeling as the ice accretion processes, because power production is reduced with any amount of ice. Therefore, an icing model for wind energy needs to model both ice accretion and ice ablation to provide information for cost-benefit analysis and de-icing solutions. Since there was not much literature on ice ablation models for atmospheric icing, only a background of ice accretion models will be given here.

The most complex models of icing use a computational fluid dynamics (CFD) code to model a flow containing liquid water droplets with a prescribed size distribution around a structure. These models typically include algorithms to determine how the particles flow around or impact the structure, the thermodynamics related to the phase change of the impacting particles, and update the model mesh for the changing shape of the structure as ice accumulates. The models may also include algorithms to model the run-back of any liquid water on the surface that does not freeze on impact for glaze icing studies.

Some of the most common models in this category are FENSAP-ICE (Habashi et al., 2004), TURBICE (Makkonen et al., 2001), and LEWICE (Wright, 2002). FENSAP-ICE is a 3D CFD solver that accounts for all ice processes. FENSAP-ICE can even model rotating helicopter blades. TURBICE and LEWICE are 2D models designed for the study of ice growth on airfoil cross-sections. These models have been shown to provide reasonable lift and drag responses to icing on wind turbine blade airfoils (Homola et al., 2010a,b; Virk et al., 2010). However, for forecasting icing on wind turbines the CFD models have two significant limitations. The

first is the computational expense. Due to the complex processes being modeled and the correspondingly high resolution required to model the detailed flow around an airfoil, running CFD models requires a large amount of computation and, therefore, are not able to run quickly enough to provide a forecast within the target window. Longer term simulations of up to 30 years are often desired for siting studies. The high computational cost of CFD icing models would make such simulations unfeasible given today's computing resources. The second limitation is that these models use steady state meteorological conditions. This means that the temperature, wind speed and cloud parameters do not change with time. This is a large problem for forecasting icing since the atmospheric conditions will often change significantly throughout an icing event. The 2D models have an additional limitation that applies to ice growth under glaze conditions. When modeling glaze icing, studies have often shown a horn like feature on the leading edge of the airfoil, (e.g., Bragg et al., 2005). However, these shapes are not often found in photos of iced turbine blades. This is likely due to the model not including the gravitational and centripetal forces. These forces would act to move the water toward the outer edge of the turbine blade, but without them ice builds up at the stagnation points.

At the other extreme in terms of amount of physics in the model, are forecast models for aircraft icing. These models rely on statistical relationships between many different parameters to provide an estimate of the icing condition, and thereby the potential icing risk for aircraft (Bernstein et al., 2005; Ellrod and Bailey, 2007). These models do not attempt to physically model icing, but rather identify locations where icing is likely to occur using the atmospheric conditions from satellite, radar, NWP model output, and other inputs. This is a reasonable approach for aircraft icing, as aircraft can be diverted around areas of significant icing potential, or can remove the ice using installed deicing solutions. A version of this approach has been utilized for wind turbines, where the relative humidity and cloud base values from ground sensors have been used to estimate icing (Ronsten et al., 2012). This approach has the advantage of using parameters that are commonly measured, however it does not take full advantage of the parameters included in NWP model results.

A third approach to modeling icing lies in between these two extremes and is represented by models such as the Makkonen model (Makkonen, 2000), which is part of the ISO standard, and the OMNICYL model (Finstad, 1986). These models use empirical relationships to estimate the percentage of incoming particles (collision efficiency) that would impact the cylinder as a function of the wind speed, cylinder diameter, and droplet size distribution. The empirical relationship has been evaluated using wind tunnel data (Makkonen and Stallabrass, 1987), and was shown to provide a reasonable estimate for the collision efficiency. The Makkonen model also includes a heat balance term so it can be used for both rime and glaze icing conditions, however it does not simulate the freezing of run-back water during glaze icing conditions.

Previous approaches for forecasting icing events on wind turbines (Oechslin, 2011; Byrkjedal, 2012b; Söderberg et al., 2013) relied on the empirically based Makkonen model, which will be the basis for the model developed in this study as well. This approach is based off the approach presented in Fikke et al. (2008), which coupled an NWP model to the Makkonen model for forecasting icing on power lines. These studies demonstrated good agreement with icing observations for the duration of events, but not for the amount of accumulation. The iceBlade model will be described in Section 6.2. An investigation of the OMNICYL model for rime ice events and comparison with the Makkonen model is presented in Section 6.3.

6.2 iceBlade model

Until recently, the Makkonen standard cylinder model was the most common icing model used for wind turbine icing forecasts (Oechslin, 2011; Byrkjedal, 2012b; Söderberg et al., 2013). Since the Makkonen model estimates ice on a rotating cylinder and not on a turbine blade (Fig. 4.2), statistical methods were used to relate the simulated ice on the cylinder to the production loss on the turbine. These approaches will be discussed in Chapter 7. However, these studies often had a timing offset in the ice forecast and the production losses, usually at the end

of the icing period. By studying the standard cylinder model approach, it was determined that the input conditions, particularly the incoming wind speed, did not match those of the outer part of the turbine blade. Additionally, these models had simplified ablation algorithms that were not well documented. Ice ablation is important for simulating wind turbine icing because periods of instrumental icing and not just meteorological icing were important for modeling the impact of icing on power loss.

The iceBlade model was developed to simulate the accumulation of ice on a wind turbine blade during in-cloud icing conditions. The iceBlade model consists of the Makkonen ice accretion model (Makkonen, 2000), and terms for sublimation, ice shedding and wind erosion of ice. This allows iceBlade to simulate the entire evolution of ice on the blade. The Makkonen model in iceBlade includes several advancements that increase its applicability to wind turbine blades. The wind speed used in the model is adjusted based on the rotational speed of the turbine. When the turbine is in operation, the leading edge of the blade does not experience the ambient wind speed, but rather a blade relative velocity that is related to its rotational speed. The blade relative velocity is much larger than the ambient wind speed at the end of the blade, away from the hub. The end of the blade also contributes the most to power production, and therefore is important for power loss studies.

Several assumptions have been included in iceBlade to simplify the model and ease its implementation. First, the blade is represented as a cylinder with diameter equal to twice the leading edge radius of the turbine blade. IceBlade only takes into account the effects of liquid phase cloud particles. This means that wet-snow is not modeled. This could potentially decrease the number of icing events and the severity of icing when mixed clouds are present, although mixed clouds were not very common in the sensitivity experiments described in Chapter 5. Finally, it is assumed that the turbine is always in operation. This is unrealistic, but as it is not possible to know all of the the criteria for shutting down the turbine, it is a necessary assumption.

The accretion and the ablation models are described in the next two sections, and the representation of the turbine in iceBlade is described in Section 6.2.3.

6.2.1 Ice accretion model

The Makkonen model of ice accretion (Makkonen, 2000), expresses the rate of ice mass growth as the product of the LWC (ω), velocity (v), cross-sectional area of the object (A), and three correction factors α_1, α_2, and α_3:

$$\frac{dM}{dt} = \alpha_1 \alpha_2 \alpha_3 \omega v A. \tag{6.1}$$

The correction factors represent processes that reduce the amount of ice accretion from its maximum value, the incoming mass flux, defined as the product of ω, v, and A. These factors range from 0 to 1 and are defined as efficiencies of collision (α_1), sticking (α_2), and accretion (α_3). By using efficiency factors to account for the loss terms, the model can be updated as improved models are developed. One example of this is the improved sticking efficiency term for wet snow icing presented in Kringlebotn Nygaard et al. (2013). IceBlade uses the factors unmodified at present, although an alternative to α_3 was investigated.

The collision efficiency term, α_1, represents the integrated collision efficiency over the cross-sectional area (E). In the Makkonen model this value is calculated using an empirical formula from Finstad et al. (1988). The empirical relationship was derived using regression analysis based on data from an investigation of water droplets in flows around cylinders by Langmuir and Blodgett (1946). It depends on the MVD of the cloud droplets, cylinder diameter (d), v, air temperature, and air density.

The sticking efficiency term, α_2, does not apply for liquid cloud droplets, as it is a term used for wet-snow accumulation, which is not included in iceBlade. Therefore, α_2 is set to 1, matching the value recommended in Makkonen (2000) for liquid droplets. A value of 1 means that all particles that hit the turbine will stick.

The accretion efficiency term, α_3, represents the fraction of incoming mass that freezes on the structure. This term is equal to 1 under rime icing conditions and has smaller values for glaze icing conditions. The accretion

efficiency is determined by the heat balance at the interface between the incoming droplets and the surface. The heat balance for the ice-water interface from Makkonen (2000) is:

$$Q_f + Q_v = Q_c + Q_e + Q_l + Q_s, \tag{6.2}$$

where Q_f is the latent heat released during freezing, Q_v is the frictional heating of air, Q_c is the loss of sensible heat to the air, Q_e is the latent heat lost through evaporation, Q_l is the heat loss to warm the incoming water to the freezing temperature, and Q_s is the heat loss due to radiation. Makkonen (2000) provided parameterizations for each of these terms that were also used in iceBlade. Most of the expressions for these terms were straight-forward and will not be repeated here. The exception was the calculation of the convective heat transfer coefficient (H). In iceBlade, H is calculated using the Nusselt number (Nu) of an airfoil. The equation to calculate Nu comes from the approach of Sherif et al. (1997), and will be described in more detail in Section 6.2.2.

Another approach for calculating α_3 was investigated using the asymptotic ice growth model of Brakel et al. (2007). This model was developed for use in aviation and would allow for different thermal properties of the substrate, and the ability to simulate different ambient temperatures on either side of the structure. During sensitivity testing, the differences between the Brakel and Makkonen models were minimal as rime icing was the dominant ice type, so α_3 did not have a large impact on the model results. However, the Brakel model may be worth investigating further for studying anti-icing technologies that rely on heating the substrate.

When using the WRF model, the incoming mass flux is calculated as a combination of q_c, q_i, and q_r along with the blade relative wind speed and α_1. Since q_r represents larger precipitating hydrometeors, it is assumed that all of those particles will impact the blade. Therefore only q_c and q_i are used to calculate α_1. This allows the iceBlade model to capture both freezing rain and in-cloud icing at the turbine. The only reason for including q_i is due to the sensitivity tests with the WSM5 parameterization scheme that showed a large amount of q_i compared with the Thompson scheme. The calculation of the mass flux is likely to be highly dependent on the microphysical parameterization used and should be adjusted when using different models.

6.2.2 Ice ablation models

Ice ablation is a general term describing processes that remove ice from a structure. There are four main ablation processes: 1) melting, 2) sublimation, 3) shedding, and 4) erosion. Melting is the conversion of ice to a liquid when the surface temperature of the ice exceeds 0°C. Sublimation occurs when ice is converted to water vapor without first forming a liquid, and depends on the humidity of the atmosphere. Unlike melting, sublimation can occur at temperatures less than 0°C. When ice loses adhesion with the surface and falls off, it is called shedding. In the iceBlade model, shedding is considered to be an absolute process leading to all ice being removed from the turbine blade. However, this is a simplification as there are many examples of partial shedding from photographs of iced turbine blades, where some ice remains on the blade. Finally, erosion occurs when the force of the air molecules or tiny atmospheric particles propelled by the wind hit the ice, and cause small pieces of ice to break off. IceBlade includes algorithms for shedding, sublimation, and erosion. Melting was not included as all ice is assumed to be removed from the blade when the temperature is above 0°C due to the shedding algorithm.

A physical ice shedding model requires detailed information about the blade surface and the microscopic accumulation of ice on that surface. Jowitt (2013) investigated the adhesion of ice on two blade samples, and found that ice had a fairly strong adhesion strength to these materials, but was not able to develop a general model due to the uncertainty in the measured contact angle. The implementation of a stochastic model for ice shedding was discussed throughout this project, however there was insufficient observational data to build the model. Therefore, a simplified shedding algorithm was developed (Davis et al., 2014a). The following simplifications were made: 1) as long as the turbine was in operation, even a slight loss of adhesion would cause the ice to be thrown from the blade; 2) adhesion would only be lost due to melting at the ice-blade interface; and 3) the power output from

the turbine always follows the idealized power curve. Given these assumptions, ice shedding was assumed to occur based on a simple threshold temperature. After testing various thresholds, the best results were found using a value of 0°C. The low threshold value is likely due to the underestimation of temperature in the WRF model results compared to nacelle temperatures as discussed in Section 3.4. Additionally, the impact of ram-rise on the temperature at the tips of the turbine blades has not been taken into account. Ram-rise is the increase in temperature due to friction at high speeds that may lead to a small warming at the tips of the turbine blades, due to the large relative wind speeds.

Ice sublimation is modeled using the explicit solution from Srivastava and Coen (1992) (Eq. 16). Equation 6 in Srivastava and Coen (1992) was modified to account for the cylindrical shape of the representative blade in iceBlade and to replace the ventilation coefficients of water vapor (f_v) and heat (f_h) with the Sherwood number (Sh) and Nu. After the modifications Equation 6 from Srivastava and Coen (1992) could be written as:

$$\left(\frac{dM}{dt}\right)_1 = \frac{A\,Sh\,D\rho_s\left(T_\infty\right)}{L\left(1+\frac{L_s D\,Sh}{k\,Nu}\rho_s'\right)}, \tag{6.3}$$

where A is the surface area as in (Eq. 6.1), D is the diffusivity of water vapor in air, $\rho_s\left(T_\infty\right)$ is the saturation vapor density at ambient air temperature $\left(T_\infty\right)$, L is the characteristic length scale, L_s is the latent heat of sublimation, k is the thermal conductivity of air, and ρ_s' is the derivative of $\rho_s\left(T_\infty\right)$. Sh is the ratio between the convective and conductive mass transfer coefficients, while Nu is the same ratio for heat transfer coefficients, and they are double f_v and f_h (Pruppacher and Klett, 2004). Sherif et al. (1997) was again used to calculate the Nu, as it was for calculating the convective heat transfer coefficient (H) in the accretion model. In Sherif et al. (1997), Nu is a function of the chord length and leading edge diameter of the an airfoil, and the non-dimensional Reynolds and Prandtl numbers. Sh can be calculated by substituting the Schmidt number for the Prandtl number. The final sublimation equation used the chord length as the characteristic length L. A constant value of 1.0 m was used for the chord length as it cancels out when at the leading edge of the turbine.

6.2.3 Turbine blade representation

Several simplifications have been made to the turbine blade geometry to reduce the complexity of the iceBlade model. Only a 1-m long segment of the turbine blade is modeled. The segment is assumed to be located approximately 85% down the blade. Several positions were tested, between 75 and 95% of the blade length, and found little sensitivity for the model results. Additionally the blade geometry is represented as a cylinder instead of an airfoil. In all studies, the blade was represented as a cylinder with a diameter of 0.144 m. This value was based on the blade of the NREL 5 MW reference turbine (Jonkman et al., 2009). For the blade on that turbine, the leading edge radius for the airfoil was defined as 2.4% of the chord length and the chord length was 3.0 m.

The blade was not modeled as rotating through space with regard to the meteorological conditions. Instead, hub height values were used. This was in part due to the similarities of the values throughout the rotor plane, but also to simplify the computations. To simulate the blade rotating through space, it would have been necessary to calculate icing at each level the turbine blade passes though. By using the hub height conditions only 1 level needed to be calculated. This assumption was tested at two sites, where it was found that the cloud parameters did not vary greatly through the relevant model levels. Figure 5.4, shows that there is minimal change in the cloud parameters below level 15 (approximately 200 m above ground level).

To calculate the blade relative velocity, a relationship between the ambient wind speed and the revolutions per minute (rpm) of the turbine is required. A curve was fit to estimate the rpm from the nacelle wind speed, using data from a common modern turbine. The rpm value was then converted to a linear speed at the location of the blade section being modeled. The use of the blade relative velocity was found to reduce the number of icing events, but increase the amount of ice accretion when icing did occur. This lead to an overall increase in both ice

accumulation and duration due to the longer ablation phase. The decrease in events is related to the α_3 term in equation 6.1. Figure 4 in Appendix B showed that as the wind speed increased, α_1 also increased. From this it can be assumed that increased mass flux from the increased α_1 and v terms are balanced by α_3. This is because as more liquid water comes into contact with the structure, more latent heat will be released due to the ice freezing. If more latent heat is released than can be removed by the environment, ice will not be formed. This relationship is illustrated in Figure 2.2.

Lastly, iceBlade does not update the size of the cylinder as ice grows on it. The Makkonen model assumes that the cylinder retains the cylindrical shape by growing evenly in all directions. For a turbine blade, most of the ice grows out of the leading edge as shown in a CFD study by Homola et al. (2010b). Therefore, in iceBlade the ice is expected to retain the same diameter for the collision efficiency calculation. The next section will investigate how realistic the assumption of a constant diameter is.

6.3 Comparison of Makkonen and OMNICYL accretion models

6.3.1 Introduction

The OMNICYL model was developed by Finstad (1986) during her Ph.D. thesis, within which the source code could be found. Unlike the Makkonen model, which was developed to model the aggregate mass without concern for where the mass formed, OMNICYL was developed to visualize where on a static cylinder ice would form, making it more relevant for turbine icing.

The two models were evaluated against wind tunnel studies performed by Makkonen and Stallabrass (1987). Makkonen and Stallabrass (1987) ran 33 ice growth experiments on a rotating cylinder in a climatic wind tunnel with varying cylinder size, duration, wind speed, air temperature, LWC, and MVD (Table 6.1) to investigate the empirical formula for the total collision efficiency (α_1 in the Makkonen model). Given the wide range of experimental conditions this dataset was a good fit for evaluating the differences between the OMNICYL and Makkonen ice accretion models.

6.3.2 Methodology

The base equation for OMNICYL is similar to the Makkonen model and could be written as:

$$\frac{dH_l}{dt} = \beta_l \, \omega \, v \, \rho_l, \tag{6.4}$$

where dH_l/dt is the change in ice height for a given location along the cylinder with time, β_l is the local collision efficiency, and ρ_l is the local ice density. β_l is calculated through a relationship between β_0 and the ratio of ϕ_l and ϕ_{max} (ϕ_r), where β_0 is the collision efficiency at the center of the leading edge of the cylinder, ϕ_l is the local angle and ϕ_{max} is the maximum angle where ice will form (Fig. 6.1). For the purposes of this model, the center of the leading edge of the cylinder is called 0°. Therefore the top of the cylinder is 90°. ρ_l is calculated as a relationship between ρ_0 and ϕ_r.

After calculating each local ice height (H_l), the area of ice for a given location could be calculated. Using the area of each section and $\bar{\rho}_l$, the section ice mass could be calculated. Integrating over all of the ice points would allow the total ice mass and average density to be calculated. The integration time could be controlled by setting the number of layers to create for a given total runtime. The model would output data for each layer, and for the total duration of the simulation.

During the first test simulations of OMNICYL it was found that the value for ρ_0 in Finstad (1986) did not match the results from the wind tunnel tests of Makkonen and Stallabrass (1987). The wind tunnel results showed that the density changed significantly depending on the conditions, as would be expected (Fig. 6.2; red line and points), but

Table 6.1: Test conditions from Makkonen and Stallabrass (1987)

Starting diameter (cm)	Duration (min)	Wind Speed ($m\,s^{-1}$)	Temperature (°C)	Liquid Water Content ($g\,m^{-3}$)	MVD (μm)
1.024	30	20	-4.5	0.36	17.1
1.024	30	20	-4.5	0.35	14.4
1.024	30	20	-9.5	0.35	14.4
1.024	30	20	-19.3	0.35	14.4
1.024	31	20	-4.5	0.33	13.1
3.183	40	20	-4.5	0.36	17.1
3.183	40	20	-4.5	0.35	14.4
3.183	40	20	-9.5	0.35	14.4
3.183	40	20	-19.3	0.35	14.4
3.183	40	20	-4.5	0.33	13.1
4.440	50	20	-4.5	0.36	17.1
4.440	50	20	-4.5	0.35	14.4
4.440	50	20	-9.5	0.35	14.4
4.440	50	20	-19.5	0.35	14.4
4.440	50	20	-4.5	0.33	13.1
7.609	50	20	-4.5	0.36	17.1
7.609	50	20	-9.5	0.36	17.1
7.609	50	20	-4.5	0.35	14.4
7.609	50	20	-9.5	0.35	14.4
7.609	50	20	-19.3	0.35	14.4
7.609	50	20	-4.5	0.33	13.1
1.024	30	36	-4.9	0.15	15.7
1.024	30	36	-4.9	0.15	13.4
1.024	30	36	-4.9	0.14	12.2
3.183	40	36	-4.9	0.15	15.7
3.183	40	36	-4.9	0.15	13.4
3.183	40	36	-4.9	0.14	12.2
4.440	50	36	-4.9	0.15	15.7
4.440	50	36	-4.9	0.15	13.4
4.440	50	36	-4.9	0.14	12.2
7.690	50	36	-4.9	0.15	15.7
7.690	50	36	-4.3	0.15	13.4
7.690	50	36	-4.9	0.14	12.2

with the fixed ρ_0 value, the OMNICYL density did not vary much (not shown). However, the Macklin integrated density ρ (Macklin, 1962), used in the Makkonen model, showed good agreement with the observations (green line). Therefore, the OMNICYL model was updated to provide a total density that was similar to the Macklin density. Since there was not a known relationship between ρ and ρ_0, an iterative method was implemented. The OMNICYL model was run with a first guess for ρ_0, and then total density was calculated. The total density was then compared with Macklin's ρ, and if the difference was larger than 10 $kg\,m^{-3}$, OMNICYL was run again with ρ_0 set to half of the initial value. As the OMNICYL model has a short run time, the iterative approach was was a reasonable way of fitting the density value. As can be seen in Figure 6.2, the fitting process lead to almost identical density values between the OMNICYL and Makkonen models.

6.3.3 Results

Figure 6.3, shows the sensitivity of the OMNICYL model to the of the number of ice layers simulated. Here it can be seen that using only 1 layer for a one hour long simulation produced an unrealistic shape of ice, compared with results from in CFD models (eg., Homola et al., 2010a). However, the model results with 6, 12, and 24

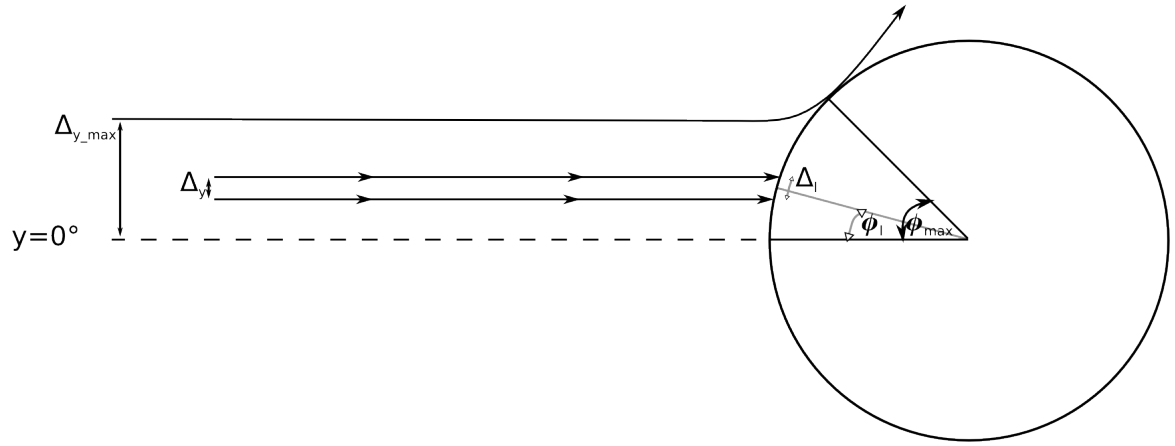

Figure 6.1: Droplet trajectories on a cylinder. Wind is from the left. ϕ_{max} is the maximum angle where ice will form, and occurs from droplets originating with a displacement y'. Layer displacement is shown with a displacement size of Δ_y, leading to a distance on the curve of δ_l and a displacement angle of ϕ_l.

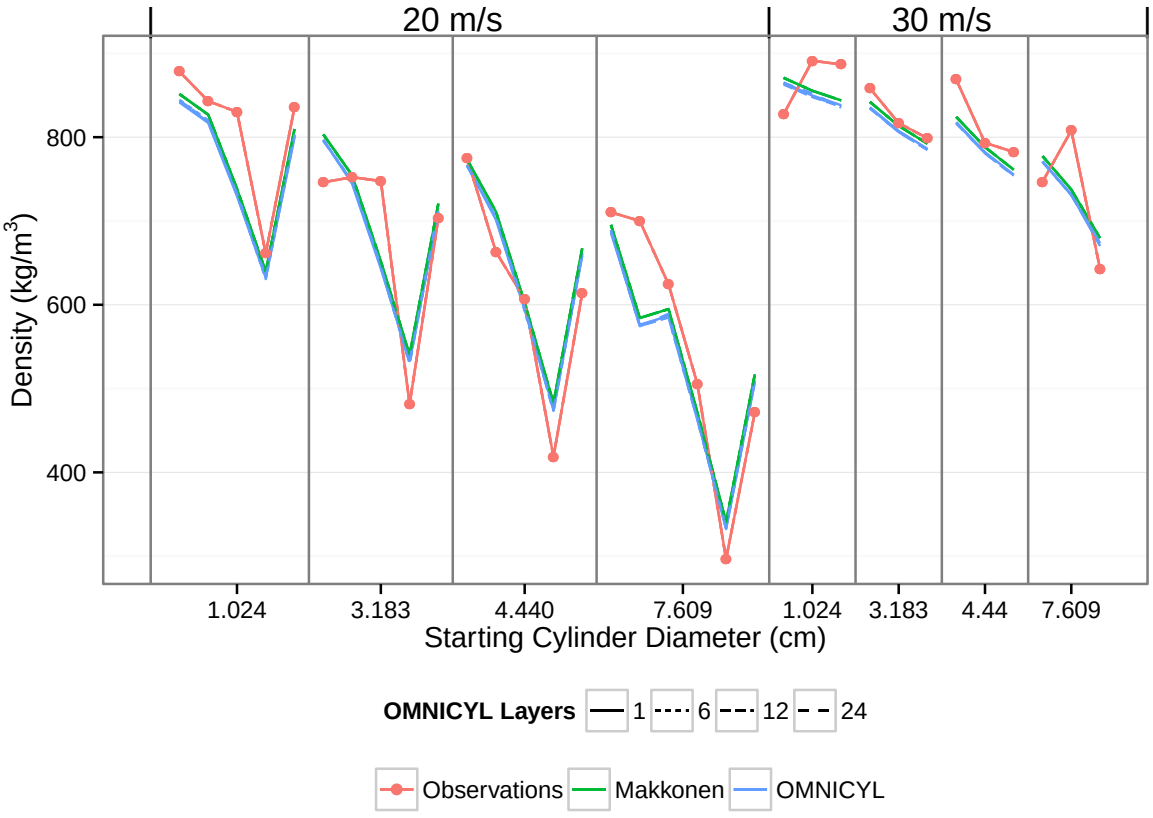

Figure 6.2: Ice density as a function of 33 different test cases of ice growth arranged from left to right by their order in Table 6.1. The vertical lines are used to separate the different starting cylinder diameters. Observations are in orange, the Makkonen model results are in green and 4 different OMNICYL model results are in blue. OMNICYL results used the updated density algorithm. The different layer tests are represented by different line types.

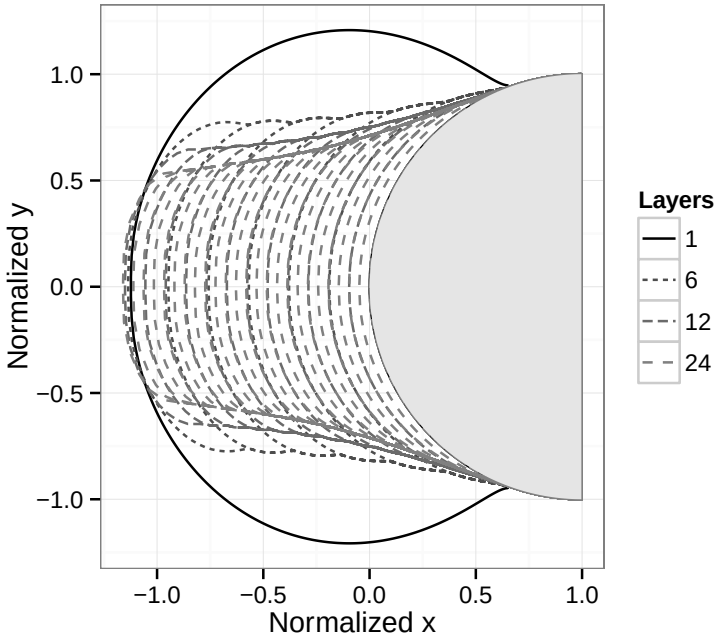

Figure 6.3: Growth of ice on a cylinder using the OMNICYL model with varying number of layers. Half of the starting cylinder is plotted, ending at 0.0 on the x-axis. The model was run for a case with MVD: 3×10^{-5} m, cylinder diameter: 14.4 cm, wind speed: 90 m s^{-1}, LWC: 0.4×10^{-5} kg m^{-3} for a duration of 1 hour.

layers produced relatively similar ice shapes. The total ice mass estimate showed a similar result, with the 1-layer simulation having significantly higher ice mass than the other model sensitivity tests.

The OMNICYL model results were compared with the Makkonen model and validated for the Makkonen and Stallabrass (1987) wind tunnel experiments. Figure 6.4 shows the observed mass, the mass estimated from the Makkonen model, and four estimates of mass by OMNICYL using the different number of layers shown in Figure 6.3. The results are ordered by test number, which grouped the experiments by starting cylinder diameter. The two sets of cylinder diameters correspond to two different wind speeds used in the wind tunnel tests. The model performance varies significantly depending on the starting cylinder diameter. For the two smallest cylinders, the OMNICYL model with only 1-layer is closest to the results from the Makkonen model, both of which drastically overestimate the observed ice mass. However, the results from the OMNICYL model with 24-layers shows a reasonable model performance for the smallest cylinder. For the cylinder starting at 3.183 cm, the 6-, 9-, and 12-layer tests all perform well compared with the observations. For the larger cylinders, the result from the 1-layer OMNICYL simulation is still an outlier, but the Makkonen model is closer to the other OMNICYL results. For the second set of tests on the larger cylinders, with wind speed equal to 36 m s^{-1}, both models perform well compared to the observations, but for the first set of tests, the ice mass on the largest cylinder is largely underestimated, with only the 1-layer OMNICYL model coming close to matching the observations.

It can be seen that the density fitting process lead to similar density values regardless of the number of model levels (Fig. 6.2). The density results are similar to those of the ice mass, with the modeled values following the observations fairly closely. For the higher wind speed tests, the density model captures the signal incorrectly from the smallest cylinder. This, however, may be a measurement error as the observed ice growth was much smaller in these cases than any of the others. For the 3.183 cm diameter cylinder, the model does an excellent job of estimating the density.

After verifying that the model was performing well compared to wind tunnel observations, a suite of sensitivity tests were set up to determine the change in shape under different cloud conditions. Figure 6.5, shows the shapes generated by different combinations of MVD and wind speed. The wind speed is shown to mostly impact the

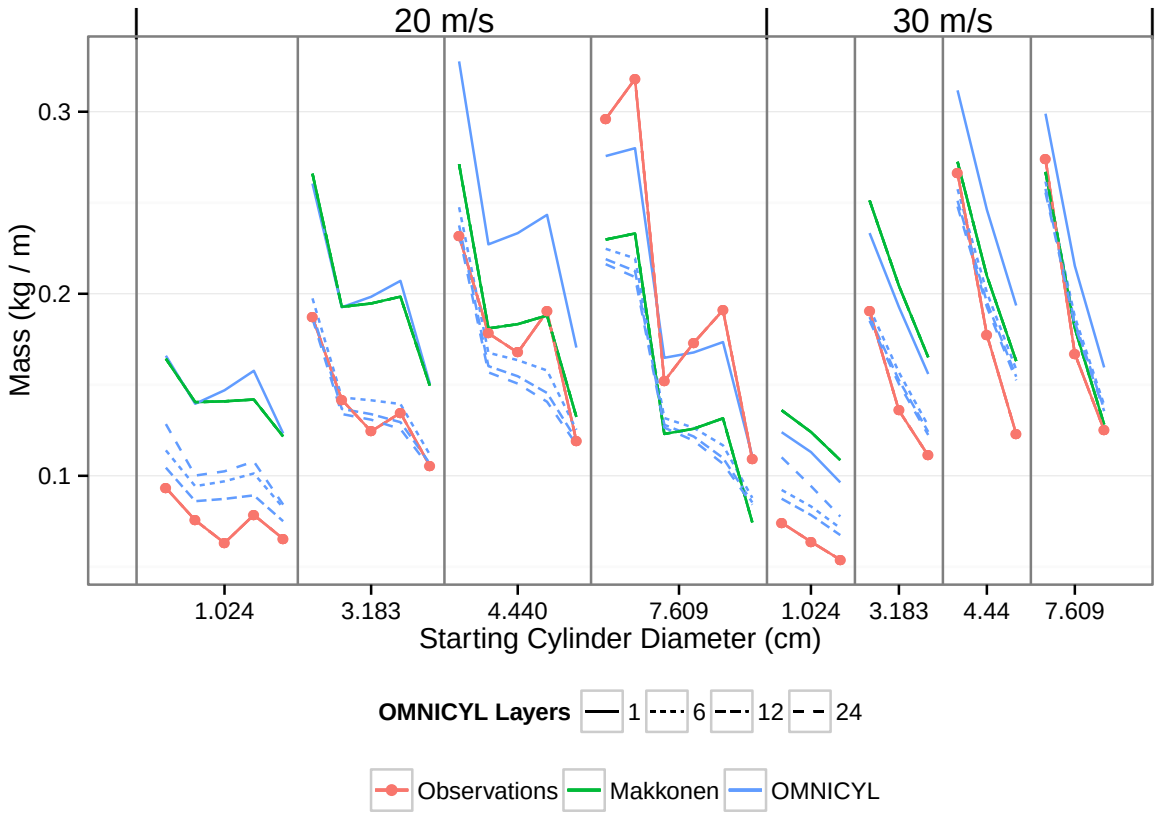

Figure 6.4: Same as Figure 6.2, but for ice mass.

amount of ice, while the MVD has a large impact on the shape of the ice growth. Only at the largest MVD values does the assumption of a static cylinder diameter appear to hold. At smaller values of MVD, the cylinder diameter appears to get smaller over time. Figure 6.6 shows the estimated ice mass for the same sensitivity tests, with different layer values for the OMNICYL model. From this result, a 6-layer OMNICYL model does a good job of matching the Makkonen model ice mass. The 1-layer OMNICYL results are significantly higher than the those from the Makkonen estimated values. It is interesting to note the impact of the α_3 term in the Makkonen model. In the test with the largest MVD and highest wind speed, the Makkonen model switched to glaze ice, leading to dramatically less ice growth than the OMNICYL model. This forms a distinct bend in the curve which is not seen in the other model results.

6.3.4 Discussion and Conclusions

The OMNICYL model provides an interesting comparison to the Makkonen model by simulating the shape of the rime ice growth. The OMNICYL model was shown to perform as well as the Makkonen model for simulating the ice mass grown on rotating cylinders in a wind tunnel study, with typically 6-layers per simulation being the optimal number. It was also shown that the assumption made in iceBlade, that ice would retain the same shape as the leading edge of the turbine, did not match the results, except at the highest droplet sizes. Interestingly, like iceBlade, OMNICYL does not update the diameter for the flow parameter calculations even when the shape of the ice was changing.

In this study there were no observed icing shapes that could be used to evaluate the model performance, but Finstad (1986) evaluated the OMNICYL ice shape against four different wind tunnel measurements and found that it could capture the general shape of ice growth. This means that it could identify the periods when the ice should be growing to a point or even expanding, which was not found in any of our studies. This suggests that the

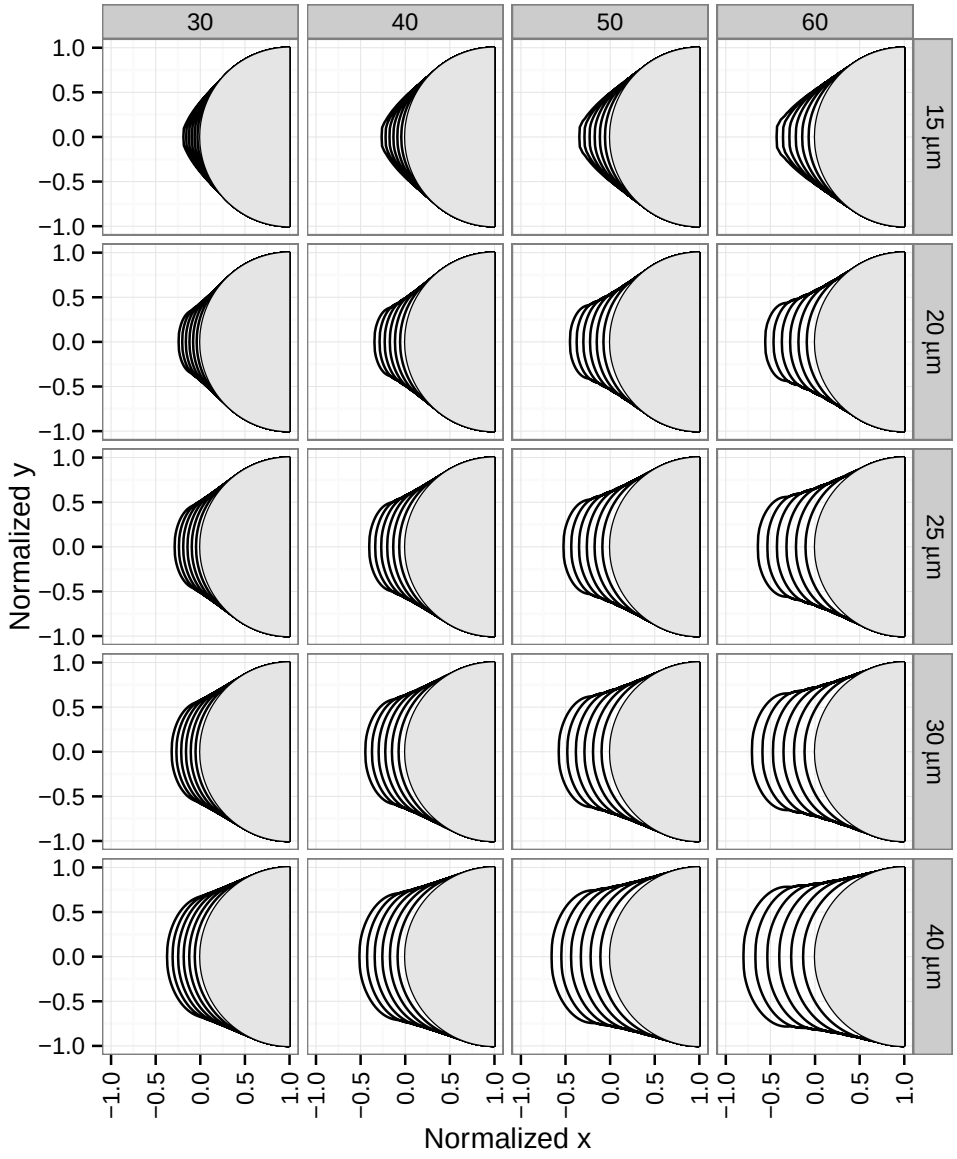

Figure 6.5: Shape of OMNICYL ice growth in x and y directions for different MVD values (μm; rows) and wind speeds ($\mathrm{m\,s^{-1}}$; columns). The shading changes with layer number. OMNICYL was run with the settings cylinder diameter: 14.4 cm, LWC: 4×10^{-04} $\mathrm{kg\,m^{-3}}$, layers: 6, duration: 1 hour, and temperature: -10°C.

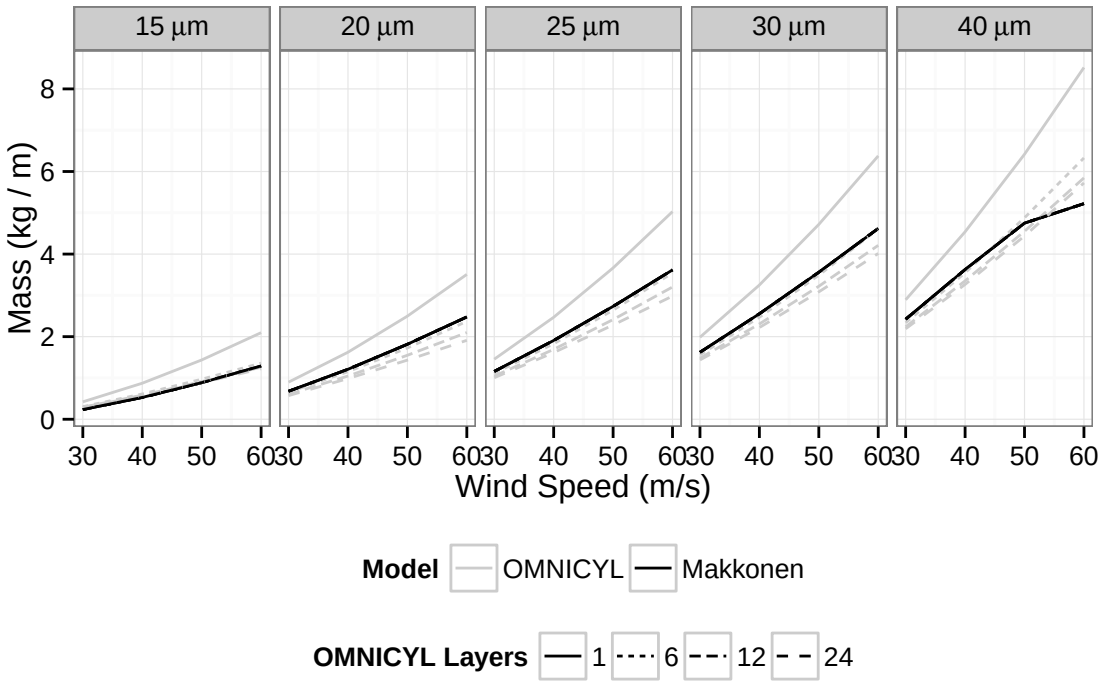

Figure 6.6: Ice mass ($\mathrm{kg\,m^{-3}}$) vs wind speed ($\mathrm{m\,s^{-1}}$) for different MVD values (μm; subplots) for the same tests as shown in Figure 6.5. The Makkonen model results are in black and OMNICYL results are in light gray. Runs of OMNICYL with different levels are shown with different line types.

assumption of a constant cylinder diameter made in iceBlade may not be too unrealistic, although the Makkonen model may be more sensitive to this value, since it does not calculate the local collision efficiencies.

Because the OMNICYL model is fairly simple and runs efficiently, it would be worth investigating the ability to add additional terms to the model that would update the effective diameter, based on the leading edge of the ice and to restart from a previously iced case. These changes would allow for the approximation of the collision efficiency and density to be updated as the ice grew, and also allow for the model to be run with a baseline ice profile. By replacing the Makkonen model with the OMNICYL model, a shape parameter could be added to the power loss models.

Unfortunately, the OMNICYL model in its current state is not fit to be implemented in the iceBlade model. This is in part due to the lack of a glaze ice algorithm. Additionally, like the CFD models the OMNICYL model is designed to operate under fixed meteorological conditions. Therefore until the ability to be restarted from a previous ice case is added it cannot adapt to the changing meteorological conditions experienced at a wind park. Still the use of alternative ice accretion models for use in iceBlade should continue to be explored.

Chapter 7

Power model with icing

This chapter investigates the the modeling of power loss of a wind turbine blade due to icing. The power loss model takes input from the ice model, NWP model, and wind farm management model to produce a power estimate that includes the impact of icing (Fig. 4.1). Here the wind farm management model was represented by the empirical power curve of all turbines in the park, fit using the mean nacelle wind speed. This implies that the error and bias of the baseline model are smaller than normal as none of the NWP uncertainty is included. The decision to not model the power directly was made to simplify the analysis, and maintain the focus on the impact of icing rather on than the ability to model the power from the NWP wind speed.

7.1 Background

It has long been known that icing can have a large effect on the power production of turbines in cold climate regions. However, it was only recently that models have been developed for studying the relationship between icing and power loss. The initial studies used the Makkonen model to model ice growth on a standard cylinder (Oechslin, 2011; Byrkjedal, 2012b; Söderberg et al., 2013). In two of these studies (Byrkjedal, 2012b; Söderberg et al., 2013), the ice mass from the standard cylinder model was used to fit a three-dimensional power curve, to estimate the power production, when there was ice on the turbine.

Since this project began, other methods have been developed. Karlsson et al. (2014) presented an approach that used the duration of the icing event to fit a three-dimensional power curve. This approach was motivated by model results, which found that the periods of ice accumulation were easier to match than the amount of ice. Therefore, they believed that using a duration term may be more applicable than the modeled ice mass. Baltscheffsky (2013) presented an updated version of the model used by Söderberg et al. (2013) that included an icing model similar to iceBlade. The ice model results were then used as input, along with NWP results, to a neural network that provided production estimates with icing effects. Davis et al. (2013b) presented a model that relied on the iceBlade model and NWP results to estimate the power loss, using a linear model. This model was then updated in Davis et al. (2013a).

The next section will describe the final version of the power loss model developed for this thesis (Sec. 7.2). This model is a further refinement of the model presented by Davis et al. (2013a). Then the paper describing the development of the model and its evaluation will be briefly described (Sec. 7.3), and the final section will provide an overview of a chapter of the Icewind project report, describing an inter-comparison study undertaken as part of the Icewind project (Sec. 7.4).

7.2 Methodology

Davis et al. (2013a) demonstrated that the MB and RMSE of a power forecast could be reduced for a wind park in cold climates by the use of a power loss model fit with results from iceBlade. The power loss model used input from iceBlade and from a meteorological model to fit a linear model for power loss. The model presented here improves on that approach through the use of a generalized additive model (GAM) (Hastie and Tibshirani, 1990; Wood, 2006). The GAM method was chosen as it allows for the model to be fit without a rigid parametric

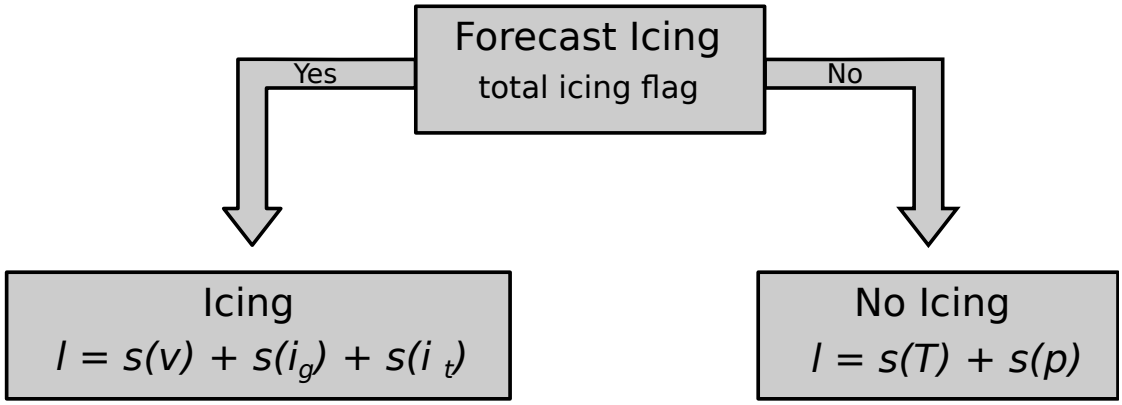

Figure 7.1: Hierarchical model design. Smoothing functions in the GAM models are represented by $s()$, l is the power loss, v is the wind speed, i_g is the ice growth mass, i_t is the total ice mass, T is the temperature, and p is the pressure.

restriction. This is important for icing, as a clear relationship between icing and turbine production is not known a priori.

Unlike the power curve approaches by Byrkjedal (2012b) and Karlsson et al. (2014), and the neural network approach by Baltscheffsky (2013), the model developed in this thesis modeled power loss and not power. One of the reasons for this approach was to allow flexibility in the choice of power prediction model. Additionally, since this thesis was not focused on modeling power using wind speeds from an NWP model, it was assumed that external models would perform better for estimating power than any model developed in this this study. Therefore, by modeling the power loss the end user could select whichever power prediction model they wanted, and use the power loss model to update that forecast for icing impacts. During the model fitting, the power loss term was converted back to power, so that it could be evaluated against the baseline power prediction that did not include the icing impact.

The power loss model was built using a hierarchical modeling approach (Cohen, 2003). The hierarchical approach chosen was a combination of a decision tree (Breiman, 1984) and two GAMs, one fit for iced periods and one for non-iced periods. Figure 7.1 shows a schematic of the hierarchical model and the GAM model equations. The decision tree only had one level, which was based on the iceBlade ice flag set to an accumulation of 0.1kg m^{-3} of ice. At the base of the decision tree were two separate GAM models. The iced model can be written as

$$l = s(v) + s(i_g) + s(i_t), \tag{7.1}$$

where l is the power loss due to icing, $s(v)$ is a smooth function of the wind speed v, built as a linear combination of thin plate splines (Wood, 2003) of the wind speed, i_g is the amount of ice accretion for a given time-step, and i_t is the total amount of accumulated ice. The non-iced model was fit using smooth functions of temperature T and atmospheric pressure p.

The GAM models were created through the combination of known physical relationships and statistical analysis. The R package *mgcv* (Wood, 2011; R Core Team, 2014) was used for fitting the GAMs. A cross-validation approach (Picard and Cook, 1984) was employed for selecting the best model. During cross-validation, additional terms were eliminated, the various smoothing functions in *mgcv* were tested, and the k-dimension of the smooths was explored. This k-dimension controls the maximum degrees of freedom in the smoothing function. The optimal k-dimensions for the model were 7 for both $s(T)$ and $s(p)$, 15 for $s(v)$, and 40 for both $s(i_g)$ and $s(i_t)$. Even though the k-dimension was set to 7 for $s(T)$ and $s(p)$, the effective degrees of freedom were often much smaller.

The hierarchical model approach was found to significantly outperform a single GAM model. This was due to the exclusion of the non-iced points in the fitting of the iced point model. The non-iced points still had significant variation in power, but as it was not related to the icing signal, this complicated the fitting of a single GAM model.

By splitting these two distinct datasets a better model could be found.

A more detailed review of the model fitting process can be found in Davis et al. (2014c), which is introduced in the following section.

7.3 Introduction to Appendix C - Paper III

Paper III "An investigation of the impact of turbine icing on wind farm production" (Appendix C) describes in detail the development of the power loss model, and shows an evaluation at six different wind parks for the winter of 2012. The aim of the study was to build a statistical model that improved the RMSE and MB of power production estimates at wind farms that had known icing conditions using the results from the iceBlade model. This paper also introduced the standard deviation technique for fitting a threshold curve for ice identification, which was evaluated in Paper I (Appendix A). Additionally the wind erosion term was added to the iceBlade model, as the ice ablation with only shedding and sublimation was found to be insufficient at some of the sites.

The final production loss model was found to reduce the bias at all six wind parks in the study and reduced the RMSE at five of the six compared to the empirical wind park power curve (without icing influence). Two different sets of training were used for evaluating the power loss model. The first used data from the wind park that was being studied, while the second used data from all 6 wind parks to fit a general model. The general model was found to perform better than the park specific model for the evaluation dataset. This was possibly due to over-fitting of the individual park power curves. However, the capability of the general power curve suggests that a general method may be able to provide estimates of production loss at wind parks where production data is not yet available, which could be useful for site assessment studies.

7.4 Introduction to Appendix D- Report I

The final Appendix (D) includes a draft chapter "Comparison of Wind Turbine Icing Production Loss Models" from the Icewind project report. During the Icewind project four different institutions built power production models that included icing impacts using vastly different approaches. It was decided that an inter-comparison would be useful for determining if any of the approaches stood out from the rest, to help reduce the duplication of effort. This would also identify the next stages of research into the impacts of icing on wind park production.

It was agreed that the results would be released anonymously. Along with the DTU model, the three other models used in the inter-comparison were discussed in Section 7.1. The Kjeller Vindteknikk model (Byrkjedal, 2012b) fit a three-dimensional power curve using wind speed and ice mass from a standard cylinder model to estimate the power with icing influence. The VTT production loss module (Karlsson et al., 2014) fits a three-dimensional power curve using the duration of an icing event, which was determined using results from the iceBlade model for the intercomparison. Finally, the WeatherTech WICE model (Baltscheffsky, 2013) uses a physical module for modeling ice accretion and ablation on a simplified turbine blade, as well as a statistical model that relates the modeled ice, and NWP model output to power production.

The inter-comparison showed that the models performed similarly, despite the differences in model design. It was also shown that there was a large discrepancy in model performance depending on the amount of icing that was identified at the site. This suggests that the models still need more development to be applied at sites without production data. Given the wide range of techniques used for the statistical modeling, it seems that the best way to improve the production loss estimates is to focus on the physical modeling, as this will provide better inputs to the statistical models.

Chapter 8

Summary and Conclusions

This thesis investigates many topics in the general area of wind turbine blade icing, and its subsequent impact on power production. While the subject of wind turbine blade icing has been researched for at least 20 years, predicting ice accumulation on the turbine blades and relating that to power loss is still a challenge. However, it is important to be able to perform these estimates, since more accurate estimates of wind turbine production during icing events can significantly reduce the cost of energy for wind parks located in cold climates regions. Additionally, when siting turbines in cold climate regions, additional information about the impact of icing can provide additional information to the developer about the expected returns.

One of the challenges in studying icing on wind turbines is the lack of observational data. This is due to both the remote installation of turbines that experience frequent icing, and the lack of sensors that can detect ice growth directly on the turbine blades. It has been shown that icing can be detected using power threshold curves, the observed power, the nacelle temperature, and the duration of reduced power output (Appendix A). It was shown that the flat percentage approach to fitting the power threshold curve did not match the variance in power at different wind speeds (Appendix A). Two approaches were found that better capture the power variance, but both rely on a large number of non-iced data-points where the turbine is operating under normal conditions, for fitting curves to the power variance. The approach using the 0.1 quantile of observed power for normal ice-free data created a curve that followed the variance of power at different wind speeds, and was found to be robust across a number of wind parks. By adding a duration limit to the detection of icing using the power curve methods, the number of false positives and the sensitivity to the quantile choice were reduced. One limitation of the power curve method for ice detection is the shutdown of turbines. This can occur for operational reasons, or for the protection of the turbine components due to measured imbalances of ice. For many wind parks, the turbines cannot be restarted until a technician is able to inspect the turbine. Therefore, the restart of the turbine may not be related to when the ice was removed. Of the methods in tested in this study, it is recommended that the quantile method of identifying the power threshold, with a minimum duration of 2 hours be used for future, retrospective studies of turbine icing.

Another key measurement for identifying icing on wind turbine blades is the nacelle temperature at each turbine. This is used as a proxy for the blade temperature, which is not measured, to ensure that conditions are cold enough for ice to form on the turbine blades. Many ice detection methods have relied on a hard threshold of 0°C. However, it was shown in this study that the nacelle temperatures could differ by as much as 2.5°C from nearby mast measurements (Sec. 3.4). Given this potential error in the nacelle temperatures, the threshold should be relaxed to a value closer to 3°C, which in my experience produced good results. By using a fairly long ice duration requirement, the relaxation of the temperature threshold should not have a significant impact as shown in the paper on ice detection (Appendix A).

Once ice has been identified, and the impact of icing on power production highlighted, it is important to be able to simulate those impacts. This thesis uses a three step process for quantifying the impact of icing on wind turbine power production (Chap. 4). First a numerical weather prediction (NWP) model is used to estimate the meteorological conditions around the wind park, then those results are used as input to a physical icing model that estimates the periods and amount of icing on the wind turbine blades, finally selected results from both the NWP model and the icing model are used as inputs to a statistical production loss model that is used to adjust a preexisting power forecast for the impact of icing.

The use of NWP model results for icing research has seen rapid growth in recent years. NWP models are required for forecasting cloud hydrometeors, which are key input parameters for icing forecasts that include in-cloud icing. NWP models are also important for providing data at locations where the necessary observations do not exist. Previous studies (e.g., Drage and Hauge, 2008; Oechslin, 2011; Kringlebotn Nygaard et al., 2011) had relied on complex microphysical schemes, such as the Thompson microphysics scheme (Thompson et al., 2008), when using NWP results as input to an icing model. These schemes contain additional processes for simulating the cloud hydrometeors allowing for a more realistic representation, but adding to the computational cost. Because of the added computation, many previous wind energy related NWP simulations were created using simpler schemes such as the WSM5 scheme (Hong et al., 2004). In this study, nine NWP sensitivity studies were run using the WRF NWP model (Skamarock et al., 2008). These studies compared different microphysical schemes and PBL schemes and evaluated their impact on hydrometeors and ice prediction (Chap. 5). The microphysical scheme was found to have a large impact on the amount and types of hydrometeors that were produced, and therefore on the resulting modeled ice mass. The SBU-YLin microphysical scheme (Lin and Colle, 2011) was found to produce smaller amounts of total cloud mass (q_t) for most sites than either the WSM5 or the Thompson scheme. The Thompson scheme showed an interesting peak in the cloud water hydrometeor (q_c) for temperatures below -10°C. This does not seem to be a realistic feature, and deserves more investigation as it likely leads to large overestimations of ice mass when used as input to a physical icing model. The WSM5 scheme was shown to produce a large amount of cloud ice (q_i), which was not seen in the model results using the other two microphysics schemes. The q_i appeared to come at the expense of the q_c when compared with the Thompson scheme (Fig. 5.2). Of the schemes studied, the Thompson scheme is still the recommended scheme, but the WSM5 scheme can provide a reasonable set of inputs for ice models. However, when using WSM5, the q_i and q_c terms should be added together due to the more rapid conversion of liquid hydrometeors to frozen hydrometeors in the WSM5 scheme.

In addition to comparing the microphysical schemes, the impact of three different PBL schemes on cloud hydrometeors and ice growth was also studied. The hydrometeors were not as sensitive to differences in PBL scheme as they were to the different microphysical schemes. However, the use of the MYNN2 scheme consistently produced larger values of q_t for all three microphysical schemes. The largest impact on the iceBlade results due to the different PBL schemes was due to the temperature differences between the three PBL schemes. The modeled temperatures were significantly higher, when using the YSU PBL scheme compared to the two other PBL schemes studied. The increased temperature reduced the estimated ice mass compared to the simulations using the other PBL schemes, due to both decreased ice growth and the earlier shedding of the ice. WRF models results from simulations using the MYJ PBL scheme, which was used in the temperature evaluation shown in Section 3.4 and for the development of the icing production loss model (Appendix C), demonstrated a large cold bias when compared with the nacelle temperature. Therefore, it is recommended to use the YSU scheme for icing studies. This is in agreement with Floors et al. (2013) that found the YSU scheme provided a reasonable representation of wind speed throughout the vertical, which is important for performing the power forecast without icing.

The physical icing model developed in this study, iceBlade, was designed to be more applicable for modeling icing on wind turbine blades than other commonly used models (Sec. 6.2). The iceBlade model advanced the state of the art for ice models used in conjunction with NWP models by simulating ice accretion under conditions that more closely represent those experienced by the outer quarter of the turbine blade, and by adding documented ice ablation algorithms for simulating ice loss over time. The most significant update for representing ice on the turbine blade was the inclusion of a blade relative velocity. The blade relative velocity relies on an RPM curve to relate the ambient wind speed to the rotational speed of the turbine blade (Fig. 4.2; left). This leads to an increased wind speed and an increased liquid water mass flux onto the blade. The iceBlade model results were evaluated initially at one wind park for one month of data (Appendix B). It was found that the iceBlade model better estimated periods of icing detected by the power curve method across a range of metrics compared to both a version of iceBlade without the enhanced wind speed and a one day persistence model. The iceBlade model was also compared with the non-turbine version for a two year period at a wind park used for the development of

the power loss model. In that study, it was found that the iceBlade model again outperformed the standard model, although by a less significant amount than in the one-month study (Appendix C). This was likely due to the ice not being removed rapidly enough. Based on these results, it is recommended that the blade rotation enhancement be utilized in all future studies of wind turbine icing.

The largest uncertainty in the physical icing model is from the ice ablation algorithms. This is in part due to the limited amount of research in this area. While ice accretion has a large impact on other industries (e.g. power lines, bridges, and aviation), those industries are mostly interested in the peak ice load, which does not rely on ice ablation. In iceBlade, algorithms for sublimation, shedding, and wind erosion were included. The sublimation algorithm is the most certain as it is based on the work of Srivastava and Coen (1992) for simulating sublimation of cloud ice for use in microphysics schemes. However, the shedding and wind erosion models are simplified and could use more development. The uncertainty in the ablation algorithms is not specific to iceBlade, McDonough (2014) presented an ice model intercomparison study with four different icing models coupled to different meteorological models. In that study, it was found that the different models captured the onset of production loss well, however, there were significant differences in the ending time of the event. There was also little agreement in the model performance from event to event. Based on these results it is important to study the ablation methods in more detail and further advance their implementation in the physical icing models.

Finally, a model was developed for power production with icing impacts (PPM_i) for wind parks. The DTU PPM_i used inputs from both the NWP model and iceBlade to adjust the power production. The final model was a hierarchical model, combining a decision tree model with a generalized additive model (GAM). The decision tree model split the data into ice / no-ice forecasts, with different GAM models being fit for both conditions. Since the DTU PPM_i was designed to estimate the power difference form an power production model, the power production was estimated for a given wind speed using an empirical park power curve that was fit using a GAM. The DTU PPM_i was evaluated at six sites in Scandinavia, with known icing problems (Appendix C). In this study, it was found that the model reduced the mean bias at all six sites, and reduced the RMSE at five of the sites compared with the power production estimate from the empirical power curve. The non-iced times were not improved and actually saw a slight decrease in the error metrics. However, the improvements in the data-points with observed icing were large enough that the estimates were improved overall.

To determine the current state of the art in PPM_i models, the DTU PPM_i model was compared with three other PPM_i models as part of the Icewind project (Appendix D). The intercomparison used the same six sites used to develop the DTU PPM_i, as well as an additional eight sites in North America. The DTU PPM_i was shown to perform well at approximately half of the sites, those that had significant icing impacts. However, at the sites that did not show large impacts from icing, the model did considerably worse. This result was found for three of the four models in the study. Of particular interest was the similarity in results for three of the four models. This was despite having vastly different statistical approaches for fitting the PPM_i models. This result suggests that the statistical approach, for estimating power from the physical model inputs, is currently not as important as the physical models themselves, given the current state of the physical models. Therefore, more emphasis should be placed on development of the physical models.

Overall, this study has provided several advancements for estimating icing on wind turbines using NWP model results. Key among them are: the importance of using the correct hydrometeors depending on the microphysical scheme being used in the NWP model; the importance of using the blade relative wind speed to capture an accurate representation of the incoming cloud mass; the uncertainty of the ablation algorithms in the development of physical icing models; and the advantages of using a hierarchical model approach for building power production models that include the impacts of icing.

Chapter 9

Future Research

Even with the advances made during this project there are still many areas for advancement of the ice modeling on wind energy and the understanding of its impact on wind turbine power production. The entire forecasting system presented in Chapter 4 needs to be set-up and tested. This involves running an NWP model in forecast mode, and implementing a wind power production model to provide inputs to the icing power loss model. Ideally this would be set-up and run for several wind farms in different environments and with different turbines, to better understand the sensitivity of the model system to these factors. Advancements can also be made for each of the models investigated and developed in this thesis.

The investigation into the impact of microphysical parameterizations on estimated hydrometeors revealed interesting differences between the different schemes, and raised several questions about the models representation of clouds in the lower boundary layer during winter. Observations of cloud LWC, MVD, and liquid fraction would aid in the validation, selection, and improvement of the microphysical parameterizations. It would be particularly helpful to measure these parameters at different heights. By having more detailed observations, Large Eddy Simulation (LES) models could be used to aid in the downscaling of the cloud parameters from the NWP model to higher resolution providing the microscale model link shown in Figure 4.1.

The physical icing model can be improved through advancements in both the accretion and ablation modeling. The accretion model should have wet-snow icing added, however, this will require an analysis of the particle trajectories of wet-snow. The particle trajectories of cloud droplets around an airfoil should also be investigated. To this end, the development of a 3D CFD icing model specifically for modeling ice growth on wind turbines would be very helpful. By employing this model over a range of different conditions, it would provide useful results for fitting empirical functions for airfoil based collision efficiencies instead of the current cylinder based values. Additionally by including the centripetal and gravitational forces that act on the surface of the turbine blade, more realistic shapes of glaze icing should be possible, enabling a more detailed investigation of the impact of glaze icing on lift and drag.

The ablation algorithms of the iceBlade model need to be verified independently. This would require a climatic wind tunnel that could control temperature and humidity after the ice accumulation took place. There is currently one such facility at Penn State University. Of particular interest would be validation of the sublimation algorithm, and improvements to the wind erosion model. The impact of wind erosion and compacting of the ice on the surface roughness is also important.

The physical icing model could also be improved through improved measurements of icing on turbine blades themselves. There have been several recent projects looking at different technologies to do just that (Moser et al., 2014; Gagnon, 2014; Kocevar et al., 2014). These techniques are currently in the early stage of development, but the data that they could provide would be invaluable for the ice modeling community.

Finally there are several improvements that could be made to the statistical modeling approach to the estimation of power loss. First the effect of the power curve on potential power loss should be added. Additionally it would be worth exploring adding an additional tier to the hierarchical model based on active icing, since periods of ice growth appear to have a different impact on power than instrumental icing. Additionally the model should be fit using additional metrics to the mean bias and RMSE as these terms were shown to provide incorrect performance estimates for some of the sites studied (Appendix C).

Bibliography

12494:2001(E), 2001: *Atmospheric icing of structures*. ISO, Geneva, Switzerland.

Baltscheffsky, M., 2013: Modelling of production losses due to icing for individual turbines in a wind farm - development of techniques for forecasting and site assessment. *Winterwind*, Östersund, Sweden.

Barber, S., Y. Wang, S. Jafari, N. Chokani, and R. S. Abhari, 2011: The Impact of Ice Formation on Wind Turbine Performance and Aerodynamics. *Journal of Solar Energy Engineering*, **133 (1)**, 011 007, doi:10.1115/1.4003187, URL http://link.aip.org/link/JSEEDO/v133/i1/p011007/s1&Agg=doi.

Baring-Gould, I., et al., 2012: EXPERT GROUP STUDY ON RECOMMENDED PRACTICES: 13. WIND ENERGY PROJECTS IN COLD CLIMATES. Tech. rep., IEA Wind Energy Task 19, 1–43 pp. URL http://arcticwind.vtt.fi/reports/RP13_Wind_Energy_Projects_in_Cold_Climates_Ed2011.pdf.

Bernstein, B. C., J. Hirvonen, E. Gregow, and I. Wittmeyer, 2012: Experiences from Real-Time LAPS-LOWICE Runs Over Sweden: 2011-2012 Icing Season. *Winterwind*, Skellefteå, Sweden, URL http://www.slideshare.net/WinterwindConference/3a-bernstein-lapslowice.

Bernstein, B. C., F. McDonough, M. K. Politovich, B. G. Brown, T. P. Ratvasky, D. R. Miller, C. a. Wolff, and G. Cunning, 2005: Current Icing Potential: Algorithm Description and Comparison with Aircraft Observations. *Journal of Applied Meteorology*, **44 (7)**, 969–986, doi:10.1175/JAM2246.1, URL http://journals.ametsoc.org/doi/abs/10.1175/JAM2246.1.

Bragg, M., A. Broeren, and L. Blumenthal, 2005: Iced-airfoil aerodynamics. *Progress in Aerospace Sciences*, **41 (5)**, 323–362, doi:10.1016/j.paerosci.2005.07.001, URL http://linkinghub.elsevier.com/retrieve/pii/S0376042105000801.

Brakel, T., J. Charpin, and T. Myers, 2007: One-dimensional ice growth due to incoming supercooled droplets impacting on a thin conducting substrate. *International Journal of Heat and Mass Transfer*, **50 (9-10)**, 1694–1705, doi:10.1016/j.ijheatmasstransfer.2006.10.014, URL http://linkinghub.elsevier.com/retrieve/pii/S0017931006005813.

Breiman, L., 1984: *Classification and Regression Trees*. CRC Press.

Byrkjedal, Ø., 2012a: Icing map for Sweden. Tech. rep., Kjeller Vindteknikk, 69 pp. URL http://www.vindteknikk.com/_extension/media/83/orig/KVT_OB%_2012_R076_Icingmap_Sweden.pdf.

Byrkjedal, Ø., 2012b: Mapping of icing in Sweden - On the influence from icing on wind energy production. *Winterwind*, Skellefteå, Sweden, URL http://www.slideshare.net/WinterwindConference/3a-byrkjedal-icingkvt.

Cattin, R., S. Kunz, A. Heimo, R. Oechslin, and M. Russi, 2008: An Improved Approach for the Determination of In-Cloud Icing at Wind Turbine Sites. *European Wind Energy Conference*, Brussels, Belgium, URL https://www.researchgate.net/profile/Rene_Cattin/publication/228491355_An_improved_approach_for_the_determination_of_in-cloud_icing_at_wind_turbine_sites/links/02e7e52a01fae51367000000?origin=publication_detail.

Chen, F. and J. Dudhia, 2001: Coupling an Advanced Land Surface-Hydrology Model with the Penn State-NCAR MM5 Modeling System. Part II: Preliminary Model Validation. *Monthly Weather Review*, **129 (4)**, 587–604, doi:10.1175/1520-0493(2001)129<0587:CAALSH>2.0.CO;2, URL http://journals.ametsoc.org/doi/abs/10.1175/1520-0493%282001%29129%3C0587%3ACAALSH%3E2.0.CO%3B2.

Cheng, W. Y. Y. and W. J. Steenburgh, 2005: Evaluation of Surface Sensible Weather Forecasts by the WRF and the Eta Models over the Western United States. *Weather and Forecasting*, **20 (5)**, 812–821, doi:10.1175/WAF885.1, URL http://journals.ametsoc.org/doi/abs/10.1175/WAF885.1.

Cohen, J., 2003: *Applied multiple regression/correlation analysis for the behavioral sciences*.

Courtney, J. F., P. Lynch, and C. Sweeney, 2013: High resolution forecasting for wind energy applications using Bayesian model averaging. *Tellus A*, **65**, doi:10.3402/tellusa.v65i0.19669, URL http://www.tellusa.net/index.php/tellusa/article/view/19669.

Davis, N., A. N. Hahmann, N.-E. Clausen, and M. Žagar, 2014a: Forecast of Icing Events at a Wind Farm in Sweden. *Journal of Applied Meteorology and Climatology*, **53 (2)**, 262–281, doi:10.1175/JAMC-D-13-09.1, URL http://journals.ametsoc.org/doi/abs/10.1175/JAMC-D-13-09.1.

Davis, N., A. N. Hahmann, N.-E. Clausen, M. Žagar, and P. Pinson, 2013a: Forecasting Production Losses by Applying the Makkonen Icing Model to Wind Turbine Blades. *The 15th International Workshop on Atmospheric Icing of Structures*, St. John's, Newfoundland and Labrador, Canada.

Davis, N., et al., 2014b: IceWind Inter-comparison of Icing Production Loss Models. *Winterwind*, Sundsvall, Sweden.

Davis, N. N., A. N. Hahmann, N.-E. Clausen, M. Žagar, and P. Pinson, 2013b: Forecasting Production Losses at a Swedish Wind Farm. *Winterwind*, Östersund, Sweden.

Davis, N. N., P. Pinson, A. N. Hahmann, N.-E. Clausen, and M. Žagar, 2014c: An investigation of the impact of turbine icing on wind farm production. *Wind Energy*, **Submitted**.

Drage, M. A. and G. Hauge, 2008: Atmospheric icing in a coastal mountainous terrain. Measurements and numerical simulations, a case study. *Cold Regions Science and Technology*, **53 (2)**, 150–161, doi:10.1016/j.coldregions.2007.12.003, URL http://linkinghub.elsevier.com/retrieve/pii/S0165232X07002121.

Dudhia, J., 1989: Numerical Study of Convection Observed during the Winter Monsoon Experiment Using a Mesoscale Two-Dimensional Model. *Journal of the Atmospheric Sciences*, **46 (20)**, 3077–3107, doi:10.1175/1520-0469(1989)046<3077:NSOCOD>2.0.CO;2, URL http://journals.ametsoc.org/doi/abs/10.1175/1520-0469(1989)046<3077:NSOCOD>2.0.CO;2.

Ellrod, G. P. and A. A. Bailey, 2007: Assessment of Aircraft Icing Potential and Maximum Icing Altitude from Geostationary Meteorological Satellite Data. *Weather and Forecasting*, **22 (1)**, 160–174, doi:10.1175/WAF984.1, URL http://journals.ametsoc.org/doi/abs/10.1175/WAF984.1.

Farzaneh, M., (Ed.) , 2008: *Atmospheric Icing of Power Networks*. Springer Netherlands, Dordrecht, doi:10.1007/978-1-4020-8531-4, URL http://link.springer.com/10.1007/978-1-4020-8531-4.

Fikke, S., et al., 2006: COST 727 : Atmospheric Icing on Structures Measurements and data collection on icing : State of the Art. Tech. Rep. 75, MeteoSwiss, 110 pp.

Fikke, S. M., J. E. Kristjánsson, and B. E. K. Nygaard, 2008: Modern Meteorology and Atmospheric Icing. *Atmospheric Icing of Power Networks*, M. Farzaneh, Ed., Springer Science+Business Media B.V., M, xvi ed., chap. 1, 1–29, doi:10.1007/978-1-4020-8531-4_1.

Finstad, K. J., 1986: Numerical and Experimental Studies of Rime Ice Accretion on Cylinders and Airfoils. Doctor of philosophy, The University of Alberta, Edmonton, Alberta.

Finstad, K. J., E. P. Lozowski, and E. M. Gates, 1988: A Computational Investigation of Water Droplet Trajectories. *Journal of Atmospheric and Oceanic Technology*, **5 (1)**, 160–170, doi:10.1175/1520-0426(1988)005<0160:ACIOWD>2.0.CO;2, URL http://journals.ametsoc.org/doi/abs/10.1175/1520-0426%281988%29005%3C0160%3AACIOWD%3E2.0.CO%3B2.

Floors, R., C. L. Vincent, S. E. Gryning, A. Peña, and E. Batchvarova, 2013: The Wind Profile in the Coastal Boundary Layer: Wind Lidar Measurements and Numerical Modelling. *Boundary-Layer Meteorology*, **147 (3)**, 469–491, doi:10.1007/s10546-012-9791-9, URL http://link.springer.com/10.1007/s10546-012-9791-9.

Foley, A. M., P. Leahy, and E. McKeogh, 2010: Wind power forecasting & prediction methods. *9th International Conference on Environment and Electrical Engineering*, IEEE, Prague, Czech Republic, 61–64, doi:10.1109/EEEIC.2010.5490016, URL http://ieeexplore.ieee.org/lpdocs/epic03/wrapper.htm?arnumber=5490016.

Frohboese, P. and A. Anders, 2007: Effects of Icing on Wind Turbine Fatigue Loads. *Journal of Physics: Conference Series*, **75**, 012 061, doi:10.1088/1742-6596/75/1/012061, URL http://stacks.iop.org/1742-6596/75/i=1/a=012061?key=crossref.c33e0dea6ebaea524d77ebf1503122b9.

Gagnon, R., 2014: A Remote Ice Detection System Suitable for Detecting Icing on Wind Turbines. *Winterwind*, Sundsvall, Sweden, URL http://www.winterwind.se/?edmc=2780.

Gent, R. W., N. P. Dart, and J. T. Cansdale, 2000: Aircraft icing. *Philosophical Transactions of the Royal Society A: Mathematical, Physical and Engineering Sciences*, **358 (1776)**, 2873–2911, doi:10.1098/rsta.2000.0689, URL http://rsta.royalsocietypublishing.org/cgi/doi/10.1098/rsta.2000.0689.

Habashi, W. G., M. Aubé, G. Baruzzi, F. Morency, P. Tran, and J. C. Narramore, 2004: FENSAP-ICE : A FULLY-3D IN-FLIGHT ICING SIMULATION SYSTEM FOR AIRCRAFT , ROTORCRAFT AND UAVS. *24th International Congress of the Aeronautical Sciences*, Yokohama, Japan, 1–10, URL http://www.icas.org/ICAS_ARCHIVE/ICAS2004/PAPERS/608.PDF.

Hastie, T. and R. Tibshirani, 1990: *Generalized Additive Models*. 1st ed., Chapman & Hall / CRC.

Haupt, S. E., 2014: Winter Wind Energy Research at NCAR. *Winterwind*, Sundsvall, Sweden, URL http://www.winterwind.se/?edmc=2790.

Heikkilä, U., A. Sandvik, and A. Sorteberg, 2010: Dynamical downscaling of ERA-40 in complex terrain using the WRF regional climate model. *Climate Dynamics*, **37 (7-8)**, 1551–1564, doi:10.1007/s00382-010-0928-6, URL http://link.springer.com/10.1007/s00382-010-0928-6.

Homola, M. C., P. J. Nicklasson, and P. a. Sundsbø, 2006: Ice sensors for wind turbines. *Cold Regions Science and Technology*, **46 (2)**, 125–131, doi:10.1016/j.coldregions.2006.06.005, URL http://linkinghub.elsevier.com/retrieve/pii/S0165232X06000760.

Homola, M. C., M. S. Virk, P. J. Nicklasson, and P. A. Sundsbø, 2012: Performance losses due to ice accretion for a 5 MW wind turbine. *Wind Energy*, **15 (3)**, 379–389, doi:10.1002/we.477, URL http://doi.wiley.com/10.1002/we.477.

Homola, M. C., T. Wallenius, L. Makkonen, P. J. Nicklasson, and P. A. Sundsbø, 2010a: The relationship between chord length and rime icing on wind turbines. *Wind Energy*, **13 (7)**, 627–632, doi:10.1002/we.

383, URL http://onlinelibrary.wiley.com/doi/10.1002/we.383/fullhttp://doi.wiley.com/10.1002/we.383.

Homola, M. C., T. Wallenius, L. Makkonen, P. J. Nicklasson, and P. A. Sundsbø, 2010b: Turbine Size and Temperature Dependence of Icing on Wind Turbine Blades. *Wind Engineering*, **34 (6)**, 615–627, doi:10.1260/0309-524X.34.6.615, URL http://multi-science.metapress.com/openurl.asp?genre=article%&id=doi:10.1260/0309-524X.34.6.615.

Hong, S.-Y., J. Dudhia, and S.-H. Chen, 2004: A Revised Approach to Ice Microphysical Processes for the Bulk Parameterization of Clouds and Precipitation. *Monthly Weather Review*, **132 (1)**, 103–120, doi:10.1175/1520-0493(2004)132<0103:ARATIM>2.0.CO;2, URL http://journals.ametsoc.org/doi/abs/10.1175/1520-0493(2004)132<0103:ARATIM>2.0.CO;2.

Hong, S.-Y., Y. Noh, and J. Dudhia, 2006: A New Vertical Diffusion Package with an Explicit Treatment of Entrainment Processes. *Monthly Weather Review*, **134 (9)**, 2318–2341, doi:10.1175/MWR3199.1, URL http://journals.ametsoc.org/doi/abs/10.1175/MWR3199.1?prevSearch=&searchHistoryKey=.

Ilinca, A., 2011: Analysis and Mitigation of Icing Effects on Wind Turbines. *Wind Turbines*, I. Al-Bahadly, Ed., InTech, chap. 8, 177–214.

Janjić, Z. I., 1994: The Step-Mountain Eta Coordinate Model: Further Developments of the Convection, Viscous Sublayer, and Turbulence Closure Schemes. *Monthly Weather Review*, **122 (5)**, 927–945, doi:10.1175/1520-0493(1994)122<0927:TSMECM>2.0.CO;2, URL http://journals.ametsoc.org/doi/abs/10.1175/1520-0493(1994)122<0927:TSMECM>2.0.CO;2?prevSearch=&searchHistoryKey=.

Jasinski, W. J., S. C. Noe, M. S. Selig, and M. B. Bragg, 1998: Wind Turbine Performance Under Icing Conditions. *Journal of Solar Energy Engineering*, **120 (1)**, 60, doi:10.1115/1.2888048, URL http://link.aip.org/link/JSEEDO/v120/i1/p60/s1&Agg=doi.

Jones, K. F., 1998: A simple model for freezing rain ice loads. *Atmospheric Research*, **46 (1-2)**, 87–97, doi:10.1016/S0169-8095(97)00053-7, URL http://linkinghub.elsevier.com/retrieve/pii/S0169809597000537.

Jonkman, J., S. Butterfield, W. Musial, and G. Scott, 2009: Definition of a 5-MW Reference Wind Turbine for Offshore System Development. Tech. Rep. February, National Renewable Energy Laboratory, 75 pp., Golden, Colorado.

Jowitt, W. R., 2013: Modelling of the de-adhesion, shedding, and throw of ice from wind turbines. Msc, Technical University of Denmark.

Kain, J. S., 2004: The Kain-Fritsch Convective Parameterization: An Update. *Journal of Applied Meteorology*, **43 (1)**, 170–181, doi:10.1175/1520-0450(2004)043<0170:TKCPAU>2.0.CO;2, URL http://journals.ametsoc.org/doi/abs/10.1175/1520-0450%282004%29043%3C0170%3ATKCPAU%3E2.0.CO%3B2.

Karlsson, T., V. Turkia, T. Wallenius, and J. Miettinen, 2014: Production Loss estimation for wind power forecasting. *Winterwind*, Sundsvall, Sweden, URL http://www.winterwind.se/?edmc=2792.

Kocevar, D., C. Kappacher, A. Pumberger, J. Löffler, and G. Greiner, 2014: Next Generation in Ice Detection. *EWEA 2014*, European Wind Energy Association, Barcelona, Spain, URL http://proceedings.ewea.org/annual2014/conference/posters/PO%_043_EWEApresentation2014.pdf.

Kringlebotn Nygaard, B. E., H. Ágústsson, and K. Somfalvi-Tóth, 2013: Modeling Wet Snow Accretion on Power Lines: Improvements to Previous Methods Using 50 Years of Observations. *Journal of Applied Meteorology*

and Climatology, **52 (10)**, 2189–2203, doi:10.1175/JAMC-D-12-0332.1, URL http://journals.ametsoc.org/doi/abs/10.1175/JAMC-D-12-0332.1.

Kringlebotn Nygaard, B. E., J. E. Kristjánsson, and L. Makkonen, 2011: Prediction of In-Cloud Icing Conditions at Ground Level Using the WRF Model. *Journal of Applied Meteorology and Climatology*, **50 (12)**, 2445–2459, doi:10.1175/JAMC-D-11-054.1, URL http://journals.ametsoc.org/doi/abs/10.1175/JAMC-D-11-054.1.

Langmuir, I. and K. Blodgett, 1946: A Mathematical Investigation of Water Droplet Trajectories. *Collected Works of Irving Langmuir, Vol. 10*, 348–393.

Lin, Y. and B. a. Colle, 2011: A New Bulk Microphysical Scheme That Includes Riming Intensity and Temperature-Dependent Ice Characteristics. *Monthly Weather Review*, **139 (3)**, 1013–1035, doi:10.1175/2010MWR3293.1, URL http://journals.ametsoc.org/doi/abs/10.1175/2010MWR3293.1.

Lindahl, S., 2014: Quantification of energy losses cause by blade icing using SCADA data. *Winterwind*, Sundsvall, Sweden, February 2012, URL http://www.winterwind.se/?edmc=2862.

Ljungberg, K. and S. Niemelä, 2011: Production of Finnish Icing Atlas. *COST Action ES1002 Workshop*, COST, Sofia Antipolis, France, URL http://www.wire1002.ch/fileadmin/user_upload/Major_events/WS_Nice_2011/Spec._posters/ES1002_extended_abstract_Ljungberg.pdf.

Macklin, W. C., 1962: The density and structure of ice formed by accretion. *Quarterly Journal of the Royal Meteorological Society*, **88 (375)**, 30–50, doi:10.1002/qj.49708837504, URL http://doi.wiley.com/10.1002/qj.49708837504.

Makkonen, L., 2000: Models for the growth of rime, glaze, icicles and wet snow on structures. *Philosophical Transactions of the Royal Society A: Mathematical, Physical and Engineering Sciences*, **358 (1776)**, 2913–2939, doi:10.1098/rsta.2000.0690, URL http://rsta.royalsocietypublishing.org/content/358/1776/2913.shorthttp://rsta.royalsocietypublishing.org/cgi/doi/10.1098/rsta.2000.0690.

Makkonen, L., T. Laakso, M. Marjaniemi, and K. J. Finstad, 2001: Modelling and prevention of ice accretion on wind turbines. *Wind Engineering*, **25 (1)**, 3–21, doi:10.1260/0309524011495791, URL http://multi-science.metapress.com/openurl.asp?genre=article%&id=doi:10.1260/0309524011495791.

Makkonen, L. and J. R. Stallabrass, 1987: Experiments on the Cloud Droplet Collision Efficiency of Cylinders. *Journal of Climate and Applied Meteorology*, **26 (10)**, 1406–1411, doi:10.1175/1520-0450(1987)026<1406:EOTCDC>2.0.CO;2, URL http://journals.ametsoc.org/doi/abs/10.1175/1520-0450%281987%29026%3C1406%3AEOTCDC%3E2.0.CO%3B2.

McDonough, 2014: Ice Intercomparison. *Winterwind*, Sundsvall, Sweden.

Mlawer, E. J., S. J. Taubman, P. D. Brown, M. J. Iacono, and S. a. Clough, 1997: Radiative transfer for inhomogeneous atmospheres: RRTM, a validated correlated-k model for the longwave. *Journal of Geophysical Research*, **102 (D14)**, 16 663, doi:10.1029/97JD00237, URL http://doi.wiley.com/10.1029/97JD00237.

Morgan, C. and E. Bossanyi, 1996: Wind Turbine Icing and Public Saftey - A Quantifiable Risk? *BOREAS III*, B. Tammelin, K. Säntti, E. Peltola, and R. Andersén, Eds., Finnish Meteorological Institute, Saariselkä, Finland, 312–326.

Moser, M., T. Schlegl, and H. Zangl, 2014: Retrofittable, autonomous and wireless icing and temperature monitoring on rotor blades for efficient anti- and de-icing. *Winterwind*, Sundsvall, Sweden, URL http://www.winterwind.se/?edmc=2843.

Nakanishi, M. and H. Niino, 2006: An Improved Mellor-Yamada Level-3 Model: Its Numerical Stability and Application to a Regional Prediction of Advection Fog. *Boundary-Layer Meteorology*, **119 (2)**, 397–407, doi:10.1007/s10546-005-9030-8, URL http://www.springerlink.com/content/j04441r721280776/.

National Centers for Environmental Prediction/National Weather Service/NOAA/U.S. Department of Commerce, 2012: NCEP FNL Operational Model Global Tropospheric Analyses, continuing from July 1999. Research Data Archive at the National Center for Atmospheric Research, Computational and Information Systems Laboratory, doi:http://dx.doi.org/10.5065/D6M043C6.

Oechslin, R., 2011: Wind Power Forecasting Considering Icing. Msc., University of Innsbruck, Austria, 47 pp., URL http://imgi.uibk.ac.at/sekretariat/master_theses/Oechslin_Roger_2011_Master.pdf.

Picard, R. R. and R. D. Cook, 1984: Cross-Validation of Regression Models. *Journal of the American Statistical Association*, **79 (387)**, 575, doi:10.2307/2288403, URL http://www.jstor.org/stable/2288403?origin=crossref.

Pruppacher, H. R. and J. D. Klett, 2004: *Microphysics of Clouds and Precipitation*. 2d ed., Kluwer Academic Publishers, New York, 975 pp.

R Core Team, 2014: *R: A Language and Environment for Statistical Computing*. Vienna, Austria, R Foundation for Statistical Computing, URL http://www.r-project.org.

Reynolds, R. W., T. M. Smith, C. Liu, D. B. Chelton, K. S. Casey, and M. G. Schlax, 2007: Daily High-Resolution-Blended Analyses for Sea Surface Temperature. *Journal of Climate*, **20 (22)**, 5473–5496, doi:10.1175/2007JCLI1824.1, URL http://journals.ametsoc.org/doi/abs/10.1175/2007JCLI1824.1.

Ronsten, G., et al., 2012: State-of-the-Art of Wind Energy in Cold Climates. Tech. rep., IEA Wind Task 19, 67 pp. URL http://arcticwind.vtt.fi/reports/Task19_SotA_WEinCC_2012_approved.pdf.

Schotanus, P., F. Nieuwstadt, and H. De Bruin, 1983: Temperature measurement with a sonic anemometer and its application to heat and moisture fluxes. *Boundary-Layer Meteorology*, **26 (1)**, 81–93, doi:10.1007/BF00164332, URL http://link.springer.com/10.1007/BF00164332.

Seifert, H. and F. Richert, 1997: AERODYNAMICS OF ICED AIRFOILS AND THEIR INFLUENCE ON LOADS AND POWER PRODUCTION. *European Wind Energy Conference*, Dublin Castle, Ireland, 458–463, October.

Seifert, H. and F. Richert, 1998: A recipe to estimate aerodynamics and loads on iced rotor blades. *BOREAS IV*, Hetta, Finland, 1–11, March 1998.

Sherif, S., N. Pasumarthi, and C. Bartlett, 1997: A semi-empirical model for heat transfer and ice accretion on aircraft wings in supercooled clouds. *Cold Regions Science and Technology*, **26 (3)**, 165–179, doi:10.1016/S0165-232X(97)00021-9, URL http://linkinghub.elsevier.com/retrieve/pii/S0165232X97000219.

Skamarock, W. C., et al., 2008: A Description of the Advanced Research WRF Version 3. National Center for Atmospheric Research, Boulder, CO, USA.

Skrimpas, G. A., C. W. Sweeney, K. S. Marhadi, B. B. Jensen, N. Mijatovic, and J. Holbøll, 2014: Detection of Wind Turbine Power Performance Abnormalities Using Eigenvalue Analysis. *ANNUAL CONFERENCE OF THE PROGNOSTICS AND HEALTH MANAGEMENT SOCIETY 2014*, Fort Worth, Texas, 1–7.

Söderberg, S., M. Baltscheffsky, and H. Bergström, 2013: ESTIMATION OF PRODUCTION LOSSES DUE TO ICING - A COMBINED FIELD EXPERIMENT AND NUMERICAL MODELLING EFFORT. *EWEA 2013*, European Wind Energy Association, Vienna, Austria.

Srivastava, R. C. and J. L. Coen, 1992: New Explicit Equations for the Accurate Calculation of the Growth and Evaporation of Hydrometeors by the Diffusion of Water Vapor. *Journal of the Atmospheric Sciences*, **49 (17)**, 1643–1651, doi:10.1175/1520-0469(1992)049<1643:NEEFTA>2.0.CO;2, URL `http://journals.ametsoc.org/doi/abs/10.1175/1520-0469%281992%29049%3C1643%3ANEEFTA%3E2.0.CO%3B2`.

Tammelin, B., 1994: Icing of Anemometer and its effect on Estimation of Wind Energy Potential. *BOREAS II*, B. Tammelin, K. Säntti, E. Peltola, and R. Andersén, Eds., Finnish Meteorological Institute, Pyhätunturi, Finland, 85–96.

Tammelin, B., M. Cavaliere, H. Holttinen, C. Morgan, H. Seifert, and K. Santti, 1998: WIND ENERGY PRODUCTION IN COLD CLIMATE (WECO). Tech. Rep. January 1996, Finnish Meteorological Institute, 1–38 pp., Helsinki, Finland.

Tammelin, B., H. Dobesch, M. Durstewich, H. Ganander, G. Kury, T. Laakso, and E. Peltola, 2005: Wind Turbines in Icing Environment : Improvement of Tools for Siting, Certification and Operation - NEW ICETOOLS. Tech. rep., Finnish Meteorological Institute, 127 pp., Helsinki, Finland.

Thompson, G. and T. Eidhammer, 2014: A study of aerosol impacts on clouds and precipitation development in a large winter cyclone. *Journal of the Atmospheric Sciences*, 140507124141006, doi:10.1175/JAS-D-13-0305.1, URL `http://journals.ametsoc.org/doi/abs/10.1175/JAS-D-13-0305.1`.

Thompson, G., P. R. Field, R. M. Rasmussen, and W. D. Hall, 2008: Explicit Forecasts of Winter Precipitation Using an Improved Bulk Microphysics Scheme. Part II: Implementation of a New Snow Parameterization. *Monthly Weather Review*, **136 (12)**, 5095–5115, doi:10.1175/2008MWR2387.1, URL `http://journals.ametsoc.org/doi/abs/10.1175/2008MWR2387.1`.

Turkia, V., S. Huttunen, and T. Wallenius, 2013: Method for estimating wind turbine production losses due to icing. Tech. rep., VTT Technology, 38 pp., Espoo, Finland. URL `http://www.vtt.fi/inf/pdf/technology/2013/T114.pdf`.

Virk, M. S., M. C. Homola, and P. J. Nicklasson, 2010: Effect of Rime Ice Accretion on Aerodynamic Characteristics of Wind Turbine Blade Profiles. *Wind Engineering*, **34 (2)**, 207–218, doi:10.1260/0309-524X.34.2.207, URL `http://linkinghub.elsevier.com/retrieve/pii/S0167610510000693http://multi-science.metapress.com/openurl.asp?genre=article&id=doi:10.1260/0309-524X.34.2.207`.

Wadham-Gagnon, M., et al., 2013: Ice Induced Vibration on Wind Turbines. *Proceedings of the 15th International Workshop on Atmospheric Icing of Structures (IWAIS XV)*, St. John's, Newfoundland and Labrador, Canada, 2–43–2–53.

Wallenius, T., et al., 2013: Special Chapter : Cold Climate Turbines ("CCTs"). *BTM World Market Update*, BTM-Consult, Ed., Navigant Research, Chicago, Illinois, USA, 2012th ed., chap. 7.

Wickman, H., 2014: Evaluation of field tests of different ice measurement methods for wind power. *Winterwind*, Sundsvall, Sweden, URL `http://www.winterwind.se/?edmc=2800`.

Wood, S. N., 2003: Thin plate regression splines. *Journal of the Royal Statistical Society: Series B (Statistical Methodology)*, **65 (1)**, 95–114, doi:10.1111/1467-9868.00374, URL http://onlinelibrary.wiley.com/doi/10.1111/1467-9868.00374/abstract.

Wood, S. N., 2006: *Generalized Additive Models: An Introduction with R*. Chapman and Hall/CRC.

Wood, S. N., 2011: Fast stable restricted maximum likelihood and marginal likelihood estimation of semi-parametric generalized linear models. *Journal of the Royal Statistical Society: Series B (Statistical Methodology)*, **73 (1)**, 3–36, doi:10.1111/j.1467-9868.2010.00749.x, URL http://doi.wiley.com/10.1111/j.1467-9868.2010.00749.x.

Wright, W., 2002: User Manual for the NASA Glenn Ice Accretion Code LEWICE Version 2.2.2. Tech. rep., National Aeronautics and Space Administration, Cleveland, Ohio. URL http://ntrs.nasa.gov/archive/nasa/casi.ntrs.nasa.gov/20020080990.pdf.

Yang, J., 2012: Simulation of icing events over Gaspé region. *Winterwind*, Skellefteå, Sweden, URL http://www.slideshare.net/WinterwindConference/3a-jing-yang.

Yang, J., K. F. Jones, W. Yu, and R. Morris, 2012: Simulation of in-cloud icing events on Mount Washington with the GEM-LAM. *Journal of Geophysical Research: Atmospheres*, **117 (D17)**, doi:10.1029/2012JD017520, URL http://doi.wiley.com/10.1029/2012JD017520.

Appendix A

Ice Detection on Wind Turbines using the Observed Power Curve

WIND ENERGY

Wind Energ. 0000; **00**:1–16

DOI: 10.1002/we

RESEARCH ARTICLE

Ice Detection on Wind Turbines Using the Observed Power Curve

Neil N. Davis[1], Øyvind Brykjedal[2], Andrea N. Hahmann[1], Niels-Erik Clausen[1], Mark Zagar[3]

<[1]DTU Wind Energy, Roskilde, DK [2]Kjeller Vindteknikk [3]Vestas, Aarhus, DK>

ABSTRACT

Icing on the wind turbine blade can lead to significant production losses during the winter months for wind parks in cold climate regions. However, there is no standard way of identifying ice induced power loss. This paper describes three methods for creating power threshold curves that can be used to separate iced production periods from non-iced production periods. The first approach relies on a percentage deviation from the manufacturer's power curve. The other two approaches fit threshold curves based on the observed variance of non-iced production data. These approaches are applied to turbines in 4 wind parks and compared to each other and observations of icing on the nacelle of one of the turbines in each park. It is found that setting an ice threshold curve using 0.1 quantile with a 2-hour minimum duration is the best approach for icing identification. Copyright © 0000 John Wiley & Sons, Ltd.

KEYWORDS

<icing; production; power curve; performance>

Correspondence

<Neil Davis, DTU Wind Energy, Roskilde, DK>. E-mail: <neda@dtu.dk>

Contract/grant sponsor

<TFI IceWind>

Contract/grant number

<1111>

Received . . .

Prepared using weauth.cls [Version: 2010/06/17 v1.00]

1. INTRODUCTION

A significant number of wind parks have been installed in cold climate locations [1]. One of the challenges of operating wind turbines in these conditions is the accumulation of ice on their blades. The accumulation of ice can lead to many problems for the turbines including; a health and safety risk from ice throw, increased fatigue on the turbine components from increased mass and potential imbalance, reduced power production due to changes in blade aerodynamics, and complete shutdown of a turbine. Due to these risks and their economic consequences, it is important to be able to determine when ice is impacting turbines, both in real time, and in retrospective analysis.

Homola et al. [2] provided an in depth review of available icing sensors for detecting icing conditions both before and after installation of a wind park. These can be summarized in three broad categories: 1) direct measurements; 2) indirect measurements from sensors at or near the wind farm; and 3) indirect measurements from the turbine. Direct measurement systems typically involve placing a sensor on a meteorological mast or on the nacelle of a wind turbine, to detect icing. These sensors measure changes in mass or signal properties, such as the damping of ultrasonic waves or a change in resonant frequency of a probe (see Tammelin et al. [3] for a comprehensive list of sensors). Different sensors are designed to measure different phases of an icing event. An icing event consists of two phases[4]. Meteorological icing occurs when atmospheric conditions exist that lead to ice accumulation. Instrumental icing occurs when ice exists on the structure. Sensors designed to capture meteorological icing include heating mechanisms that remove and measure ice when it is detected. This allows the sensor to determine the period of active accumulation. Instrumental icing sensors, retain the accumulated ice allowing it to be removed naturally, thereby capturing the full period of potential icing impacts.

Indirect ice detection from meteorological sensors use heated and non-heated sensors to determine if the non-heated sensor is iced. Cup anemometers and wind vanes are commonly used because at least one type, heated or non-heated, is typically installed at all wind parks. The indirect ice detectors identify periods of instrumental icing on the non-iced sensor. The indirect detection of ice on turbines is typically performed in one of two ways. Vibration data can be used to detect changes in the turbine's normal operation [5]. By investigating these periods, likely icing events can be identified. The second approach utilizes measured power and wind speed to detect deviations from the manufacturers power curve (P_m). The power curve deviation approach is identified by Homola et al. [2] as an approach that should always be used for installed turbines, but provides no insight into how these deviations should be estimated.

The focus of this paper is on indirect icing using the power curve deviation. Three different methods for creating power threshold (PT) curves are explored. The most common method creates a threshold power curve based on a flat percentage of P_m (PT_{PERC}). The percentage varies, Wadham-Gagnon et al. [6] used a threshold of 85%, although thresholds of 92.5 and 80% are also used. Davis et al. [7] developed an approach for creating a threshold power curve using the standard deviation of the power for wind speed bins of 0.1 $m\,s^{-1}$ (PT_{SD}). Finally, an approach using the 0.1 quantile of the power data for each wind speed bin was used by Karlsson et al [8] (PT_{QUANT}). The ice estimates from these three approaches are compared to each other, a nacelle mounted direct measurement sensor, and webcam detected nacelle icing at four wind parks with known icing events.

DOI: 10.1002/we
Prepared using weauth.cls

Table I. Time periods of data collection for each wind park in the study.

Wind Park	Starting Date	Ending Date
A	2012-11-01	2014-03-10
B	2013-03-01	2014-03-10
C	2012-11-01	2014-03-10
D	2013-03-12	2014-03-12

The rest of the paper is laid out as follows: Section 2 describes the dataset used in this study and highlights the data processing; Section 3 describes the methodology of the three different ice thresholds; Section 4 presents the PT curves and comparison with observed icing; and in Section 5 we discuss and make some concluding remarks.

2. DATA PROCESSING

Data from four wind parks in areas with known icing is used for this study with time periods shown in Table I . It should be noted that wind parks A and C have two winter seasons and only one summer season. For confidentiality reasons the parks are anonymized, identified with capital letters (A, B, C, and D), and the power has been normalized by the rated power of the turbine. Vestas turbines were installed at all four sites, one site has the V82 model, two sites the V90 model, and the final site the V100 model turbines. All four sites are located in Sweden and experience losses in the energy production due to blade icing. P_m was obtained for all four sites. Observations of nacelle wind speeds, temperature, and observed power were provided along with P_m and a quality assurance flag (QA) was created using the method described in Section 2.2. Additionally, atmospheric parameters (air density and air pressure) were derived from numerical weather prediction (NWP) model output. The modeled air pressure and nacelle temperature were used for the wind speed density correction described in Section 2.1. Finally, three observational measures of ice were obtained from the nacelle of one of the turbines in each wind park. An ice mass measurement was provided from an iceMonitor direct ice sensor [9]. The iceMonitor uses the ISO standard method for measuring atmospheric ice on structures [10], which involves measuring the ice load ($\mathrm{g\,m^{-1}}$) on a freely rotating cylinder with a diameter of 0.03 m and a length of 1.0 m. The two other ice observations were derived from webcam images of the meteorological instrumentation on the nacelle. Passive icing was defined as the period when ice was present on the instruments and sections of the nacelle, corresponding to periods of instrumental icing. Active icing was defined as periods when ice appeared to be actively accumulating on the instruments, corresponding to meteorological icing periods. As active icing only applies to periods when ice is increasing on the turbine, it was not included in the evaluation.

2.1. Wind speed density correction

When working with power measurements, the first step should always be to follow the IEC standard process of adjusting the wind speed for the atmospheric density [11]. In this process, the wind speed is adjusted based on the amount of energy it would contain at a standard atmospheric density of $\rho_0 = 1.225\ \mathrm{kg\,m^{-3}}$. The standard density is based on a standard

DOI: 10.1002/we
Prepared using weauth.cls

atmosphere with a base temperature of 15°C and a surface pressure of 1013.25 hPa. The density of air when the wind speed was measured is first calculated using the ideal gas law:

$$\rho = \frac{p}{R_0 T}, \tag{1}$$

where ρ is the air density, p is the air pressure, T is the air temperature, and $R_0 = 287.058\,\mathrm{J\,kg^{-1}\ K^{-1}}$ is the gas constant of dry air. As there was no pressure measurement at the wind park, the value from an NWP model output was used. The wind speed is then adjusted using the relationship:

$$v_{eq} = v\left(\frac{\rho}{\rho_0}\right)^{1/3}, \tag{2}$$

where v_{eq} is the equivalent wind speed at standard density and v is the nacelle wind speed. Throughout the rest of the paper, when wind speed is discussed, it is v_{eq}.

2.2. Data cleaning

Before any analysis, points that appear to be in error need to be identified and removed from the dataset. For turbine power measurements, this is particularly important since the operating state of the turbine can cause the output power to deviate from P_m for reasons other than icing. The identification of such points needs to be carried out before fitting PT_{SD} and PT_{QUANT}. Depending on the data, different approaches to data cleaning can be applied. For this study, data-points were removed when the turbine was identified to be in a derated state. A derated turbine is forced to a power limit other than rated power. Data-points were also removed based on the error codes from the turbines. A detailed list of error codes was not available, however, an error flag was provided for every 10-minute period. If the error flag indicated that the turbine was in error, the data-point was removed. The data-points before and after the error code were also removed, since the duration of the error was unknown and it could have occurred at any time during the 10-minute period. This will also account for any start delays that would occur if the turbine was stopped during the error event. Finally, a number of data-points had missing data and were also removed.

3. ICING THRESHOLD METHODOLOGY

The use of a PT curve is a reasonable approach to determine icing times for use in power loss estimation, allowing for both the retroactive and real time estimation of power loss. Three different approaches were used for creating PT, and three sensitivity values were tested for each approach, leading to the creation of nine different PT curves. The following sections will first describe each of the approaches, followed by a description of the method for detection of ice from the various PT curves.

DOI: 10.1002/we
Prepared using weauth.cls

3.1. Flat percentage

The flat percentage method, hereafter referred to as PERC, assumes that the threshold for icing can be defined as

$$p_{perc} = p_m \frac{a}{100}, \tag{3}$$

where p_{perc} is a value along PT_{PERC}, p_m is a value along P_m, and a is the percentage deviation. Common values for a range from 7.5% to 20%, values of 7.5%, 15%, and 20% were tested in this study. Neither historical turbine performance nor data cleaning are important for creating PT_{PERC}, since this approach relies only on Pm. However, since P_m is not specific to the individual turbine conditions, it cannot capture the impact of local effects, such as wakes or topography. Therefore, P_m may not fully represent the performance of each turbine, leading to the over- or under-estimation of ice solely due to local factors.

3.2. Standard deviation

The standard deviation approach, hereafter referred to as SD, aims to separate icing events from the normal variance of the power at different wind speeds. The power variance was estimated for clean, ice-free data, known hereafter as NO_ICE, of the power by using only data where the nacelle temperature was above 4°C by calculating the standard deviation for each 0.1 $\mathrm{m\,s^{-1}}$ bin of wind speed. Standard deviation was used since it is a well understood metric that provides a measure of variance in the same units as the data. However, standard deviation is not considered to be a robust statistic, which is defined as a method that performs well on non-normal distributions and on datasets that contain outliers. It is expected that turbine power would be non-normally distributed near and above rated wind speed, due to the rated power limit. This was not a significant issue for the data-sets in this study. However, outliers in the power data, which existed even after data cleaning, did lead to outliers in the standard deviation curve (σ_{raw}) above rated power (Fig. 1; left; gray curve).

To reduce the noise in σ_{raw}, a smoothing function was applied in the form of a generalized additive model (GAM) [12]. The GAM is a variant of a generalized linear model that can make use of smoothing functions for the input terms, allowing for a parametric model fit. This was useful for smoothing σ_{raw} as the relationship between standard deviation and wind speed was both unknown and likely to change from turbine to turbine. The GAM was fit using the *mgcv* package of R [13, 14], using a thin plate regression spline (TPRS) [15] of the wind speed. TPRS was chosen since it is a low rank smoother, meaning that there are far fewer coefficients than the number of data points due to the introduction of a penalty term. The degrees of freedom in the TPRS was limited to 5 to eliminate most of the noise in σ_{raw} (Fig. 1; left). Finally, the link function of the GAM was set to an inverse Gaussian distribution, restricting the smooth to positive values for the data in this study. Because of the small number of data-points at high wind speeds, where the standard deviation is expected to be 0, outliers above rated power could still have a large impact on the smoothed standard deviation curve σ_{GAM} . To account for this, values of 0 standard deviation were added to σ_{raw} between 25 and 30 $\mathrm{m\,s^{-1}}$ before smoothing. By removing the noise caused by the outliers, σ_{GAM} better captures the signal of the data, however, it should be noted that it does not reach 0 below the cut-in wind speed (Fig. 1; left).

DOI: 10.1002/we
Prepared using weauth.cls

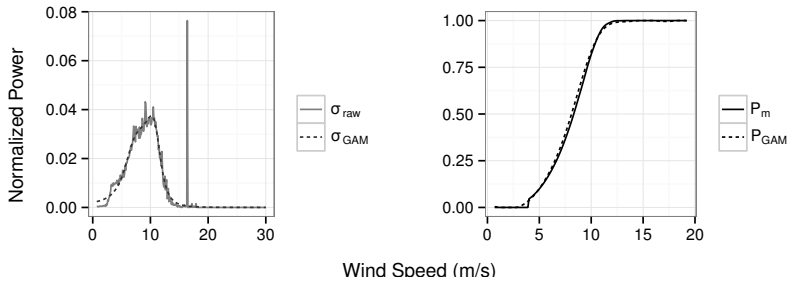

Figure 1. Curves used for fitting PT_{SD}. standard deviation vs wind speed (left) , for the non-smoothed (σ_{raw}) and smoothed (σ_{GAM}) standard deviation curves. Power vs wind speed, for P_m and P_{GAM}(right).

To create PT_{SD}, σ_{GAM} needed to be subtracted from a representative power curve. A GAM was fit to the NO_ICE dataset to provide an empirical power curve (P_{GAM}). P_{GAM} was fit using a TRPS of the wind speed, again using *mgcv*. P_{GAM} generally followed P_m for most turbines as the local effects were minimal and there were enough clean data points (Fig 1; right). However, for some turbines in this study, P_{GAM} did not accurately capture the rated power at high wind speeds because of outliers that were not removed in the cleaning process. After fitting the empirical power curve, the PT_{SD} curves were estimated using the equation

$$p_{SD} = p_{GAM} - b\,\sigma_{GAM}, \tag{4}$$

where p_{SD} is the power at a point on PT_{SD}, and p_{GAM} is a point on P_{GAM}, and b is a constant scaling parameter. We used values of b =1.5, 2.0, and 2.5 for the sensitivity tests.

3.3. Quantile

The third approach for generating a PT curve was described by Karlsson et al [8] at the 2013 Winterwind Conference. They used the 0.1 quantile of the non-iced observed power for each wind speed, hereafter identified as QUANT. The unlike standard deviation, quantiles are a robust metric, and can be used to capture the variance of a variable. In this study, the quantiles were applied to 0.1 m s^{-1} bins as in SD. After fitting the bins, it was found that the raw quantile curves (q_{raw}) were quite ragged, due to noise in the observations. Therefore, a smoothing method was again applied. q_{raw} did not have as extreme of outliers as σ_{raw}, so a LOESS smoother [16] was used. The LOESS smoother is a fully parametric smoother that is easier to setup than a GAM, but not as flexible. A span of 0.4 was used signifying that 40% of the total quantile curve would be used to fit the local regressions. Since the quantiles already represented power data, PT_{QUANT} is defined as the smoothed quantile curve. Sensitivity tests were created using quantile parameters of 0.05, 0.1 and 0.2.

Another challenge presented by QUANT concerned the fitting of wind speeds that were outside the range of the NO_ICE dataset. This was particularly problematic for smaller datasets (1 month of data). To solve this problem, all missing values were set to 2% of P_m, as these points were always at wind speeds where power should not vary significantly. The final limitation ensured that PT_{QUANT} was always less than 99% of rated power. This limitation was added because PT_{QUANT} would occasionally have values above rated power after smoothing, thereby classifying data-points at rated power as icing, which is incorrect. One nice feature of PT_{QUANT} is that it does not rely on either P_m or P_{GAM}.

DOI: 10.1002/we
Prepared using weauth.cls

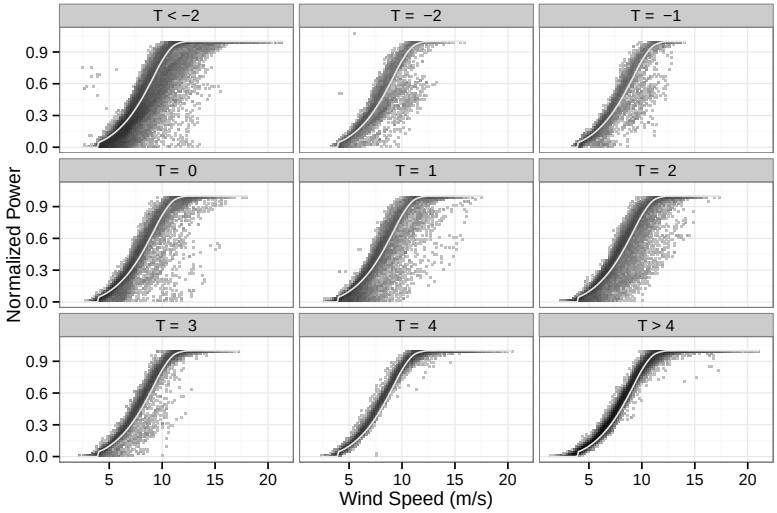

Figure 2. Power vs wind speed for different nacelle temperature bins for all turbines in Park C. The boxes represent areas of 0.2m s^{-1} by 0.02 normalized power, which are shaded based on the number of points that fall in the area (darker signifies more points). The gray line is P_m. Each sub-plot contains data for a given temperature bin (°C), with the upper left being all data-points colder than -2°C and the lower right being all data-points warmer than 4°C, all other plots contain data for individual nacelle temperature values.

3.4. Icing identification

Icing points were identified in an iterative process. First all non-QA points that had nacelle temperatures less than or equal to 3°C and an observed power below the PT curve were marked as icing. The temperature threshold was found through a visual examination of the cleaned turbine data (Fig. 2). An evaluation of nacelle temperatures against mast measurements at the Høvsøre test facility found a positive 2.5°C bias in the nacelle temperature at one of the two turbines studied [17], suggesting that a nacelle temperature bias of this magnitude is not uncommon.

After the initial ice identification, the QA points were examined. QA points that occurred immediately after an icing period were included as icing, assuming the ice led to the error. During this examination, the end of each ice period was also relaxed by removing the temperature criteria. Under these assumptions, iced turbines do not become ice free until the power production is above the PT curve. The QA data was included to allow the duration of each icing period (ICE_{DUR}) to be calculated. ICE_{DUR} can be used as an additional criteria for identifying icing. It prevents random points that fall across PT during cold periods from being identified as icing. Appropriate threshold values for ICE_{DUR} will be explored in Section 4.

4. RESULTS AND DISCUSSION

The different PT curves are first compared among themselves and NO_ICE. Then different values for ICE_{DUR} are compared and a value selected for the remaining comparison. Finally, the ice points identified by the PT curves are compared with the ice periods identified by the iceMonitor sensor and webcam data.

DOI: 10.1002/we
Prepared using weauth.cls

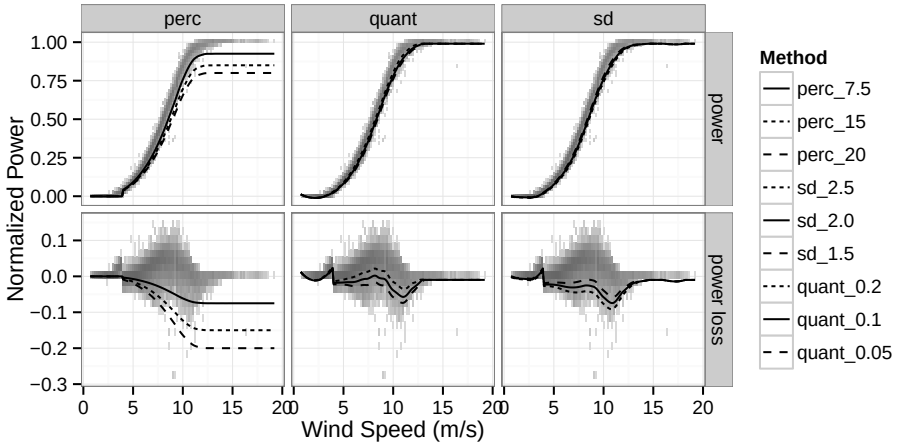

Figure 3. Wind speed versus power (top row) and wind speed versus power difference (bottom row) for NO_ICE data from a single turbine in park C. The shaded values are the same as in Figure 2, for observations with temperature greater than 4°C. The different columns are for the different methods of calculating the ice threshold, flat percentage (perc), quantile (quant) and standard deviation (sd). The different line types denote the different threshold values by method.

4.1. Threshold curves

The top row of Figure 3, shows the NO_ICE power curve and nine PT curves. The best method should follow the bottom of the NO_ICE power curve, while ignoring points that are clear outliers. As expected, PT_{QUANT} and PT_{SD} follow the bottom of the NO_ICE power curve better than PT_{PERC}, for all threshold values. The PT_{QUANT} and PT_{SD} sensitivity tests do not show much variation, unlike PT_{PERC} where there is a large difference above $10\,m\,s^{-1}$. Interestingly all three PT curves go flat around $12\,m\,s^{-1}$, the PT_{QUANT} and PT_{SD} curves simply have a smoother transition through the knee of the power curve, between 10 and 12 /ms.

The bottom row of Figure 3 shows the power difference from P_m, defined as the power loss. The observed power shows a clear trend of no power loss and small variance below cut-in, followed by a positive power difference increasing until approximately $8\,m\,s^{-1}$, where it decreases until it falls below zero between 10 and $13\,m\,s^{-1}$. Above $13\,m\,s^{-1}$ it returns to zero. The spread of the data is small below cut-in and above rated wind speed, but large on the slope of the power curve, reaching a peak around $8\,m\,s^{-1}$. The trend in the power difference mirrors the difference between P_{GAM} and P_m (Fig. 1; right). It also agrees with Ribeiro et al [18], who presented theoretical performance curves for wind turbines under different turbulence conditions. They showed that at high turbulence intensities production in the lower part of the power curve would be above P_m, but near the knee of the power curve production would be below P_m.

The PT_{QUANT} and PT_{SD} curves mostly follow the same pattern as the observed power loss, however the values are not as large where the observed data has positive power differences, and more extreme for observed negative power differences. Also, there is a jagged feature near the cut-in wind speed in PT_{QUANT} and PT_{SD}. The PT_{PERC} curves do not follow the observed power difference. Rather than increasing between 5 and $8\,m\,s^{-1}$, the PT_{PERC} power difference continues to drop, and the power difference never returns to 0 above the rated wind speed. The PT_{QUANT} curve with a 0.2 quantile threshold, goes above 0.0 power difference around $8\,m\,s^{-1}$, this signifies that the iced power threshold would be above P_m for those

DOI: 10.1002/we
Prepared using weauth.cls

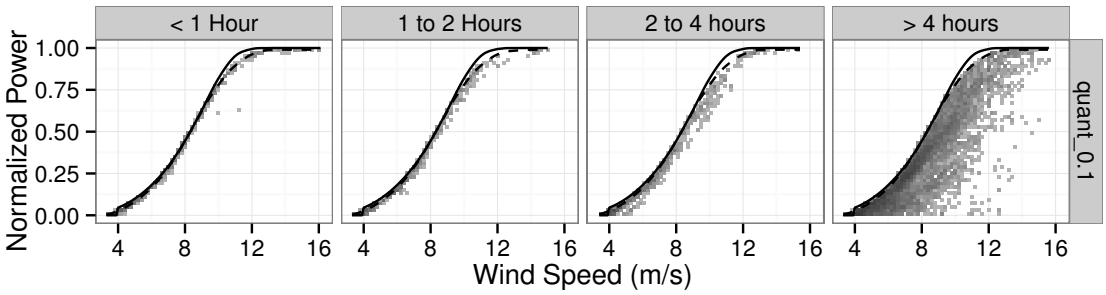

Figure 4. Wind speed versus power for points identified as icing for a turbine at site C. The different columns show the different ICE_{DUR}. The observed data is represented using the same binning method as in Figure 2. The solid line is P_m and the dashed line is P_{quant} with a threshold of 0.1.

wind speeds. This is due to the turbines over-performance at those wind speeds compared to P_m. From this analysis, it would be expected that QUANT and SD would perform better than PERC.

4.2. Ice duration criteria

Analyzing the NO_ICE power curves (Fig. 3; top row), it could be seen that the value of some of the NO_ICE data was below the the PT curves. Therefore, the PT curves should not be used as strict thresholds for identifying ice points, so an ICE_{DUR} threshold should be applied. Figure 4 shows the impact of ICE_{DUR} on the identified icing points. When ICE_{DUR} is less than 2 hours the majority of points are very close to PT_{QUANT}. However, for longer icing periods, the identified points spread out from PT_{QUANT}. Only PT_{QUANT} with a threshold of 0.1 is shown, but the pattern holds for all PT curves. Therefore, an ICE_{DUR}threshold of 2 hours seems be reasonable for ice identification. Setting a 2-hour ICE_{DUR} threshold would require 12 consecutive periods of power below the PT curve for icing to be identified, due to the 10-minute period of the data.

To evaluate the impact of the 2-hour ICE_{DUR} threshold, all points that had power values less than the PT value were examined for select sensitivity parameters. These points were separated into groups that were cold enough to be designated as icing, and those that were not (Fig. 5). The ICE_{DUR} values show the ratio of points still falling below the threshold, after applying the ICE_{DUR} restriction. For points cold enough to be iced, there is a small reduction in the number of identified points across all methods. However, for the points that had power below the PT curves but were too warm, there is a very large decrease in the number of detected events for the QUANT and SD methods. The PERC method retained a significant number of points in the warm-ICE_{DUR} category. These points occurred largely for wind speeds below 7.5 $m\,s^{-1}$, where PT_{PERC} was closer to P_m. The limited number of warm points identified by SD and QUANT suggests that 2 hours is a reasonable length for ICE_{DUR}. However, using such a long duration may miss shorter periods of icing. Since the icing values with ICE_{DUR} less than 2 hours were shown to be close to the PT curves, and therefore, close to P_m, this should have minimal impact on the estimated power loss due to icing. Even the bins of ice between 2 and 4 hours do not show exceptionally large deviations from the P_m when compared with the NO_ICE power curves (Fig. 3).

DOI: 10.1002/we
Prepared using weauth.cls

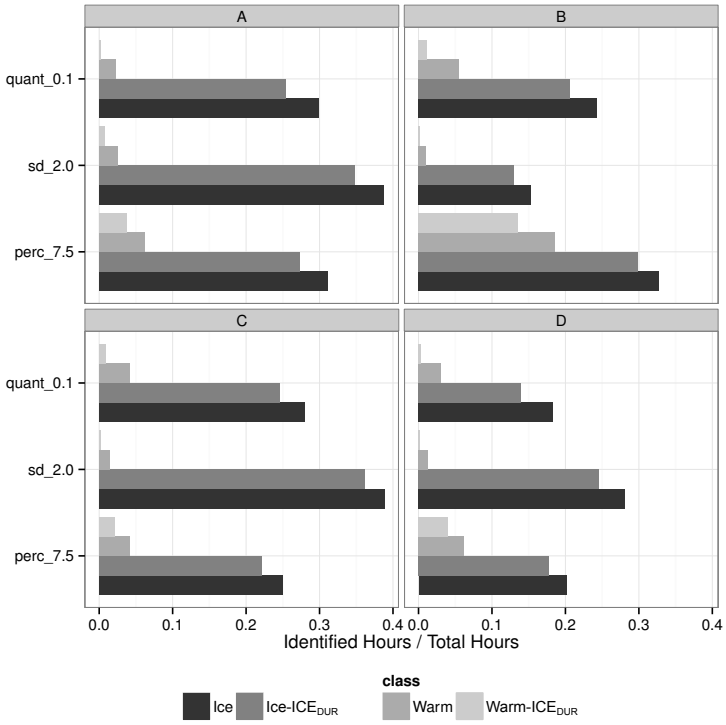

Figure 5. Ratio of identified hours in the categories: Ice, Ice-ICE$_{DUR}$, Warm, and Warm-ICE$_{DUR}$ to total hours for selected sensitivity values of each threshold method across the different wind parks (A-D). Colors indicate the subset of the data used, where Ice is the points identified as icing, and Warm is the points that would have been identified as icing, but were too warm. ICE$_{DUR}$ indicates that the 2-hour duration restriction was added for those points.

4.3. Comparison with observed icing

To evaluate the different ice detection algorithms, the ratio of the number of identified icing hours to the total number of standard operating hours was calculated for each turbine (RATIO). Figure 6 shows the distribution of RATIO for turbines in the different wind parks. Iced hours from the PT methods include the the 2-hour ICE$_{DUR}$ requirement. At sites A and C, the turbine derived values differ dramatically from the iceMonitor results. The iceMonitor estimates that over 60% of the operating hours at site A were iced, far more than any other method. However, at site C, the iceMonitor estimates only 10% of the operating hours at site C as iced, which is significantly less than the PT methods. This suggests a limitation of the iceMonitor for wind turbine applications. It can detect when there are large changes in the ice load, but due to offset issues and noise in the measurements, it is not possible to distinguish a small amount of ice from no ice. The sensor is thus not very well suited to detect periods of ice / no ice. The webcam based passive_ice detection, however, falls within the range of the power curve estimates at all sites except site C. This difference was found to be due to a number of missing observations in the passive_ice measurement during icing periods.

The difference in the icing hours between PERC, QUANT, and SD are larger than those between the sensitivities for each method. This suggests that all methods are fairly robust to the parameter selection. At three of the four sites (A, C, and D), the SD method estimates more hours of icing than the other two methods, however, at site B it estimates fewer

DOI: 10.1002/we
Prepared using weauth.cls

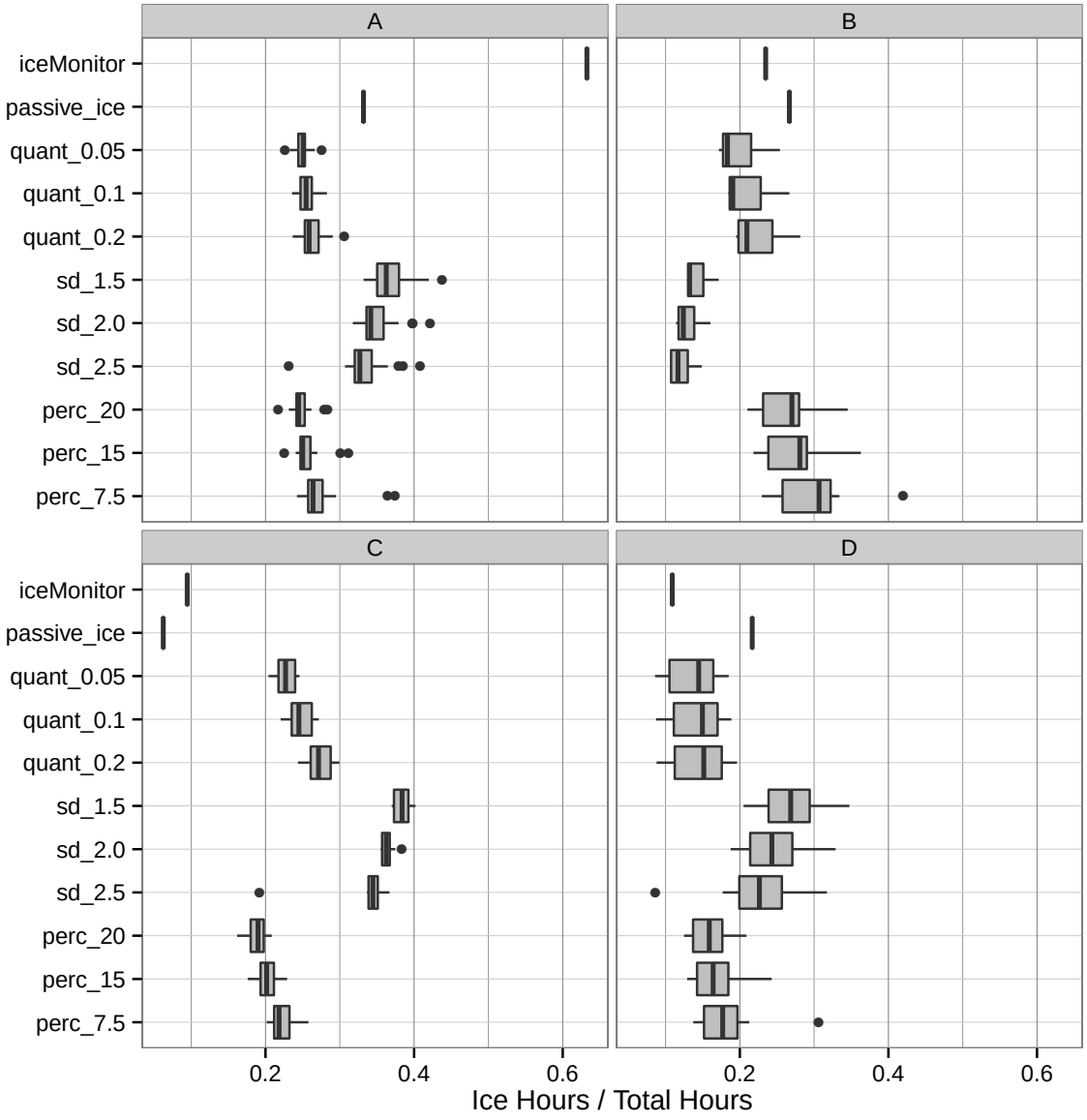

Figure 6. RATIO for each ice identification method across the different wind parks (A-D). Ice threshold methods combine the method and threshold value, iceMonitor denotes that sensor, and passive_ice denotes the webcam estimated icing identification. Boxplots are used to show the distribution of the threshold based methods for all of the turbines in the wind park. Individual points indicate data more than 1.5 times larger than the inter-quartile distance. Note that the observed methods were only at 1 turbine, so therefore do not have a distribution.

hours. There is considerable overlap between the PERC and QUANT results in terms of the number of hours of icing. The QUANT method shows significant variation in the number of icing hours at the different turbines for sites B and D, and has the most variance of the methods at site C. This is somewhat surprising due to the non-robust nature of the SD method, which we assumed would lead to larger differences in icing hours depending on the turbine.

It was noted that the large number of points with temperature greater than 4°C that fell below PT_{PERC} with a threshold of 7.5%, (Fig. 5), was likely due to the over-identification of points at low wind speeds. To better understand the impact

DOI: 10.1002/we
Prepared using weauth.cls

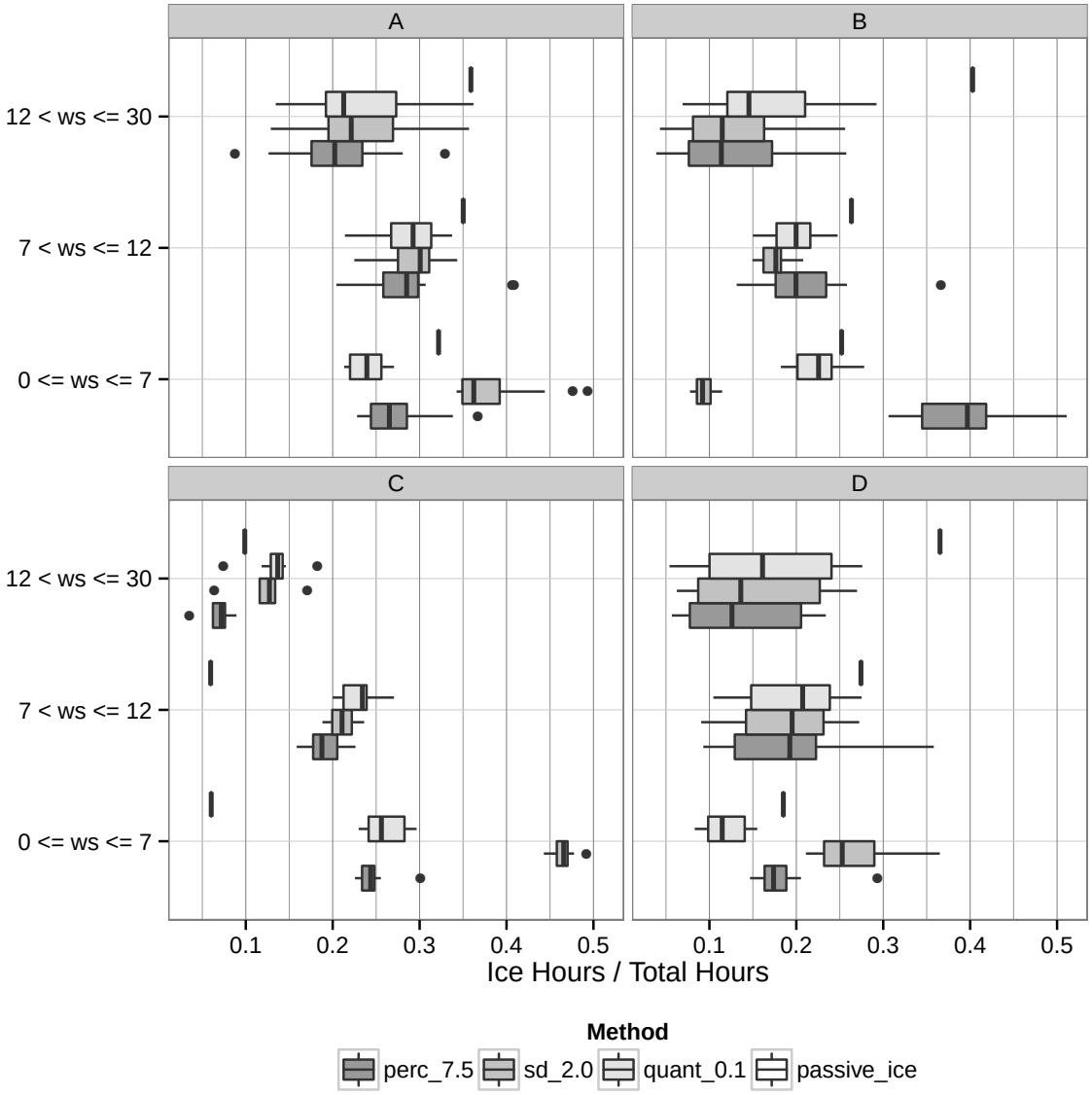

Figure 7. RATIO versus different wind speed (ws) bins at each wind park (A-D). Boxplots are used to summarize the different turbines at each wind park as in figure 6. The different colors denote the ice detection method. Ice threshold methods combine the method and threshold value, and passive_ice denotes the webcam estimated icing identification.

of the wind speed on the detection methods, the RATIO was compared for three different wind speed bins (Fig. 7). The difference in RATIO across the different wind parks from the SD method were largely due to ice detected at low wind speeds, wind speeds less than or equal to 7 $\mathrm{m\,s^{-1}}$. This may be due to the smoothing applied during the fitting of the SD method. It can be seen in Figure 1 that σ_{GAM} is much larger for wind speeds less than 3 $\mathrm{m\,s^{-1}}$ than σ_{raw}. Additionally, $\mathrm{P_{GAM}}$ does not have the sharp cut-off around 4 $\mathrm{m\,s^{-1}}$ found in $\mathrm{P_m}$. The results for wind speeds less than 7 $\mathrm{m\,s^{-1}}$ vary more across the parks for the PERC and QUANT methods as well, but the differences are not as large as for the SD method. For wind speeds close to rated power, between 7 and 12 $\mathrm{m\,s^{-1}}$, PERC generally estimates fewer icing hours than SD and

DOI: 10.1002/we
Prepared using weauth.cls

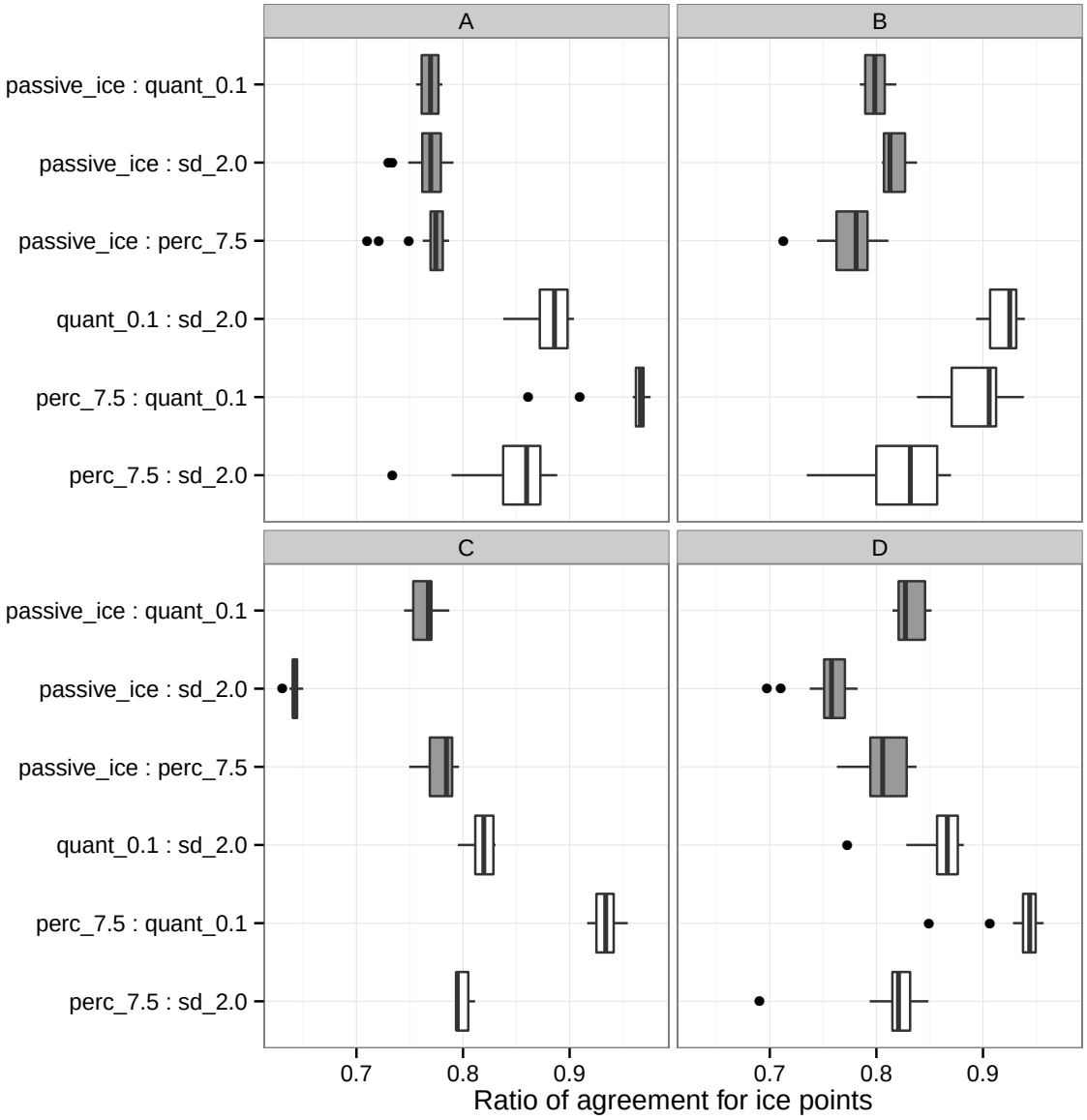

Figure 8. Boxplot showing the distribution of matched ice events for all of the power curve methods and webcam observations. The boxplot shows the spread across the different turbines in a given wind park.

QUANT, and the difference is even larger above rated power, as expected. All three methods show larger variance across the different turbines in a given park for the highest wind speed bin. This is likely due to there being a small number of icing events with wind speeds above rated power.

Thus far, the comparisons have focused on the number of iced hours, without requiring an exact match in the ice prediction. To identify the agreement between the various methods, the number of matching values, ie. both ice or both non-ice, were summed and then divided by the total value, providing a ratio of agreement (Fig. 8). Almost all methods show a ratio of agreement above 0.7, however, as icing is only identified around 20% of the time, this is not significant. As expected, the passive_ice method and the PT methods have less agreement than the different methods. This is likely caused

by the different conditions on the nacelle compared to the blade tips. An earlier study, modeling turbine icing, found that including the enhanced wind speed at the blade tips, due to the rotational speed of the blade, improved the estimation of periods of low production [19]. The meteorological instruments used for the passive ice detection method, will not have this increased rotational speed, and therefore are likely to not capture the icing periods as well. The PERC and SD methods show the most disagreement, with the QUANT method agreeing more with the SD method at site B. This is a somewhat surprising result, as PT_{QUANT} and PT_{SD} were shown to have similar shape (Fig. 3).

5. CONCLUSIONS

In this study three different techniques for identifying icing from an observed power curve were examined. The periods of icing detected by these methods were compared with two direct icing observations to determine the feasibility of the various approaches. The PERC method is useful for new sites since it does not require a long data record, being based on P_m. The PT_{PERC} using a deviation of 7.5% agreed the most with the two other methods, and identified more iced hours than the 15% or 20% thresholds (Fig. 6). It was shown, however, that PT_{PERC} did not capture the variation in observed power. Above the rated wind speed, PT_{PERC} was too low, (Fig. 3), and therefore, captured fewer icing hours than other methods (Fig. 7). At lower wind speeds, the opposite was true. PT_{QUANT} followed the lower values of the clean observed power curve, leading to a good agreement with the power difference (Fig. 3). Interestingly, the ratio of PT_{QUANT} to $P_m$was greater than 1 at some wind speeds, this was due to the turbine over-performing P_m due to either local effects or turbulence. The results from PT_{QUANT} did not show much sensitivity to different quantile values. This was somewhat surprising, but was due to the addition of the 2 hour ICE_{DUR} requirement. The inclusion of ICE_{DUR} was most significant for the PERC and QUANT methods, as both of these methods identified many more points during warm periods than the SD method (Fig. 5). The PT_{SD} curves closely matched the PT_{QUANT} curves for the sample turbine (Fig. 3), but it proved to not be as robust across the range of sites, leading to large differences in the number of estimated icing hours compared to PERC and QUANT depending on the wind park. This was largely a result of the challenge in estimating icing at lower wind speeds (Fig. 7). Based on the challenges experienced in fitting the PT_{SD} curves, this approach should only be used for datasets without any large outliers, and will perform best on a large dataset.

In addition to fitting the different threshold curves, the duration of icing events was examined. It was shown that for periods identified as icing lasting less than 2 hours, the power deviation was well within the range of the cleaned power data (Figs. 4 and 2). Therefore, a restriction of icing identification to only events lasting more than 2 hours seems reasonable.

The iceMonitor sensor did not agree well with any of the power metrics and any site except site B. This was largely due to noise in the data that prevented the sensor from accurately identifying ice / no-ice conditions. The passive webcam based method, however, agreed with the results at three of the four sites, only diverging from the consensus at site C. An investigation into this site revealed that many of the passive_ice data were missing and this likely reduced the amount of ice identifying at this site. It was shown, however, that while the number of icing hours was similar between the PT methods

DOI: 10.1002/we
Prepared using weauth.cls

and the passive_ice measurement, the periods did not necessarily match up, as passive_ice had the lowest agreement with the other methods (Fig. 8). This is likely due to the impact of wind speed on ice growth as shown in Davis et al. [19].

Given the findings of this study, it is recommend to use the QUANT method with a 0.1 threshold, as suggested by Karlson et al. [8]. However, we would recommend using a 2-hour ICE_{DUR} threshold to ensure that points which dip below the threshold for a short period of time are not classified as icing. For sites without at least 1 year of operational data the PERC method with a threshold of 7.5% is recommended, again using a 2-hour ICE_{DUR} threshold.

ACKNOWLEDGEMENTS

This work was supported financially by the Top-Level Research Initiative (TFI) project, Improved forecast of wind, waves and icing (IceWind), Vestas Wind Systems A/S, and the Nordic Energy Industry.

The statistical modeling and data-analysis was carried out using the R Project for Statistical Computing [14].

REFERENCES

1. Wallenius T, Peltola E, Lehtomäki V, Antikainen P, Bluemink GJ, Wadham-Gagnon M, Dillingh J, Clausen NE, Klintsröm R. Special Chapter : Cold Climate Turbines ("CCTs"). *BTM World Market Update*, BTM-Consult (ed.). 2012 edn., chap. 7, Navigant Research: Chicago, Illinois, USA, 2013.
2. Homola MC, Nicklasson PJ, Sundsbø Pa. Ice sensors for wind turbines. *Cold Regions Science and Technology* Nov 2006; **46**(2):125–131, doi:10.1016/j.coldregions.2006.06.005. URL `http://linkinghub.elsevier.com/retrieve/pii/S0165232X06000760`.
3. Tammelin B, Dobesch H, Durstewich M, Ganander H, Kury G, Laakso T, Peltola E. Wind Turbines in Icing Environment : Improvement of Tools for Siting , Certification and Operation - NEW ICETOOLS. *Technical Report*, Finnish Meteorological Institute, Helsinki, Finland 2005.
4. Cattin R, Kunz S, Heimo A, Oechslin R, Russi M. An Improved Approach for the Determination of In-Cloud Icing at Wind Turbine Sites. *European Wind Energy Conference*, Brussels, Belgium, 2008. URL `https://www.researchgate.net/profile/Rene_Cattin/publication/228491355_An_improved_approach_for_the_determination_of_in-cloud_icing_at_wind_turbine_sites/links/02e7e52a01fae51367000000?origin=publication_detail`.
5. Skrimpas GA, Sweeney CW, Marhadi KS, Jensen BB, Mijatovic N, Holbøll J. Detection of Wind Turbine Power Performance Abnormalities Using Eigenvalue Analysis. *ANNUAL CONFERENCE OF THE PROGNOSTICS AND HEALTH MANAGEMENT SOCIETY 2014*, Fort Worth, Texas, 2014; 1–7.
6. Wadham-Gagnon M, Lehtomäki V, Bolduc D, Jolin N, Boucher B, Rissanen S, Karlsson T, Bechoefer E, Sandel K. Ice Induced Vibration on Wind Turbines. *Proceedings of the 15th International Workshop on Atmospheric Icing of*

Structures (IWAIS XV), St. John's, Newfoundland and Labrador, Canada, 2013; 2–43–2–53.

7. Davis NN, Pinson P, Hahmann AN, Clausen NE, Žagar M. An investigation of the impact of turbine icing on wind farm production. *Wind Energy* 2014; **Submitted**.
8. Karlsson T, Turkia V, Wallenius T, Miettinen J. Production Loss estimation for wind power forecasting. *Winterwind*, Sundsvall, Sweden, 2014.
9. ASFT Industries. The ice load survellance sensor ICE MONITOR. URL `http://www.asft.se/pdf/weather/IceMonitor_ASFT.pdf`.
10. 12494:2001(E). *Atmospheric icing of structures*. ISO: Geneva, Switzerland, 2001.
11. 61400-12-1. *Wind Turbines - Part 12-1: Power Performance Measurement of Electricity Producing Wind Turbines*. First edit edn., IEC, 2005.
12. Hastie T, Tibshirani R. *Generalized Additive Models*. 1 edn., Chapman & Hall / CRC, 1990.
13. Wood SN. Fast stable restricted maximum likelihood and marginal likelihood estimation of semiparametric generalized linear models. *Journal of the Royal Statistical Society: Series B (Statistical Methodology)* Jan 2011; **73**(1):3–36, doi:10.1111/j.1467-9868.2010.00749.x. URL `http://doi.wiley.com/10.1111/j.1467-9868.2010.00749.x`.
14. R Core Team. *R: A Language and Environment for Statistical Computing*. R Foundation for Statistical Computing, Vienna, Austria 2014. URL `http://www.r-project.org`.
15. Wood SN. Thin plate regression splines. *Journal of the Royal Statistical Society: Series B (Statistical Methodology)* Feb 2003; **65**(1):95–114, doi:10.1111/1467-9868.00374. URL `http://onlinelibrary.wiley.com/doi/10.1111/1467-9868.00374/abstract`.
16. Cleveland WS, Grosse E, Shyu WM. Local regression models. *Statistical Models in S*, Chambers JM, Hastie TJ (eds.). chap. 8, Chapman and Hall: New York, 1992; 309–376.
17. Davis NN. Forecasting Wind Turbine Icing Conditions: Production loss and Impacts. Ph.d. thesis, Technical University of Denmark 2014.
18. Ribeiro C, Buxton B, Cox S. A STUDY OF TURBINE PERFORMANCE UNDER COLD WEATHER DRIVEN STABLE. *Winterwind*, Sundsvall, Sweden, 2014; 1–13. URL `http://www.winterwind.se/?edmc=2845`.
19. Davis N, Hahmann AN, Clausen NE, Žagar M. Forecast of Icing Events at a Wind Farm in Sweden. *Journal of Applied Meteorology and Climatology* Feb 2014; **53**(2):262–281, doi:10.1175/JAMC-D-13-09.1. URL `http://journals.ametsoc.org/doi/abs/10.1175/JAMC-D-13-09.1`.

Appendix B

Forecast of Icing Events at a Wind Farm in Sweden

Forecast of Icing Events at a Wind Farm in Sweden

NEIL DAVIS, ANDREA N. HAHMANN, AND NIELS-ERIK CLAUSEN

DTU Wind Energy, Roskilde, Denmark

MARK ŽAGAR

Vestas Wind Systems A/S, Aarhus, Denmark

(Manuscript received 20 December 2012, in final form 28 August 2013)

ABSTRACT

This paper introduces a method for identifying icing events using a physical icing model, driven by atmospheric data from the Weather Research and Forecasting (WRF) model, and applies it to a wind park in Sweden. Observed wind park icing events were identified by deviation from an idealized power curve and observed temperature. The events were modeled using a physical icing model with equations for both accretion and ablation mechanisms (iceBlade). The accretion model is based on the Makkonen model but was modified to make it applicable to the blades of a wind turbine rather than a static structure, and the ablation model is newly developed. The results from iceBlade are shown to outperform a 1-day persistence model and standard cylinder model in determining the times when any turbine in the wind park is being impacted by icing. The icing model was evaluated using inputs from simulations using nine different WRF physics parameterization combinations. The combination of the Thompson microphysics parameterization and version 2 of the Mellor–Yamada–Nakanishi–Niino PBL scheme was shown to perform best at this location. The distribution of cloud mass into the appropriate hydrometeor classes was found to be very important for forecasting the correct icing period. One concern with the iceBlade approach was the relatively high false alarm rates at the end of icing events due to the ice not being removed rapidly enough.

1. Introduction

Onshore wind farms are one of the most cost-effective ways to generate electricity (Hau 2013), leading to their large role in the development of plentiful clean energy for the future. In many parts of the world, the most lucrative available sites for wind energy extraction have already been placed into production. This is forcing wind farm developers to look to sites that are more complex and carry additional risks or uncertainties, such as offshore, forested, and cold climate locations. As of 2012, wind parks in cold climates account for approximately 4.1% of the 240 GW of global wind energy capacity (Ronsten et al. 2012). For wind parks in cold climates, one of the largest sources of risk comes from atmospheric icing on the turbine blades.

Atmospheric icing occurs on all structures that are exposed to moisture at temperatures below 0°C. There have been extensive studies of atmospheric icing both on cylinders, largely related to overhead power lines summarized in Farzaneh (2008), and on airfoils, mostly in the aviation community (e.g., Gent et al. 2000; Bragg et al. 2005). The challenge of atmospheric icing has also been studied for wind energy, with several international collaborations on the topic (e.g., Fikke et al. 2006; Ronsten et al. 2012), as well as a dedicated conference on wind energy in cold climates (Winterwind International Wind Energy Conference). The use of mesoscale models to estimate icing has been applied for studies in aviation (e.g., Thompson et al. 1997; Wolff et al. 2009), for both power-line icing and turbine icing in the power industry (e.g., Fikke et al. 2008; Dierer et al. 2011), and for comparisons with icing on standard cylinders (Bernstein et al. 2012; Byrkjedal 2012a,b; Soderberg and Baltscheffsky 2012; Yang 2012).

There are three main types of atmospheric icing: 1) in-cloud icing is generated by supercooled water droplets in clouds or fog that contact a surface and freeze upon impact, often leading to rime ice that has a rough appearance and milky look due to trapped air that decreases its density; 2) freezing rain occurs when rain falls

Corresponding author address: Neil Davis, Dept. of Wind Energy, Technical University of Denmark, Risø Campus, Frederiksborgvej 399, P.O. Box 49, 4000 Roskilde, Denmark.
E-mail: neda@dtu.dk

DOI: 10.1175/JAMC-D-13-09.1

onto structures with temperatures below 0°C, commonly forming glaze ice that has a high density and clear appearance; 3) wet snow icing occurs under special meteorological conditions that allow snow with a liquid surface to accumulate on structures when the ambient temperature is close to freezing. The focus of this study is on in-cloud icing only.

In-cloud icing on turbine blades increases the safety, financial, and maintenance risks when developing and operating a wind farm in cold climates. Accumulated ice on the blades can fall or be thrown from the turbine, requiring careful planning to minimize the risk to people and property near the wind farm (Seifert et al. 2003). The added mass, caused by the ice, places additional loads on the turbine that can lead to increased maintenance and shorten turbine lifetimes. Finally, ice accumulation changes the aerodynamic properties of the blades themselves and can lead to reduced energy production during the icing season. Homola et al. (2012) showed that the power curve (i.e., the relationship between wind speed and power) for a simulated wind turbine is reduced by around 28% between the cut-in wind speed, where the turbine is able to produce electricity, and the rated wind speed, where the turbine is producing its rated power output, for a turbine blade with moderate ice growth. Barber et al. (2011) investigated two wind farms in Switzerland and found that icing leads to a 2% loss of annual energy production (AEP) at a farm with moderate icing where the ice accumulation is not severe enough to lead to flow separation on the airfoil, and a 17% loss in AEP at a farm that experiences extreme icing leading to flow separation.

Thus far, most research into icing on wind turbines has related to observations (e.g., Fikke et al. 2006; Ronsten et al. 2012), ice throw (e.g., Seifert et al. 2003; Cattin et al. 2007), and computational fluid dynamics (CFD) modeling focused on the type and amount of icing formed on the blades and the impact of that icing on airfoil performance under different fixed meteorological conditions (e.g., Makkonen et al. 2001; Homola et al. 2010a; Virk et al. 2010; Homola et al. 2012; Virk et al. 2012). There have been a few conference presentations on forecasting icing at Winterwind, but these have mostly focused on forecasting ice on a standard cylinder using the Makkonen (2000) model and then relating the standard icing results to the turbine using statistical algorithms (e.g., Dierer et al. 2011; Byrkjedal 2012a; Soderberg and Baltscheffsky 2012; Yang 2012). Bernstein et al. (2012) reported that the correlation between measured icing load on a cylinder and actual power loss is weak because significant ice loads may persist on cylinders while power recovers at the turbines. They also found that active icing is better correlated with power loss. The standard cylinder approach has been shown to reasonably capture the ice loading of a standard cylinder mounted near the turbine, but only limited agreement with the power output was found (Byrkjedal 2012a).

This study introduces the iceBlade model that was developed with the goal of providing a better relationship between the forecast periods of icing and reduced power output. This was accomplished by modifying the inputs to the Makkonen ice accretion model to better represent the conditions on the wind turbine blade, as well as including algorithms for ice sublimation, and a method for modeling total ice shedding. It will be shown that the results from the iceBlade model, driven by mesoscale model outputs, can successfully reproduce the periods of icing observed at a wind park in Sweden.

The rest of the paper is organized as follows. In section 2, the data from the wind park are described, and the method of determining icing from the observations values is presented. Section 3 describes the models used in this study, first presenting the iceBlade model, then the mesoscale model that provides the inputs to iceBlade, and finally the coupling of the two models. In section 4, the observations and model results are presented and discussed. In section 5, the main conclusions are presented.

2. Wind farm data

This study focuses on power production and meteorological data from a wind farm in central Sweden. The site is fairly noncomplex, with land use dominated by forest and small lakes. The farm consists of 48 Vestas Wind Systems A/S V90 turbines, and the dataset contains 10-min-average data for the month of January 2011. Data were missing for most turbines for the period between 16 and 19 January. In addition to the production and meteorological data, all turbines provided status counters. Two of these counters were used for quality assurance (QA) of the dataset. The first counter provided the number of seconds, out of the optimal 600 s, that the wind was within the required range for producing power. This means that the wind speed was between the cut-in wind speed of $4\,\mathrm{m\,s^{-1}}$ and the cutoff wind speed of $25\,\mathrm{m\,s^{-1}}$, above which the turbine stops producing for safety reasons. The second counter provided the number of seconds the turbine was in normal operation. All time steps where either of these values deviated from the optimal value by more than 10 s were flagged as QA time steps and dropped from the analysis. To form a more homogeneous dataset, five turbines were removed from the analysis. This left 43 turbines to represent the wind farm in the study.

Each turbine reported instantaneous meteorological measurements from its nacelle for wind direction, wind

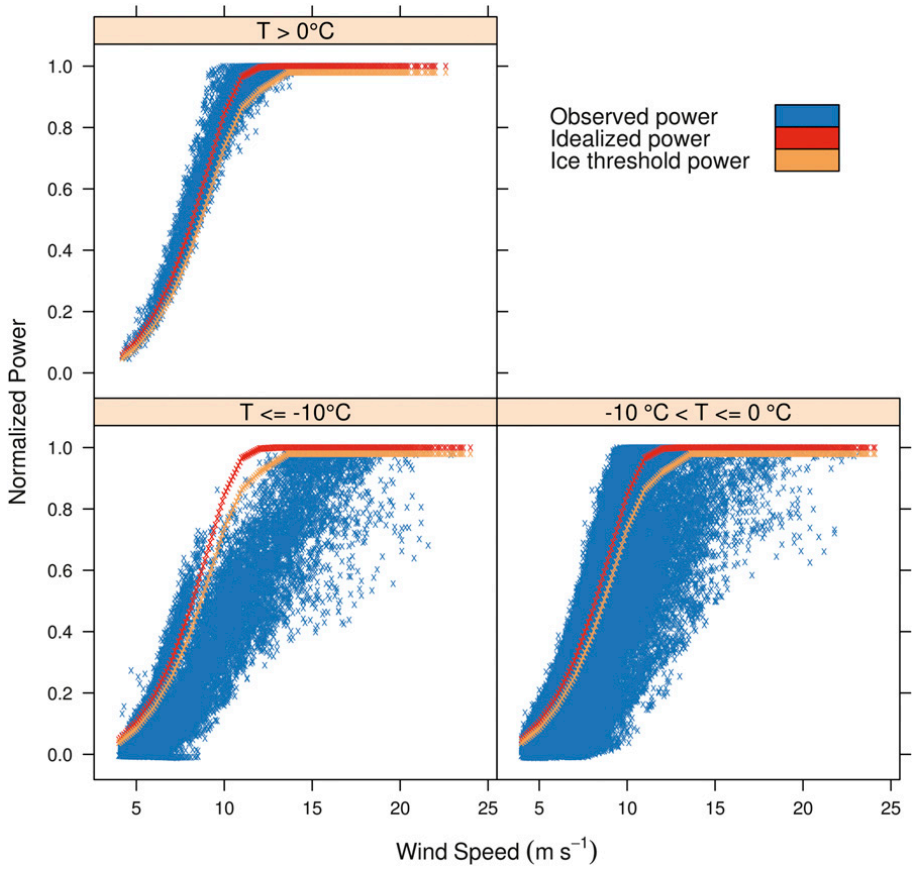

FIG. 1. Idealized (red or orange) and observed (blue) power curves for each turbine in the wind park: red curves show the idealized power curve as provided by WAsP data tables for the unadjusted nacelle wind speeds, and orange curves show the threshold used for observed icing events defined in (1). The panels represent various temperature bins: (top) $T > 0$°C, (bottom right) $-10° < T \leq 0$°C, and (bottom left) $T \leq 10$°C.

speed, wind speed standard deviation, and temperature. Only temperature and wind speed were used in this study. The temperature measurements had a rather coarse precision of 1°C created by rounding the decimal observations. The measured wind speed data were already adjusted to account for the speedup experienced due to the placement of the anemometer on the nacelle. Also, as the wind speed was taken at the turbine, any wake loss is already accounted for in the wind speed so no additional modification is required.

An idealized power curve for the V90 turbine was calculated using data provided by the Wind Atlas Analysis and Application Program, version 10 (WAsP; Troen and Petersen 1989), to evaluate the turbine performance. Figure 1 compares the observed power curve for all 43 turbines with two idealized curves for three different temperature bins (above 0°C, from 0° to −10°C, and below −10°C). The idealized curves represent 1) the unadjusted idealized power curve calculated using the raw nacelle wind speed and 2) a fitted curve for the ice threshold defined below. The observed power curve shows good agreement with the idealized power curves when the temperature was above 0°C, with similar spread on each side of the power curve. However, for temperatures less than or equal to 0°C the observed yield was consistently lower than the estimated value from the idealized power curve. Very few points fell above the idealized curves; for the coldest temperature bin, this suggests that the turbines were iced during the entire period when the temperature was below −10°C. It is expected that this feature would not be seen with a larger dataset that contained more points with temperatures lower than −10°C.

As there were no direct icing observations for any of the turbines, a proxy dataset was created. This was done by fitting a curve to the bottom of the observed power curve for temperatures above 0°C (blue curve in Fig. 1). This curve is calculated as

$$f(p) = p \times 0.8 + [v^3/\max(v^3)], \quad (1)$$

where p is the idealized power at a given wind speed and v is the wind speed. The threshold power $f(p)$ was limited to a maximum value of 0.98. The curve allowed for a transition between a high deviation value of 20% at wind speeds below the rated wind speed ($12\,\mathrm{m\,s^{-1}}$) when the power curve has a steep slope, and therefore a larger deviation, and the flat portion of the curve above the rated wind speed, where there is less variation in the power output. Using the icing threshold curve calculated in Eq. (1), an icing observation was defined as a data point that fell below that curve when the temperature was less than 0°C. This assumes that all of the power loss observed at cold temperatures was the result of icing. This is a reasonable assumption, as at colder temperatures an increase in yield is typically expected due to the increased air density. Vertical wind shear is also expected to increase at cold temperatures; however, Antoniou et al. (2009) found that wind shear causes less than the 20% impact that we are using as our icing cutoff.

Because of the large variability in icing from each of the 43 turbines, three different wind park icing occurrence time series, representing different numbers of affected turbines, were created: 1) ANY was considered to have occurred when any of the 43 turbines in the park experienced icing, 2) MOST wind park icing was considered to have occurred when the majority (>50%) of active turbines had icing events, and 3) ALL wind park icing was considered to have occurred when all active turbines had icing events.

The temperature and wind speed values from the turbines were also examined. The temperature data showed an average spread of 2.6°C across the 43 turbines. There was also one turbine that was a clear outlier at the beginning of the period; excluding that turbine reduces the spread to 2.5°C. The wind speed also had a very large mean spread of $5.14\,\mathrm{m\,s^{-1}}$. This spread was likely due to the micro-siting of the turbines, where several turbines were placed in areas where the wind was increased due to local effects. Given the large spread of the data and the existence of outliers in the dataset, the median temperature and wind speed were chosen to compare with the model data.

The National Centers for Environmental Prediction Automated Data Processing Global Upper Air and Surface Weather Observations dataset (documented and available online at http://rda.ucar.edu/datasets/ds337.0/) was used as an independent meteorological dataset for additional mesoscale model verification. From this dataset, three surface stations located within 100 km of the wind farm were chosen (Fig. 2, inset). The surface stations recorded station pressure, specific humidity, temperature, and wind speed, and provided a more detailed model evaluation than was possible using only the wind park data. The surface stations have been renamed from south to north as stations A, B, and C. Station A is located on a small island in a large lake, station B is located in a field with forest nearby, and station C is located next to a river surrounded by grasslands and forest.

From the ANY icing observation dataset, a baseline persistence model was created for comparison with the iceBlade model. This model used a 1-day forecast, where missing data were treated as an unavailable forecast. Given the relatively long time periods of the icing and nonicing events in this dataset (Fig. 3), it is presumed that the persistence model would be difficult to beat. However, it should be noted that for other locations and periods the persistence model may not perform as well.

3. Models

a. *The iceBlade icing model*

The iceBlade model is a new model developed to approximate the mass of ice that accumulates on a wind turbine blade during in-cloud icing conditions. The model is presently designed to only estimate the effects of liquid-phase cloud particles accreting on a simplified blade represented by a cylinder, with an incoming velocity based on the rotational speed of a wind turbine under similar conditions. The model presently neglects wet snow icing, which may be significant at certain locations, but did not appear to be important for this particular wind farm. IceBlade consists of the Makkonen (2000) accretion model, with inputs suitable for wind turbines, and ablation models for sublimation and shedding. The accretion and the ablation models are described in the next two sections. The representation of the turbine in the model is described in section 3a(3).

1) ICE ACCRETION MODEL

Makkonen (2000) presented a model to calculate the rate of ice mass growth based on the mass flux of cloud particles (a product of the mass concentration of particles ω, the velocity, and the cross-sectional area of the object A) and three correction factors α_1, α_2, and α_3:

$$\frac{dM}{dt} = \alpha_1\alpha_2\alpha_3\omega v A\,. \quad (2)$$

The correction factors, which can range in value from 0 to 1, represent processes that reduce the amount of ice accretion from its maximum value, the incoming mass flux. These factors are defined as efficiencies of collision (α_1), sticking (α_2), and accretion (α_3). The usage of

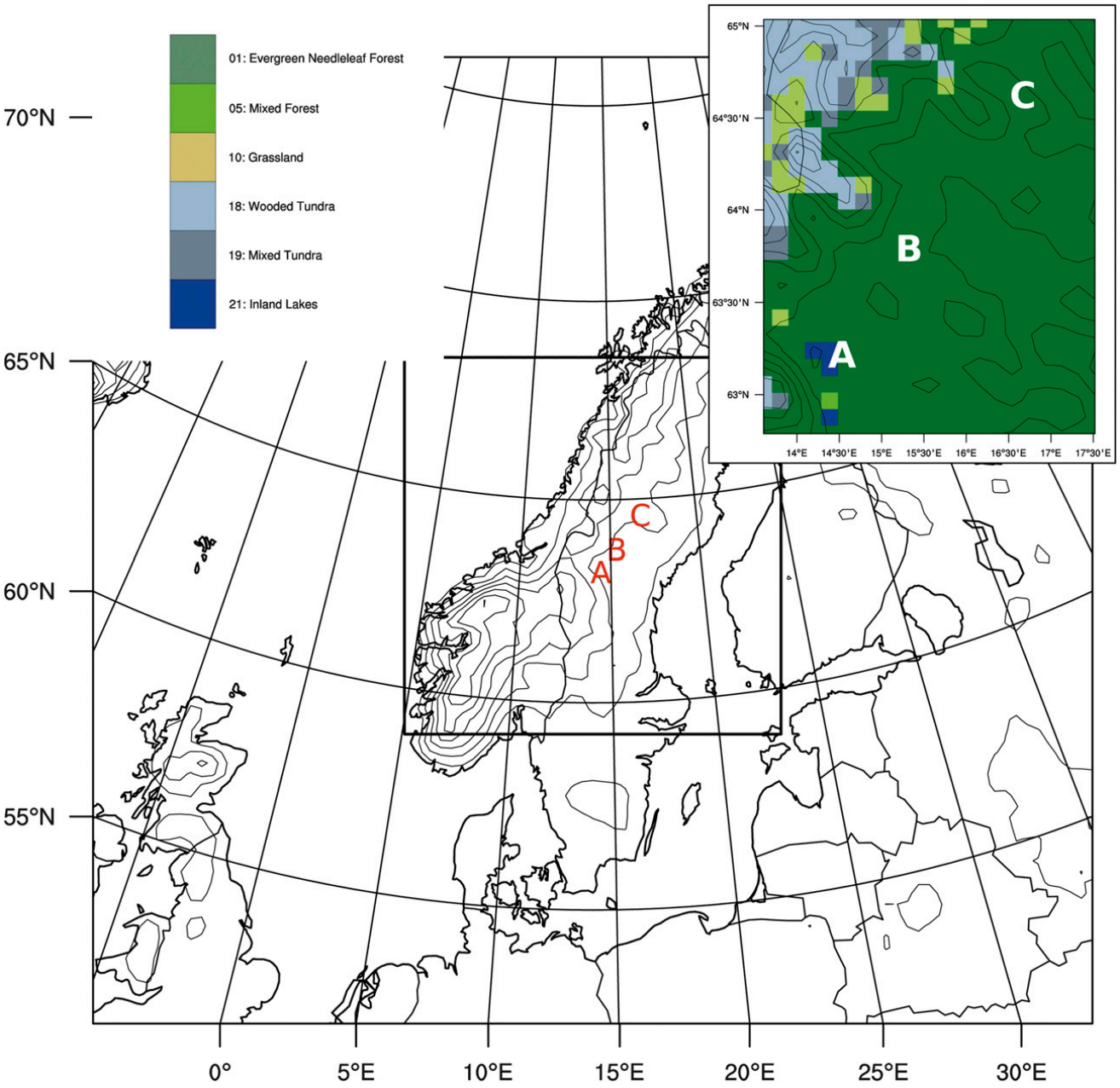

FIG. 2. Terrain contours from 0 to 1600 m with 200-m intervals for the outer WRF domain. The inner WRF domain is marked by the rectangle, and the wind park location is identified by a black circle. The inset map shows a zoomed-in region of the domain around the three meteorological stations, showing the WRF land use from the inner nest, and contours from 100 to 900 with 100-m intervals.

efficiency factors allows for different models to be constructed quickly by replacing the factors with updated methods, allowing for the easy extension of the model to new areas of research. IceBlade uses the unmodified factors at present; therefore, only a simple description of each is provided below.

The collision efficiency term α_1 represents the total collision efficiency E. This value can be calculated using an empirical formula [Eq. (1) in Finstad et al. (1988)] derived using regression analysis based on data from an investigation of water droplets in flows around cylinders by Langmuir and Blodgett (1961). In addition to E, Finstad et al. (1988) derived relationships for calculating the maximum impingement angle $\alpha_{\max}$, stagnation line velocity v_0, and stagnation line collision efficiency β_0. The integration of all collision efficiencies between $\pm\alpha_{\max}$ is represented by E.

The sticking efficiency term α_2 approximates the loss of incoming cloud particles that either bounce off the structure (frozen) or generate splash, which reduces the

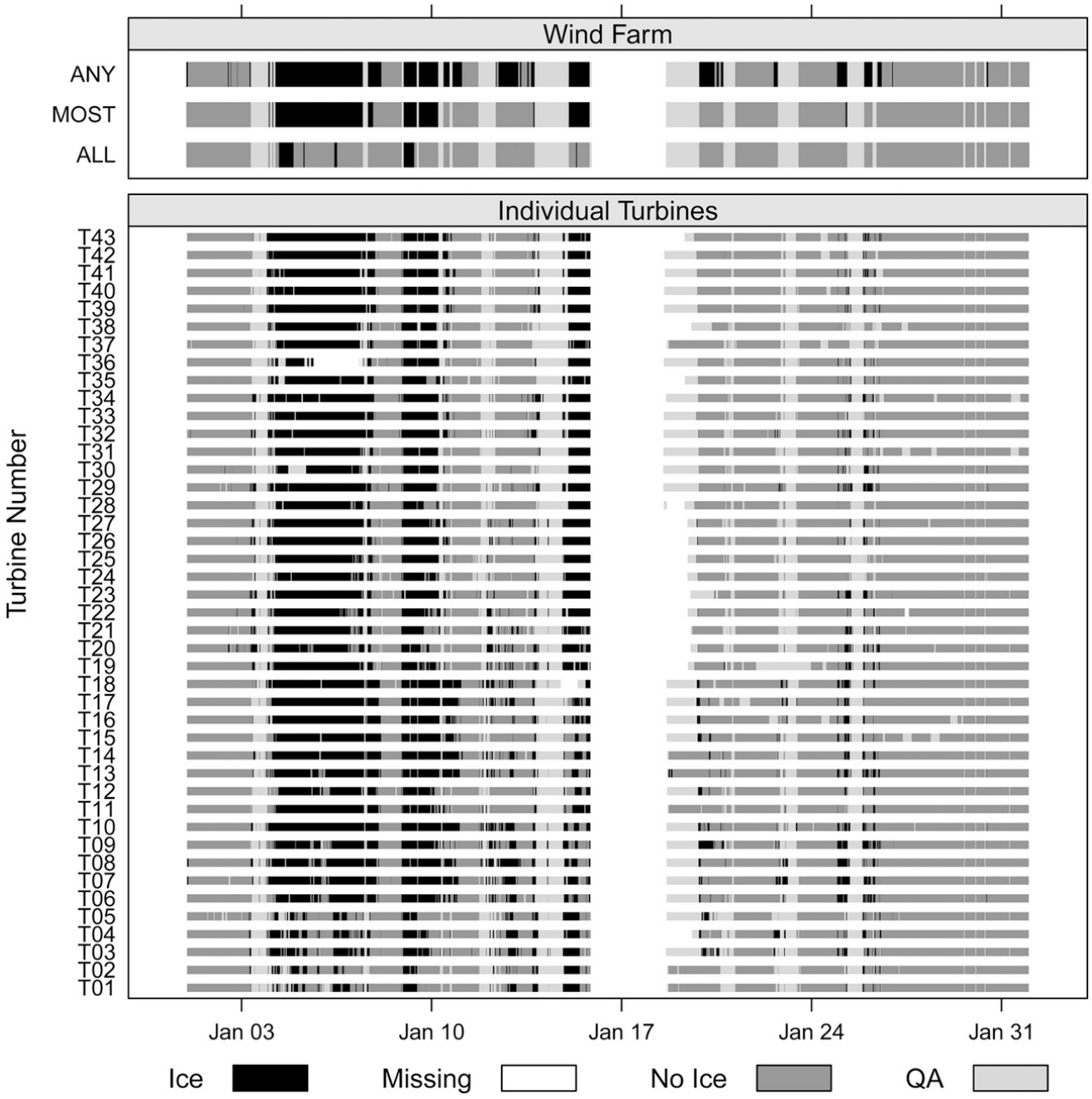

FIG. 3. (top to bottom) Time series of observed icing for ANY, MOST, and ALL turbines and for each (T43–T01) turbine. White space denotes a period for which turbine data were not available, light gray indicates data obtained when the turbine was not in optimal operation for the full 10-min period, dark gray denotes periods during which there was no icing, and black shows icing periods.

mass available for accretion. From Makkonen (2000), the loss from supercooled water droplets is almost zero, corresponding to an α_2 of 1. As iceBlade is designed for modeling work with liquid droplets only at present, α_2 is always set to 1.

The final efficiency term α_3 estimates the ratio of incoming mass that freezes upon impact with the structure. During rime icing conditions all impacting particles freeze, leading to an α_3 value of 1. Under glaze icing conditions only a portion of the incoming mass freezes. The amount of mass that is frozen is controlled by the heat balance at the interface between the incoming droplets and the surface. In Makkonen (2000), this is represented by

$$Q_f + Q_v = Q_c + Q_e + Q_l + Q_s, \tag{3}$$

where Q_f is the latent heat released during freezing, Q_v is the frictional heating of air, Q_c is the loss of sensible

heat to the air, Q_e is the heat lost to evaporation, Q_l is the heat loss in warming the impinging water to the freezing temperature, and Q_s is the heat loss due to radiation. The terms in Eq. (3) have been parameterized in Makkonen (2000) and will not be replicated here. In our experience, the efficiency term α_3 defined using the parameterizations of Eq. (3), can be applied to both rime and glaze icing situations, provided the result is limited to a range of 0 to 1.

Based on the assumptions presented above, there are two inherent limitations of the Makkonen model as applied in iceBlade:

(i) the model is applicable only to cylindrical objects—this also implies that the ice shape itself retains a cylindrical shape as it grows, and
(ii) the model is applicable only to supercooled water droplets.

2) Ice ablation models

Ice ablation refers to all processes that remove ice from a structure. There are three main ablation processes: 1) melting, 2) sublimation, and 3) shedding. Melting and sublimation are physical processes that are based on the heat and moisture balance between the ice and the ambient air when the temperature is above and below the freezing point. Ice shedding occurs when ice falls from the structure due to a loss of adhesion. For a section of the structure, ice shedding can be described as either total shedding, where the entire mass of accumulated ice is removed from the structure, or partial shedding, where the ice loses cohesion with another part of the ice, rather than losing adhesion to the structure. IceBlade includes algorithms for sublimation and total shedding described in detail below.

Total ice shedding is based on microscopic interactions between ice and the blade surface, and its modeling requires detailed information about the blade surface and the way the ice accumulated on that surface. Since one of the design parameters of iceBlade is the application to different turbines under various conditions, it was decided that the implementation of a physical shedding algorithm was too turbine specific and currently outside of the model's scope. Therefore, a simplified method was developed based on the following assumptions: 1) when a turbine is in operation, even a slight loss in adhesion would cause the ice to be thrown from the turbine due to the forces present on the rotating blade; 2) the only loss of adhesion is due to melting at the blade surface; and 3) the turbine is always operating according to the idealized power curve. These assumptions greatly underestimate the shedding that occurs since it can often happen at temperatures below 0°C, due to turbulence, or blade flexing. Given those assumptions, total shedding is implemented by removing all ice from the blade when the ambient temperature is above 0.5°C for 1 h. This threshold was tested at this location and found to be reasonable; however, it may need to be modified for other sites. Because of the relatively low temperature threshold for total shedding, ice melt is not included in the iceBlade model at this time.

Ice sublimation is modeled using the explicit solution [Eq. (16) from Srivastava and Coen (1992)]. To account for the change in shape, from spherical to cylindrical, the following modifications were made to Eq. (6) in Srivastava and Coen (1992):

$$\left(\frac{dm}{dt}\right)_1 = \frac{4\pi r D f_v \rho_s(T_\infty)}{1 + \dfrac{L_s D f_v}{k f_h}\rho_s'}, \tag{4}$$

where D is the diffusivity of water vapor in air, f_v is the ventilation coefficient for water vapor, $\rho_s(T_\infty)$ is the saturation vapor density at ambient air temperature (T_∞), L_s is the latent heat of sublimation, k is the thermal conductivity of air, f_h is the ventilation coefficient for heat, and ρ_s' is the differentiation of $\rho_s(T_\infty)$. From Pruppacher and Klett (2004) it can be found that $2f_v = \mathrm{Sh}$ and $2f_h = \mathrm{Nu}$, where Sh is the Sherwood number and Nu is the Nusselt number. The Sherwood and Nusselt numbers are dimensionless numbers that provide the ratio between convective and conductive transfers of mass and heat, respectively. The Sherwood number is defined as

$$\mathrm{Sh} = KL/D, \tag{5}$$

where K is the mass transfer coefficient and L is a characteristic length. For a sphere, L is typically the diameter. By using Eq. (5) and substituting for f_v and f_h, Eq. (4) can be rewritten as

$$\left(\frac{dm}{dt}\right)_1 = \frac{A\,\mathrm{Sh} D \rho_s(T_\infty)}{L\left(1 + \dfrac{L_s D \mathrm{Sh}}{k\mathrm{Nu}}\rho_s'\right)}, \tag{6}$$

where A is the surface area as in Eq. (2). Sherif et al. (1997) presented a formula for the Nusselt number of an airfoil as a function of its chord length and leading-edge diameter, using the Reynolds and Prandtl numbers. Using this same formula, it is possible to calculate the Sherwood number by substituting the Schmidt number with the Prandtl number. The iceBlade sublimation equation is found by combining these calculations of the Sherwood and Nusselt numbers with Eq. (6), while using the chord length as the characteristic length L. The chord

length term cancels out between the two equations allowing a constant value of 1.0 to be used in iceBlade.

3) TURBINE REPRESENTATION

To reduce the complexity of the model, several simplifications have been made to the representation of a fully rotating turbine blade. IceBlade models a 1-m-long segment of the turbine blade as a cylinder, located approximately 85% down the length of the 41-m-long blade. Since specific information about the airfoil used on the turbines in this study was unavailable, a cylinder diameter of 0.144 m was taken from the National Renewable Energy Laboratory's 5-MW reference turbine (Jonkman et al. 2009). The cylinder diameter is based on the leading-edge radius for the airfoil being 2.4% of the chord length, with a chord length of 3.0 m.

Rather than represent the blade as rotating through space, the iceBlade model was designed so that the blade is always located in the same meteorological conditions. This eliminates the calculation of how much time the blade segment spends at various points in the rotor plane. How this relates to the mesoscale modeling, and its impact on this study, are discussed in more detail in section 3c.

The largest difference between the rotating turbine blade and a standard cylinder is the incoming velocity term. Since the blade is rotating at tip speeds approaching 90 m s^{-1}, the ambient wind speed has to be converted to a blade-relative velocity. Again, the data required to calculate an appropriate revolutions-per-minute (rpm) curve were unavailable for the turbines at the studied site, so a generic curve based solely on the ambient wind speed was used in its place. The rpm value was then converted into a linear speed at a distance of 34.85 m from the center of rotation. In initial tests (not shown), it was found that this change reduced the number of icing events but increased the amount of ice accumulated during events when icing did occur. This is likely due to an increase in mass flux resulting from the increased velocity. The increased flux decreases the α_3 term in Eq. (2), reducing or preventing ice growth at temperatures near or above 0°C. However, when the ambient temperature is cold enough to freeze the increased mass flux, ice will accumulate more rapidly.

The final change between iceBlade and the Makkonen model for a standard cylinder is that the iceBlade model does not update the size of the cylinder between time steps. When the Makkonen model is run on a standard cylinder, it is assumed that the cylinder will retain its shape and therefore the change in diameter can be reasonably calculated from the ice mass and density. For the turbine blade, which is always orientated in one direction, most of the ice grows out of the leading edge, as seen in the CFD study by Homola et al. (2010b). This suggests that the ice growth simply extends the chord length rather than making the leading edge thicker and therefore would not have a significant impact on either the collision efficiency or the surface area facing the flow.

b. *Meteorological modeling*

Meteorological modeling for this study was undertaken using the Weather Research and Forecasting (WRF) mesoscale model, version 3.3 (Skamarock et al. 2008). This model has been shown to accurately represent the liquid water content of low-level clouds at high resolutions; however, questions remain about its ability to represent the size of the cloud particles via their median volumetric diameter (MVD) (Nygaard et al. 2011). The WRF model was driven with initial and boundary conditions from the Global Forecast System's Final Analysis Product (FNL), with sea surface temperatures from the National Oceanic and Atmospheric Administration's Optimum Interpolation Sea Surface Temperature dataset (OISST), version 2 (Reynolds et al. 2007). The FNL data were also used as input to grid four-dimensional data assimilation nudging on the outer nest. The nudging was applied on all levels above level 15, approximately 500 m, with all nudging coefficients set to 7.5×10^{-5}. The nudging was not included below level 15 because of the increased influence of mesoscale features near the surface. The simulation was run for 30 days, in three 10-day periods, with 24 h of spinup per period. Two modeling domains were run, with the outer domain having a grid spacing of 30 km and the inner domain with grid spacing of 10 km. The wind farm was located near the center of both domains (Fig. 2). Sixty-three vertical levels were used, 26 of which were within the lowest 1000 m.

The physics options of the model were the defaults of the Rapid Radiative Transfer Model longwave radiation scheme (Mlawer et al. 1997), the Dudhia shortwave radiation scheme (Dudhia 1989), the Noah land surface model (Chen and Dudhia 2001), and the Kain–Fritsch cumulus parameterization scheme (Kain 2004), with three microphysics and three PBL schemes tested in a sensitivity matrix leading to a total of nine sensitivity simulations. For microphysical schemes, the Stony Brook University–Y. Lin (SBU-YLin; Lin and Colle 2011), Thompson (Thompson et al. 2008), and WRF single-moment five-class cloud microphysics (WSM5; Hong et al. 2004) schemes were selected. These schemes provided a good range of complexity, with the Thompson scheme having the most predictive variables, while WSM5 and SBU-YLin offer fewer predicted variables and have shorter run times. The three PBL schemes were the Mellor–Yamada–Janjić (MYJ; Janjić 1994), version 2 of the Mellor–Yamada–Nakanishi–Niino

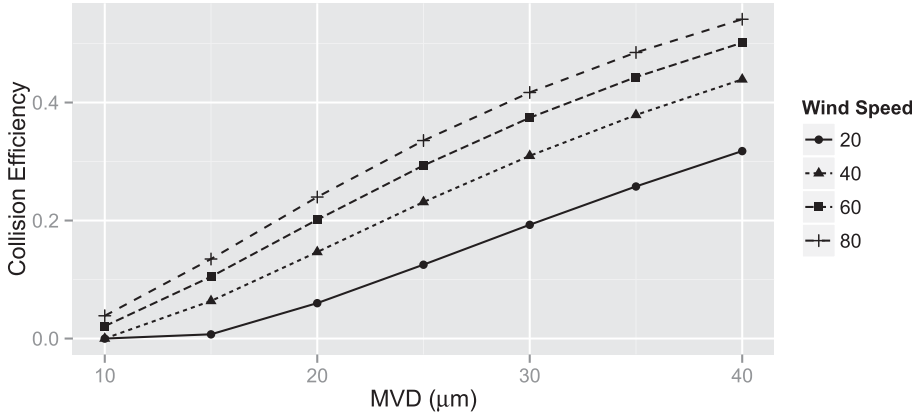

FIG. 4. Collision efficiency α_1 vs MVD (μm) for various wind speeds ($m\,s^{-1}$) for a cylinder with diameter of 0.144 cm.

(MYNN2; Nakanishi and Niino 2006), and the Yonsei University (YSU; Hong et al. 2006) schemes. Both the MYJ and the MYNN2 schemes are 1.5-order turbulent kinetic energy local closure schemes, while the YSU scheme is a nonlocal *k*-mixing scheme. Another difference is in the mixing of hydrometeors for the different schemes; in the MYNN2 scheme only the cloud water mixing ratio Q_c is mixed, while in the YSU and the MYJ schemes both Q_c and the cloud ice mixing ratio Q_i are mixed. The YSU scheme was modified to correct an error found in WRF 3.4.1. This error led to higher turbulence values in stable conditions and unrealistically high wind speeds at lower levels. The YSU and MYNN2 schemes used the Monin–Obukhov scheme from the fifth-generation Pennsylvania State University–National Center for Atmospheric Research Mesoscale Model for the surface layer, while the MYJ option used its own surface layer scheme.

The MVD of a cloud has been shown to be an important parameter in ice accretion modeling due to the dependence of the collision efficiency, α_1, on this term. The relationship between MVD, wind speed, and α_1 is shown in Fig. 4. MVD is shown to have a larger effect on α_1 at higher wind speeds. For a wind speed of $60\,m\,s^{-1}$, similar to what is expected in the iceBlade model, α_1 almost triples from 0.15 to 0.4 for MVD values between 15 and 30 μm. As MVD is not a prognostic variable for any of the microphysical schemes being used, several sensitivity tests were carried out to estimate its impact on the icing forecast. Both the SBU-YLin and Thompson schemes use a gamma distribution for cloud water particles. Nygaard et al. (2011) presented an equation to calculate the MVD from the gamma distribution based on the droplet concentration N_c and cloud liquid water content (LWC_c). The WSM5 scheme uses a monodisperse cloud water distribution. Both of these distributions were tested for all three schemes to evaluate the differences. Since there were no estimates of N_c at the evaluation site, three prescribed values were chosen as sensitivity tests: 100, 250, and $350\,cm^{-3}$. The first two prescribed N_c values are those suggested by Thompson et al. (2008) for oceanic (clean) and onshore (polluted) air, while Nygaard et al. (2011) presented several measurements of N_c larger than $500\,cm^{-3}$, suggesting a value greater than $250\,cm^{-3}$ might be appropriate. The SBU-YLin and Thompson schemes were only run once with their default values for N_c of 10 and $100\,cm^{-3}$, respectively. For the monodisperse tests, fixed MVD values of 10, 15, 20, and 25 μm were chosen, based on the calculated MVD distributions. These distributions generally had a peak around 15 μm and extended over the entire prescribed range (10–25 μm).

c. Coupling of iceBlade with WRF

All of the inputs to iceBlade are from the outputs of the nine WRF sensitivity runs. The wind park covers four 10 km × 10 km WRF grid cells, but in our tests there was little variation in the iceBlade results across the grid cells, so all presented results are from the northwest grid cell. Because of the high vertical resolution of the WRF model, five model levels crossed the turbines rotor plane, but as discussed in section 3a(3), iceBlade was designed to only use one height for input. To account for this, initial tests were conducted comparing the results from different model levels, as well as averaged values across the five levels. These results show only a minimal impact on the icing estimates, so it was decided that the WRF output would only be extracted from the model level that was approximately 80 m above the model terrain. The height of 80 m was chosen since this is the most common hub height for wind turbines and is used in current wind farm assessment studies.

TABLE 1. Percentage of time during January 2011 with observed icing at a wind farm in central Sweden, excluding time when the turbine data were not available. Number of available time steps and total number of possible time steps are shown in parentheses, separated by a slash.

Averaging period	ANY	MOST	ALL
10 min (3310/4608)	56.44	29.46	8.67
1 h (552/768)	57.10	29.35	9.60
8 h day^{-1} (26/32)	65.38	26.92	11.54

The ω term of the Makkonen model required additional processing of the WRF outputs as a result of there being two liquid hydrometeor species, determined by size, in each of the microphysical schemes used. The cloud water mixing ratio Q_c and rainwater mixing ratio Q_r variables were used to calculate cloud LWC (ω_c) and rain LWC (ω_r). The cloud MVD and ω_c were then used to calculate the cloud collision efficiency α_{1c}. The total LWC (ω_t) was then calculated as

$$\omega_t = \omega_c \alpha_{1c} + \omega_r . \quad (7)$$

The collision efficiency for rain was assumed to always be 1, as rainwater was assumed to be collected in its entirety due to the large drop size. In Eq. (2), ω_t was then used to represent both the ω and α_1 terms. The ambient wind speed was calculated from the u and v wind components that were rotated to Earth relative, and unstaggered in the horizontal.

After running iceBlade, a binary icing time series was created using a threshold of 0.001 kg of ice to signify ice accumulation on the blade. This threshold related well to the ANY observed icing dataset. These two datasets were used for most of the evaluation in this study.

4. Results and discussion

a. Observed icing

As described in section 2, an observational icing dataset was created using the turbine temperature, power production, and idealized icing threshold curve. Thus, power loss is not a term that can be examined separately under the different icing conditions since it was part of the criteria for observed icing. However, it is possible to examine the amount of time each of the turbines was iced to gain a better understanding of how the icing impacts each turbine. Table 1 shows the percentage of available times when the turbine was under icing conditions for different time intervals. The 10-min values are based on the raw values from the turbines. Hourly icing was defined by the raw turbine data extracted at the top of the hour (0 min). Daily icing was defined as days where eight or more hours had ice. The 10-min and hourly data have very similar percentages across all categories. This suggests that the hourly data do a reasonable job of capturing the underlying signal in the 10-min data. Daily icing events show larger percentages for the ANY and ALL categories, likely related to the 8-h threshold, but a smaller percentage of time for the MOST category. The decrease in the MOST category suggests that this group varies more throughout icing periods than does either the ANY or ALL categories.

Given the large differences among the three categories of turbine icing, the percentage of icing for each turbine was examined using the 10-min data. It was found that the amount of icing time ranged from 17% to 43% for the various turbines with a median value of 32.6%. The lowest values are found in turbines, numbered 1–5, that did not experience the same amount of icing during the early part of the month. There were between four and five widespread icing events during the month, with periods of melting between them (Fig. 3). Given the number of events, this dataset should provide a good evaluation of the icing model as it will test both the accumulation and ablation algorithms.

b. Meteorological evaluation

The WRF model outputs were evaluated for the area surrounding the wind farm using data from three surface stations located within 100 km of the wind park, as well as the wind park itself (Fig. 2, inset). At the wind park, temperature and wind speed were evaluated, while the surface sites also included variables allowing for the evaluation of humidity and pressure. The evaluations of wind speed, humidity, and pressure will be briefly discussed with an in-depth discussion of the temperature evaluation, because temperature is a key input to both the accretion and ablation models.

The results from the WRF model showed a moist (positive) bias at all three stations for all simulations, with the exception of those using the MYJ PBL scheme at station A. Results at station A showed the least bias across sensitivities while results from station C had the largest bias. This suggests there may be a temperature dependence given the orientation of the stations, with station C being the most northerly. The results from sensitivities using the MYJ PBL scheme consistently had the lowest humidity values for each of the microphysics schemes. The results from sensitivities using the Thompson microphysical scheme had the largest moist bias. The pressure bias was very small at less than 1% for all stations and did not show much of a signal across the different model sensitivities.

Modeled wind speeds at 10 m were compared at stations A, B, and C (Fig. 5). At the wind farm the modeled wind speeds were taken from the layer closest to 80 m, the level used as input to iceBlade. At stations B and C,

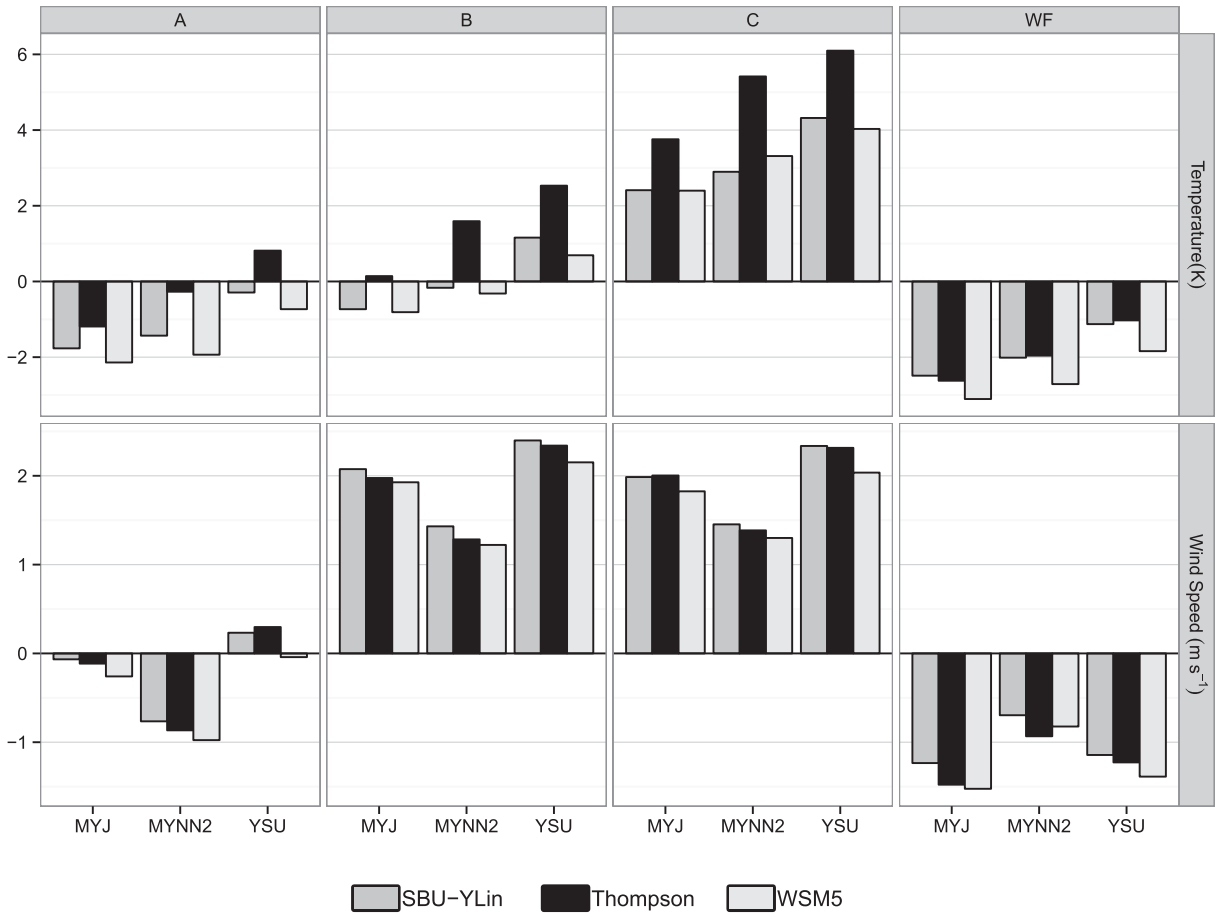

FIG. 5. Mean temperature and wind speed bias for January 2011 at each of the surface stations (A, B, C) and the wind farm (WF) for (top) temperature bias (K) and (bottom) wind speed bias ($m\,s^{-1}$). The two gray shades and black signify the different microphysical schemes, and the results are grouped by the PBL schemes.

the modeled bias was positive across all sensitivities while at the wind farm the bias was always negative. At station A, the results from simulations using the MYNN2 PBL scheme had a negative bias while the other two PBL schemes had a positive bias. The model results were most accurate at station A and at the wind farm, while at stations B and C the bias was over 100%. This is not an uncommon result for 10-m wind speeds, because the observational stations are often impacted by the local characteristics of the station that are not captured by the model. For station A, which is located on a lake, these impacts should be smaller, and at the 80-m height of the turbine there are also fewer impacts of the local surface conditions. The PBL scheme choice had the greatest impact on the 10-m wind speed with the MYNN2 scheme consistently having slower wind speeds than the other two models. Some of these differences can be attributed to the PBL scheme's sensitivity to atmospheric stability (Draxl et al. 2014). The results across the different microphysics schemes had fairly consistent trends with the highest wind speeds occurring in simulations using the SBU-YLin scheme, while the slowest wind speeds were consistently found in results from model simulations using the WSM5 scheme. However, the differences between the microphysics schemes with a common PBL scheme were only a few percent.

Like the wind speeds, the height of the temperature measurements varied between the three meteorological stations and the wind farm. At the wind farm, data were again compared using model data extracted from the layer closest to 80 m while at the meteorological stations the 2-m temperature was taken from the model results. The modeled temperature bias varied the most among the variables studied across both stations and model sensitivities (Fig. 5). The largest biases are found at station C followed by those at the wind farm. Both the choice of PBL scheme and microphysical scheme had a large impact on the model's performance. At the surface stations, the results from simulations using the Thompson scheme were consistently much warmer than the results from simulations using the other microphysical schemes.

However, at the wind farm the results from the SBU-YLin and Thompson simulations were similar while the results from the simulations using the WSM5 scheme were much cooler. The temperature time series at the wind farm showed that the mean cold bias was largely the result of the WRF model dramatically underestimating the temperature during the coldest periods of the study. The opposite was found at station C, where the model was not able to capture the lowest temperatures. This suggests that the temperature gradient between 2 and 80 m may not be accurately represented in the model. However, there is also some uncertainty in the accuracy of the observed temperature from the nacelles, with reported errors of up to 2°C when compared with mast measurements. It is believed this may be in part due to the heating of the local atmosphere around the turbine by the electronics in the nacelle.

The variance of the temperature data was captured fairly well and the results showed good agreement for when the modeled temperature was above 0.5°C, the key threshold for triggering shedding events in the iceBlade model. However, at temperatures just below 0°C there could be a rather large cold bias in the model, which would encourage more ice growth than actually occurred. This was not a significant issue since the majority of accretion periods for both the WRF model and the observed temperature were well below −5°C, and therefore insensitive to the temperature because all incoming particles would have frozen.

The large temperature deviations found at the wind farm are troubling from a forecasting perspective. This did not likely have a large impact on the icing forecast, since the largest deviations occurred when the temperature was below −10°C, which is cold enough to freeze the incoming mass flux for this study. The cold bias may have been important in the partitioning of hydrometeors between the liquid and solid phases in the various microphysics schemes, as well as the creation of clouds due to the reduced capacity of the atmosphere to hold water vapor at lower temperatures.

c. *Icing model comparison*

IceBlade was run using the outputs from all nine WRF sensitivity studies, using seven different distributions of MVD. Except where noted, the analysis focused on the gamma distribution of MVD using an N_c of 250 cm^{-3}. Throughout this section, when a specific scheme or pair of schemes is mentioned, it is in reference to the model results from a simulation using those schemes. The evaluation was performed against the ANY wind farm icing time series. The ANY time series was selected as the key variable for short-term icing forecasts is the total wind farm production.

The periods of icing from the iceBlade model results were compared to the ANY observational dataset using a contingency table method that identified four model states: 1) correct hit, 2) miss, 3) correct nonevent, and 4) false alarm. Figure 6 shows a time series of the occurrence of the contingency table. All sensitivity studies show a majority of correct forecasts. From the number of incorrect forecasts it is evident that the SBU-YLin microphysical scheme and the YSU PBL scheme produce fewer icing events than the other schemes do. The YSU results are likely due to the warmer temperatures produced in that scheme. The most common type of incorrect forecast (miss or false alarm) varies between the different WRF sensitivities, suggesting that the choice of optimal scheme will depend on which incorrect forecast type is more important. For example, the Thompson–MYNN2 results have few missed cases but a large number of false alarm cases. Meanwhile, the SBU-YLin–MYJ results show very few false alarms but many misses.

Figure 7 shows the hit and false alarm rates for each of the sensitivity tests using different values of N_c to calculate the MVD based on the function from Nygaard et al. (2011). Several simulations have hit rates over 0.8 and the Thompson–MYNN2 hit rate is close to 1.0. The high hit rate values correspond to sensitivity tests that produce more icing, as these simulations also have false alarm rates over 0.2. The choice of N_c had little impact on either the hit rate or the false alarm rate. This suggests that the periods of icing were independent of this value despite its impact on the MVD distribution. As MVD was expected to have a large impact on icing accumulation, this result was surprising but can be explained by examining the time series of the ice mass (Fig. 8).

Figure 8 shows the accumulated ice mass over time for all of the monodisperse MVD values and the 250 N_c gamma-distributed MVDs. The ice accumulates at different rates depending on the MVD value, leading to large differences in ice amounts. However, since the ice removal was dominated by shedding events, the difference in ice amount did not translate to the duration of the events. It should be noted that these results may change if the assumed distribution in the microphysical schemes were changed, rather than only imposing the new MVD in the iceBlade model, as this could feed back into the amount of liquid water and types of hydrometeors predicted by the model. This may also explain some of the differences between the Thompson and SBU-YLin schemes, as there was an order of magnitude difference in their N_c values.

For simulations using a monodisperse MVD of 10 μm, the ice growth was minimal, causing events that were

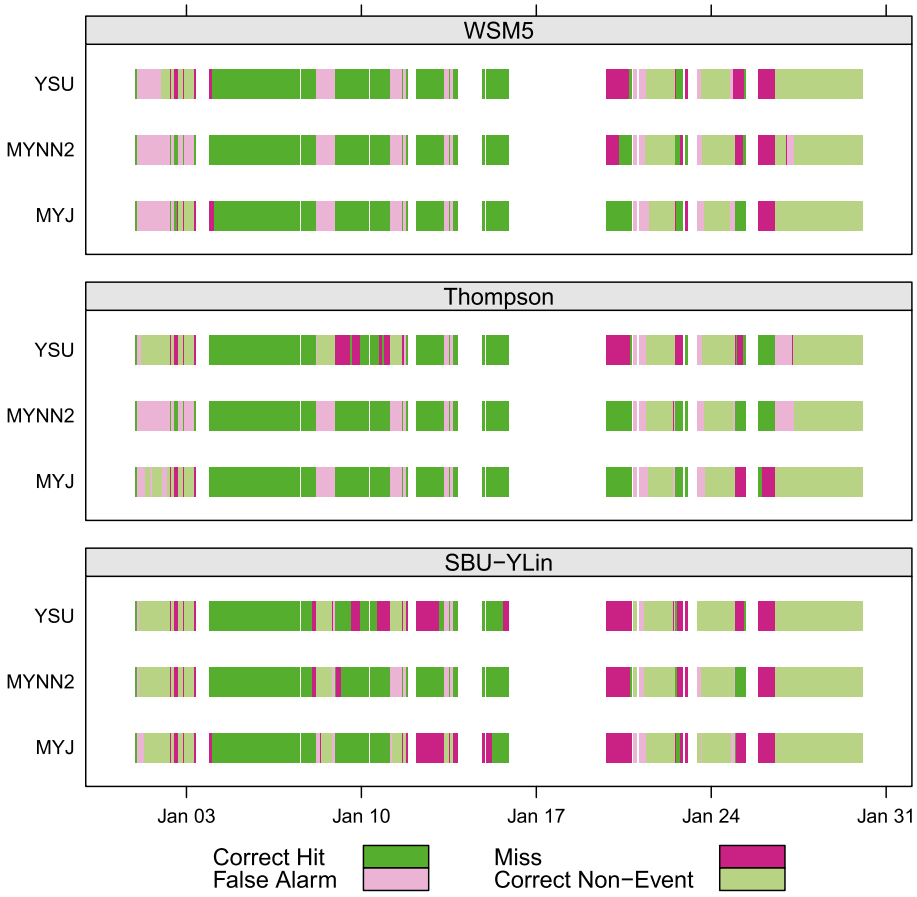

FIG. 6. Comparison of modeled and observed icing periods from the ANY dataset as a function of (top to bottom) microphysics and, within each microphysics scheme, the YSU, MYNN2, and MYJ PBL schemes. The color codes match the entries of a contingency table (not shown); green denotes good predictions, and pink denotes poor predictions. White space denotes either missing or removed data.

shorter in duration than the other MVD values. However, when using larger MVD values the duration of icing is almost identical, despite the large differences in ice mass. For the largest prescribed MVD (25 μm) the ice mass grows to a value almost 3 times larger than in the 15-μm test. The gamma distributed MVD often shows lower ice mass than any but the smallest of the prescribed MVD cases. This result was expected, as the distribution of the gamma-distributed MVD had a peak near 15 μm.

The ice-mass analysis also aids in our understanding of the differences in the icing event time series (Fig. 6). The increased number of missed events in the SBU-YLin simulations was caused by reduced accumulation during active icing periods. The lower ice accumulation led to the removal of ice earlier via the sublimation process; unlike in the other schemes where the ice was only removed by the total shedding events. This led to the large number of misses at the end of the icing events in the SBU-YLin sensitivity tests.

While the choice of microphysical scheme had a significant impact on the model performance, it is particularly interesting to examine the difference between the PBL schemes with the same microphysical schemes. The YSU scheme produced many more missed events, regardless of the microphysical scheme being used, while also generating lower ice masses throughout the period. This was a result of increased sublimation—approximately double that of the other two schemes, caused by the higher temperatures found in the YSU scheme. The temperature difference between the three PBL schemes also had a large impact on the ice accumulation, as the coldest scheme, MYJ, forecast more ice accumulation over the month than either of the other schemes.

To further evaluate the model performance, iceBlade was compared against three other icing duration forecasts. The first was the iceBlade model run on a standard cylinder, which is similar to the approach taken by Byrkjedal (2012a); however, as iceBlade does not

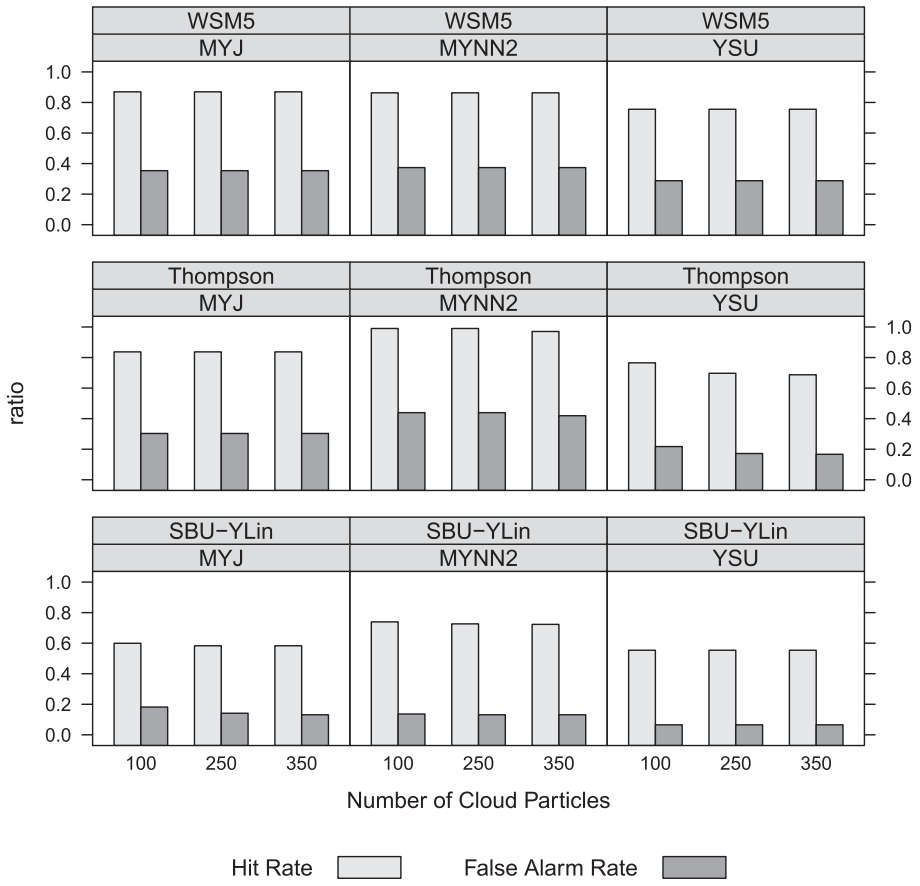

FIG. 7. Sensitivity of the hit and false alarm rates as a function of the N_c parameter used to calculate the MVD for all nine WRF simulations at the grid cell containing the wind farm.

increase the size of the cylinder as the ice grows, it can be assumed that the cylinder results are overestimated when compared with the standard Makkonen model, because the increased cylinder size would reduce the collision efficiency. The second alternative model was a threshold-based model that has been used at Vestas to estimate the periods of icing on turbines for annual energy estimates. The threshold used here forecast icing when the temperature was below 0°C and the sum of the mixing ratios of Q_c and Q_r was above $0.05\,\mathrm{g\,kg^{-1}}$. The final alternative model was the persistence model described in section 2.

To compare the different icing models, several skill scores commonly used in meteorological forecast evaluation (Wilks 2006) were selected: the Heidke skill score (HSS), Kuiper skill score (KSS), threat score (TS), Pierce skill score (PSS), and equitable threat score (ETS). The skill scores present different views of the model's performance: HSS shows the fractional improvement in the proportion of correct forecasts over chance, KSS is the difference between the hit rate and false alarm rate, and PSS is the difference between the miss rate and the false alarm rate. TS and ETS relate the number of hits to the sum of all observations with the exception of correct nonevents, where ETS offsets the tendency of TS to be influenced by the climatology of the event by subtracting the hits expected by chance from both the numerator and the denominator. For all of these scores, 1 is the best possible forecast.

In almost all cases, the results from iceBlade are shown to outperform those from the other models (Fig. 9). The threshold method is shown to perform very poorly in this evaluation, because it does not include a persistence term for leaving ice on the blade after an accretion event. As expected from the results in Byrkjedal (2012a), the standard cylinder does not show much skill in estimating the periods of icing identified by the power production curve. This is largely due to the small amount of ice accretion that occurs on the standard cylinder allowing for rapid ice removal by sublimation. The lower ice accretion on the standard cylinder is most likely due to the large difference between the ambient wind speed and the relative wind speed of the blade. The persistence model performs almost as well as the iceBlade model, as was expected due to the relatively long periods of the icing and no-icing events. During transition seasons or at

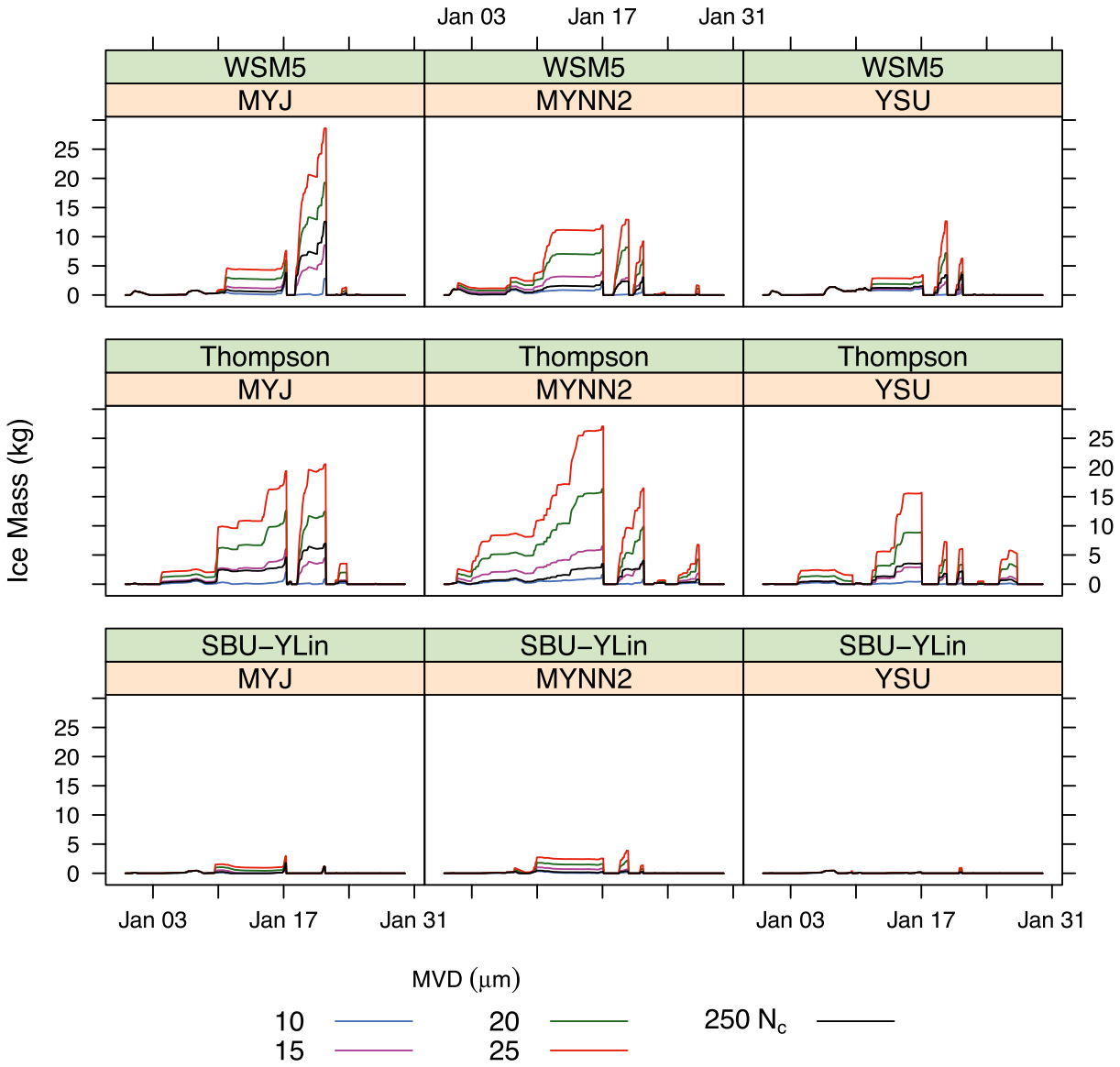

FIG. 8. Time series of total accumulated ice mass (kg) from beginning of the modeling period for each of the nine WRF simulations at the grid cell containing the wind farm. Different colors indicate the various prescribed MVD values. The black line signifies the calculated MVD with an N_c set to 250 cm^{-3}.

a location that experiences shorter icing events, the persistence model would likely not perform as well, while the skill of iceBlade in these conditions is currently unknown. In comparing the different mesoscale model sensitivities, the SBU-YLin microphysical scheme and the YSU PBL scheme both perform worse across simulations compared with the other schemes. The differences between PBL schemes are smaller than those across the microphysical schemes and the Thompson–MYNN2 setup slightly outperforms the other schemes overall; however, either the MYJ or MYNN2 scheme coupled with the Thompson or WSM5 scheme seems to be an appropriate choice for this location.

The precipitation and cloud properties of each model simulation were compared to better understand the differences in icing amounts between the WRF sensitivity studies. The precipitation rate, timing (Fig. 10), and accumulation were similar across all nine simulations. Total monthly precipitation varied by less than 10% of the monthly precipitation total across the nine simulations, with the lowest precipitation values being in the WSM5–YSU and Thompson–MYJ cases. The total precipitation value includes rain, snow, and graupel from both the microphysical and convective schemes; however, for this period the convective precipitation contributed less than 1% of the total precipitation.

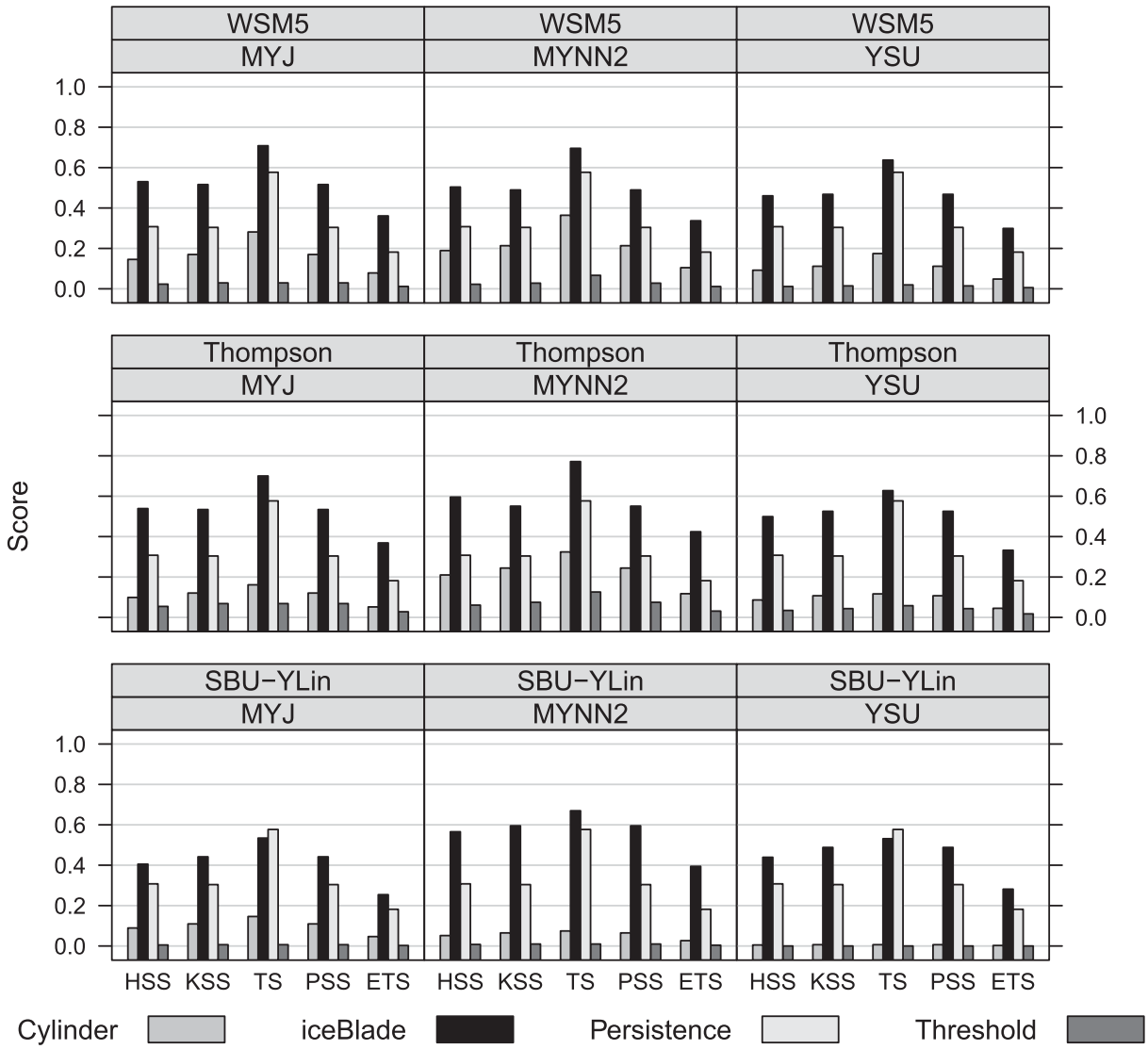

FIG. 9. Model skill scores for iceBlade run on a standard cylinder, iceBlade, a 1-day persistence forecast, and a threshold method for the nine WRF sensitivities at the grid cell containing the wind farm. The skill scores shown are HSS, KSS, TS, PSS, and ETS, calculated using the verification package of the R software.

Given the similar monthly precipitation amounts, selecting the correct physics options for icing is not possible based on precipitation alone. This is due to the icing model relying on the accurate prediction of all clouds, not just precipitating clouds.

Figure 11 shows the total hydrometeor mixing ratio separated into the four relevant hydrometeor types from each of the nine model simulations. The cloud parameters provide a better match to the iceBlade results than was found with the precipitation rates, as SBU-YLin clearly has a smaller total hydrometeor mixing ratio at 80 m. This suggests that the SBU-YLin scheme may precipitate the cloud more rapidly, due to the similar precipitation (Fig. 10) and reduced cloud. The SBU-YLin scheme was found to also have the lowest amount of liquid-phase hydrometeors ($Q_c + Q_r$). Since the iceBlade model only includes liquid hydrometeors, this points directly to the reduction of icing periods in the SBU-YLin sensitivity tests. It is also interesting that the WSM5 microphysical scheme is the only microphysical scheme to produce any significant cloud ice (Q_i) at this height, suggesting either a reduction in Q_c or Q_s compared with the other two schemes. The increased Q_i in the WSM5 scheme suggests that cloud ice is more readily formed at warmer temperatures in the WSM5 scheme, and that Q_i is slower to accumulate to the snow phase and form Q_s. The Thompson scheme shows less Q_r than do either of the other two schemes but much larger Q_c amounts. This balance between the Q_c and Q_r hydrometeor classes could explain the similarities between the

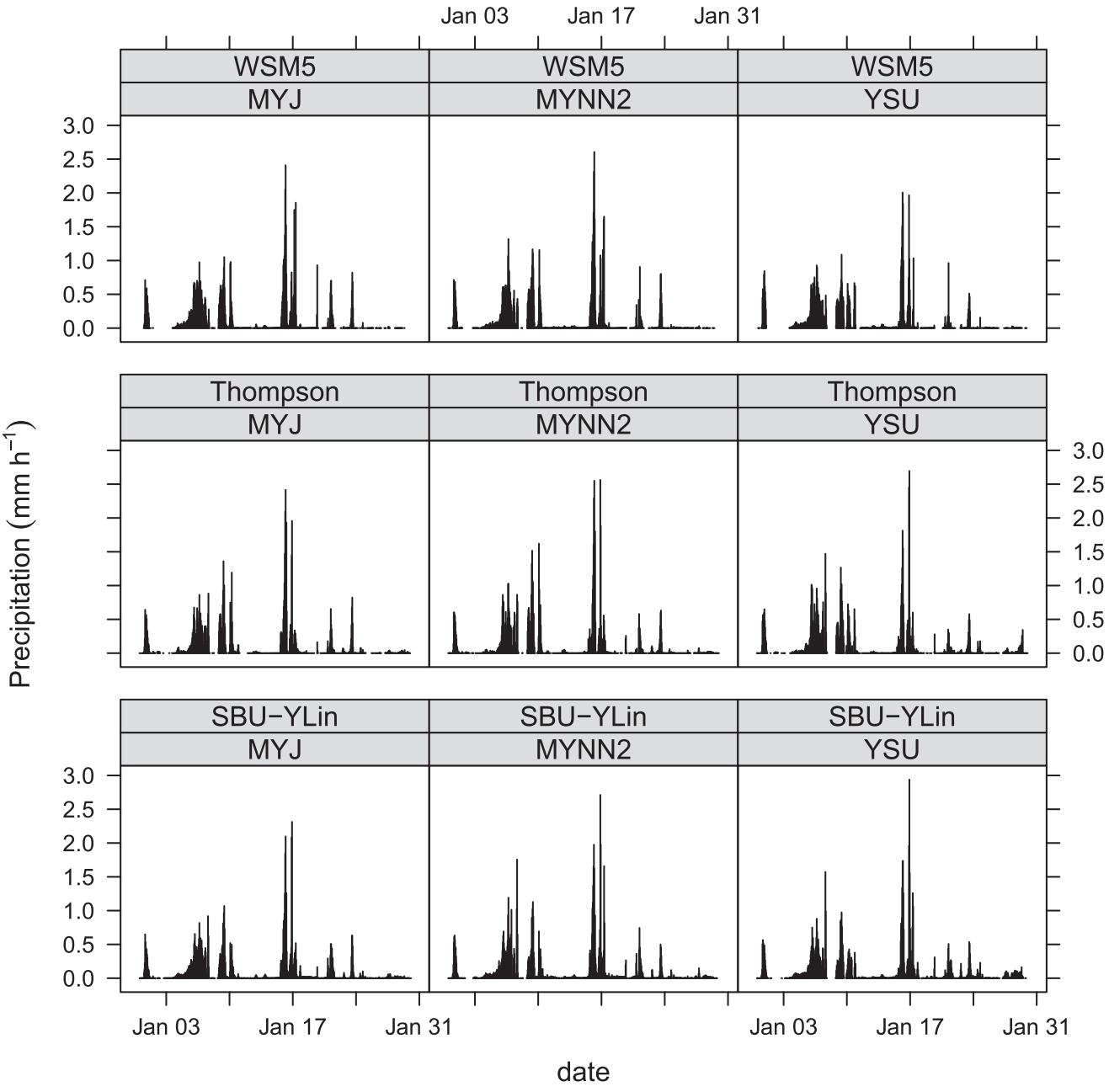

FIG. 10. Time series of total hourly precipitation rate (mm h^{-1}) from each of the nine WRF simulations at the grid cell containing the wind farm.

icing forecasts of the WSM5- and Thompson-driven sensitivities, due to the high collision efficiency of Q_r. The reduced precipitation and Q_r in the Thompson scheme could also be due to the higher N_c parameter relative to the SBU-YLin scheme, which would lead to smaller cloud droplets, as the larger cloud water droplets in the SBU-YLin scheme should more rapidly convert to precipitation.

This study did not focus on forecasting the atmospheric conditions, but instead was run using a hindcast approach to determine if the method of coupling iceBlade to WRF was feasible at this station. The performance in a forecasting mode is somewhat uncertain, as the additional uncertainties in the meteorological data, due to uncertainties in the input conditions, would suggest a decrease in model performance. However, as energy forecasts are typically produced only for 1–2 days into the future, the results may also be improved. Additionally, this station was located in relatively flat terrain, allowing for a coarser resolution to provide reasonable cloud parameters. It is expected that in areas with increased topographical complexity, the model resolution will become more important for determining the correct timing and magnitude of cloud events.

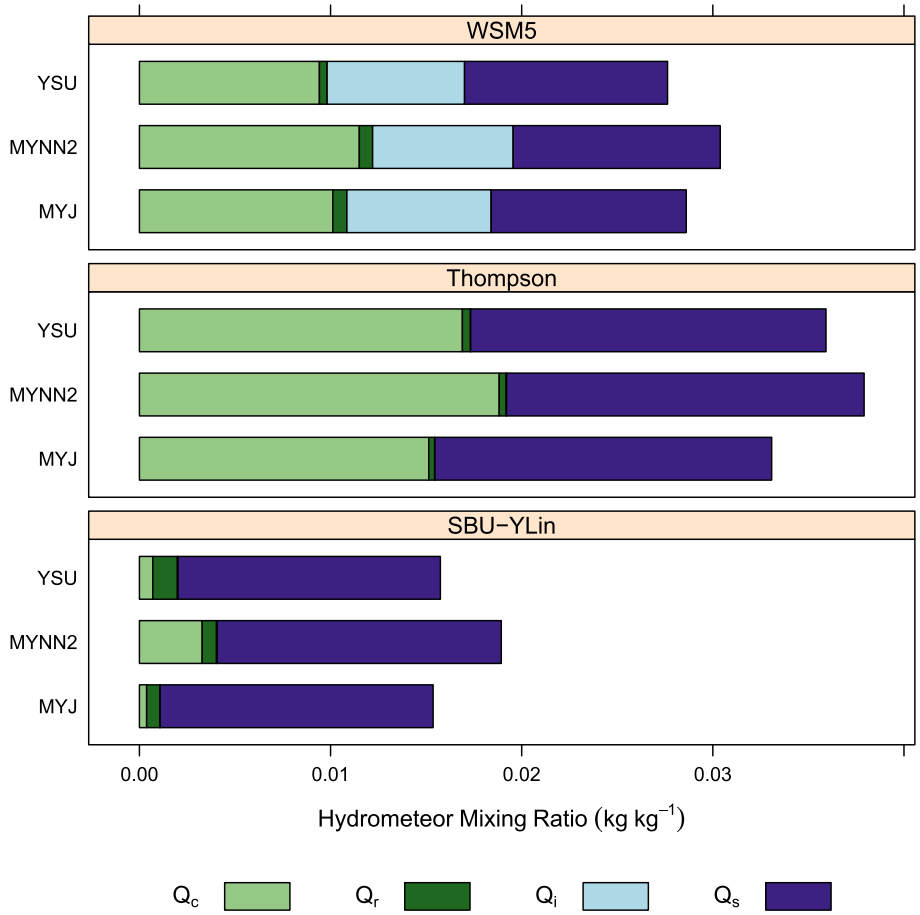

FIG. 11. Monthly sum of cloud mixing ratio (kg kg^{-1}) by hydrometeor type for each of the nine WRF simulations at the grid cell containing the wind farm at 80 m AGL. The darker colors identify larger hydrometeors (rain and snow). The hydrometeors from WRF are cloud droplets (Q_c), rain (Q_r), ice (Q_i), and snow (Q_s).

5. Conclusions

This study has shown that iceBlade, driven by outputs from the WRF model, can provide improved forecasts of icing on a wind turbine blade compared to a persistence model, a threshold-based method, and a standard cylinder model. The observed icing dataset, created using a relationship between the observed and idealized power output and the observed nacelle temperature, allowed for the evaluation to focus on icing that impacted the turbine performance. The comparison with the cylinder approach demonstrated that the increased effective wind speed of a rotating turbine blade contributes greatly to the icing duration and improves model performance.

The choice of microphysical and PBL schemes in the WRF model were found to have a large impact on the estimated ice mass, and a smaller but still significant impact on icing duration, even when the models largely agree on the forecast precipitation. Therefore, an evaluation of precipitation is unlikely to be meaningful when selecting the model schemes for an icing forecast. This was due to the importance of the accurate forecast of both the amount and partitioning of hydrometeors in the microphysical schemes, rather than the precipitation rate. For the PBL schemes, the temperature difference was the main cause of variations in icing forecasts. In addition to the atmospheric model physics themselves, the ice-mass forecast by iceBlade was shown to be very sensitive to the MVD distribution used for Q_c. It seems the approach used by Nygaard et al. (2011) performed well for this study and would continue to be a good starting point for future studies for all three of the microphysical schemes presented here.

The results suggest that the iceBlade model is capable of providing short-term icing forecasts at this location that could aid in day-to-day decision making, such as pricing on the energy market or when to enable deicing or anti-icing systems. Given a long enough meteorological simulation, the iceBlade model has the potential to be used for developing icing climatologies, which

would aid the wind energy industry in the key areas of site selection, maintenance planning, cost–benefit analysis, and deployment of deicing and anti-icing systems.

Acknowledgments. This work was supported financially by the Top-Level Research Initiative (TFI) project, Improved Forecast of Wind, Waves and Icing (IceWind), Vestas Wind Systems A/S, and the Nordic Energy Industry. The atmospheric data for input and boundary conditions for this study are available from the Research Data Archive (RDA), which is maintained by the Computational and Information Systems Laboratory (CISL) at the National Center for Atmospheric Research (NCAR). NCAR is sponsored by the National Science Foundation (NSF). The original data are available from the RDA (http://dss.ucar.edu) in dataset ds083.2. The authors thank Greg Thompson and the anonymous reviewers of this manuscript for their valuable comments and suggestions that greatly improved the quality of this contribution.

REFERENCES

Antoniou, I., S. M. Pedersen, and P. B. Enevoldsen, 2009: Wind shear and uncertainties in power curve measurement and wind resources. *Wind Eng.,* **33,** 449–468.

Barber, S., Y. Wang, S. Jafari, N. Chokani, and R. S. Abhari, 2011: The impact of ice formation on wind turbine performance and aerodynamics. *J. Sol. Energy Eng.,* **133,** 011007, doi:10.1115/1.4003187.

Bernstein, B. C., J. Hirvonen, E. Gregow, and I. Wittmeyer, 2012: Experiences from real-time LAPS-LOWICE runs over Sweden: 2011–2012 icing season. *Winterwind Int. Wind Energy Conf.,* Skellefteå, Sweden, Swedish Wind Power Association. [Available online at http://www.slideshare.net/WinterwindConference/3a-bernstein-lapslowice.]

Bragg, M., A. Broeren, and L. Blumenthal, 2005: Iced-airfoil aerodynamics. *Prog. Aerosp. Sci.,* **41,** 323–362.

Byrkjedal, O., 2012a: Mapping of icing in Sweden—On the influence from icing on wind energy production. *Winterwind Int. Wind Energy Conf.,* Skellefteå, Sweden, Swedish Wind Power Association. [Available online at http://www.slideshare.net/WinterwindConference/3a-byrkjedal-icingkvt.]

——, 2012b: The benefits of forecasting icing on wind energy production. *Winterwind Int. Wind Energy Conf.,* Skellefteå, Sweden, Swedish Wind Power Association. [Available online at http://www.slideshare.net/WinterwindConference/3-forecast-kvt.]

Cattin, R., S. Kunz, A. Heimo, G. Russi, M. Russi, and M. Tiefgraber, 2007: Wind turbine ice throw studies in the Swiss Alps. *European Wind Energy Conf.,* Vol. 1, Milan, Italy, European Wind Energy Association, 3–7.

Chen, F., and J. Dudhia, 2001: Coupling an advanced land surface–hydrology model with the Penn State–NCAR MM5 modeling system. Part II: Preliminary model validation. *Mon. Wea. Rev.,* **129,** 587–604.

Dierer, S., R. Oechslin, and R. Cattin, 2011: Wind turbines in icing conditions: Performance and prediction. *Adv. Sci. Res.,* **6,** 245–250.

Draxl, C., A. N. Hahmann, A. Peña, and G. Giebel, 2014: Evaluating winds and vertical wind shear from Weather Research and Forecasting model forecasts using seven planetary boundary layer schemes. *Wind Energy,* **17,** 39–55.

Dudhia, J., 1989: Numerical study of convection observed during the Winter Monsoon Experiment using a mesoscale two-dimensional model. *J. Atmos. Sci.,* **46,** 3077–3107.

Farzaneh, M., Ed., 2008: *Atmospheric Icing of Power Networks.* Springer, 381 pp.

Fikke, S., and Coauthors, 2006: COST 727: Atmospheric icing on structures measurements and data collection on icing: State of the art. MeteoSwiss Tech. Rep. 75, 110 pp.

——, J. E. Kristjánsson, and B. E. K. Nygaard, 2008: Modern meteorology and atmospheric icing. *Atmospheric Icing of Power Networks,* M. Farzaneh, Ed., Springer, 1–29.

Finstad, K. J., E. P. Lozowski, and E. M. Gates, 1988: A computational investigation of water droplet trajectories. *J. Atmos. Oceanic Technol.,* **5,** 160–170.

Gent, R. W., N. P. Dart, and J. T. Cansdale, 2000: Aircraft icing. *Philos. Trans. Roy. Soc.,* **358A,** 2873–2911.

Hau, E., 2013: Wind turbine economics. *Wind Turbines: Fundamentals, Technologies, Application, Economics,* 3rd, translated ed., Springer, 845–870.

Homola, M. C., T. Wallenius, L. Makkonen, P. J. Nicklasson, and P. A. Sundsbø, 2010a: The relationship between chord length and rime icing on wind turbines. *Wind Energy,* **13,** 627–632.

——, ——, ——, ——, and ——, 2010b: Turbine size and temperature dependence of icing on wind turbine blades. *Wind Eng.,* **34,** 615–627.

——, M. S. Virk, P. J. Nicklasson, and P. A. Sundsbø, 2012: Performance losses due to ice accretion for a 5 MW wind turbine. *Wind Energy,* **15,** 379–389.

Hong, S.-Y., J. Dudhia, and S.-H. Chen, 2004: A revised approach to ice microphysical processes for the bulk parameterization of clouds and precipitation. *Mon. Wea. Rev.,* **132,** 103–120.

——, Y. Noh, and J. Dudhia, 2006: A new vertical diffusion package with an explicit treatment of entrainment processes. *Mon. Wea. Rev.,* **134,** 2318–2341.

Janjić, Z. I., 1994: The step-mountain eta coordinate model: Further developments of the convection, viscous sublayer, and turbulence closure schemes. *Mon. Wea. Rev.,* **122,** 927–945.

Jonkman, J., S. Butterfield, W. Musial, and G. Scott, 2009: Definition of a 5-MW reference wind turbine for offshore system development. National Renewable Energy Laboratory Tech. Rep. NREL/TP-500-38060, 75 pp. [Available online at mhk.pnnl.gov/wiki/images/b/bb/Jonkman_et_al_2009.pdf.]

Kain, J. S., 2004: The Kain–Fritsch convective parameterization: An update. *J. Appl. Meteor.,* **43,** 170–181.

Langmuir, I., and K. Blodgett, 1961: A mathematical investigation of water droplet trajectories. *Collected Works of Irving Langmuir,* Vol. 10, C. G. Suits, Ed., Pergamon Press, 10, 348–393.

Lin, Y., and B. A. Colle, 2011: A new bulk microphysical scheme that includes riming intensity and temperature-dependent ice characteristics. *Mon. Wea. Rev.,* **139,** 1013–1035.

Makkonen, L., 2000: Models for the growth of rime, glaze, icicles and wet snow on structures. *Philos. Trans. Roy. Soc.,* **358A,** 2913–2939.

——, T. Laakso, M. Marjaniemi, and K. J. Finstad, 2001: Modelling and prevention of ice accretion on wind turbines. *Wind Eng.,* **25,** 3–21.

Mlawer, E. J., S. J. Taubman, P. D. Brown, M. J. Iacono, and S. a. Clough, 1997: Radiative transfer for inhomogeneous atmospheres: RRTM, a validated correlated-*k* model for the longwave. *J. Geophys. Res.,* **102** (D14), 16 663–16 682.

Nakanishi, M., and H. Niino, 2006: An improved Mellor-Yamada level-3 model: Its numerical stability and application to a regional prediction of advection fog. *Bound.-Layer Meteor.,* **119,** 397–407.

Nygaard, B. E. K., J. E. Kristjánsson, and L. Makkonen, 2011: Prediction of in-cloud icing conditions at ground level using the WRF model. *J. Appl. Meteor. Climatol.,* **50,** 2445–2459.

Pruppacher, H. R., and J. D. Klett, 2004: *Microphysics of Clouds and Precipitation.* 2nd ed. Kluwer Academic, 975 pp.

Reynolds, R. W., T. M. Smith, C. Liu, D. B. Chelton, K. S. Casey, and M. G. Schlax, 2007: Daily high-resolution-blended analyses for sea surface temperature. *J. Climate,* **20,** 5473–5496.

Ronsten, G., and Coauthors, 2012: State-of-the-art of wind energy in cold climates. IEA Wind Task 19, 67 pp. [Available online at http://arcticwind.vtt.fi/reports/Task19_SotA_WEinCC_2012_approved.pdf.]

Seifert, H., A. Westerhellweg, and J. Kröning, 2003: Risk analysis of ice throw from wind turbines. *Boreas VI,* Pyhä, Finland, Finnish Meteorological Institute, 18 pp. [Available online at http://s3.amazonaws.com/windaction/attachments/999/RiskAnalysisofIceThrow-SeifertPapers.pdf.]

Sherif, S., N. Pasumarthi, and C. Bartlett, 1997: A semi-empirical model for heat transfer and ice accretion on aircraft wings in supercooled clouds. *Cold Reg. Sci. Technol.,* **26,** 165–179.

Skamarock, W. C., and Coauthors, 2008: A description of the Advanced Research WRF version 3. NCAR Tech. Note NCAR/TN–475+STR, 113 pp. [Available online at www.mmm.ucar.edu/wrf/users/docs/arw_v3.pdf.]

Soderberg, S., and M. Baltscheffsky, 2012: Long-term estimates and variability of production losses in icing climates. *Winterwind Int. Wind Energy Conf.,* Skellefteå, Sweden, Swedish Wind Power Association. [Available online at http://www.slideshare.net/WinterwindConference/longterm-estimates-and-variability-of-production-losses-in-icing-climates-stefan-sderberg-magnus-baltscheffsky-weathertech-scandinavia.]

Srivastava, R. C., and J. L. Coen, 1992: New explicit equations for the accurate calculation of the growth and evaporation of hydrometeors by the diffusion of water vapor. *J. Atmos. Sci.,* **49,** 1643–1651.

Thompson, G., R. T. Bruintjes, B. G. Brown, and F. Hage, 1997: Intercomparison of in-flight icing algorithms. Part I: WISP94 Real-Time Icing Prediction and Evaluation Program. *Wea. Forecasting,* **12,** 878–889.

——, P. R. Field, R. M. Rasmussen, and W. D. Hall, 2008: Explicit forecasts of winter precipitation using an improved bulk microphysics scheme. Part II: Implementation of a new snow parameterization. *Mon. Wea. Rev.,* **136,** 5095–5115.

Troen, I., and E. Petersen, 1989: *European Wind Atlas.* Risø National Laboratory, Roskilde, Denmark, 656 pp.

Virk, M. S., M. C. Homola, and P. J. Nicklasson, 2010: Relation between angle of attack and atmospheric ice accretion on large wind turbine's blade. *Wind Eng.,* **34,** 607–613.

——, ——, and ——, 2012: Atmospheric icing on large wind turbine blades. *Int. J. Energy Environ.,* **3,** 1–8.

Wilks, D. S., 2006: *Statistical Methods in the Atmospheric Science.* 2nd ed. Academic Press, 627 pp.

Wolff, C., F. McDonough, M. Politovich, and G. Cunning, 2009: Forecast icing product: Recent upgrades and improvements. *First AIAA Atmospheric and Space Environments Conf.,* San Antonio, Texas, American Institute of Aeronautics and Astronautics, Paper AIAA 2009-3531.

Yang, J., 2012: Simulation of icing events over Gaspé region. *Winterwind Int. Wind Energy Conf.,* Skellefteå, Sweden, Swedish Wind Power Association. [Available online at http://www.slideshare.net/WinterwindConference/3a-jing-yang.]

Appendix C

Production Loss Model Due To Wind Turbine Blade Icing

WIND ENERGY

Wind Energ. 0000; **00**:1–22

DOI: 10.1002/we

RESEARCH ARTICLE

An investigation of the impact of turbine icing on wind farm production

Neil N. Davis[1], Pierre Pinson[2], Andrea N. Hahmann[1], Niels-Erik Clausen[1], Mark Žagar[3]

<[1]DTU Wind Energy, Roskilde, DK [2]DTU Electro, Lyngby, DK [3]Vestas, Aarhus, DK>

ABSTRACT

Wind park power production in cold climate regions is significantly impacted by ice growth on turbine blades. This can lead to significant errors in power forecasts and estimations of expected power production during turbine siting. A modeling system is presented that uses a statistical modeling approach to estimate the power loss due to icing, using inputs from both a physical icing model driven and a numerical weather prediction model. A new approach for identifying iced power observations was used to calculate the observed power loss caused by icing. Production estimates using the final production loss model reduce the RMSE when compared with the empirical wind park power curve (without icing influence) at five of six wind parks and while reducing the mean bias at all six wind parks. In addition to performing well when fit to each wind park, the production loss model was shown to improve the estimate of power when fit using all six wind parks, suggesting it may also be useful for wind parks where production data is not provided.

KEYWORDS

<icing; production>

Correspondence

<Neil Davis, DTU Wind Energy, Roskilde, DK>. E-mail: <neda@dtu.dk>

Contract/grant sponsor

<TFI IceWind>

Contract/grant number

<1111>

Received . . .

1. INTRODUCTION

Production loss due to icing is one of the main challenges for expanding wind energy in cold climate regions. The BTM World Market Update 2012 included a chapter on cold climate turbines[1], where it was estimated that 24% of the currently installed turbine capacity is located in cold climate regions. Heavy icing regions, where icing is expected to have a major impact on annual energy production, contain 4% of installed turbines world-wide. The wind-based electricity production in moderate to heavy icing regions is expected to grow from 11.5 GW at the end of 2012 to 19.5 GW by 2017. Therefore, accurate estimates of icing production loss are needed both for the proper siting of these new wind farms, and to provide more accurate production forecasts for power system operation and electricity markets. Improved production forecasts in turn provide better returns to developers (due to lower regulation costs in electricity markets), while better supporting power system operators in their various tasks [2].

Before modeling icing related power loss, one first has to determine whether the power loss is due to icing or other factors. Homola et al. [3] provided a comprehensive review of ice sensors for wind turbines. These included direct sensors placed on a nearby mast or the turbine nacelle and indirect sensors such as web-cam images. They concluded that ice measured using direct sensors did not match the periods of decreased power production. The use of web-cam imagery was the best approach, however available light was a limiting factor.

For the sites in this study, web-cam imagery was not available, thus an indirect and data-driven approach for identifying icing, based on a deviation from the turbines empirical power curve was developed. Relying on power measurements for identifying icing is reasonable for studies where the impact of icing on power is required. However, if ice detection is required for other purposes, such as the safety of maintenance personnel, other approaches may be more appropriate.

To capture the impact of icing on power loss, a physical ice model is needed to estimate the amount of ice on the turbine blades. The ice model needs to simulate both ice growth and ice ablation processes. Atmospheric ice growth occurs when atmospheric water in any phase sticks to and freezes on an exposed structure [4]. Ice ablation refers to the removal of ice by any method. Common ice ablation methods are melting, sublimation, shedding, and erosion. Melting is a phase change process where ice converts to liquid water, and occurs when the ambient temperature is above 0°C. Under sublimation ice is converted straight to water vapor and depends on the humidity of the atmosphere. Ice shedding occurs when large pieces of ice fall off or are thrown from a structure, while erosion occurs due to the abrasive force of the wind removing small pieces of ice. This is the same method that erodes soil and rocks over time [5, 6].

The iceBlade model, described by Davis et al. [7], was used as the icing model for the current study. It includes a modified version of the Makkonen model [8] for growth of atmospheric ice on rotating cylinders. The modifications make it more applicable for wind turbine icing. They include an adjustment of the incoming wind speed based on the rotational speed of the turbine, a heat transfer coefficient for airfoils, and a static cylinder diameter. The iceBlade model includes methods for sublimation and total shedding of ice, and was improved in this study through the addition of a term for wind erosion.

Wind Energ. 0000; **00**:1–22 © 0000 John Wiley & Sons, Ltd.
DOI: 10.1002/we
Prepared using weauth.cls

Statistical approaches are generally preferred for estimating icing related power loss, due to the computational expense of physical approaches. The corresponding models typically belong to two different approaches. The first approach is to create a three-dimensional power curve, where power output is modeled as a continuous function of both wind speed and accumulated ice mass, e.g., [9]. Alternatively, Karlsson et al. [10] presented a three-dimensional power curve that used ice duration rather than accumulated ice mass. The second approach employs statistical techniques to combine multiple fields from icing and meteorological models into a production estimate. For example, Baltsheffsky [11] designed a neural network to obtain production estimates that accounted for the impact of icing, using as input, results from an icing model similar to iceBlade, as well as more common numerical weather prediction (NWP) model outputs. Davis et al. [12] fit a linear regression model using several output variables from both iceBlade and an NWP model, demonstrating that the mean bias (MB) and root mean squared error (RMSE) of production estimates could be reduced by including terms important to the icing process. The present study builds on a similar approach through the use of a generalized additive model (GAM) [13, 14]. The flexibility of the GAM allows models to be fit without relying on possibly rigid parametric restrictions. Since the relationship between icing parameters (e.g. ice mass, duration, and density) and turbine production is unknown, the replacement of the linear model used in [12] with a GAM is a logical next step.

This study will also explore the possibility to obtain a general model for estimating icing related production losses by fitting two models to the wind park power loss. The first will include only data from the wind park being modeled, while the general fit will use data from all six wind parks. This latter strategy would eventually allow for the application of the general model to new and existing wind farms where the necessary data for local estimation may not be available. The remainder of the paper is laid out as follows. Section 2 describes the observational datasets available for this study, as well as the data preprocessing. Subsequently, Section 3 presents both the meteorological and revisited iceBlade models, as well as a detailed description of the proposed statistical approach to the modeling of icing-related power loss. Section 4 gathers the results from our empirical investigation, while Section 5 contains the discussion and a set of concluding remarks.

2. INDIRECT ICING IDENTIFICATION IN AVAILABLE DATA

2.1. Datasets

Observations were collected from a subset of turbines at six wind parks in Scandinavia. For confidentiality reasons, the parks are anonymized and the power production was normalized by the rated power. All parks were equipped with Vestas V90 turbines and had reduced production during the winter that was likely caused by icing. This dataset is a subset of a larger dataset being used for an inter-comparison study as part of the Icewind project [15], and was selected to ensure uniformity across the turbine type. The parks are identified with capital letters relating to the full Icewind dataset. The data covers two winter seasons from June 2010 until July 2012 and includes 10-minute records of nacelle-measured temperature and wind speed, power output of the turbine, and several quality assurance (QA) flags from the SCADA system. The QA flags were used to remove data when the turbine was not in normal operation. This was typically due to winds below the

DOI: 10.1002/we
Prepared using weauth.cls

cut-in speed of the turbine or when the turbine was placed in a derated state. Additional data was removed for wind speeds below 5.5 $\mathrm{m\,s^{-1}}$ because there was a large deviation in power production at lower wind speeds during non-icing periods. There should be minimal impact on the production loss estimates due to their removal, as the power output is small at low wind speed.

2.2. Inferring icing events

The observational dataset did not include a direct measure of icing, therefore, observed icing periods had to be empirically determined. A common approach for identifying icing is by finding power and wind speed observations at cold temperatures with a significant deviation from the manufacturer's power curve ($\mathrm{PC_m}$). These points are commonly identified using a flat 20% deviation. However, this approach likely identifies too few of the icing values at higher wind speeds. The percentile deviation suggests that there is a larger variability in power at higher wind speeds, but the data shows the opposite. At wind speeds above the rated wind speed, the turbine's control system uses the surplus energy to reduce the variance in power output leading to lower variability. In a previous study [7], a simple curve was fit to transition from a 20% deviation below rated power to a 2% deviation above rated power. However, when this curve was applied to the parks in this study only a few turbines data matched the curve. Therefore, a more statistically robust approach was developed for identifying icing using the standard deviation of the observed power.

An ice threshold curve ($\mathrm{PC_i}$) was defined as a curve that separates iced points from non-iced points when the temperature was below 0°C. $\mathrm{PC_i}$ was based on the empirical power curve ($\mathrm{PC_e}$) and standard deviation curve of each turbine. $\mathrm{PC_e}$ was used rather than $\mathrm{PC_m}$ to account for the local conditions at each turbine, since these effects were found to be significant for several turbines.

$\mathrm{PC_e}$ was fit for each turbine using a GAM with the formula

$$p = s(v), \tag{1}$$

where p is the observed power and $s(v)$ is a smooth function of the wind speed (v). The smooth function was built as a linear combination of thin plate splines of v. To ensure the data used in the fitting process did not include iced points, only points with a temperature above 5°C were used. The R package *mgcv* [16, 17] was used for fitting the GAM and the k-dimension was set to 20. This k-dimension controls the maximum degrees of freedom in the model. It was determined by fitting several GAM models and visually comparing the fit to the cloud of observed power for temperatures above 5°C.

The variance of power at different wind speeds was found by calculating the standard deviation of power for each 0.1 $\mathrm{m\,s^{-1}}$ bin of wind speed. The standard deviations were then smoothed using a LOESS smoother [18] with a span of 0.4. The smoothing removed outliers where there were fewer points, providing a more representative curve of the variance. $\mathrm{PC_i}$ was calculated by:

$$PC_i = PC_e - 2\sigma_s, \tag{2}$$

DOI: 10.1002/we
Prepared using weauth.cls

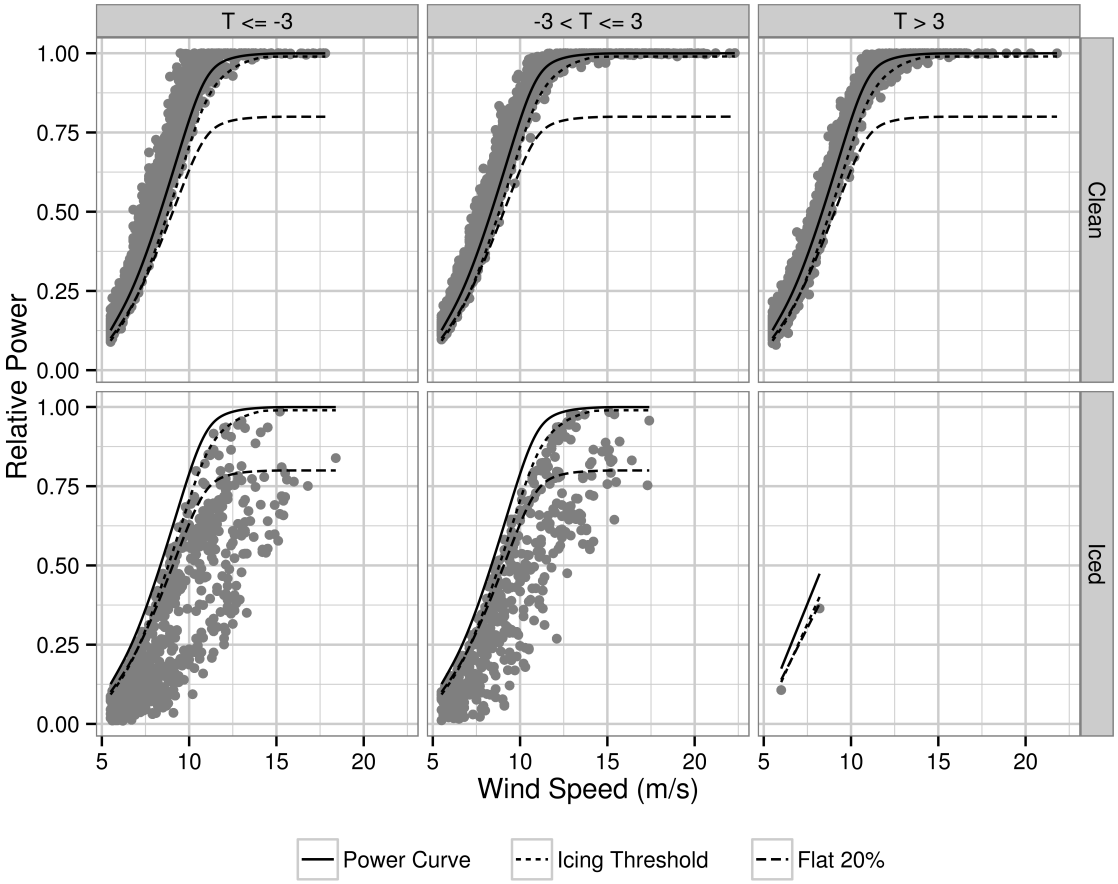

Figure 1. Observed and empirical power curves (PC_e) for a single turbine. The columns identify different temperature bins, while the rows separate points identified as clean or iced. The solid line is the empirical power curve for points with temperature above 5°C, Flat 20% (Long dashed) is a 20% deviation from the PC, and Icing Threshold (PC_i; short dashed) is the threshold derived from the standard deviation based approach.

where σ_s is the smoothed standard deviation at a given wind speed. At some points above rated power σ_s was 0, for these points PC_i was set to 1% of PC_e.

Figure 1 shows the observed, empirical, and ice threshold power curves for one of the turbines in the dataset. The top-right plot approximates the reference data for non-iced turbine production. This plot shows that the standard deviation based method captures the shape of PC_e better than the 20% threshold.

PC_i was used to identify icing points with a temperature threshold of 3°C. The ending time of icing was adjusted to include points removed during the QA process and points that were not considered icing due to the temperature threshold. This limited the end of an icing event to the point when the power returned above PC_i. A final criteria to the ice detection algorithm was added that required an icing event to have a minimum duration of 30 minutes (three consecutive data points). As seen in the top row of Figure 1, there are several points in all temperature bins that are above PC_i, due to this requirement. From the iced point plots (bottom row), it could be seen that the new approach identifies many icing points

DOI: 10.1002/we

above 10 $\mathrm{m\,s^{-1}}$ that would not be captured by the flat 20% deviation. As no direct measurement of icing was available, a more robust evaluation of these two approaches was not possible.

After the QA and icing detection were carried out using 10-minute values, the data was aggregated into park averaged values at the top of the hour (minutes equal to 0) to match the output of the meteorological model (see Section 3.1). Park averaging was performed differently for the continuous variables, the QA flag, and the icing flag. For the continuous variables (temperature, power, and wind speed), the arithmetic mean of all non-QA turbines in the park was used. The park's QA state was determined based on a threshold of 50% of the turbines being in a QA state, while park icing was identified if two or more of the turbines were determined to be iced. An empirical power curve for the entire wind park ($\mathrm{PC_{park}}$) was fit using Eq. (1).

3. DESCRIPTION OF THE METEOROLOGICAL AND STATISTICAL MODELS

3.1. Meteorological model

The meteorological model fields are from a global modeling study carried out at Vestas Wind Energy Systems. The study was undertaken to aid in understanding the long term wind climatology at specific locations. The meteorological variables targeted in the setup were wind speed, wind direction, temperature, and density. However, the entire model output was archived allowing for this dataset to be utilized for ice related studies as well.

The Weather Research and Forecasting (WRF) model [19] was run at a 3 km grid resolution with 62 vertical levels, 17 of which were located within the lowest 1 km of the surface. The input and boundary conditions were from the Global Forecast System (GFS) analysis [20], and the boundary conditions were updated every 6 hours. The physical parameterizations used were the WRF single moment 5-class microphysics scheme [21], rapid radiative transfer model for longwave radiation [22], Dudhia shortwave radiation scheme [23], Eta Similarity surface layer physics, Noah Land Surface Model [24], MYJ Planetary Boundary Layer (PBL) scheme [25], and Kain Fritsch cumulus scheme [26].

The following outputs from WRF were provided from a grid cell near the center of each of the wind parks for the following surface variables: terrain height, surface shortwave and longwave radiation, and non-convective precipitation. Four-dimensional data was provided for wind speed, temperature, pressure, water vapor mixing ratio, and four mixing ratios representing different cloud parameters (hydrometers) produced in the model microphysics (cloud water, rain, ice, and snow). The four-dimensional variables were interpolated from the model levels to heights of 40m, 80m, 120m, 160m and 200m above the model topography.

3.2. Icing model

The icing model used in this study is the iceBlade model described in [7] with a few modifications. The original version of the iceBlade model represents the turbine blade as a 1-m long cylinder with a 0.144 m radius, based on a NACA64_A17 airfoil with a chord length of 3.0 m. The airfoil geometry was taken from the NREL 5 MW offshore wind turbine [27].

DOI: 10.1002/we
Prepared using weauth.cls

The inflow wind speed for the iceBlade model is based on the turbines RPM at a distance of 85% of the blade length. The meteorological conditions remain constant for the entire hour between the meteorological model output times. Ice is modeled to form straight out from the leading edge, retaining a constant diameter. Ice ablation occurs through sublimation and shedding algorithms. The shedding algorithm removes all ice from the blade when the temperature reaches 0°C. The low threshold temperature is in part a result of the underestimation of temperature, commonly called a cold bias, in the WRF model shown in Section 4. The iceBlade model was driven using only the 80-m WRF results after an analysis showed minimal differences when other vertical levels are used (not shown). This original version of the iceBlade model was modified in two ways for the current study.

The initial simulations for the parks in this study using iceBlade showed that the length of the icing periods were largely underestimated. A previous study [7] found that the combination of WSM5 microphysics and the MYJ PBL scheme produced large amounts of cloud ice compared to other setups. Based on these results, cloud ice was added to cloud water before calculating the liquid water mixing ratio. This improved the model results for the icing periods and should better match the actual cloud composition.

The second adjustment to the iceBlade model was to the speed of ice ablation. The dominant ice removal method in iceBlade, at temperatures below 0°C, is the sublimation of ice. At these temperatures sublimation is a relatively slow process as the saturation vapor pressure is low. The higher the saturation vapor pressure, the faster ice can sublimate. The observed power production data suggested that ice ablated quickly from the turbine blades, even during periods where the temperature was well below 0°C, suggesting that that the ice was ablating quickly. We believe this is due to the wind erosion of ice on the blade. A literature review did not uncover any studies of wind erosion specific to ice on structures. The likely mechanisms of wind erosion are the force of the wind passing over the rough surface of the ice, and relatively high velocity aerosol particles impacting the ice, which also relates to the force of the wind [5]. Therefore, the wind kinetic energy was chosen as the main input to the wind erosion term. A range of values were tested and the model performance was evaluated using the equitable threat score (ETS), false alarm rate, and miss rate [28]. The optimal fit for this data set was found to be

$$E = 5 \times 10^{-6} v^3, \tag{3}$$

where E is the wind erosion and v is the wind speed. The ETS was relatively insensitive to the value of the fit.

The iceBlade model was run under two settings: the blade setting and a standard cylinder setting. In the standard cylinder setting, the enhanced velocity from the blade rotation was turned off and the cylinder size was decreased from 0.144 m to 0.03 m. From the iceBlade model the accumulated ice mass (ICE_g), ablated ice mass (ICE_r), total ice mass (ICE_t), and an ice flag were produced at each time step. ICE_t is the running total of ICE_g and ICE_r. The ice flag used a threshold of 0.1 kg m^{-1}.

DOI: 10.1002/we
Prepared using weauth.cls

3.3. Statistical power loss models

Instead of modeling a power value with icing effects, the power loss caused by the icing model effects was modeled to reduce the uncertainty introduced by the WRF-simulated wind speeds. The power loss, p_l, was defined as

$$p_l = p - p_{park}, \tag{4}$$

where p is the observed power and p_{park} is the power based on PC_{park} as defined in Section 2. While p_l was used in the model, the results were evaluated against the observed power to allow for comparisons with PC_{park}. The estimated power loss was converted back to power as

$$p_e = p_{el} + p_{park}, \tag{5}$$

where p_e is the estimated power, and p_{el} is the estimated loss.

A hierarchical modeling approach [29] was implemented to allow the fitting of different models for iced and non-iced periods. The hierarchical model was a combination of a decision tree [30] and a GAM. The decision tree was pruned at the first level based on the iceBlade ice flag. The decision tree separates GAM models fit to the "yes" and "no" cases. GAMs were chosen since their semi-parametric methodology would be useful given the uncertainty of the relationship between the various iceBlade outputs and the power loss.

The GAM models were built using a combination of known physical relationships and statistical analysis. Initially, all of the icing terms and relevant meteorological terms were correlated with the power loss and each other using Kendall's rank correlation [31]. This helped to identify the key terms for fitting the model. Several terms with high correlation to power loss were dropped as they also had high correlation with more relevant predictors. After this initial screening, a cross-validation approach [32] was used to select the terms of the model, analyze the difference between the various smooths available for GAMs, and select the k-dimension for each term.

The cross-validation approach randomly split the first year of data into 12 sections, each with approximately 500 data points. The splits were defined to ensure a similar ratio of observed ice to non-iced points as in the entire first year dataset. Eight of the sections were combined for use as the training dataset, with the remaining four sections being used as the test dataset, providing 495 combinations for validation. Density functions of the mean bias (MB) and root mean squared error (RMSE) were plotted to study the model performance. The mean bias is defined as

$$MB = \overline{(m - o)}, \tag{6}$$

where m is the model result and o is the observed value and the overbar signifies the arithmetic mean.

Using cross-validation, the GAM model for points with icing was,

$$p_{el} = s(v) + s(i_g) + s(i_t), \tag{7}$$

DOI: 10.1002/we
Prepared using weauth.cls

where $s(v)$, $s(i_t)$, and $s(i_t)$ are smooths of wind speed, $\mathrm{ICE_t}$, and $\mathrm{ICE_g}$. The optimal k-dimensions for these parameters were found to be 15 for $s(v)$ and 40 for both $s(i_t)$ and $s(i_g)$. The k-dimension in a GAM sets the upper limit on the degrees of freedom given by the smoothing functions. The non-iced GAM model was defined as

$$p_l = s(T) + s(p), \tag{8}$$

where s(T) was the smooth of temperature and s(p) the smooth of pressure from the WRF model output. The k-dimension was set to 7 for both $s(T)$ and $s(p)$, although the effective degrees of freedom were often much lower. Both GAM models used thin plate splines [33] as the smoothing function. The empirical power curve already provided a good estimate of the non-iced data points, therefore the non-iced GAM model was not studied in detail.

The mixed model approach significantly outperformed a single GAM model, by improving the iced points without significantly reducing the performance of the non-iced points. However, this approach required the correct identification of icing periods, leading to the changes made to the iceBlade model ablation algorithm previously described in Section 3.2.

After the model parameters were determined, an evaluation model was created for the second year of data, by training it on the entire first year of data. To investigate the applicability of a general model, two different sets of data were used to fit the final model. The first model used data from each individual wind park to determine the fit (PARK). The second fit used the data from all of the wind parks (ALL). This comparison allows for the determination of how independent the response of the different parks is to the statistical model. If the relationship is found to be universal, the model could also be used for siting of turbines in areas without turbines.

4. RESULTS OF THE EMPIRICAL INVESTIGATION

The results from the component models, WRF and iceBlade, as well as the results from the statistical power loss models were evaluated. The WRF model was evaluated for temperature revealing a cold bias. The cloud fields could not be verified as there were no cloud-related measurements at the wind parks. The iceBlade model was evaluated by studying both time-series and statistical measures. The evaluation highlights the improvements of the iceBlade model over the standard cylinder approach, as well as the importance of the wind erosion term on the model results. An example of the cross-validation analysis shows the improvement of the fit using the new approach. Finally, the results from the power loss modeling are presented to show the changes in RMSE and mean bias.

4.1. WRF results

Figure 2 compares the park averaged nacelle temperature to WRF simulated temperature at each of the wind parks. The WRF model does a reasonable job capturing the overall signal of the temperature, with a high correlation (Table I) and a relatively tight grouping of points around the regression line. However, there is a large cold bias at each park. Since the slope of the regression line is greater than 1, it can be said that the cold bias is larger at colder temperatures.

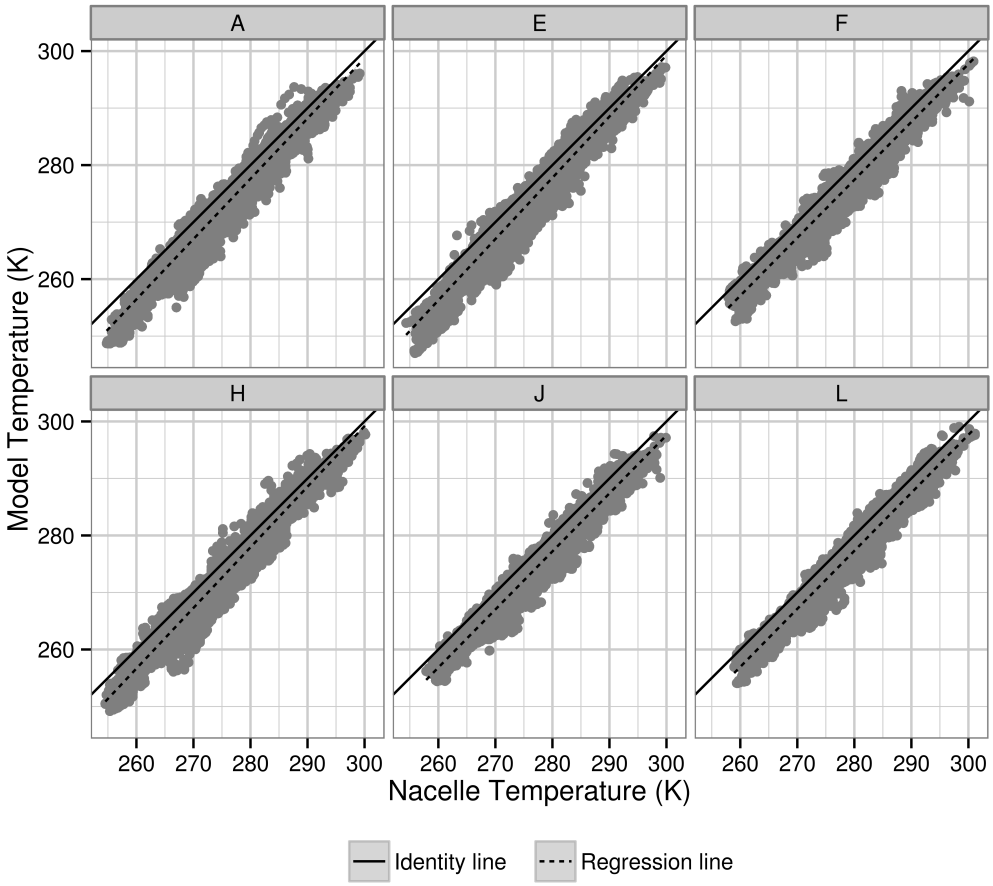

Figure 2. Comparison of nacelle temperature to WRF modeled temperature, interpolated to 80m above ground level, at each wind park (sub-plots). Regression (dashed) and identity (solid) lines are shown to aid in the evaluation.

Table I compares the statistics of the modeled and observed temperatures. RMSE_adj is defined as

$$RMSE\_adj = \sqrt{\overline{[(m - MB) - o]^2}}. \tag{9}$$

The large difference between RMSE and RMSE_adj shows that much of the model error is a result of the bias with an RMSE_adj around 1.5°C at each park. However, as conditional bias correction was not performed, the large slope of the temperature bias, would lead to an over-correction of warmer points and under-correction at colder points

4.2. iceBlade results

Since the ice observations were defined as a simple yes/no flag, a contingency table [28] was used to evaluate the iceBlade ice flags that were created using a threshold mass of 0.1 kg m^{-1}. A contingency table (Table II) compares modeled events with observed events and evaluates how many times a result is a *true positive* (a), *false alarm* (b), *miss* (c), or *true negative*

DOI: 10.1002/we
Prepared using weauth.cls

Table I. Mean bias (MB), root mean squared error (RMSE), Pearson's correlation coefficient (Cor_R), linear slope (slope) and RMSE with the mean bias removed from the model data (RMSE_adj) of WRF simulated temperature compared with the nacelle averaged temperature for each wind park labeled A-L. All parameters are non-dimensional.

park	MB (°C)	RMSE (°C)	Cor_R	slope	RMSE_adj (°C)
A	−2.72	3.22	0.98	1.06	1.72
E	−2.58	3.17	0.98	1.08	1.85
F	−2.64	3.00	0.99	1.02	1.43
H	−2.37	2.96	0.98	1.06	1.76
J	−2.82	3.13	0.99	1.02	1.36
L	−2.72	3.02	0.99	1.02	1.33

(d). From the contingency table several scores can be calculated. The false alarm rate (F), defined as

$$F = \frac{b}{b+d}, \tag{10}$$

and the miss rate (M), defined as

$$M = \frac{c}{a+c}, \tag{11}$$

are scores which identify errors in the model and have a range 0 to 1, where lower values are better. The equitable threat score (ETS) [28] takes into account both false alarms and missed events and is designed to provide reasonable scores for rare events, such as turbine icing . The ETS is defined as

$$ETS = \frac{a - a_r}{a+b+c-a_r}, \tag{12}$$

where a_r is $(a+b)(a+c)/n$ and n is the total number of events. The ETS has a range of -1/3 to 1, with 1 being a perfect model and a value below zero suggesting that the chance estimate is more skilled than the actual model.

Table II. Contingency table.

Event modeled	Event Observed		
	Yes	No	
Yes	a	b	model yes
No	c	d	model no
	observed yes	observed no	

Figure 3 shows a time-series of the iceBlade simulated ice mass, for a 1-m long section of the turbine blade at wind park A, with the periods colored by contingency table result. The blade setting results in more periods of significant ice growth than the standard cylinder setting. This in turn leads to much larger values of ICE_t. For the standard cylinder setting there are no hours where ICE_g is above the $0.1 \mathrm{kg\,m^{-1}}$ threshold, during this period. However, ICE_t shows an icing period which lasts from 9 November until the end of the month. The wind erosion term has a large impact on blade icing, but much less

DOI: 10.1002/we
Prepared using weauth.cls

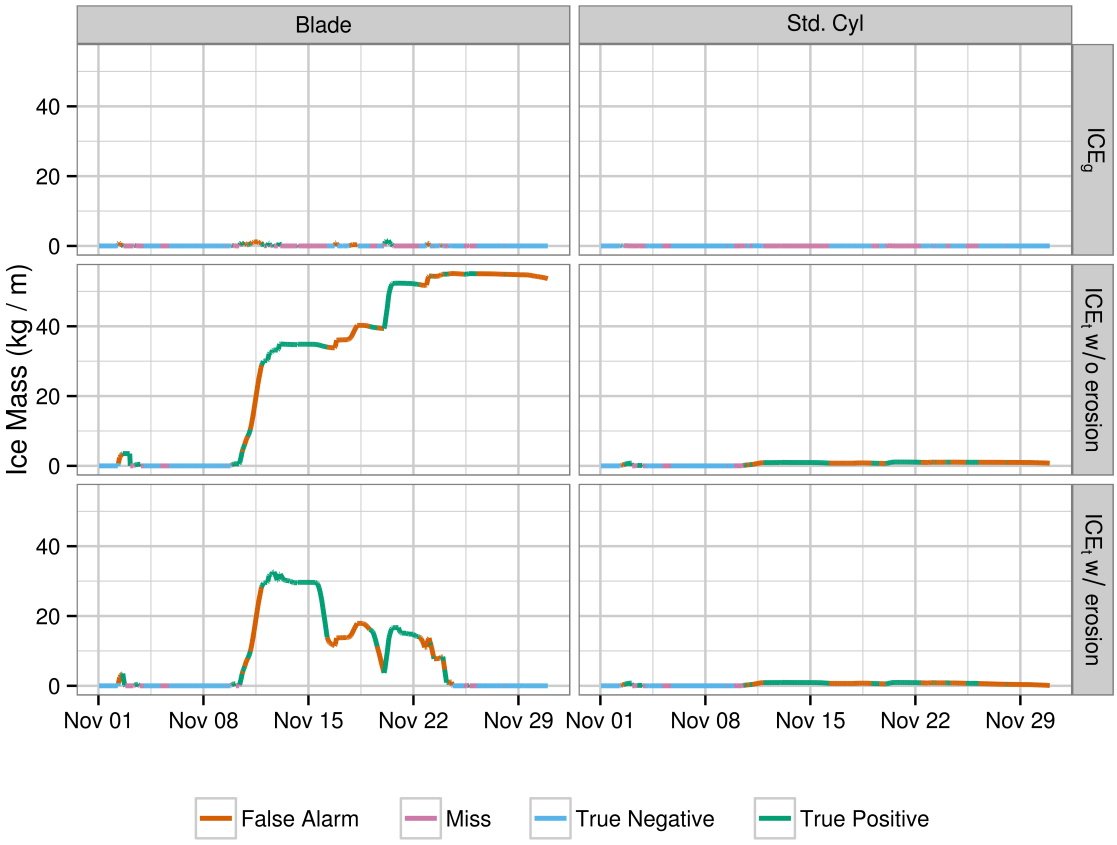

Figure 3. Time-series of modeled ice mass (kg m^{-1}) at wind park A for November 2010. The columns show the results using the iceBlade method (left) and the standard cylinder Makkonen model (right). The rows show ICE$_g$ (top row), ICE$_t$ without wind erosion (middle row), and ICE$_t$ with wind erosion (bottom row). The colors denote the four possible outcomes of the model results compared with observations.

on the standard cylinder, due to the higher wind speeds with the blade icing setting. The increased ablation from the wind erosion term leads to fewer false alarms. However, even in results using the blade icing method, a large number of false alarms occur during this period.

Figure 4 shows M, F, and ETS for the entire two year period at park A. For both the blade and cylinder methods, ICE$_g$ has a very high M and correspondingly low ETS, despite a low F. The inclusion of the wind erosion term reduces F, but also increases M. The F and M values are similar in magnitude for ICE$_t$ with wind erosion, which was a goal of the fitting algorithm for the wind erosion term. The large decrease in F compared to the smaller increase in M leads to a large improvement in ETS when the erosion term is added to the model. As in the time-series (Fig. 3), the improvements from adding the wind erosion term are found to be much smaller for the standard cylinder. Based on this analysis, the blade method with wind erosion was the model chosen for the statistical modeling.

DOI: 10.1002/we
Prepared using weauth.cls

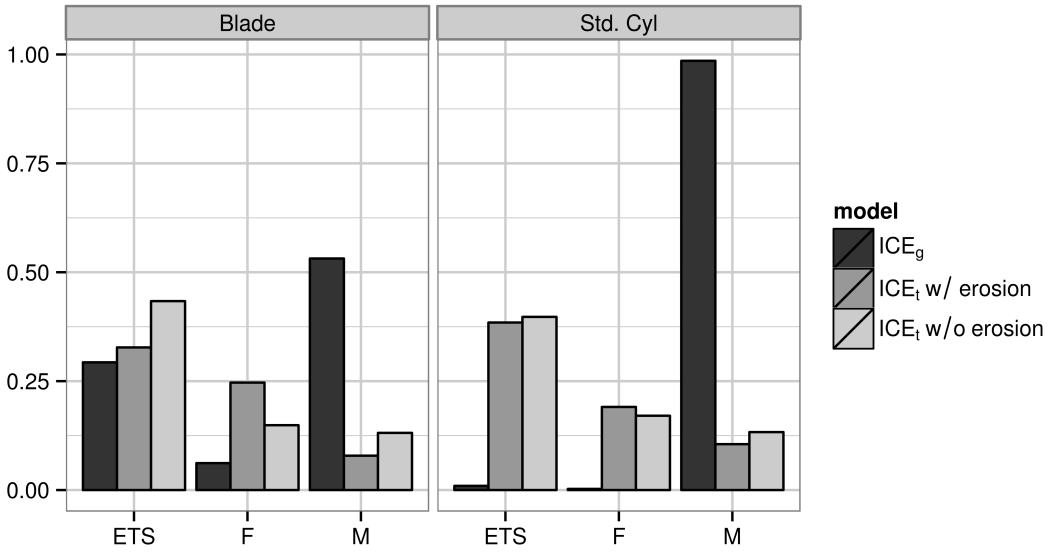

Figure 4. Values of the Equitable Threat Score (ETS), False alarm rate (F) and Miss rate (M) for the icing period prediction at wind park A. The fill represents the three icing results. The columns show the results from the blade and standard cylinder geometries.

4.3. Statistical modeling results

Figure 5 shows an example of the cross-validation density plot used to evaluate the different models of power loss as described in Section 3.3. The density plot shows the probability density function of the model error from the 495 model fits created during the cross-validation. A density plot can be thought of as a histogram with a very small bin width so the peaks of the density surface identify the values for the bulk of the models. The comparison shown includes the final mixed model fit (GAM model) described in Section 3.3, a model with the same terms but where the GAM is replaced by an ordinary least squares linear model (Linear model), and PC_{park} (Power Curve). The linear and GAM models show similar results for the mean model bias, with large overlap of the density curves. However, the GAM model has significantly lower RMSE for the observed ice times and lower RMSE overall. As expected PC_{park} had very high bias and error, due to the lack of icing correction. Both model fits show significant improvement compared to PC_{park} for the iced data. However, for the non-iced points, the addition of the statistical model increases both MB and RMSE. Since the improvement for the icing points is much larger, the total dataset shows a substantial decrease in error as well.

Figure 6 shows density plots of the hourly absolute error for the final model fit, with PARK showing the model fit to data only at that park, and ALL was fit using data from all parks. While in Figure 5, the densities were based on the results from many model fits, here they are based on each modeled hour. For the first year, the PARK model always performed best. However, at parks E, F, and L the ALL model results are similar to the PARK model. This was expected as the fit should be more accurate for individual parks when only their data was used. However, for the second year, the ALL model performs best at five of the six parks. In the first year, the RMSE is improved at all parks for both PARK and ALL, compared with

DOI: 10.1002/we
Prepared using weauth.cls

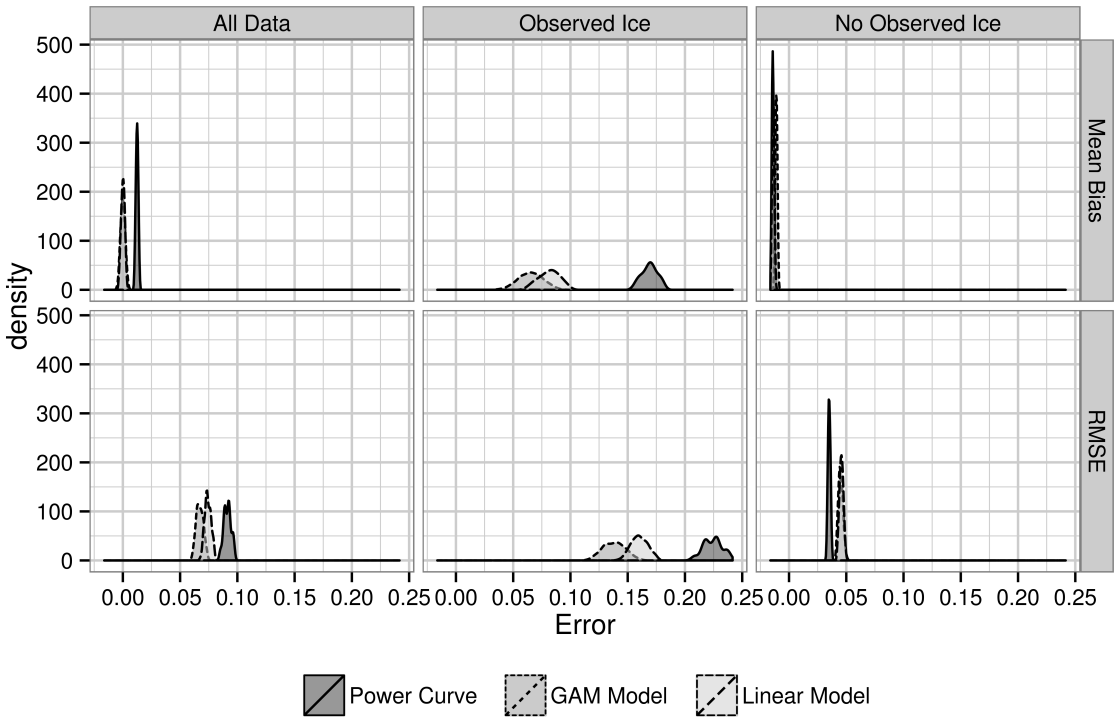

Figure 5. Density plots of power mean bias (top row) and RMSE (bottom row) for 495 cross-validation simulations for Park A and the first year of data. The columns show different splits of the dataset. The colors and line-types signify three different estimates of the power. Power Curve is PC_{park}, GAM Model adjusts PC_{park} using the GAM model fit, and Linear Model is using the linear model fit.

PC_{park} (Table III). In the second year, PARK performs the same or worse than PC_{park} at five of the six parks for RMSE. Site E presents an interesting case for comparison between the bulk statistics, such as RMSE, and the information contained in the density plot. For the second year, both PARK and ALL errors were more likely to fall below 0.1 than the power curve method, but PARK produced a few points that had very large errors. When the errors were averaged, PARK and PC_{park} had the same RMSE, while the RMSE was reduced for ALL .

Figure 7 shows the model bias. Both PARK and ALL shift the distribution so it is more centered on zero compared to PC_{park}, and the mean bias generally has the same trend. As with the error plot, the performance of PARK and ALL varied greatly depending on the site and year being modeled, and PARK generally performed better for the first year while ALL generally performed better for the second year. The conflicting results between the bulk and comprehensive error analyses for year two at Park E in the error plot were also found in the bias results. Here PARK had a large number of bias values less than -0.2, signifying a fairly large bias on either side of zero. However, the mean bias was only 0.01, as the large positive and negative biases canceled out. ALL has fewer points far away from zero, at site E, but has a larger mean bias than PARK. Provided with both the density plot and bulk statistics, it is is clear that the ALL model is the better model at this site, however, if only the bulk statistics were used the result would not be as clear.

DOI: 10.1002/we
Prepared using weauth.cls

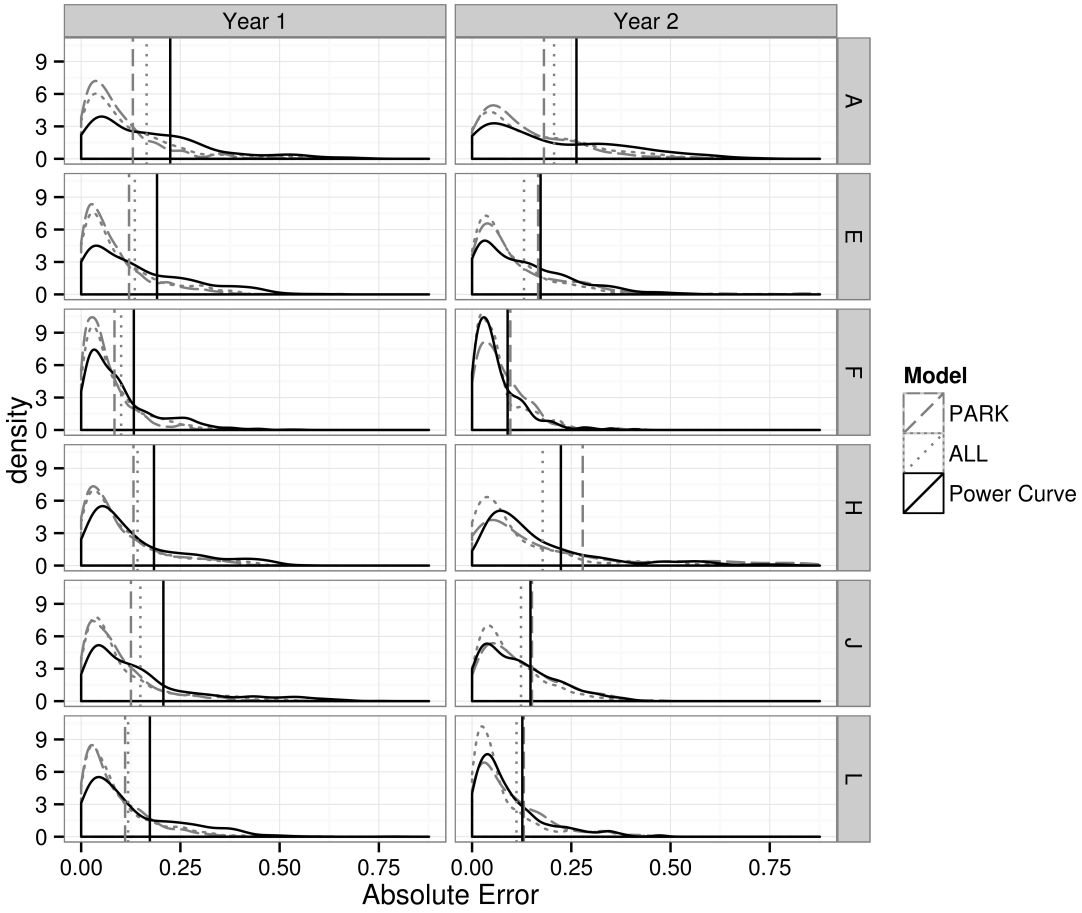

Figure 6. Density plot of absolute error for points with observed icing at each wind park for PC_{park} (power curve; solid black), the model fit for park (PARK; long dashed gray), and the model fit with all parks (ALL; dotted gray). The vertical lines show the RMSE value. Year 1 is the year used for fitting the models, and year 2 is the verification year.

5. DISCUSSION AND CONCLUSIONS

Modeling icing on a wind turbine is a challenging task.This study has shown that the iceBlade model, driven by inputs simulated using the WRF model, can reasonably capture periods of icing at several wind parks. Additionally, the error in estimated power can be improved by using a statistical model to relate icing to the power loss. In this section, we will discuss the results in more detail and describe some of the challenges and possible solutions to them.

5.1. Simulated cold bias

The WRF-simulated temperatures were found to have a large cold bias compared with the nacelle temperature (Table I). This is consistent with results found in other studies using the WRF model [34, 35]. The temperature bias has a large impact on the simulation of icing, as both the ice accretion and ice ablation terms are highly sensitive to temperature,

DOI: 10.1002/we
Prepared using weauth.cls

Table III. RMSE and MB for the unadjusted power curve, the model fit to the park, and the model fit to all parks for hours with observed icing. Minimum value for each metric and park are in bold.

		Year 1		Year 2	
park	variable	RMSE	MB	RMSE	MB
A	PARK	**0.13**	**0.06**	**0.18**	**0.12**
A	ALL	0.16	0.10	0.21	0.15
A	Power Curve	0.22	0.17	0.26	0.20
E	PARK	**0.12**	**0.05**	0.17	**0.01**
E	ALL	0.14	0.07	**0.13**	0.08
E	Power Curve	0.19	0.14	0.17	0.13
F	PARK	**0.08**	**0.04**	0.10	**0.04**
F	ALL	0.10	0.04	0.09	0.04
F	Power Curve	0.13	0.10	**0.09**	0.06
H	PARK	**0.13**	0.08	0.28	0.18
H	ALL	0.14	**0.08**	**0.18**	**0.10**
H	Power Curve	0.18	0.14	0.22	0.16
J	PARK	**0.13**	**0.05**	0.15	0.11
J	ALL	0.15	0.07	**0.12**	**0.09**
J	Power Curve	0.21	0.15	0.15	0.12
L	PARK	**0.11**	0.06	0.13	0.09
L	ALL	0.12	**0.05**	**0.11**	**0.06**
L	Power Curve	0.17	0.12	0.13	0.09

particularly around 0°C. The cold bias was approximately 0.5°C greater during periods of ice accretion than the values in Table I. The impact of the colder temperatures is likely one factor in the rapid ice accretion that occurs on 10 November when the observations did not show any icing signal (Fig. 3). During this event, the observed temperature was between -5°C and -7.5°C, while the WRF-simulated temperature was approximately 2.5°C colder throughout the period. While both temperatures are cold enough for ice to form, the colder temperatures in WRF would lead to a larger percentage of incoming water to freeze on impact.

There are three likely sources of the cold bias. One of the most likely causes is a warm bias in the nacelle temperatures, compared to the ambient temperature. The nacelle temperatures are known in the industry to have a wide range of accuracy, and the large number of observed icing points that occur between 0°C and 3°C (Fig. 1) suggests a warm bias in the measurements. Inaccurate terrain height is another potential source of the modeled temperature bias. However, it was found that the WRF model terrain heights were always lower than the observed heights, leading to warmer modeled temperatures Finally, the WRF parameterizations used in this study may be contributing to the cold bias. An earlier study investigating different WRF physics parameterizations [7] found that the combination of the WSM5 microphysics and MYJ PBL scheme had a significantly larger cold bias than other schemes. Therefore, the accuracy of the model temperature estimate could likely be improved by using different physics options.

5.2. Ice modeling

IceBlade was evaluated against a binary dataset for icing that was created using an ice threshold curve as described in Section 2. In Davis et al. [7], the blade setting was found to significantly outperform the standard cylinder setting for detecting periods of icing. However, in this study the two methods produced similar ETS scores, with the blade setting only

DOI: 10.1002/we
Prepared using weauth.cls

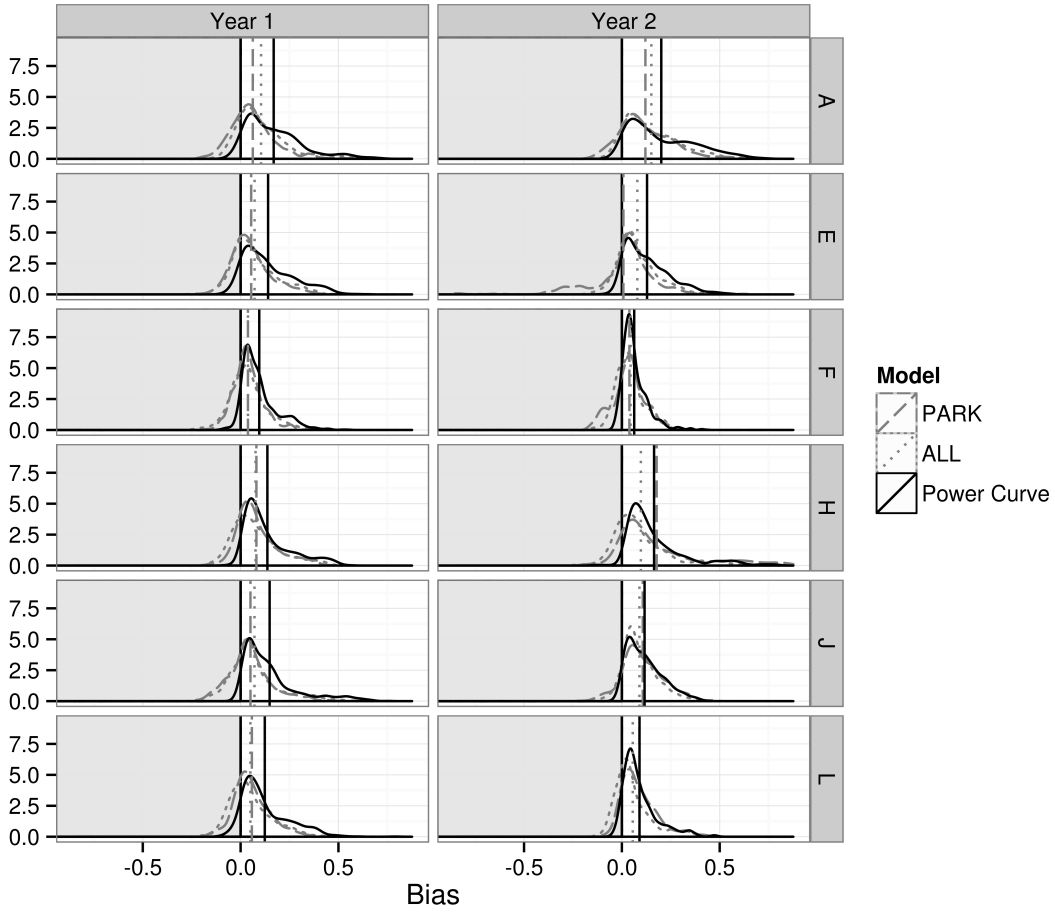

Figure 7. Same as fig. 6, but for bias and mean bias statistics. Light gray shading denotes bias values less than 0.

slightly outperforming the cylinder setting after the wind erosion term was added (Fig. 4). However, ICE_t was significantly different between the two methods (Fig. 3). The larger and more dynamic ice mass values of the blade setting consistently returned better estimates of the production loss. The standard cylinder tends to produce more periods of ice growth, but when ice does form on the blade, the accumulation is larger. The larger accumulation takes longer to be removed leading to longer total icing periods. Therefore, while the overall skill scores of the two models are similar, the periods of icing are quite different.

The inclusion of the wind erosion term was key to the performance of the blade setting. Without the wind erosion term, the blade setting included a significant number of false alarm events and overall produced too much ice (Fig. 4). This highlights the importance of accurate modeling of the ice ablation process. It should be noted that the algorithm for wind erosion included in this study is uncertain. Wind erosion can be caused by two factors, the force of the wind blowing pieces of ice off the blade, and the abrasive force of aerosols in the atmosphere contacting the ice and breaking off pieces of the ice. Neither of these forces are well understood for turbine icing, therefore an empirical fit was used. However, because

there were no direct ice mass measurements on wind turbines, the empirical fit was made using only the iced / not-iced flag created from the power observations. This provided little input when trying to fit a function to the complex time-series of the ice mass shown in Figure 3. Therefore, more research is needed to better quantify the impact of wind erosion on turbine icing.

McDonough et al. [36], presented an icing model inter-comparison that showed a strong agreement for the onset of icing between the various models, but a large spread in the results for the ending of an icing event. The uncertainty in the ending of ice events agrees with the results presented here and suggests that more research is needed into the ablation of ice on wind turbines. Given the importance of icing to the wind industry, a dedicated measurement campaign into ice ablation is necessary to better understand how this process occurs on a turbine blade. This step is likely to find the largest gains for the modeling of ice on wind turbines. In addition, because the power threshold approach cannot be used when turbines are not in normal operating mode, the measurement of icing directly on the turbine blades is also important for the control of deicing systems and health and safety evaluations.

5.3. Power loss modeling

Given the large uncertainties in the physical icing model, the modeling of icing related power loss is a challenge. The use of a hierarchical modeling approach was found to be a large improvement over a one-size-fits-all model. The problem presented by icing is an application that is well-suited for the hierarchical approach, as the parameters that affect power during icing, mostly the ice mass and shape, do not have any impact on the power loss during non-icing periods. Of course, this requires the physical models to do a reasonable job of capturing periods with icing

There has not been a consensus on the parameters that should be used to best model power loss in the literature. Some studies have relied on ICE_t [9], another study suggested that only periods of ICE_g were important [37], still others have suggested using the duration of icing [10]. Our approach was similar to the approach of Baltsheffsky [11] in that a large number of terms were included, and statistical analysis aided the final selection. In the end, only ICE_t, ICE_g,, and the wind speed remained significant. Many other parameters were highly correlated with the ice mass terms and removed to avoid duplicating information. Given the importance of ICE_t and ICE_g, it can be assumed that as the physical models improve, the power loss model should also improve. Therefore, the best way to improve the prediction of production loss due to icing is to invest in improvements to NWP models, physical icing models, and observational data collection. It is expected that using an NWP model setup for the specific wind park locations, and designed for estimating the parameters important for icing would also improve the prediction.

It was somewhat surprising that the model including data from all wind parks during the fitting process (ALL) performed better than the model fit with only that parks data (PARK) for the second year (Fig. 7 and 8). During the model fitting process, testing different k-dimensions and variables, only the PARK method was used. An analysis of the smoothing terms found that they were fairly linear for ALL. However, for PARK there were often high amplitude curves in the ice mass smooths. This suggests that during the cross-validation, the k-dimension was set too large for these terms and should be smaller in future work.

DOI: 10.1002/we
Prepared using weauth.cls

During cross-validation only MB and RMSE were used to evaluate the model. The final results for site E however, demonstrated how these bulk statistics can be a misleading value when examining the model fit (Fig. 7). This was particularly true of MB. At this site, PARK had the best MB score for year two, however, ALL had many more forecasts close to zero and far fewer large error forecasts. This highlights the importance of looking at all of the data when assessing model performance and not strictly relying on summary statistics. It could be that the reliance on the bulk statistics lead to the over-fitting of the PARK model.

While the model built for power loss showed good results, there are still improvements that would be worth investigating. The first relates to the choice of power loss as the predicted parameter. While the modeling of power loss produced reasonable results, when converting it back to power, we had to limit the results to a value between zero and one, as the statistical model did not have knowledge of these limits. Additionally, as shown in Section 2, the position on the power curve is related to the magnitude of potential power loss. Therefore, modeling power directly could provide a better result. However it should be noted that to do this, the mesoscale winds would need to be adjusted so they better match the observed winds. This was something we chose not to do for this study, instead focusing only on the icing impact.

Bernstein et al. [37], mentioned that in their experience production loss was most common during periods of active ice growth. However, when only ICE_g was used, there were many missed periods of lower power production (Fig. 4). When fitting the statistical model, ICE_g was found to be significant, which suggests that the impact of ice on power production is different when the ice is growing. This was also seen in the observed dataset where there is a large initial drop in power at the onset of icing that diminishes with time. This could be in part due to an increase in roughness during active icing that is quickly eroded when the ice stops growing. Two attempts to model this behavior were undertaken in this study. First a roughness parameter was estimated based on the ice density modeled by iceBlade, with the assumption that a lower density corresponded to a rougher surface. This term only had a slight correlation with power loss, potentially because it was only updated when ice was actively accumulating. Therefore, the impact of erosion and compaction on the roughness of the surface were not included. A roughness algorithm, which included these effects, would presumably provide a better estimate for the production loss model. The second attempt at capturing the change in production loss with time was by counting the hours since last ice accretion, but this term did not have a significant impact on the model fit.

5.4. Conclusions

In this study we set out to answer two questions: could a model for power loss be developed which improves the estimate of power, and could a general model using results from multiple parks provide insight that could potentially be used for wind park siting. The estimate of power was improved by developing a statistical model for power loss using an icing model driven from inputs of a meteorological model. This model reduced both the bias and error of the estimate on a second year of data after being fit for the first year. Additionally, it was shown that fitting a model for a single park is not as useful as fitting for multiple parks, this likely is due to the fitting of multiple parks including a more robust signal compared with the site specific noise. This suggests that given enough data for many wind parks, a model could be developed which would aid in the siting of wind parks.

DOI: 10.1002/we
Prepared using weauth.cls

ACKNOWLEDGEMENTS

This work was supported financially by the Top-Level Research Initiative (TFI) project, Improved forecast of wind, waves and icing (IceWind), Vestas Wind Systems A/S, and the Nordic Energy Industry.

The statistical modeling and data-analysis was carried out using the R Project for Statistical Computing [17].

REFERENCES

1. Special Chapter: Cold Climate Turbines. *BTM World Market Update*. chap. 7, Navigant Research: Copenhagen, Denmark, 2013.
2. Giebel G, Brownsword R, Kariniotakis G, Denhard M, Draxl C. The State-Of-The-Art in Short-Term Prediction of Wind Power. *Technical Report* 2011. URL `http://anemos.cma.fr`.
3. Homola MC, Nicklasson PJ, Sundsbø Pa. Ice sensors for wind turbines. *Cold Regions Science and Technology* Nov 2006; **46**(2):125–131, doi:10.1016/j.coldregions.2006.06.005. URL `http://linkinghub.elsevier.com/retrieve/pii/S0165232X06000760`.
4. 12494:2001(E). *Atmospheric icing of structures*. ISO: Geneva, Switzerland, 2001.
5. Chepil W, Woodruff N. The Physics of Wind Erosion and its Control. *Advances in Agronomy* 1963; **15**:211–302, doi:10.1016/S0065-2113(08)60400-9. URL `http://www.sciencedirect.com/science/article/pii/S0065211308604009`.
6. Laity JE, Bridges NT. Ventifacts on Earth and Mars: Analytical, field, and laboratory studies supporting sand abrasion and windward feature development. *Geomorphology* Apr 2009; **105**(3-4):202–217, doi:10.1016/j.geomorph.2008.09.014. URL `http://www.sciencedirect.com/science/article/pii/S0169555X08004340`.
7. Davis N, Hahmann AN, Clausen NE, Žagar M. Forecast of Icing Events at a Wind Farm in Sweden. *Journal of Applied Meteorology and Climatology* Feb 2014; **53**(2):262–281, doi:10.1175/JAMC-D-13-09.1. URL `http://journals.ametsoc.org/doi/abs/10.1175/JAMC-D-13-09.1`.
8. Makkonen L. Models for the growth of rime, glaze, icicles and wet snow on structures. *Philosophical Transactions of the Royal Society A: Mathematical, Physical and Engineering Sciences* Nov 2000; **358**(1776):2913–2939, doi:10.1098/rsta.2000.0690. URL `http://rsta.royalsocietypublishing.org/content/358/1776/2913.shorthttp://rsta.royalsocietypublishing.org/cgi/doi/10.1098/rsta.2000.0690`.
9. Byrkjedal Ø. Mapping of icing in Sweden - On the influence from icing on wind energy production. *Winterwind*, Skellefteå, Sweden, 2012. URL `http://www.slideshare.net/WinterwindConference/3a-byrkjedal-icingkvt`.
10. Karlsson T, Turkia V, Wallenius T, Miettinen J. Production Loss estimation for wind power forecasting. *Winterwind*, Sundsvall, Sweden, 2014.

11. Baltscheffsky M. Modelling of production losses due to icing for individual turbines in a wind farm - development of techniques for forecasting and site assessment. *Winterwind*, Östersund, Sweden, 2013.
12. Davis N, Hahmann AN, Clausen NE, Žagar M, Pinson P. Forecasting Production Losses by Applying the Makkonen Icing Model to Wind Turbine Blades. *The 15th International Workshop on Atmospheric Icing of Structures*, St. John's, Newfoundland and Labrador, Canada, 2013.
13. Hastie T, Tibshirani R. *Generalized Additive Models*. 1 edn., Chapman & Hall / CRC, 1990.
14. Wood SN. *Generalized Additive Models: An Introduction with R*. Chapman and Hall/CRC, 2006.
15. Davis N, Hahmann AN, Clausen NE, Pinson P, Žagar M, Byrkjedal Ø, Karlsson T, Wallenius T, Turkia V, Soderberg S, *et al.*. IceWind Inter-comparison of Icing Production Loss Models. *Winterwind*, Sundsvall, Sweden, 2014.
16. Wood SN. Fast stable restricted maximum likelihood and marginal likelihood estimation of semiparametric generalized linear models. *Journal of the Royal Statistical Society: Series B (Statistical Methodology)* Jan 2011; **73**(1):3–36, doi:10.1111/j.1467-9868.2010.00749.x. URL http://doi.wiley.com/10.1111/j.1467-9868.2010.00749.x.
17. R Core Team. *R: A Language and Environment for Statistical Computing*. R Foundation for Statistical Computing, Vienna, Austria 2014. URL http://www.r-project.org.
18. Cleveland WS, Grosse E, Shyu WM. Local regression models. *Statistical Models in S*, Chambers JM, Hastie TJ (eds.). chap. 8, Chapman and Hall: New York, 1992; 309–376.
19. Skamarock WC, Klemp JB, Dudhia J, Gill DO, Barker DM, Duda MG, Huang XY, Wang W, Powers JG. A Description of the Advanced Research WRF Version 3 2008.
20. National Centers for Environmental Prediction/National Weather Service/NOAA/US Department of Commerce. NCEP FNL Operational Model Global Tropospheric Analyses, continuing from July 1999. 2012, doi:http://dx.doi.org/10.5065/D6M043C6.
21. Hong SY, Dudhia J, Chen SH. A Revised Approach to Ice Microphysical Processes for the Bulk Parameterization of Clouds and Precipitation. *Monthly Weather Review* Jan 2004; **132**(1):103–120, doi:10.1175/1520-0493(2004)132<0103:ARATIM>2.0.CO;2. URL http://journals.ametsoc.org/doi/abs/10.1175/1520-0493(2004)132<0103:ARATIM>2.0.CO;2.
22. Mlawer EJ, Taubman SJ, Brown PD, Iacono MJ, Clough Sa. Radiative transfer for inhomogeneous atmospheres: RRTM, a validated correlated-k model for the longwave. *Journal of Geophysical Research* Jul 1997; **102**(D14):16 663, doi:10.1029/97JD00237. URL http://doi.wiley.com/10.1029/97JD00237.
23. Dudhia J. Numerical Study of Convection Observed during the Winter Monsoon Experiment Using a Mesoscale Two-Dimensional Model. *Journal of the Atmospheric Sciences* Oct 1989; **46**(20):3077–3107, doi:10.1175/1520-0469(1989)046<3077:NSOCOD>2.0.CO;2. URL http://journals.ametsoc.org/doi/abs/10.1175/1520-0469(1989)046<3077:NSOCOD>2.0.CO;2.

24. Chen F, Dudhia J. Coupling an Advanced Land Surface-Hydrology Model with the Penn State-NCAR MM5 Modeling System. Part II: Preliminary Model Validation. *Monthly Weather Review* Apr 2001; **129**(4):587–604, doi:10.1175/1520-0493(2001)129<0587:CAALSH>2.0.CO;2. URL http://journals.ametsoc.org/doi/abs/10.1175/1520-0493%282001%29129%3C0587%3ACAALSH%3E2.0.CO%3B2.
25. Janjić ZI. The Step-Mountain Eta Coordinate Model: Further Developments of the Convection, Viscous Sublayer, and Turbulence Closure Schemes. *Monthly Weather Review* May 1994; **122**(5):927–945, doi:10.1175/1520-0493(1994)122<0927:TSMECM>2.0.CO;2. URL http://journals.ametsoc.org/doi/abs/10.1175/1520-0493(1994)122<0927:TSMECM>2.0.CO;2?prevSearch=&searchHistoryKey=.
26. Kain JS. The Kain-Fritsch Convective Parameterization: An Update. *Journal of Applied Meteorology* Jan 2004; **43**(1):170–181, doi:10.1175/1520-0450(2004)043<0170:TKCPAU>2.0.CO;2. URL http://journals.ametsoc.org/doi/abs/10.1175/1520-0450%282004%29043%3C0170%3ATKCPAU%3E2.0.CO%3B2.
27. Jonkman J, Butterfield S, Musial W, Scott G. Definition of a 5-MW Reference Wind Turbine for Offshore System Development. *Technical Report February*, National Renewable Energy Laboratory, Golden, Colorado 2009.
28. Wilks DS. *Statistical Methods in the Atmospheric Science*. second edn., Academic Press: London, UK, 2006.
29. Cohen J. *Applied multiple regression/correlation analysis for the behavioral sciences*. 2003.
30. Breiman L. *Classification and Regression Trees*. CRC Press, 1984.
31. Kendall MG. A new measure of rank correlation. *Biometrika* 1938; **30**:81–93.
32. Picard RR, Cook RD. Cross-Validation of Regression Models. *Journal of the American Statistical Association* Sep 1984; **79**(387):575, doi:10.2307/2288403. URL http://www.jstor.org/stable/2288403?origin=crossref.
33. Wood SN. Thin plate regression splines. *Journal of the Royal Statistical Society: Series B (Statistical Methodology)* Feb 2003; **65**(1):95–114, doi:10.1111/1467-9868.00374. URL http://onlinelibrary.wiley.com/doi/10.1111/1467-9868.00374/abstract.
34. Cheng WYY, Steenburgh WJ. Evaluation of Surface Sensible Weather Forecasts by the WRF and the Eta Models over the Western United States. *Weather and Forecasting* Oct 2005; **20**(5):812–821, doi:10.1175/WAF885.1. URL http://journals.ametsoc.org/doi/abs/10.1175/WAF885.1.
35. Heikkilä U, Sandvik A, Sorteberg A. Dynamical downscaling of ERA-40 in complex terrain using the WRF regional climate model. *Climate Dynamics* Oct 2010; **37**(7-8):1551–1564, doi:10.1007/s00382-010-0928-6. URL http://link.springer.com/10.1007/s00382-010-0928-6.
36. McDonough. Ice Intercomparison. *Winterwind*, Sundsvall, Sweden, 2014.
37. Bernstein BC, Hirvonen J, Gregow E, Wittmeyer I. Experiences from Real-Time LAPS-LOWICE Runs Over Sweden: 2011-2012 Icing Season. *Winterwind*, Skellefteå, Sweden, 2012. URL http://www.slideshare.net/WinterwindConference/3a-bernstein-lapslowice.

Appendix D

Comparison of Wind Turbine Icing Production Loss Models

Chapter 1

Production Loss Model Inter-comparison

Neil N. Davis, Andrea N. Hahmann, Niels-Erik Clausen, Pierre Pinson, Mark Žagar, Øyvind Byrkjedal, Timo Karlsson, Tomas Wallenius, Ville Turkia, Stefan Söderberg, Magnus Baltscheffsky

1.1 Introduction

Model inter-comparisons can provide valuable insight into the understanding of key features of the phenomena being studied. They help to determine areas of model uncertainty as well as areas where the models appear to be less sensitive. In addition they can help model developers better understand the limitations of their approaches. Four of the project partners in Icewind have independently developed four unique models of wind park power production that include impacts due to atmospheric icing (PPM_i). It was determined that due to the large variation in model design that it would be useful to undertake a model inter-comparison. This could help identify any faults within the models themselves, and also help determine the optimal next steps for PPM_i development and other research into the impact of icing on wind turbines.

One of the greatest challenges in designing an inter-comparison is obtaining access to data for all parties. The Technical University of Denmark (DTU) undertook the responsibility of obtaining an anonymous dataset of wind park icing which would be appropriate for this study. Requirements were determined by the research groups and all data needed by the models was included.

This inter-comparison was designed to provide an overview of the state of the art PPM_i models and not to identify winning and losing approaches. Therefore, the the models have been anonymized in the results and discussion section using roman numerals (I-IV).

The rest of the report is laid out as follows, the observations are described in section 1.2; each of the four production loss models are described in section 1.3; the inter-comparison results are found in section 1.4; and finally the results and conclusions are included in section 1.5.

1.2 Inputs

Before the input datasets could be obtained, the scope of the inter-comparison needed to be determined. This was created through collaboration of the four research teams. The final requirements were that the data needed to cover two complete winters, with the winters of 2010-2011 and 2011-2012 as the two targeted years. This would allow the teams one year

Figure 1.1: Map of Wind Parks used in the study.

for model fitting and a second year for evaluation. While the use of the first year of data for model fitting was an option for all groups, only DTU and VTT used it this way. Kjeller Vindteknik and WeatherTech Scandivia both used datasets external to this study to fit their models. Additionally, Davis et al. [1] and Soderberg et al. [2] have shown that the numerical weather prediction (NWP) setup has a large impact on icing rates. Therefore, all groups needed to use the same NWP model results as inputs to their PPM_i models. This allowed the evaluation to focus on the differences in the ice and production loss models rather than the differences in meteorological model setup.

The wind park data needed to include the observed power, wind speed, temperature, and a set of QA parameters to identify hours where the wind park power was not ideal due to either turbine shut-down or other external factors other than icing. While the NWP model output needed to include a variety of surface measurements and four-dimensional data. The wind park and NWP data will be described in more detail in the following sections.

1.2.1 Wind Park Data

Wind park data was collected for a total of 15 sites across the northern hemisphere, with seven sites in Scandinavia and the remaining eight sites in North America (Fig. 1.1). 10-minute turbine data was supplied for a subset of turbines at each site. This data included the nacelle measured temperature and wind speed, the power output of the turbine, and several quality assurance (QA) variables. DTU examined the QA variables and utilized them to identify data-points when each turbine was not in normal operation. Low wind speed was the most common cause of the turbine not being in normal operation. Additionally, all data where the wind speed was below 5.5 $\text{m}\,\text{s}^{-1}$ were removed due to the large deviation in power output at those lower speeds. The large variance in power made it difficult to identify icing periods at those speeds, and since turbines only produce about 10% of their rated power at those times, it was determined to not be a significant loss for the study. Another common cause of non-normal operation was due to the turbine being in a derated state. A derated turbine is a turbine that has been limited to a rated power below its nameplate power.

The observational dataset did not include a direct measure of icing, instead the observed icing periods were empirically determined by DTU. The approach used in this study was based on the standard deviation of power at each wind speed, as well as the duration of the decreased power deficit. A detailed description of this method can be found in Davis et al. [3].

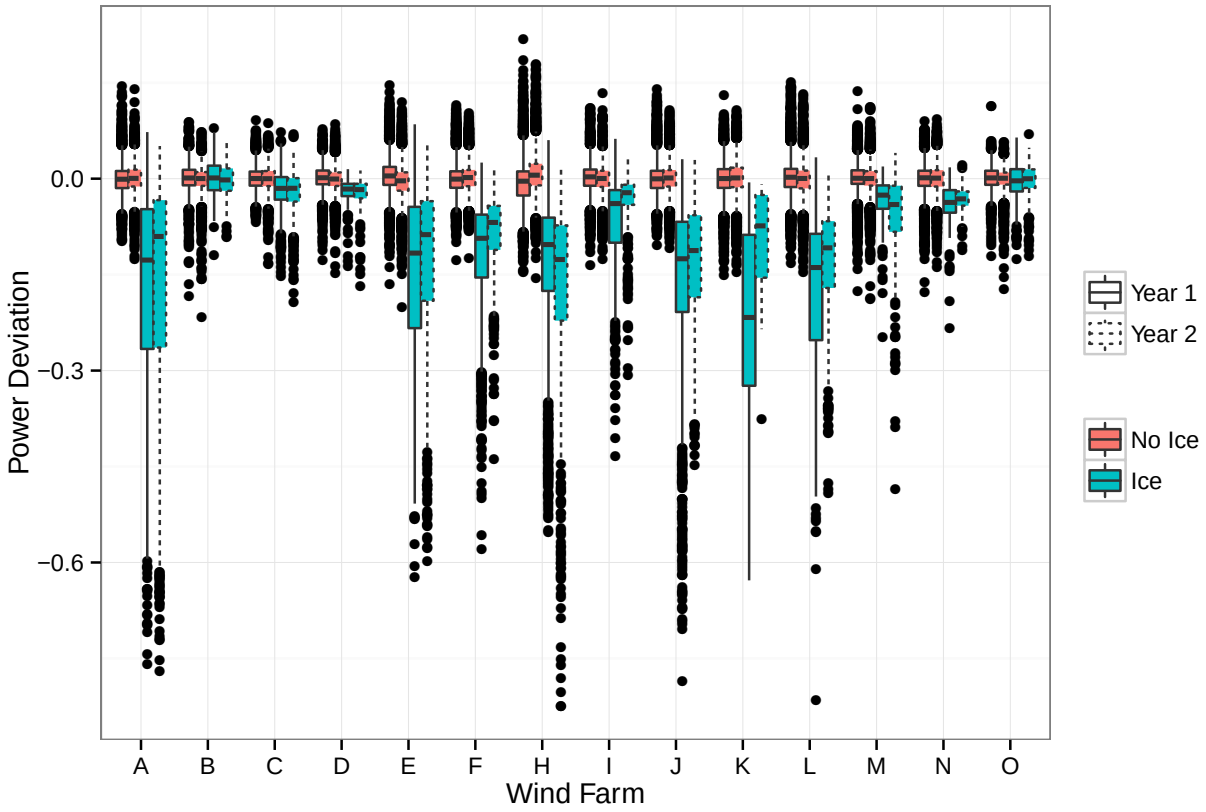

Figure 1.2: Observed power deviation (observed - power curve estimate) by year and observed icing. The two years are identified by the solid or dashed lines, while points with observed icing are in blue, and those without observed icing are in red. The box is drawn to highlight points between the 25th and 75th percentiles of the data, with the middle line highlighting the median value. The lines extending from the box extend another 1.5 times the inter-quartile range, while the dots highlight points which fall outside of that value, and would statistically be considered outliers if the distribution was normal.

To create the final wind park level dataset, the 10-minute data was subset to include only the top of the hour (00 minutes) data-points to match the temporal resolution of the meteorological model. The aggregation from turbine data to wind park data was carried out differently for continuous variables and the flag variables. For continuous variables (temperature, wind speed, and power) the data was aggregated taking the arithmetic mean of all normally operating turbines. The wind park QA flag was based on a 50% threshold, so when more than 50% of the turbines were not in normal operation, the park was determined to not be in normal operation. Therefore, many of the averaged continuous variables were only for a subset of the turbines in the park. Finally park icing was triggered if any turbines experienced icing. This threshold allowed the park to operate relatively normally while iced, unlike the turbine threshold.

For the baseline power estimate (PPM), a park power curve was fit for each park using only the wind speed as described in Davis et al. [3]. A Generalized Additive Model (GAM) [4] was used for this purpose with a thin plate smoother [5]. This approach allowed the power curve to be fit without needing to define the relationship between wind speed and power.

Figure 1.2 shows four distributions of the power deviation from the park power curve for each of the parks (A-O). The distributions highlight the difference between the non-iced and iced categories of the wind park, where it can be seen that there is a large difference in power deviation between the two classifications for parks A, E, F, H, I, J, K, and L. However, for parks B, C, D, M, N, and O there is less difference. Additionally, the two years were compared to determine if year 1 would make a reasonable baseline year for estimating year 2. From this analysis it appears that for most sites the power deviations are similar in both years, with the exception of site I, and K.

1.2.2 NWP model results

The NWP model results were provided by Vestas Wind Systems, where they were created for a global modeling study to investigate the long term wind climatology at specific locations. Therefore, the variables wind speed, wind direction, temperature, and air density were targeted in their model setup. The entire model output was archived in case other variables increased in importance or were needed for future studies, allowing for this dataset to be applicable for this ice related study.

The Weather Research and Forecasting (WRF) model version 3.3 [6] was chosen for the global study, and run at a 3 km grid resolution with 62 vertical levels. The vertical levels were setup up so the highest resolution was near the surface with 17 of the levels being located in approximately the lowest 1 km of the atmosphere. The Global Forecast System (GFS) analysis [7], was used to supply the input and boundary conditions with the boundary conditions updated every 6 hours. The physics options chosen were: the WRF single moment 5-class microphysics scheme [8], rapid radiative transfer model for longwave radiation [9], the Dudhia shortwave radiation scheme [10], Eta Similarity surface layer physics, the Noah Land Surface Model [11], the MYJ Planetary Boundary Layer (PBL) scheme [12], and Kain Fritsch cumulus scheme [13].

Hourly outputs of the following variables were provided at each wind park: surface outputs of terrain height, non-convective precipitation, and shortwave and longwave radiation, and four-dimensional data for wind speed, temperature, pressure, water vapor mixing ratio, and four cloud mixing-ratios representing different hydrometeors produced in the model microphysics (cloud water (QCLOUD), rain (QRAIN), ice (QICE), and snow (QSNOW)). The data was interpolated from the model levels to heights of 40m, 80m, 120m, 160m and 200m above the model surface. These data were combined with the wind park data for use in the study.

1.3 PPM_i descriptions

As described in section 1.2, all PPM_i models used the same meteorological model output, however, since not all of the models had similar capabilities in predicting power from the WRF wind speed, all teams were instructed to use the nacelle wind speeds and provide a gross power estimate without icing in addition to their power loss estimate. This suggests that the estimated power losses will be smaller than could be expected had the meteorological model results been used, but also ensures the results are tied more to the production loss approach than the ability to estimate power from the modeled wind speeds.

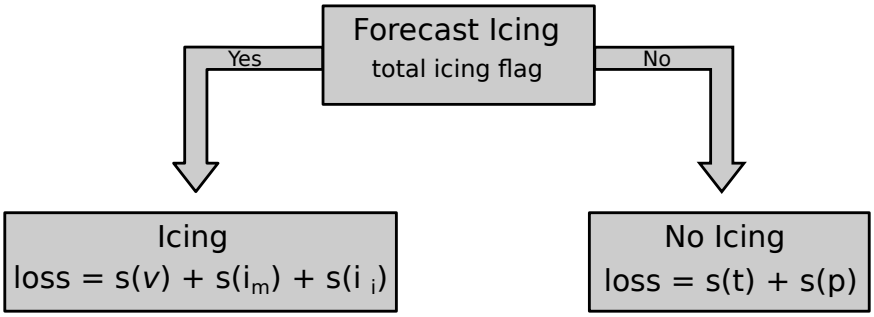

Figure 1.3: DTU power loss model design. GAM smoothing terms are identified by $s()$, v is the wind speed, i_m is the active ice mass accumulated over 1 hour, i_i is the total ice mass, t is the temperature, and p is the pressure.

1.3.1 DTU iceBlade and production loss

The icing and production loss models used by DTU are described in detail in Davis et al. [3]. That study also looks at the six Scandinavian sites used in this inter-comparison. The DTU approach uses the iceBlade icing model, developed as part of the Icewind project, in combination with a statistical production loss model that is fit to groups of wind parks.

The iceBlade icing model simulates icing on a 1-m long turbine section, represented as a cylinder with a diameter of 0.144 cm, and an inflow speed based on the turbines RPM at a radius equal to 85% of the blade length. The simulated ice retains a constant cylinder diameter, as though it was just an extension of the leading edge of the airfoil. To calculate the total ice load, ice removal (ablation) terms need to be included. The iceBlade includes algorithms for three methods of ice ablation: 1) total shedding is modeled such that all ice falls from the turbine when the temperature is above 0°C; 2) sublimation is modeled based on a mass balance equation [1]; 3) wind erosion is also included through a numerical fit based on the wind kinetic energy [3].

Icing was modeled at 80-m since the relevant parameters did not vary much across the heights in the WRF model results. The inputs to iceBlade were from the WRF simulation results without adjustment. The incoming cloud mass was a combination of the QCLOUD, QRAIN and QICE terms. The QRAIN term was assumed to contain large cloud droplets and therefore, all QRAIN droplets were assumed to impact the blade. The QCLOUD and QICE terms were summed, and then a collision efficiency was calculated using the empirical fit from Finstad et al. [14]. The QICE term was included, since the WSM5 scheme has been shown to produce too much cloud ice, leading to a deficit of QCLOUD and therefore a reduced amount of icing [1]. This was particularly significant at some of the sites in this study, where including only the liquid hydrometeors lead to a dramatic underestimation of icing periods.

In the DTU PPM_i, the statistical model was fit so that power loss was estimated rather than the power directly. This allowed the development to focus on the importance of icing directly rather than relying on an estimation of power from the wind speed. Power loss was defined as the observed power minus the estimated power. To estimate power loss, a hierarchical model approach [15] was implemented. This allowed for different models to be fit for iced and non-iced data-points. In our usage, the hierarchical model was a combination of a decision tree [16] and generalized additive models (GAM) [4] as shown in figure 1.3.

The total icing flag was set using the instrumental icing from the blade method with a threshold of 0.1 $\mathrm{kg\,m^{-1}}$. The GAM model for icing used both active ice mass and total ice mass for fitting the power loss term, when icing was predicted

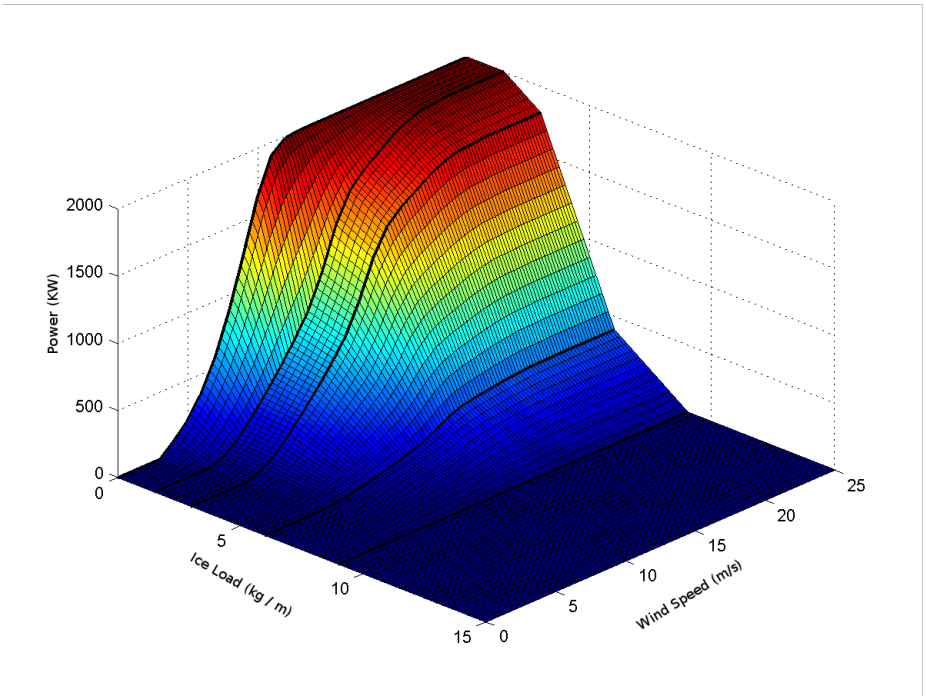

Figure 1.4: Two-parameter power curve P(V,M), function of ice load and wind speed.

at the wind park. The model was fit with data from only six of the sites (A, E, F, H, J, L) as this was identified as the best approach used in Davis et al. [3] for modeling those sites. Using the same model in this study, allowed the model team to investigate application of the model to sites that were not used to fit the model. A detailed explanation of the variable fitting is found in [3].

To support the VTT model, described in section 1.3.3, the iceBlade model, was run before the data was distributed to the project partners to produce four different icing values. The model was run for both the blade method described above, and in a standard cylinder setting. The standard cylinder method removes enhanced wind speed from the iceBlade model, and estimates ice growth on a cylinder with diameter of 0.03 m. This is the modeling approach recommended by the ISO standard for atmospheric icing on structures [17]. Two different ice values were then returned for both the blade and cylinder methods: 1) meteorological icing, which corresponds to the ice accumulated for a given hour; 2) Instrumental ice load is the total ice mass from both the accumulation and ablation processes.

1.3.2 Kjeller Vindteknikk production loss

Kjeller Vindteknikk developed a PPM_i (KVT) that uses the principle of a two parameter, wind speed and ice load, power curve based on the wind tunnel experiments of Seifert and Richert [18]. The ice load is defined as the total ice mass built up on a standard cylinder. The power curve used in this study was created based on operational data from three wind parks in Sweden (Fig. 1.4), rather than the wind parks in this study. The power curve was not refit for this study since a comparison of the simulated ice loads found found that the two years of data were not representative of each other.

Table 1.1: Observed vs WRF Terrain Height (from Davis et al [3]).

Site ID	Observed	WRF	Difference
A	700	544	-156
E	500	421	-79
F	450	359	-91
H	515	399	-116
J	525	451	-74
L	415	357	-58

The ice load used by KVT is based on the standard cylinder ice model from Makkonen [19]. The ISO standard cylinder is used which has a length of 1 m and diameter of 30 mm [17]. Periods of active icing were defined as times when the icing rate exceeds 10 g hr^{-1}, which is equivalent to a 0.5 mm layer of ice on the standard cylinder.

To account for the difference between the WRF topography and the observed site topography (Table 1.1), a correction is applied to the moisture parameters before the icing model is run. This is performed by lifting the air using the vertical profile of temperature and moisture in the model. The lifting leads to a lower pressure and temperature of the air, which allows for more water to condense and increases the amount of cloud water. In this study, the cloud parameters QCLOUD and QRAIN were lifted to a height of 130 m above the observed topographic height which approximates the tip height of the turbines. However, the wind speed used in the model was the raw WRF output at 80-m above the model topographic height.

To calculate the total ice mass, ice removal needed to be included in the KVT model. The KVT ice model includes algorithms for melting and sublimation, as well as a term that represents the erosion of small pieces of ice. All three terms are represented through an energy balance model given by

$$Q = Q_h + Q_e + Q_n, \tag{1.1}$$

where Q is the net energy, Q_h is the sensible heat flux, Q_e is the latent heat flux, and Q_n is the net radiation term. Melting begins when Q is positive, and a detailed description of the melting processed can be found in Harstveit [20]. When studying ice observations, it is often found that once ice begins to melt, it is rapidly removed due to ice shedding. However, this is not included in the KVT model. This suggests that the ice load may remain on the simulated cylinder for too long, but in the KVT model ice loss is still quite rapid during the melting stage, so any error should be short. The sublimation process was found to be particularly important for sites where the temperature remains below freezing for long stretches during winter. The sublimation rate is calculated by evaluating the energy balance between outgoing long-wave radiation and the latent heat flux released during the sublimation process. During the sublimation process, ice becomes brittle leading to small pieces of ice being removed from the cylinder continuously, wind erosion. This ice loss is included in the KVT model by multiplying the sublimation rate by a factor of 2.5.

1.3.3 VTT production loss module

The PPM_i module developed by VTT is described thoroughly in Karlsson [21]. The design goal of this module was to produce a simple method, in an engineering fashion, to estimate icing induced production losses. Production losses were defined as a simple multiplier describing the relation of power, including the icing impact and the theoretical power of the turbine at a given wind speed.

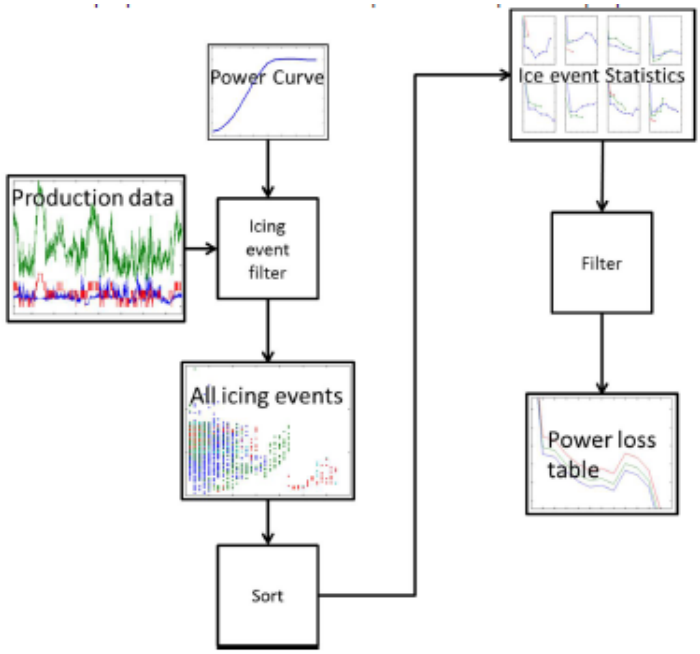

Figure 1.5: Flow chart of the VTT production loss module building process.

To maintain the flexibility of the approach, it was determined that more detailed parameters such as the airfoil aerodynamics, turbine controller, and icing shape and size should not to be used as input. Instead, these factors were thought of as random noise in a larger dataset. The goal is that by using a large enough dataset the individual icing events can be accumulated into a strong signal that can then be applied to future icing events. The module was built statistically, using real production data.

The final production loss module uses the length of the icing event, defined as length of time where there is ice on the turbine, and wind speed as inputs. This enables any icing model which provides a period of icing to be used as input to the module. Icing length was selected since it was found to have a direct impact on the power loss, while wind speed was chosen as it has a large impact on the ice accretion rate according to the icing rate formula given by the ISO standard for atmospheric icing on structures [17]. During model development, it was found that the exclusion of wind speed, and fitting the model to only event length would overestimate the losses. This is due to the large relative power losses at wind speeds less than 6 $\mathrm{m\,s^{-1}}$. The losses were more reasonable when wind speed was included in the fitting process.

The module built a set of power loss curves as a function of the length of the icing event, using the icing events from the dataset described in section 1.2. Since the dataset could be incomplete, missing data points were estimated using extrapolation. The module building process is illustrated in figure 1.5.

For this study, the total ice load from the iceBlade model was used to find the duration of icing events. The model was fit using the first year of inputs, with the second year being used for validation.

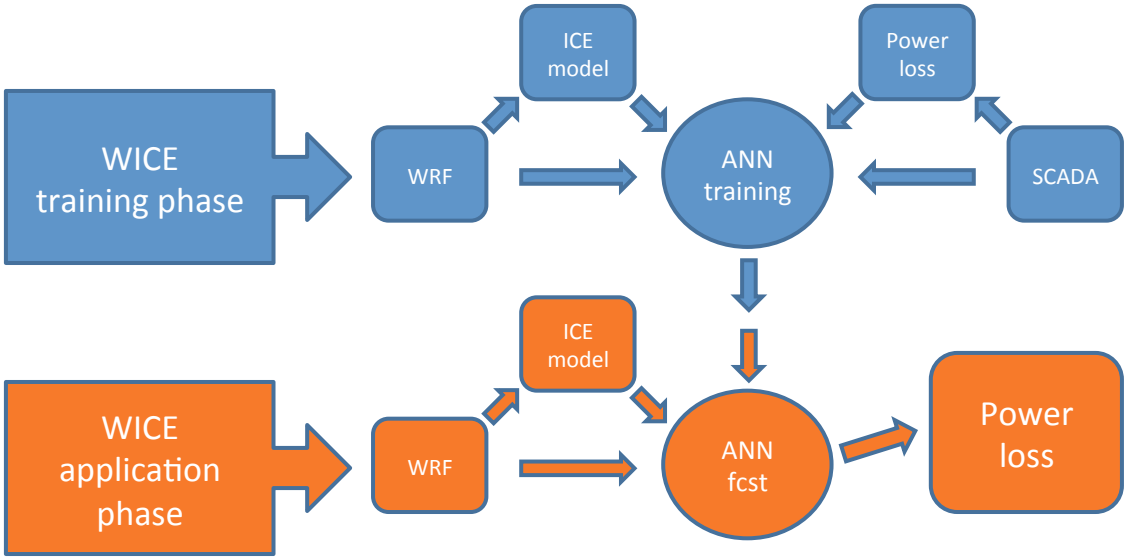

Figure 1.6: Flow chart of the WeatherTech WICE model concept.

1.3.4 WeatherTech WICE model

The PPM_i developed by WeatherTech (WICE) includes a physical module for modeling ice accretion and ice removal on a simplified wind turbine blade, and a statistical module that relates the modeled ice and the properties of the atmosphere to the performance of the turbine. A conceptual description of WICE is given in Figure 1.6.

The ice modeling is based on the Makkonen model [19] with some adjustments to make the results more representative of ice accretion on a wind turbine blade. A cylinder size comparable to the leading edge of the blade is used. Both QCLOUD and QRAIN are used in the ice accretion formula. A relative wind speed based on the rotation of the turbine is used for both the incoming liquid water mass flux and sublimation calculations. The relative wind speed is calculated for a point at two-thirds of the blade length. Above a threshold temperature, a formulation to account for melting and shedding is also used in the ice removal calculation.

To relate the atmospheric conditions and modeled ice on the blade to turbine performance an artificial neural network (ANN) is used. Output from the WRF model and ice model as well as operational turbine data are used as input to the ANN. The target for the ANN training is the power loss due to icing. To avoid over fitting, the training dataset was split in different parts to make sure that training and evaluation was performed on independent data. To find appropriate settings for the ANN, an iterative procedure was carried out during which training was performed for different wind farms and varying time periods.

The version of the WICE model used in this inter-comparison was trained on several years of SCADA data from 6 Swedish wind farms and WRF model data with 1km horizontal resolution. The wind farm data supplied in this inter-comparison was not used for training since that dataset was smaller. This could have an impact on the model performance since the WICE model was trained using model data from a WRF setup, with different physics schemes and different resolution.

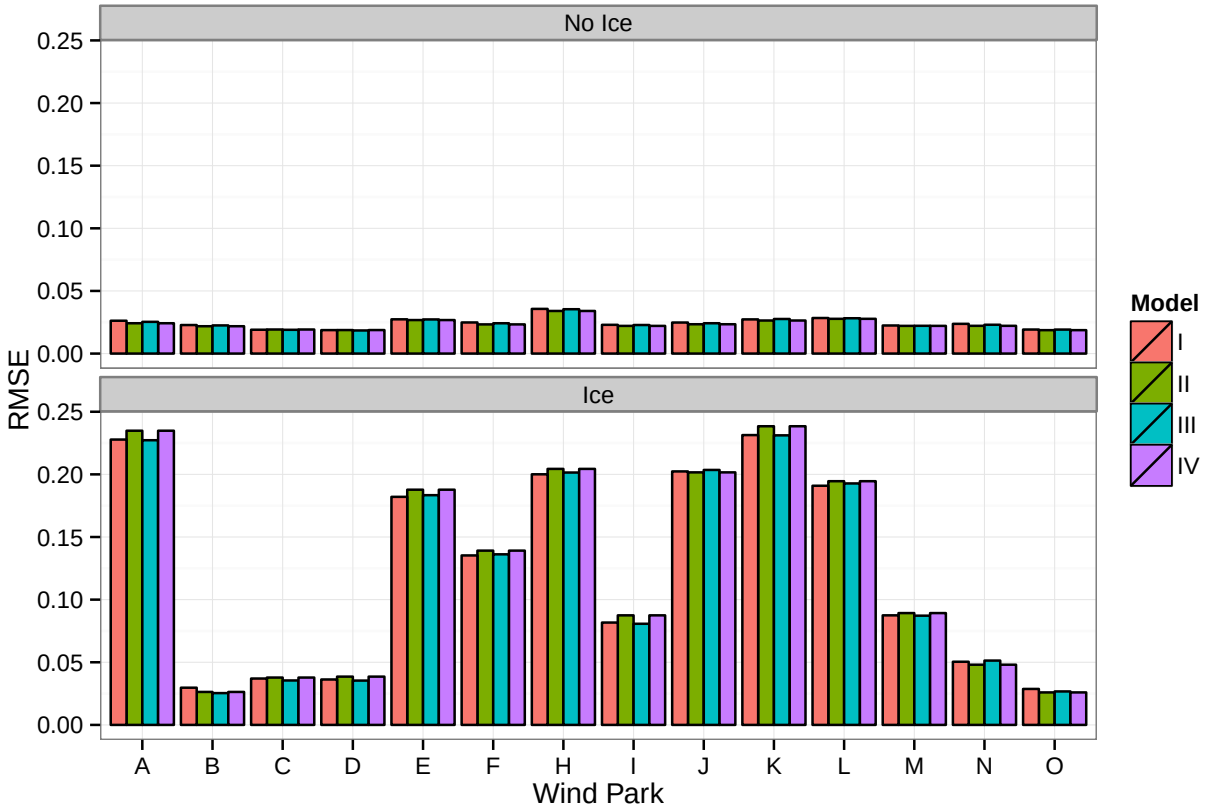

Figure 1.7: RMSE of the modeled wind park power without including the icing related power loss. Top panel is for periods without observed icing, while the bottom panel is for periods with observed icing. The colors denote the different ice production loss models.

1.4 Results

Throughout the results section the models have been randomized and labeled with roman numerals from one to four (I, II, III, IV). The model differences are compared using the terms error and bias. Error (e) is defined as

$$e = |M - O|, \tag{1.2}$$

where M is the model result and O is the observed value, the bars signify the absolute value. Bias (b) is defined as

$$b = M - O. \tag{1.3}$$

Figure 1.7 shows the root mean square error (RMSE) for the predicted power without the ice models included, for all wind parks and both years of data. This provides a baseline for each model to ensure that the differences identified, when comparing the icing models, are a result of the differences in the PPM_i methods and not the non-iced power estimation. The models perform similarly to each other at each wind park, when ice impacts are not included, there are slightly

larger differences between the models for the iced data. Additionally, the points without observed icing are captured very well, with RMSE less than 0.05 at all wind parks (Fig. 1.7; top panel). The iced points, however, show large deviations depending on the site. The models have reasonable performance, for sites with minimal icing (B, C, D, M, N, and O), but for the sites with a lot of icing induced power loss, the RMSE values are often near 0.20, four times that of the non-iced points.

Figure 1.8 shows the probability density function of the model error for all of the models at all wind parks for the second year of data, for points that had an observed icing signal. For these plots a perfect model would have a single line at 0.0 signifying the entire distribution had 0 error. For most models and sites, the bulk of the distribution is below 0.1. However, there are several sites with a significant number of errors above 0.2. For example, model I at site J has a large number of points above 0.2, and at site N there is a secondary peak in the distribution for model III around 0.2. At the sites that have a large number of iced points, models II, III, and IV show similar performance, while model I frequently shows larger errors. However, at sites with lower ice amounts model I to performed best.

Figure 1.9 is the same as figure 1.8, but for the model bias. Again a perfect model would have a single line at 0.0, which is now near the center of the plots. This plot shows that model I tends to over correct the power loss at sites with significant icing, such as A, F, and J. A similar result can be found for model III at sites C, I, and N. Model IV shows wide peaks at sites C and I, which are both low ice impact sites for the second year. At all sites the peaks are near 0.0 signifying the models do a reasonable job capturing the bias.

Figure 1.10 shows the change in RMSE due to the ice model. A negative value is good since this suggests a decrease in the RMSE compared to the baseline model. The two colors in each panel signify the different years, where the first bar is the first year of data, and the second bar is the second year of data. All of the models show larger RMSE for all of the data, although the change is fairly small. This is in part due to the very small errors in the non-ice adjusted estimate, which was fit using observed wind speeds. For the ice only points, all models except model I show fairly large reductions in RMSE at many of the sites, and particularly the sites with the largest icing impacts. For both years model I increases the RMSE of the power value in most cases. All models show slightly decreased performance in year 2, which is particularly interesting given that two of the models were not fit to the first year of data.

Figure 1.11 is the same as figure 1.10, except the mean bias is the error metric being studied. The mean bias is calculated by first calculating the bias at all of the points, and then taking the arithmetic average. To account for the fact that the mean bias includes negative numbers, the absolute value of each mean bias was taken before finding the difference between the models. Therefore, the metric being shown is the change in the distance of the mean bias from zero. The difference between the iced dataset and all data is even larger in the mean bias than for RMSE. For all data (top plot), there were no changes larger than 0.05. However, for the iced only data, the PPM_i models improved the mean bias estimate by more than 0.10 at several wind parks. For all models, except model I, wind parks that showed improvement in RMSE also had improvements in mean bias, but the magnitudes of the changes varied between the two metrics. For model I, the bias is often corrected to a value closer to zero, however the RMSE was found to have increased at all sites. This again points to the model over correcting several of the points for models II, III, and IV. Sites F, H, and J show much larger improvements during the first year than the second year. Interestingly model I shows much better performance in bias for the second year than the first, for the iced data. This doesn't hold for all data suggesting that model I included too many points as iced, thereby decreasing the power curve estimate for periods that were not iced. This result suggests that the first year was not representative enough for the model fitting to be able to represent the second year. The year to year

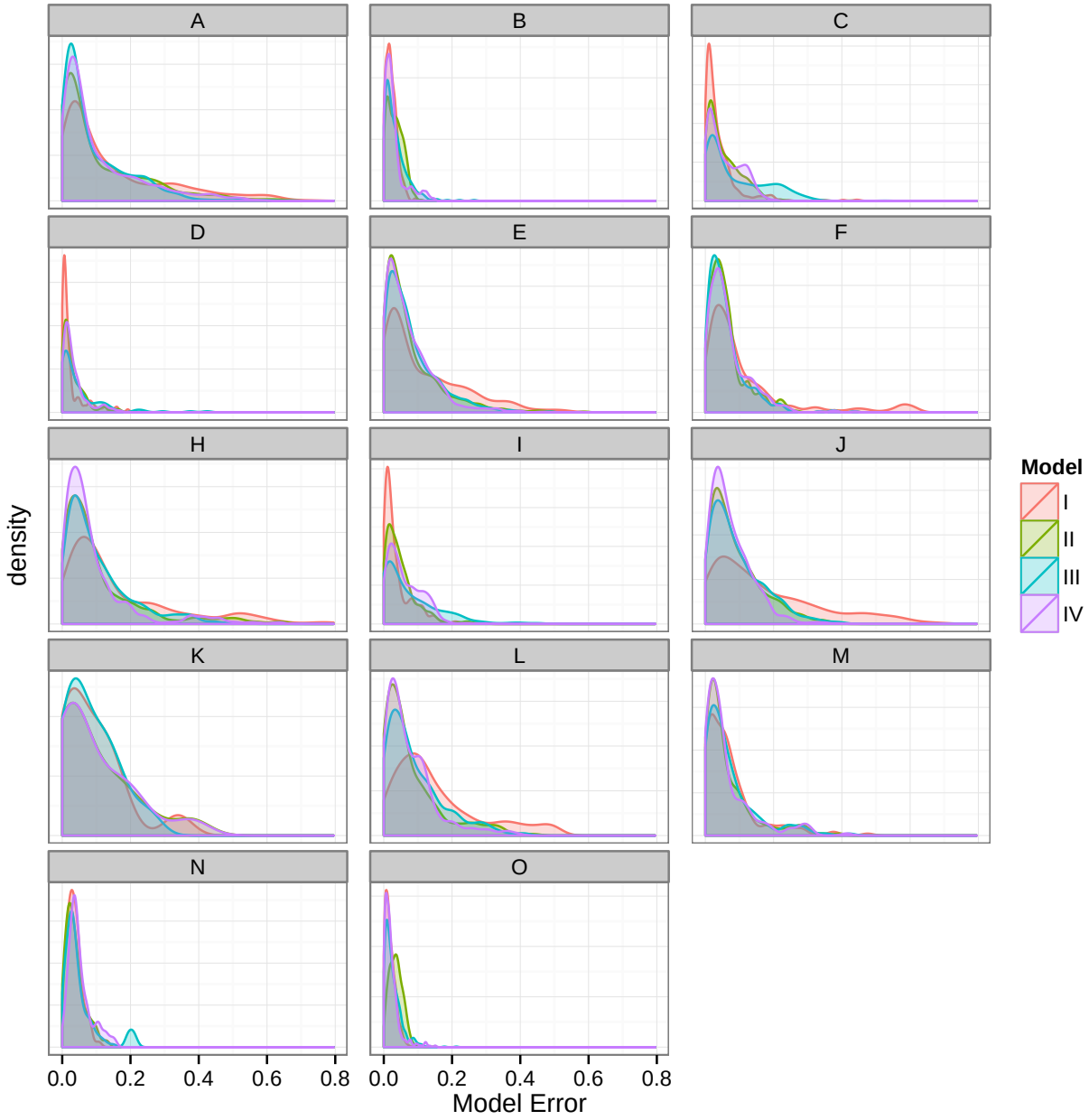

Figure 1.8: Density plots showing the amount of observations for each error value. The different colors denote the different models, and the different panels represent the different wind parks in this study. Only data from year two with observed icing is shown.

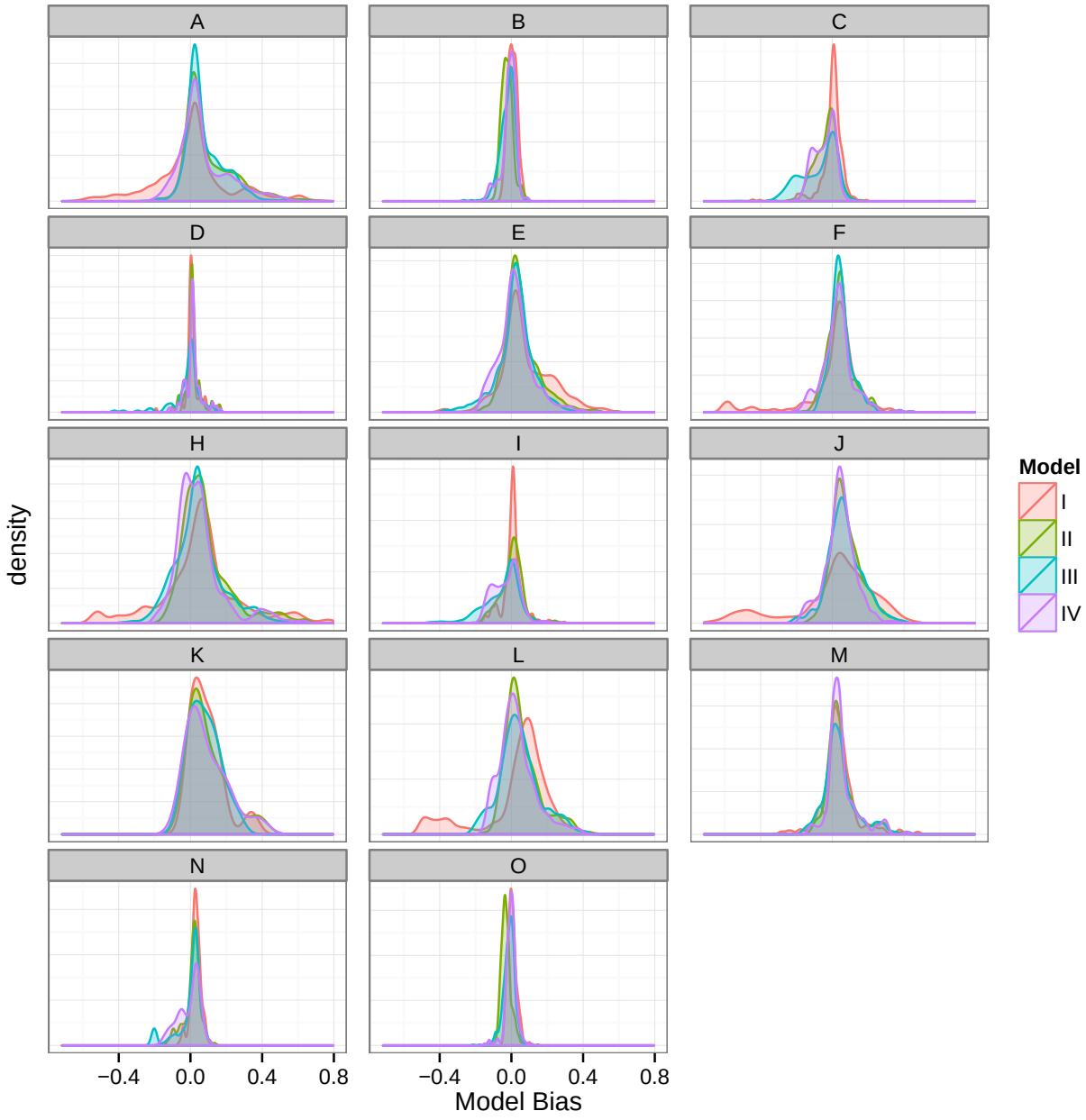

Figure 1.9: Same as 1.8 but for model bias.

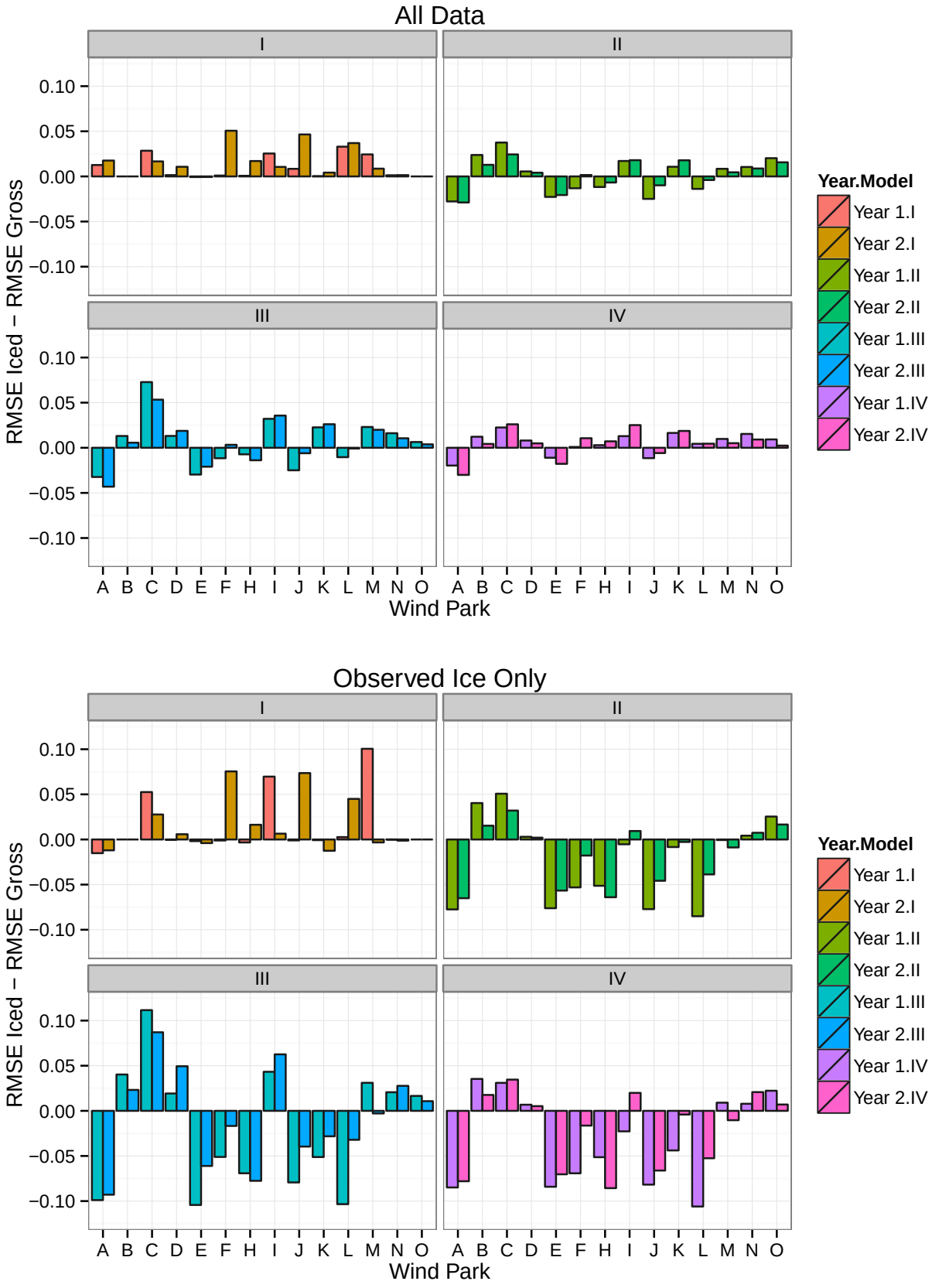

Figure 1.10: Change in RMSE when ice production loss adjustment is included. The top graph shows the change for all data, while the second change only includes points where ice was observed. Panels differentiate the different models, while the different color shades denote the different years.

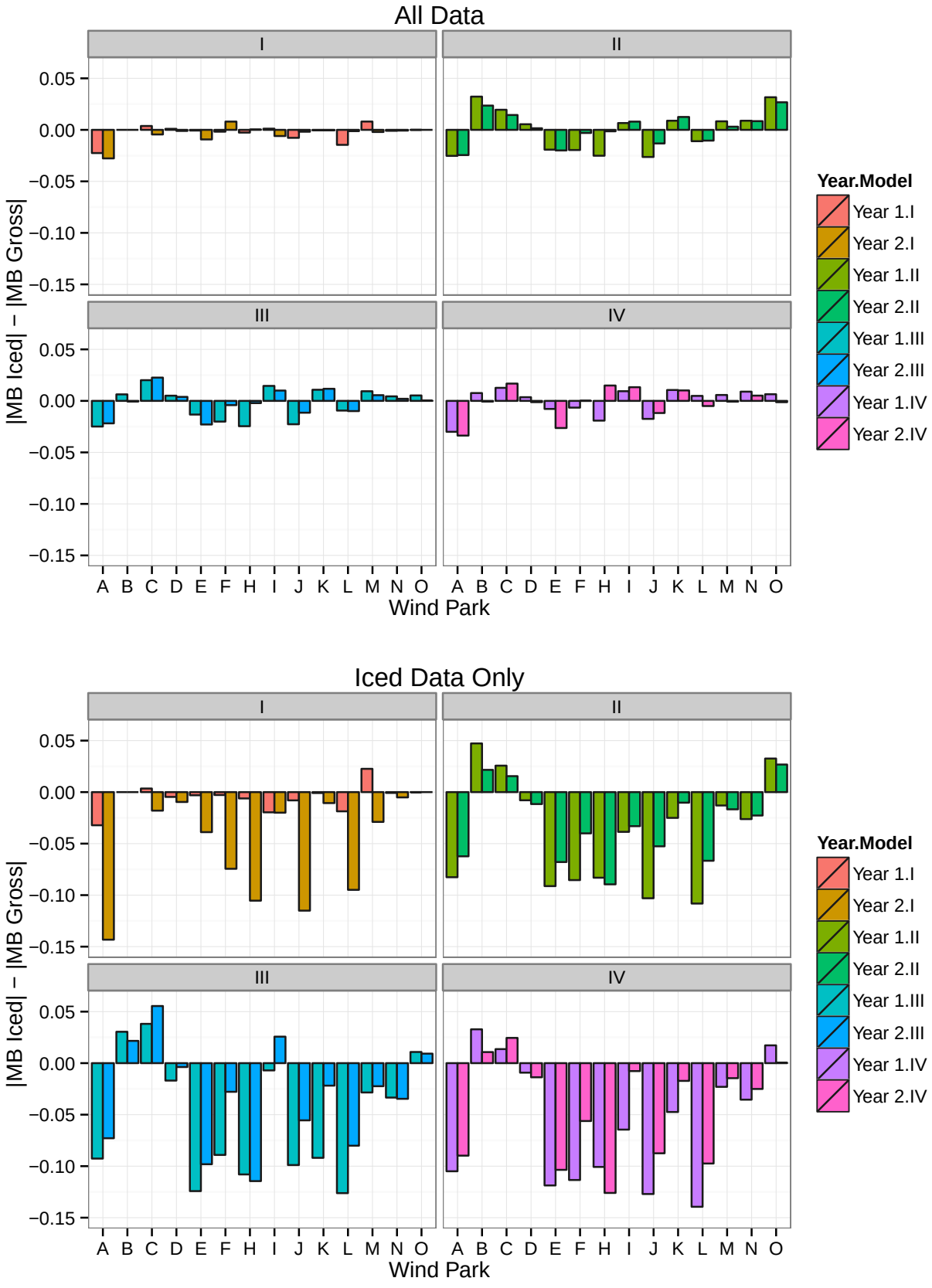

Figure 1.11: Same as figure 1.10, but for model mean bias. To estimate deviation from 0.0, the sign of the mean bias of each model was removed before the differencing.

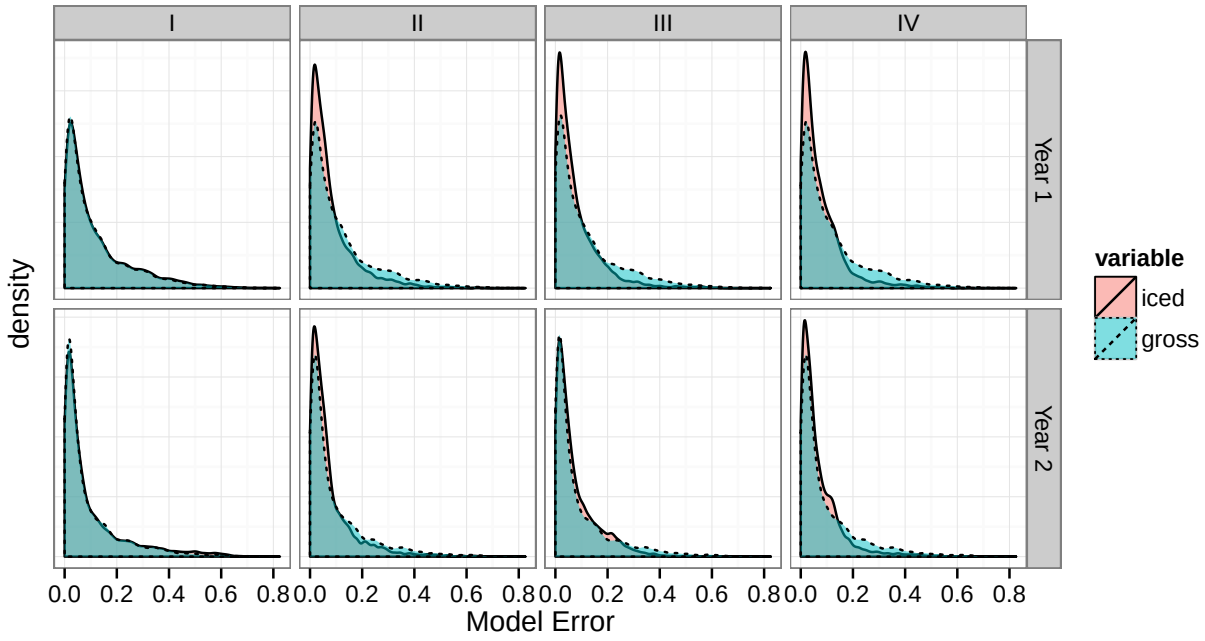

Figure 1.12: Distribution plot of model error as in figure 1.8, but comparing iced and gross model estimates. Pink color denotes the model errors when the ice model production loss is included, while blue is the version without the icing model correction. The top row of figures is for the first year, and the second row is for the second year. The columns denote the different models. Only data points where icing was observed.

differences for the other models agreed with those found in the RMSE plot. Although at site H, all models showed more improvement in power estimation during year 2 than year 1. This was likely due to the larger icing related power lower loss during year 2 than year 1.

Figures 1.12 and 1.13 provide a detailed comparison of each ice model compared to the baseline power curve model. These are density plots for error and bias, combining data from all of the wind parks. The top row shows the difference for the first year, while the bottom row shows results from the second year. For model I the distributions of error were hardly changed between the two estimates, with the gross model having slightly more values around zero in the second year. However, there were a large number of points that shifted from from the positive side of the plot to the negative side (Fig. 1.13). Many of those points had negative biases larger than the positive bias values. This confirms what was found in the previous plots that model I over corrected the icing loss, leading to an increase in error at several sites. Models II, III, and IV perform similarly in both model error and bias. For the first year they all had large improvements in model error, with an increase in the number points below 0.1 error. However, for the second year the reduction in model errors was not as pronounced. The bias plot shows similar features, with the second year correction not being as large as the first year, but the difference between the two years was not as large.

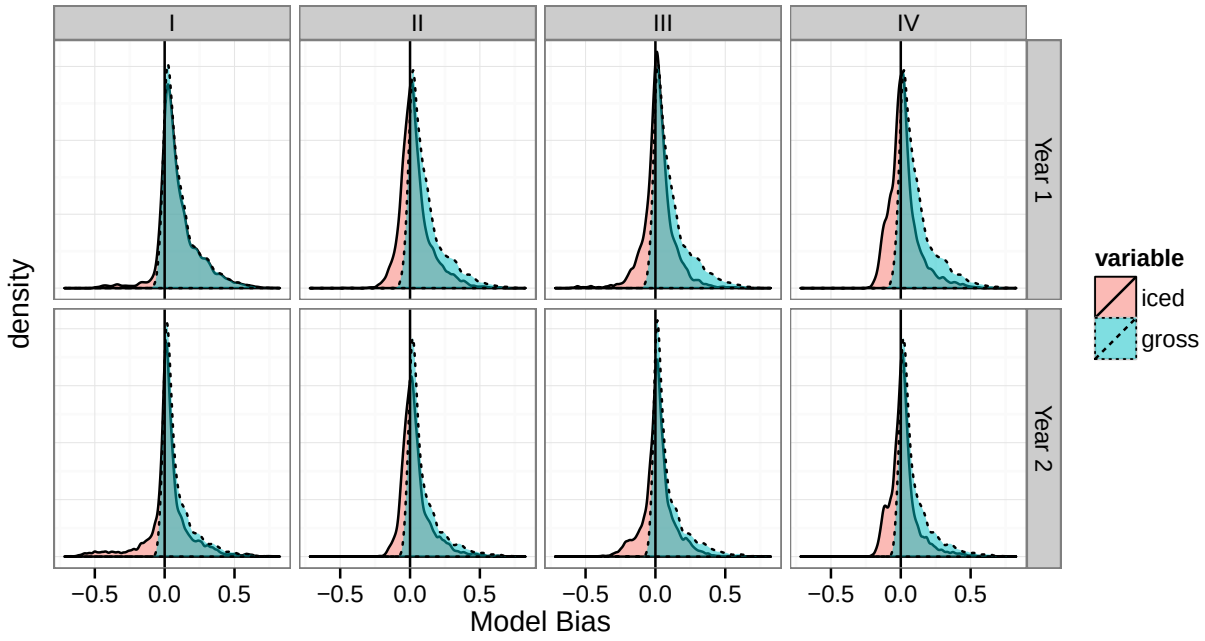

Figure 1.13: Same as 1.12, but for model bias.

1.5 Summary and Conclusions

Ice buildup on wind turbines can add a many additional risks to projects in cold climate regions. One of the largest risks is the potential for decreased power production from iced turbine blades. However, this inter-comparison has shown that the risk of power loss can be reduced through the use of advanced modeling. Three of the four models showed improvements in both RMSE and mean bias at most of the sites with large icing impacts. Model (I), showed the largest improvements in year 2 for mean bias, but had slight increase in RMSE at all sites.

While the models performed similarly to one another, their performance varied greatly across the wind farms. The models tended to do poorly, at the parks with little icing impact, with increased error and bias compared to the non-adjusted estimates. This suggests the models may not be generalized enough to be applied to sites that have not been installed. The ability to use the icing models for siting will require the study of many more parks and wide ranges of turbines.

The four production loss models used in this study vary greatly in their inputs and design. Two of the models fit only one additional term from an icing model to the standard power curve of the wind park, while the other two models combined many different inputs from the physical meteorological and ice models. Despite the differences, three of the four production loss models produced very similar results. This suggests that the model used for estimating the production loss is not as important as the inputs from the physical models.

In this study, there was not significant difference in the physical meteorological and icing models. By design, the meteorological inputs were prescribed, and therefore, identical across the modeling teams. The ice models were also

similar, with the accretion algorithms being based on the Makkonen model, coupled to a fairly simplistic ablation models that primarily consisted of sublimation for temperatures below 0°C, and rapid melting / shedding at temperatures above 0°C.

Given these results the emphasis of future work should focus on physical model development. Based on another inter-comparison study [22], the difference in the model results was likely at the end of the icing periods. That study demonstrated that different icing models tended to agree on and capture the onset of the production loss, but had significant differences in the ending time of the icing event. These models both ended the icing event too soon and extended them too long depending on the event. Therefore, the focus of physical model improvements should be on the ablation algorithms. Additional measurements are then needed to allow more advanced treatment of ice sublimation and erosion on wind turbine blades. The measurements would be most beneficial if they measured the change in ice mass directly on a turbine blade in operation. Measurements of the key meteorological parameters for sublimation are also important.

New measurements could also help to verify and improve the meteorological models. While not examined in this inter-comparison, previous studies [1, 2] have found that differences in meteorological model configuration can lead to differences in ice model results as large as those seen across the different models used in this study. By adding LIDARs and other cloud sensors at wind parks, the different meteorological model setups can be evaluated. The icing models could also be modified to better account for any systematic errors in the meteorological modeling, with better model results. This may include changes, such as the inclusion of the cloud-ice term into the cloud water term as was used in the iceBlade model in this study.

Another area of uncertainty in the results is due to the identification of the ice events from the power curve. In this study, about one-half of the sites showed little impact from icing, despite being installed in climates that would suggest icing is a problem. This may have simply been due to a flaw in the ice detection algorithm employed. The power-curve ice detection method used in this study cannot identify periods where the turbine was stopped. Stops are known to be a major driver in the losses wind parks experience due to icing, but they are not addressed in this study due to the difficulty in detecting stops caused by icing rather than a different event. As newer measurement techniques are developed to detect ice masses directly on the blades, the stops will hopefully be accounted for correctly. In the McDonough study [22], it was noted that the four modeling teams involved in the inter-comparison found four different values for the amount of production lost. This was avoided in this study since DTU provided the ice / no ice flag for the different wind parks to all participants, but there is little certainty that the approach used was the best one.

The inter-comparision of production loss models performed as part of this project has provided a good deal of information to the different modeling teams, and demonstrated the current state of the art for estimating icing related production losses. It has also provided useful information as to what additional information is needed to further advance the models, and what parts of the process have the greatest uncertainty.

Bibliography

[1] Davis N, Hahmann AN, Clausen NE, Žagar M. Forecast of Icing Events at a Wind Farm in Sweden. *Journal of Applied Meteorology and Climatology* Feb 2014; **53**(2):262–281, doi:10.1175/JAMC-D-13-09.1. URL http://journals.ametsoc.org/doi/abs/10.1175/JAMC-D-13-09.1.

[2] Söderberg S, Baltscheffsky M, Bergström H, Thorsson P, Unden P, Esbjörn O. Mesoscale modelling of icing climate: Sensitivity to model and model setup. *Winterwind*, Östersund, Sweden, 2013. URL http://www.winterwind.se/2013/download/Mesoscale modelling of icing climate Sensitivity to model and model setup - S%C3%B6derberg Stefan WeatherTech Scandinavia.pdf.

[3] Davis N, Pinson P, Hahmann AN, Clausen NE, Žagar M. Estimating wind turbine production loss due to icing. *Wind Energy* 2014; **Submitted**.

[4] Wood SN. *Generalized Additive Models: An Introduction with R*. Chapman and Hall/CRC, 2006.

[5] Wood SN. Thin plate regression splines. *Journal of the Royal Statistical Society: Series B (Statistical Methodology)* Feb 2003; **65**(1):95–114, doi:10.1111/1467-9868.00374. URL http://onlinelibrary.wiley.com/doi/10.1111/1467-9868.00374/abstract.

[6] Skamarock WC, Klemp JB, Dudhia J, Gill DO, Barker DM, Duda MG, Huang XY, Wang W, Powers JG. A Description of the Advanced Research WRF Version 3 2008.

[7] National Centers for Environmental Prediction/National Weather Service/NOAA/US Department of Commerce. NCEP FNL Operational Model Global Tropospheric Analyses, continuing from July 1999. 2012, doi: http://dx.doi.org/10.5065/D6M043C6.

[8] Hong SY, Dudhia J, Chen SH. A Revised Approach to Ice Microphysical Processes for the Bulk Parameterization of Clouds and Precipitation. *Monthly Weather Review* Jan 2004; **132**(1):103–120, doi:10.1175/1520-0493(2004)132<0103:ARATIM>2.0.CO;2. URL http://journals.ametsoc.org/doi/abs/10.1175/1520-0493(2004)132<0103:ARATIM>2.0.CO;2.

[9] Mlawer EJ, Taubman SJ, Brown PD, Iacono MJ, Clough Sa. Radiative transfer for inhomogeneous atmospheres: RRTM, a validated correlated-k model for the longwave. *Journal of Geophysical Research* Jul 1997; **102**(D14):16 663, doi:10.1029/97JD00237. URL http://doi.wiley.com/10.1029/97JD00237.

[10] Dudhia J. Numerical Study of Convection Observed during the Winter Monsoon Experiment Using a Mesoscale Two-Dimensional Model. *Journal of the Atmospheric Sciences* Oct 1989; **46**(20):3077–3107, doi:10.1175/1520-0469(1989)046<3077:NSOCOD>2.0.CO;2. URL http://journals.ametsoc.org/doi/abs/10.1175/1520-0469(1989)046<3077:NSOCOD>2.0.CO;2.

[11] Chen F, Dudhia J. Coupling an Advanced Land Surface-Hydrology Model with the Penn State-NCAR MM5 Modeling System. Part II: Preliminary Model Validation. *Monthly Weather Review* Apr 2001; **129**(4):587–604, doi:10.1175/1520-0493(2001)129<0587:CAALSH>2.0.CO;2. URL http://journals.ametsoc.org/doi/abs/10.1175/1520-0493%282001%29129%3C0587%3ACAALSH%3E2.0.CO%3B2.

[12] Janjić ZI. The Step-Mountain Eta Coordinate Model: Further Developments of the Convection, Viscous Sublayer, and Turbulence Closure Schemes. *Monthly Weather Review* May 1994; **122**(5):927–945, doi:10.1175/1520-0493(1994)122<0927:TSMECM>2.0.CO;2. URL http://journals.ametsoc.org/doi/abs/10.1175/1520-0493(1994)122<0927:TSMECM>2.0.CO;2?prevSearch=&sea

[13] Kain JS. The Kain-Fritsch Convective Parameterization: An Update. *Journal of Applied Meteorology* Jan 2004; **43**(1):170–181, doi:10.1175/1520-0450(2004)043<0170:TKCPAU>2.0.CO;2. URL http://journals.ametsoc.org/doi/abs/10.1175/1520-0450%282004%29043%3C0170%3ATKCPAU%3E2.0.CO%3B2.

[14] Finstad KJ, Lozowski EP, Gates EM. A Computational Investigation of Water Droplet Trajectories. *Journal of Atmospheric and Oceanic Technology* Feb 1988; **5**(1):160–170, doi:10.1175/1520-0426(1988)005<0160:ACIOWD>2.0.CO;2. URL http://journals.ametsoc.org/doi/abs/10.1175/1520-0426%281988%29005%3C0160%3AACIOWD%3E2.0.CO%3B2.

[15] Cohen J. *Applied multiple regression/correlation analysis for the behavioral sciences*. 2003.

[16] Breiman L. *Classification and Regression Trees*. CRC Press, 1984.

[17] 12494:2001(E). *Atmospheric icing of structures*. ISO: Geneva, Switzerland, 2001.

[18] Seifert H, Richert F. A recipe to estimate aerodynamics and loads on iced rotor blades. *BOREAS IV*, March 1998, Hetta, Finland, 1998; 1–11.

[19] Makkonen L. Models for the growth of rime, glaze, icicles and wet snow on structures. *Philosophical Transactions of the Royal Society A: Mathematical, Physical and Engineering Sciences* Nov 2000; **358**(1776):2913–2939, doi:10.1098/rsta.2000.0690. URL http://rsta.royalsocietypublishing.org/content/358/1776/2913.short http://rsta.royalsocietypublishing.org/cgi/doi/10.1098/rsta.2000.0690.

[20] Harstveit K, Byrkjedal Ø, Berge E. Validation of Regional In-Cloud Icing Maps in Norway. *IWAIS*, Andermatt, Switzerland, 2009.

[21] Karlsson T, Turkia V, Wallenius T. Icing production loss module for wind power forecasting system. *Technical Report*, VTT Technical Research Centre of Finland, Espoo, Finland 2013. URL http://www.vtt.fi/inf/pdf/technology/2013/T139.pdf.

[22] McDonough. Ice Intercomparison. *Winterwind*, Sundsvall, Sweden, 2014.

This thesis was submitted as partial fulfillment of the requirements for a PhD degree based on work carried out at the Department of Wind Energy at the Technical University of Denmark (DTUWind Energy) over a three year period. Financial support was provided by the Top-Level Research Initiative (TFI) project, Improved Forecast of Wind, Waves and Icing (Icewind), Vestas Wind Systems A/S, and the Nordic Energy Industry. The thesis was submitted in August 2014.

Main Supervisor: Senior Scientist, Andrea N. Hahmann, DTU Wind Energy.
Co-Supervisor: Senior Scientist, Niels-Erik Clausen, DTU Wind Energy.
Co-Supervisor: Specialist, Mark Žagar, Vestas Wind Systems A/S.

DTU Wind Energy
Technical University of Denmark

Risø Campus, Building 118
Frederiksborgvej 399 P.O. Box 49
DK-4000 Roskilde
www.vindenergi.dtu.dk

ISBN 978-87-92896-61-2